



Investigating the role of TIM3 in regulating
the tumour-specific CD8 T-cell response using
a 3D tumour spheroid model.

Carissa C. W. Wong

A thesis submitted in partial fulfilment of the requirements
for the degree of Doctor of Philosophy.

School of Medicine

Cardiff University

September 2021

Word count: 62,025

Abstract

Within the solid tumour microenvironment (TME), immunosuppressive mechanisms limit the cytotoxic potential of tumour-specific CD8 T-cells, including the ligation of coinhibitory receptors expressed on tumour-infiltrating lymphocytes (TILs). TIM3 is a receptor that is highly expressed on exhausted CD8 TILs in the TME and has been described to transmit both costimulatory and coinhibitory signalling. However, contextual regulators of TIM3 signalling are unclear. Additionally, it is unknown to what extent the therapeutic effects of TIM3 blockade, commonly observed in preclinical models, are mediated by direct blockade of TIM3 signalling on CD8 T-cells or other cell types which indirectly promote the anti-tumour CD8 T-cell response.

Using reductionist *in vitro* 2D monolayer and 3D tumour spheroid models of murine renal carcinoma (Renca) and primary CD8 T-cells from neoantigen-specific TCR transgenic mice, the context-dependent role of TIM3 in directly regulating the antigen-specific cytotoxic CD8 T-cell response was investigated. TIM3 overexpression by CD8 T-cells inhibited T-cell cytotoxicity within the 3D Renca model, in a manner reversible by TIM3 blockade. In contrast, TIM3 overexpression enhanced IFN γ secretion and slightly enhanced cytotoxicity by CD8 T-cells within the 2D Renca model, in a manner unaffected by TIM3 blockade. Using overexpression of a truncated form of TIM3 on CD8 T-cells, these divergent effects were found to be dependent upon the TIM3 cytoplasmic tail. TIM3 overexpression enhanced the ability of CD8 T-cells to form cell couples with 2D Renca cells and the interface stability within cell couples.

CEACAM1, a putative TIM3 ligand, was found to abrogate both TIM3-dependent CD8 T-cell suppression in the 3D Renca model and TIM3-dependent CD8 T-cell stimulation in the 2D Renca model, when overexpressed by CD8 T-cells *in cis* with TIM3. CEACAM1 overexpression *in trans* by Renca tumour target cells inhibited T-cell cytotoxicity in the tumour spheroid and monolayer models, in a manner dependent and independent of TIM3, respectively.

Acknowledgements

I am so grateful to my supervisors Christoph Wülfing, Awen Gallimore and David Morgan for mentoring and inspiring me throughout this project. Your critical feedback, kindness and generosity have helped me to grow as a scientist. Thank you also to my F-floor colleagues and mentors who have provided useful feedback throughout my studies and all the staff at CMM.

Thank you to all those who run the GW4 MRC Biomed DTP, including Colin Dayan and Erica Lewis. I am incredibly grateful to the MRC for funding my studentship and this wonderful opportunity. Thank you to David Sheppard for being a lovely mentor. Thanks also to the admin staff at the Cardiff School of Medicine for helping me with all Cardiff-related questions and members of the Gallimore lab who have made my trips to Cardiff enjoyable.

Huge thanks to Andy Herman, Lorena Sueiro Ballesteros and Helen Rice, who have run the flow cytometry facility incredibly well and never failed to brighten those Monday mornings in the FACS room. Thank you so much to Katy Jepson, Alan Leard, Dominic Alibhai, Stephen Cross and Mark Jepson and all those at the Wolfson Bioimaging Facility. You have been the silver lining to trouble-shooting all sorts of microscope issues, at all sorts of hours. In particular, thank you so much to Stephen Cross for being an incredible and kind source of knowledge and advice during months of image analysis development and troubleshooting.

Thank you to Jiahe, Hanin, Luis, Hamida, Jack, Emily, David, Lea, Ore, Laura, Gaia and everyone else who have been wonderful lab colleagues and office mates. I am so grateful to Yikui, Jorge, Drinalda, Sin Lih and Misa for being wonderful friends and a source of scientific advice. Thank you to Misa, Sin Lih and Harry for proof-reading parts of my thesis. Thank you also to all the other friends who have supported me in Bristol or from a distance.

I am endlessly grateful to Ahmah and Kong Kong for inspiring me to make the most of every day. Thank you to Mimi and Didi for being wonderful grandparents. Thanks to Mum, Dad, Chris and Tibs for supporting me through all of my endeavours and education. Thank you to Henry for supporting me through the highs and lows of this project and making me smile every day.

Table of Contents

Chapter 1 Introduction	18
1.1 The Immune System	18
1.2 The Innate Immune System.....	18
1.2.1. Physical barriers.....	18
1.2.2. Innate immune cells	19
1.3 The Adaptive Immune System.....	19
1.3.1. B Lymphocytes.....	20
1.3.2. T Lymphocytes	22
1.4 Cancer	58
1.5 Cancer Immunotherapy.....	58
1.5.1. Tumour immunosurveillance and immunoediting.....	58
1.5.2. Tumour immunosurveillance by T-cells.....	59
1.5.3. The tumour microenvironment (TME)	64
1.5.4. Checkpoint blockade therapies	67
1.5.5. Adoptive T-cell transfer therapies benefit from checkpoint blockade	70
1.5.6. 3D models of the immune response to solid tumours.....	71
1.5.7. The RencaHA + CL4 T-cell Model	75
1.5.8. Immunosuppression in the Renca tumour microenvironment.....	77
1.6 Aims of this project.....	78
Chapter 2 Methods.....	79
2.1 Mice	79
2.2 Media and Reagents	79
2.2.1. Vanilla and IL-2 medium	79
2.2.2. Fluoroborite vanilla medium	79
2.2.3. Phoenix Medium.....	79
2.2.4. Chloroquine	79
2.2.5. Imaging Buffer, FACS/MACS buffer	79

2.3 Cloning	80
2.4 Cell line maintenance	80
2.4.1. Renca cells	80
2.4.2. Phoenix cells	81
2.4.3. Mixed splenocyte reaction: priming of CL4 T-cells.....	82
2.4.4. Priming and culture of polyclonal CD8 T-cells	82
2.5 Spheroids	83
2.5.1. Spheroid culture	83
2.5.2. Haematoxylin and Eosin staining of spheroids.....	83
2.5.3. Hypoxia staining of spheroids.....	84
2.5.4. Viability staining of spheroids.....	85
2.6 Flow cytometry staining	85
2.6.1. T-cell staining.....	85
2.6.2. Renca staining.....	85
2.6.3. Antibody table	87
2.7 Microscopic cytotoxicity assays.....	87
2.7.1. 2D microscopic cytotoxicity assay	87
2.7.2. 3D microscopic cytotoxicity assay	88
2.8 Imaging calcium signalling, T-cell polarisation and interface stability	91
2.8.1. Calcium imaging.....	91
2.8.2. Analysis of coupling frequencies and T-cell morphological polarisation	92
2.8.3. Analysis of T-cell interface stability	92
2.9 Statistical tests.....	93
Chapter 3 Development of a tumour spheroid model	94
3.1 Introduction	94
3.2 Results.....	98
3.2.1. RencaHA ^{tdT} spheroid growth over time	98
3.2.2. The viability profile of RencaHA ^{tdT} MCTS.....	101
3.2.3. RencaHA ^{tdT} spheroids do not display hypoxia	101

3.2.4. HA ^{pep} -pulsed <i>versus</i> unpulsed RencaHA ^{tdT} target cells induced increased IFN γ secretion and comparable cytotoxic function by CL4 T-cells, while decreasing the time taken for target cell death to initiate	104
3.2.5. Development of RencaHA cell lines that express fluorescent sensors for Caspase 8 and Granzyme B activity to enable determination of T-cell cytotoxicity pathways.	109
3.2.6. Development of an image analysis ‘Cancer segmentation’ macro enabled the measurement of various SIL and spheroid spatiotemporal parameters.....	111
3.2.7. Adding high numbers of T-cells per well of RencaHA ^{tdT} spheroids can limit the efficacy of image analysis to identify individual SILs	114
3.2.8. Increasing the number of T-cells added per well of RencaHA ^{tdT} spheroids increases SIL density but has no significant impact on spheroid death, infiltration depth or SIL volume.....	114
3.2.9. DRAQ7 stains dead cells at the RencaHA ^{tdT} spheroid surface and not the dead core of spheroids in the presence of T-cells.....	115
3.2.10. T-cells kill RencaHA ^{tdT} spheroids from the outside-in	118
3.2.11. 2 μ M CTV can be used to stain T-cells with limited toxicity.....	120
3.2.12. HA ^{pep} -specific CL4 T-cells but not polyclonal CD8 T-cells significantly kill spheroids	122
3.2.13. CL4 T-cells increase polyclonal SIL density when plated into the same well of spheroids	125
3.2.14. RencaWT ^{tdT} and RencaHA ^{tdT} spheroids are differentially infiltrated by CL4 T-cells	128
3.3 Discussion	132
3.3.1. Generation of a RencaHA ^{tdT} cell line enabled growth of Renca tumour spheroids that were amenable to 3D imaging, using Matrigel as a scaffold	132
3.3.2. RencaHA ^{tdT} spheroids display a central dead core surrounded by a viable rim of cells.....	133
3.3.3. 10-day-old RencaHA ^{tdT} spheroids do not display hypoxia.....	133
3.3.4. The time of onset of CL4 T-cell killing is faster in the presence of 2 μ g/ml HA ^{pep} -pulsed <i>versus</i> unpulsed RencaHA ^{tdT} cells, but HA ^{pep} -pulsing does not change the rate of killing.....	134

3.3.5. An image analysis macro was developed to quantify spatiotemporal parameters of CL4 T-cell: spheroid interactions and 200,000 CL4 T-cells per well of spheroids provided a suitable effector: target ratio for 3D microscopic cytotoxicity assays.....	135
3.3.6. SILs did not penetrate deeply into RencaHA ^{tdT} spheroids, but killed at the spheroid surface	136
3.3.7. T-cell killing of RencaHA ^{tdT} spheroids during 3D microscopic cytotoxicity assays is dependent on the presence of cognate antigen	136
3.3.8. Conclusion	139
Chapter 4 Divergent TIM3 signalling in the 2D and 3D RencaHA/CL4 models.....	140
4.1 Introduction	140
4.2 Results.....	145
4.2.1. TIM3 overexpression suppresses CL4 CD8 T-cell killing in 3D and is reversible via acute anti-TIM3 blockade.	145
4.2.2. The TIM3 cytoplasmic tail mediates the suppressive effect of TIM3 overexpression on CL4 CD8 T-cell killing in 3D that is reversible by acute TIM3 blockade.....	150
4.2.3. TIM3 overexpression did not significantly affect T-cell cytotoxicity in the 2D system, but enhanced IFN γ secretion.	157
4.2.4. TIM3 overexpression does not affect T-cell calcium signalling upon coupling to targets but does alter the ability of T-cells to couple to targets.....	157
4.2.5. TIM3 overexpression improves T-cell polarisation and the stability of the interface when T-cells couple to targets.	162
4.2.6. The TIM3 cytoplasmic tail mediated the enhanced IFN γ secretion, coupling frequency and improved interface stability of TIM3 overexpressing CL4 T-cells in 2D	165
4.2.7. Cell surface expression of MHC-I, CEACAM1 and Galectin-9 did not differ between RencaHA ^{tdT} cells cultured in 2D and 3D.....	168
4.3 Discussion	171
4.3.1. TIM3 overexpression by CL4 T-cells suppresses T-cell cytotoxicity in the RencaHA ^{tdT} 3D model, in a manner reversible by acute anti-TIM3 blockade and dependent upon the TIM3 cytoplasmic tail.	171

4.3.2. In the RencaHA ^{tdT} 2D model, TIM3 overexpression had no significant effect on T-cell cytotoxicity or calcium flux but in a cytoplasmic tail-dependent manner: enhanced IFN γ secretion, and T-cell coupling frequencies.	172
4.3.3. Conclusion	175
Chapter 5 Regulation of tumour-specific CD8 T-cell function by CEACAM1 and TIM3...	176
5.1 Introduction.....	176
5.2 Results	187
5.2.1. Transduction of CL4 T-cells with DNA constructs encoding CEACAM1 was associated with decreased transduction efficiency, but coexpression of CEACAM1 and TIM3 <i>in cis</i> was achieved.	187
5.2.2. CEACAM1 overexpression alone had no effect on T-cell cytotoxicity <i>versus</i> control T-cells in the 2D and 3D Renca models.....	188
5.2.3. In the 3D Renca model, coexpression of CEACAM1 with TIM3 <i>in cis</i> on CD8 T-cells abrogated TIM3-dependent inhibitory signalling, in a manner not reversible by acute TIM3 blockade.	194
5.2.4. In the 2D Renca model, coexpression of CEACAM1 with TIM3 <i>in cis</i> abrogated TIM3-dependent stimulatory signalling, in a manner not reversible by acute TIM3 blockade.	201
5.2.5. CEACAM1 <i>in trans</i> inhibits tumour-specific CD8 killing but enhanced IFN- γ secretion irrespective of TIM3 expression by T-cells.	205
5.2.6. CEACAM1 <i>in trans</i> does not suppress tumour-specific CD8 T-cell calcium flux during cell coupling to targets or the ability of the T-cells to couple to targets but causes defective T-cell polarisation and reduced stability of the T-cell: target cell interface in 2D.	208
5.2.7. Renca cells that overexpress CEACAM1 form spheroids with altered morphology.	214
5.2.8. CEACAM1 overexpression by RencaHA ^{tdT} spheroids <i>in trans</i> inhibits tumour-specific CD8 T-cell killing in the 3D Renca model.	216
5.2.9. CEACAM1 acts <i>in trans</i> to suppress tumour-specific CD8 T-cell killing and the suppression is reversible by acute TIM3 blockade, suggesting CEACAM1 <i>in trans</i> can act as a functional ligand for TIM3	222
5.3 Discussion	229

5.3.1. Technical caveats to consider: investigating the role of CEACAM1 <i>in cis</i> in modulating TIM3-dependent T-cell signalling.....	230
5.3.2. CEACAM1 coexpression with TIM3 <i>in cis</i> abrogated the suppressive effect of TIM3 overexpression on T-cell cytotoxicity.....	231
5.3.3. CEACAM1 coexpression with TIM3 <i>in cis</i> abrogated the stimulatory effect of TIM3 overexpression on T-cell cytotoxicity and IFN- γ secretion in the RencaHA ^{tdT} 2D model.....	233
5.3.4. CEACAM1 overexpression <i>in trans</i> by RencaHA targets suppressed CL4 T-cell cytotoxicity in both the 2D and 3D models, but the suppressive effect was only reversible via acute TIM3 blockade in the 3D model.	233
5.3.5. CEACAM1 overexpression <i>in trans</i> by RencaHA targets caused defective T-cell polarisation and interface stability, with no effect on coupling frequencies or calcium signalling, during T-cell coupling with Renca targets in the 2D model.	235
5.3.6. Conclusion	236
Chapter 6 General Discussion.....	238
6.1 Overview of project rationale and aim.....	238
6.2 Development and characterisation of a 3D RencaHA model to study the tumour-specific CL4 CD8 T-cell response.....	241
6.3 Divergent TIM3 signalling in the 3D <i>versus</i> 2D RencaHA model	243
6.4 CEACAM1 <i>in cis</i> abrogates TIM3 signalling in the 3D and 2D RencaHA models ...	246
6.5 CEACAM1 <i>in trans</i> induces inhibitory signalling through TIM3.....	248
Chapter 7 Bibliography	250
Chapter 8 Supplementary Figures	278
8.1 FACS gating for isolating GFP-positive retrovirally transduced CL4 T-cells.	278
8.2 Gating for flow cytometry analysis of RencaHA ^{tdT} cells from 2D and 3D culture. .	279
8.3 Gating strategy to determine TIM3 and CEACAM1 cell surface expression on GFP-positive CL4 T-cells transduced with TIM3-GFP, CEACAM1-TIM3-GFP and CEACAM1-GFP retroviral constructs.	280
8.4 Gating strategy for isolating RencaHA ^{tdT} and RencaHA ^{CEAC1} cells to confirm CEACAM1 expression levels by antibody-staining and flow cytometry.	282

Table of Figures

Figure 1.1 Immunoglobulin structure.....	21
Figure 1.2 MHC I and MHC II antigen presentation pathways	26
Figure 1.3 Thymic T-cell development	29
Figure 1.4 TCR signalling and CD28 costimulation	33
Figure 1.5 CD8 T-cells induce target cell death via two main pathways	38
Figure 1.6 MTOC translocation and structure of the immune synapse	43
Figure 1.7 Inhibitory and costimulatory TIM3 signalling.....	56
Figure 1.8 The cancer-immunity cycle.....	63
Figure 1.9 The RencaHA and CL4 CD8 T-cell model.....	76
Figure 1.10 Schematic overview of thesis key findings.	Error! Bookmark not defined.
Figure 2.1 Retroviral transduction of CL4 T-cells using the ecotropic Phoenix packaging cell line.....	82
Figure 3.1. RencaHA ^{tdT} spheroid growth over time.....	99
Figure 3.2. Schematic to show integration of Renca spheroid and T-cell culture timelines.	100
Figure 3.3. 10-day-old spheroids exhibited a dead core.	102
Figure 3.4. 10-day-old spheroids did not display hypoxia.....	103
Figure 3.5. The HA ^{pep} expression level of unpulsed RencaHA ^{tdT} cells was not sufficiently different from RencaHA ^{tdT} 2µg/ml HA ^{pep} -pulsed targets to alter the rate of CL4 killing during a 2D microscopic killing assay, but did lead to lower IFN γ production by the CL4. The time before RencaHA ^{tdT} target cells were killed by CL4 was reduced when target cells were HA ^{pep} -pulsed <i>versus</i> unpulsed.	106
Figure 3.6. The rate of CL4 killing was comparable between RencaHA ^{tdT} unpulsed and 0.002µg/ml HA ^{pep} -pulsed RencaWT ^{tdT} targets during a 2D microscopic killing assay.	108
Figure 3.7 RencaHA lines expressing fluorescent sensors for granzyme B (RencaHA ^{GzmB}) and caspase 8 (RencaHA ^{Casp8}) activity were generated and enabled measurement of T-cell-dependent apoptosis; Renca cells were susceptible to GzmB-mediated apoptosis in the presence of T-cells but were unaffected by Fas-FasL dependent death in the absence of T-cells.....	110
Figure 3.8. Schematic to show strategy for imaging and image analysis.....	113
Figure 3.9. Incubation of 500, 000 T-cells per well of spheroids resulted in SIL densities that reduced the efficacy of image segmentation to identify individual SILs, DRAQ7 did not stain the dead core of spheroids when T-cells are present.	116
Figure 3.10. Titration of CL4 T-cell number per well of RencaHA ^{tdT} spheroids.	117

Figure 3.11. CL4 SILs killed RencaHA ^{tdT} spheroids outside-in.	119
Figure 3.12. Titration of CFSE and CTV for staining T-cells.	121
Figure 3.13. CL4 but not polyclonal CD8 SILs killed HA ^{pep} -pulsed RencaHA ^{tdT} spheroids, polyclonal CD8 T-cells suppressed the cytotoxicity of CL4 T-cells and CL4 T-cells displayed a more blasted morphology than polyclonal T-cells.	123
Figure 3.14. The presence of CL4 T-cells increased polyclonal CD8 SIL density, while polyclonal CD8 cells displayed higher motility <i>versus</i> CL4 T-cells.	126
Figure 3.15. Spheroid volume and shape were homogeneous between CL4, polyclonal, both CL4 + polyclonal and spheroid only groups.	127
Figure 3.16. CL4 SILs differentially infiltrated RencaWT ^{tdT} and RencaHA ^{tdT} spheroids by 12h post plating T-cells + spheroids.	130
Figure 3.17. Spheroid volume and shape was homogenous between RencaWT ^{tdT} and RencaHA ^{tdT} spheroids that were used to assess the role of antigen specificity.	131
Figure 4.1 TIM3-GFP overexpression suppressed CL4 T-cell cytotoxicity and was reversed by acute incubation with TIM3 blocking antibody in the 3D microscopic cytotoxicity assay.	148
Figure 4.2 Differences in SIL density and spheroid dimensions did not account for differences in cytotoxicity resulting from TIM3 overexpression.	149
Figure 4.3 The TIM3 cytoplasmic tail mediated the suppressive effect of TIM3-GFP overexpression in 3D by inhibition of spheroid death and delaying the onset of spheroid death.	153
Figure 4.4 Differences in spheroid dimensions did not account for differences in cytotoxicity resulting from TIM3 overexpression, but SIL density was higher in the TIM3 ^{cyt-ve} -GFP groups.	154
Figure 4.5 Spheroid death volumes normalised to SIL density levels indicated that the TIM3 cytoplasmic tail mediated the suppressive effect of TIM3-GFP overexpression in 3D by inhibition of spheroid death.	155
Figure 4.6 TIM3-GFP overexpression did not significantly affect CL4 T-cell cytotoxicity during co-incubation with K ^d HA-pulsed 2D RencaHA ^{tdT} target cells in the 2D microscopic cytotoxicity assay, but enhanced IFN γ secretion by CL4 T-cells.	159
Figure 4.7 TIM3-GFP overexpression did not affect calcium flux within CL4 T-cells upon tight cell coupling to 2 μ g/ml or 2ng/ml K ^d HA-pulsed 2D Renca target cells but enhanced the frequency of T-cells that formed tight couples.	160
Figure 4.8 Overexpression of TIM3-GFP by CL4 T-cells, under higher and lower peptide stimulus conditions, did not and did affect T-cell elongation, respectively.	
Overexpression of TIM3-GFP by CL4 T-cells decreased the percentage of T-cells with off-	

interface lamellipodia and delayed the onset of off-interface lamellipodia in the context of both higher and lower peptide stimulus.	164
Figure 4.9 Data indicated that the TIM3 cytoplasmic tail enhanced the rate of killing and IFN γ secretion levels of TIM3-overexpressing CL4 under both higher and lower peptide stimulus conditions, with differences more evident in the context of a lower peptide stimulus. Under lower peptide stimulus, the TIM3 cytoplasmic tail also seemed to stabilise the interface between CL4 T-cells and target cells.	166
Figure 4.10 Cell surface expression levels of CEACAM1, Galectin-9 and MHC I did not significantly differ between Renca cells grown in 3D and 2D.	170
Figure 5.1 Graphical chapter overview: investigating how CEACAM1 <i>in cis</i> (on CL4 T-cells) and <i>in trans</i> (on Renca cells) coregulates tumour-specific CD8 T-cell function with TIM3, using the 2D and 3D Renca models and TIM3 blockade (using the RMT3-23 anti-TIM3 monoclonal antibody (mAb)).....	186
Figure 5.2 Transduction of CL4 T-cells with DNA constructs encoding CEACAM1 was associated with a decreased transduction efficiency, but coexpression of CEACAM1 and TIM3 <i>in cis</i> was achieved.	190
Figure 5.3 CEACAM1 overexpression did not affect CL4 T-cell cytotoxicity in the 3D or 2D RencaHA ^{tdT} models.	193
Figure 5.4 In the 3D microscopic cytotoxicity assay, CEACAM1 co-expression with TIM3 <i>in cis</i> enhanced and inhibited CL4 cytotoxicity compared to CL4 T-cells which overexpressed solely TIM3 or CEACAM1, respectively. Differences in SIL density and spheroid dimensions did not account for differences in cytotoxicity resulting from TIM3 and/or CEACAM1 overexpression.	197
Figure 5.5 Acute TIM3 blockade using incubation with anti-TIM3 mAb did not affect the cytotoxicity of CL4 T-cells which co-expressed CEACAM1 and TIM3 <i>in cis</i> during the 3D microscopic cytotoxicity assay. Differences in spheroid dimensions did not contribute to the lack of effect of acute TIM3 blockade of CL4 T-cells which co-expressed CEACAM1 and TIM3 <i>in cis</i> . SIL densities were indicated to differ between groups.....	199
Figure 5.6 CEACAM1 co-expression with TIM3 <i>in cis</i> suppressed CL4 T-cell cytotoxicity and IFN γ secretion during co-incubation with K ^d HA-pulsed 2D RencaHA ^{tdT} target cells in the 2D microscopic cytotoxicity assay, compared to either TIM3 or CEACAM1 overexpressing CL4 T-cells, while TIM3 overexpressing T-cells secreted a higher level of IFN γ compared to CEACAM1 overexpressing T-cells.	203
Figure 5.7 Acute TIM3 blockade using incubation with anti-TIM3 mAb did not affect cytotoxicity or IFN γ secretion by CL4 T-cells which co-expressed CEACAM1 and TIM3 <i>in cis</i> , during the 2D microscopic cytotoxicity assay.	204

Figure 5.8 RencaHA cells were transduced to overexpress CEACAM1-tdTomato. CEACAM1 *in trans* had no affect on calcium flux or coupling frequency of Ftractin CL4 T-cells. CEACAM1 *in trans* inhibits CL4 T-cell killing irrespective of TIM3 expression level or acute anti-TIM3 blockade.....206

Figure 5.9 CEACAM1 *in trans* overexpressed by Renca had no effect on calcium flux or coupling frequency of Ftractin CL4 T-cells to 2D targets.....211

Figure 5.10 CL4 T-cells that coupled to Renca targets that overexpressed CEACAM1 *in trans* displayed a longer morphology and a higher frequency of off-interface lamellipodia irrespective of TIM3 expression level by CL4 T-cells. T-cells which overexpressed TIM3-GFP, but not Ftractin-GFP, showed a faster onset of off-interface lamellipodia when coupling to targets that overexpressed CEACAM1 *in trans*. With Renca^{CEAC1} targets, at early timepoints, CL4 that overexpressed TIM3-GFP *versus* Ftractin-GFP showed a longer morphology, and a lower percentage of cells that displayed off-interface lamellipodia was higher, while time of off-interface lamellipodia did not differ.213

Figure 5.11 RencaHA^{CEAC1} spheroids displayed a more irregular and elongated morphology compared to RencaHA^{tdT} spheroids.215

Figure 5.12 CEACAM1 *in trans* overexpression by RencaHA spheroids was indicated to inhibit the cytotoxicity of CL4 that overexpressed Ftractin-GFP. SIL densities and volumes at the surface of spheroids did not differ between groups.....218

Figure 5.13 CEACAM1 *in trans* overexpression by RencaHA spheroids inhibited cytotoxicity of CL4 that overexpressed TIM3-GFP. SIL densities at the surface of spheroids differed between groups, but spheroid volumes did not differ.220

Figure 5.14 Acute TIM3 blockade had no effect on CEACAM1-mediated suppression of CL4 T-cells that overexpressed Ftractin-GFP. SIL densities differed between conditions, spheroid volumes did not. Normalisation of spheroid death to SIL densities showed suppression of T-cell cytotoxicity by CEACAM1 but this was not reversed by acute anti-TIM3 blockade.225

Figure 5.15 Acute TIM3 blockade reversed CEACAM1-mediated suppression of CL4 T-cells that overexpressed TIM3-GFP. SIL densities differed between conditions, spheroid volumes did not. Normalisation of spheroid death to SIL densities showed suppression of T-cell cytotoxicity by CEACAM1 that was partially reversed by acute anti-TIM3 blockade.227

Figure 5.16 Summary: how TIM3 regulates tumour-specific CL4 CD8 T-cell function in the 2D and 3D Renca tumour models and the role of CEACAM1 *in trans* and *in cis*.....228

Figure 6.1 Schematic overview of key thesis findings.240

Figure 8.1 Gating strategy for retrovirally transduced CL4 T-cells that were isolated by fluorescence-activated cell sorting (FACS) for GFP-positivity, 72h post-transduction. ...278

Figure 8.2 Flow cytometric gating strategy for Renca cells from 2D and 3D culture to obtain live single cells for antibody-staining for CEACAM-1, MHC-I and Galectin-9 expression.....279

Figure 8.3 TIM3-GFP⁺⁺ cells expressed 1.8-fold more TIM3 than CEACAM1-TIM3-GFP⁺⁺ cells, CEACAM1-GFP cells expressed 1.2-fold more CEACAM1 than CEACAM1-TIM3-GFP⁺⁺ cells.....280

Figure 8.4 RencaHA^{tdT} and RencaHA^{CEAC1} cells were sorted to obtain live single cells. ...282

Abbreviations

ADAM	a disintegrin and metalloprotease
ADAP	adhesion and de-granulation adaptor protein
AhR	aryl hydrocarbon receptor
AID	activation-induced cytidine deaminase
AIRE	autoimmune regulator
Akt	activation of protein kinase
APC	antigen-presenting cells
Arp2/3	actin-related protein 2/3
ATT	adoptive T-cell transfer
BCR	B-cell receptor
BID	BH3-interacting domain death agonist
cAMP	cyclic adenosine monophosphate
CDR	complementarity-determining region
CEACAM1	carcinoembryonic antigen-related cell adhesion molecule 1
CHO	Chinese hamster ovary
CLIP	class-II associated invariant chain peptide
CLR	C-type lectin receptors
CRD	carbohydrate recognition domains
CTLA4	cytotoxic T-lymphocyte associated protein-4
DAG	diacylglycerol
DAMP	damage-associated molecular patterns
DED	death effector domain
DN	double-negative
ELISA	enzyme-linked immunosorbent assays
Eomes	eomesodermin
ER	endoplasmic reticulum
FADD	Fas-associated death domain

FasL	Fas ligand
FGL1	fibrinogen-like protein 1
GADS	growth factor receptor-bound protein 2-related adapter downstream of Shc
GRB2	growth factor receptor-bound protein 2
GSK3	glycogen synthase kinase-3
GzmB	granzyme B
IDO	indoleamine-2,3-deoxygenase
ICOS	inducible costimulator
Ig	immunoglobulin
ILC	innate lymphoid cells
IP3	inositol 1,4,5-triphosphate
IS	immune synapse
ITAMs	immunoreceptor tyrosine activation motifs
ITIM	immunoreceptor tyrosine-based inhibitory motif
Itk	inducible tyrosine kinase
iTregs	inducible regulatory T-cells
ITSM	immunoreceptor tyrosine-based switch motif
ITT	immunoglobulin tail tyrosine
LAG3	lymphocyte activation gene-3
LCMV	chronic lymphocytic choriomeningitis
LPS	lipopolysaccharide
MAPK	mitogen-activated protein kinase
MHC	major histocompatibility complex
MG	matrigel
MIIC	MHC class II compartments
MPEC	memory-precursor effector cells
mTEC	medullary thymic epithelial cell
MTOC	microtubule-organising centre

NFAT	nuclear factor of activated T-cells
NFκB	nuclear factor kappa-light-chain-enhancer of activated B cells
NK	natural killer
NLR	nucleotide-binding oligomerisation domain-like receptor
NPF	nucleation-promoting factor
nTreg	natural regulatory T-cell
OIL	off-interface-lamellipodia
PAG	phosphoprotein associated with glycosphingolipid-enriched microdomains
PAMP	pathogen-associated molecular pattern
PD1	programmed cell death 1
PI3K	phosphatidylinositol-3-kinase
PKCθ	protein kinase C-theta
PLC	peptide loading complex
pMHC	peptide- MHC
pTreg	peripheral regulatory T-cell
RICD	restimulation-induced cell death
RLR	RIG-I-like receptors
S1P	sphingosine-1-phosphate
S1PR	sphingosine-1-phosphate receptor
SEB	<i>Staphylococcus aureus</i> enterotoxin B
SHP1	Src homology region 2 domain-containing phosphatase 1
SHP2	Src homology region 2 domain-containing phosphatase 2
SLEC	short-lived effector T-cells
SLO	secondary lymphoid organ
SLP76	Src homology 2 domain containing leukocyte phosphoprotein of 76 kDa
TAP	transporter associated with antigen processing
Tbet	T-box transcription factor
TCM	central-memory T-cell

TCR	T-cell receptor
TEM	effector-memory T-cell
TIGIT	T-cell immunoglobulin and ITIM domain
TIM3	T-cell immunoglobulin and mucin domain-containing protein 3
TLR	Toll-like receptor
TME	tumour microenvironment
TNFR	tumour necrosis factor receptor
tTreg	thymic regulatory T-cell
VAV1	Vav guanine nucleotide exchange factor 1
WASp	Wiskott-Aldrich syndrome protein
ZAP70	zeta chain-associated 70kDa tyrosine phosphoprotein
β_2 M	beta-2 microglobulin

Chapter 1 Introduction

1.1 The Immune System

The immune system is a diverse group of cells that has evolved to protect the body from disease-causing microorganisms, called pathogens (1, 2). Central to its role, the immune system can distinguish between self and non-self which prevents the mounting of immune responses that can damage host tissue (1, 2). When the ability to recognise self is lost, autoimmune disease results. Coevolution between pathogens and the immune system has also given the immune system the ability to tolerate non-harmful, commensal microorganisms that may be beneficial to the host, such as gastrointestinal microbiota (3). Immune tolerance mechanisms help to prevent unnecessary immune responses, maintaining tissue homeostasis and limiting collateral damage to healthy tissue (1-3). A benefit of the evolved immune response against pathogens is that neoplastic cells can also be recognised by the immune system because malignant transformation often produces differences between healthy self and neoplastic cells (4). Therefore, cancer cells can appear as non-self and a target for immune-mediated destruction (4). Cellular stress signals resulting from mechanical tissue damage can also activate the immune response to facilitate tissue repair (5); similar pathways to the wound healing response can also be triggered in tumours to support tumour growth (4). There are two main branches of the immune system: the innate and the adaptive immune system. Dynamic cooperation between the innate and adaptive immune system generates a protective immune response which supports host survival, while the multi-pronged inhibition of this response in tumours is a key barrier to immune destruction of cancer cells and a target for cancer immunotherapy (1, 6).

1.2 The Innate Immune System

The innate immune system is comprised of physical barriers, cellular immune responses and small molecule defences which are encoded in the germ line (2, 7). The cellular innate immune response has evolved to recognise the most common molecular patterns found among microbes and external toxins (2, 7). Therefore, the innate immune system is poised to rapidly respond, in a matter of minutes, to an invading pathogen or toxin (7).

1.2.1. Physical barriers

The first defence of the innate immune system involves physical barriers: epithelial layers made of cells joined together by tight junctions form a barrier to the external environment, secreted mucous lines epithelial surfaces and helps to trap microorganisms, and tiny hair-like projections called cilia move in waves to continuously waft mucous away for removal (1, 2, 7).

1.2.2. Innate immune cells

Innate immune cells include a wide range of cell types which differentiate from pluripotent haematopoietic stem cells in the bone marrow, do not have somatically recombined receptors, and lack the capacity for immunological memory (1, 2, 7). Cells of the innate immune system recognise evolutionarily conserved pathogen-associated molecular patterns (PAMPs), which include bacterial cell wall components such as lipopolysaccharide (LPS), or viral nucleic acids (2, 7). Innate immune cells can also recognise the molecular features of damaged or dying host cells, called damage-associated molecular patterns (DAMPs) (1, 7). Innate immune cells recognise PAMPs and DAMPs via pattern recognition receptors (PRR), which include Toll-like receptors (TLRs), nucleotide-binding oligomerisation domain-like receptors (NLRs), RIG-I-like receptors (RLRs) and C-type lectin receptors (CLRs) (1, 8).

The majority of innate immune cells derive from a common myeloid progenitor in the bone marrow, except for natural killer (NK) cells and innate lymphoid cells (ILCs), which are of lymphoid lineage. Innate immune cells have various primary roles. Phagocytes such as neutrophils and macrophages kill pathogens via engulfment into endocytic vesicles called phagosomes (2). Subsequent fusion of phagosomes with lysosomes exposes the pathogens to antimicrobial peptides and enzymes (2). Granulocytes such as eosinophils, basophils and mast cells contain dense cytoplasmic granules of anti-microbial proteins and histamine which they release upon activation; this enables killing of parasites that are too large for phagocytosis (2). Natural killer (NK) cells express both activating and inhibitory receptors (9, 10). Activating receptors recognise ligands that are upregulated during cellular stress because of infection or malignant transformation (9, 10). Inhibitory receptors recognise host cells by binding to major histocompatibility complex (MHC) molecules expressed by self-tissue and signal to suppress NK cell cytotoxicity (9, 10). Downregulation of MHC I by host cells upon viral infection or malignant transformation removes this inhibitory signal and activates the NK cell to kill by secreting granzymes and perforin into the target cell, which induces apoptosis (9, 10). ILCs fall into subsets that have similar transcriptional and functional programs to T helper cells (T helper cell subsets are discussed in Section 1.3.2.10) but lack somatically recombined receptors (11). ILCs release cytokines and regulate T-cell responses (11). Dendritic cells (DCs) are important in the priming of T-cells, providing a bridge between innate and adaptive immune responses (discussed later) (12).

1.3 The Adaptive Immune System

The adaptive immune system is made up of lymphoid cells that express somatically recombined antigen receptors and have the capacity for immunological memory. The adaptive immune response requires the proliferation of a small population of antigen-specific cells and therefore takes longer to respond than the innate immune system.

1.3.1. B Lymphocytes

B-cells recognise antigen via membrane-bound immunoglobulin, called the B-cell receptor (BCR), which consists of two heavy and two light chains connected to each other by disulphide bonds (1, 13). A schematic of the immunoglobulin structure is shown in Figure 1.1. Each heavy and light chain is comprised of constant and variable domains (1, 13). The main effector function of B-cells is the secretion of immunoglobulin by terminally differentiated B-cells called plasma cells (1, 13). The immunoglobulin (Ig) produced by a single B cell clone recognises a specific antigen(1, 13). Each of the two antigen-binding sites of an Ig molecule (also called an antibody) is made up of six complementarity-determining regions (CDRs), three located in each of the variable domains in the heavy chain and the light chain, which come together to form the hypervariable antigen binding site (1, 13). Based on conformational complementarity, specific antigens will bind to the CDRs of a given antibody (1, 13). The antibody domains that bind antigen are called the IgV domains, whereas the rest of the antibody is comprised of less variable constant domains (1, 13). There are two types of Ig light chain, lambda (λ) and kappa (κ), which are thought to impart some functional differences (1, 13). Furthermore, there are five major classes of immunoglobulin based on the type of heavy chain: IgM, IgG, IgD, IgA and IgE (1, 13). The heavy chain constant regions determine the type, localisation and function of the antibody (1, 13). Antibodies have various functional activities including: neutralisation of toxins produced by pathogens, which prevents toxins entering and damaging cells; opsonisation where antibodies coat pathogens to promote engulfment by phagocytes; activation of the complement system (a group of proteins which circulate in the blood) which can lead to direct lysis of the cell and promote phagocytosis (1, 13).

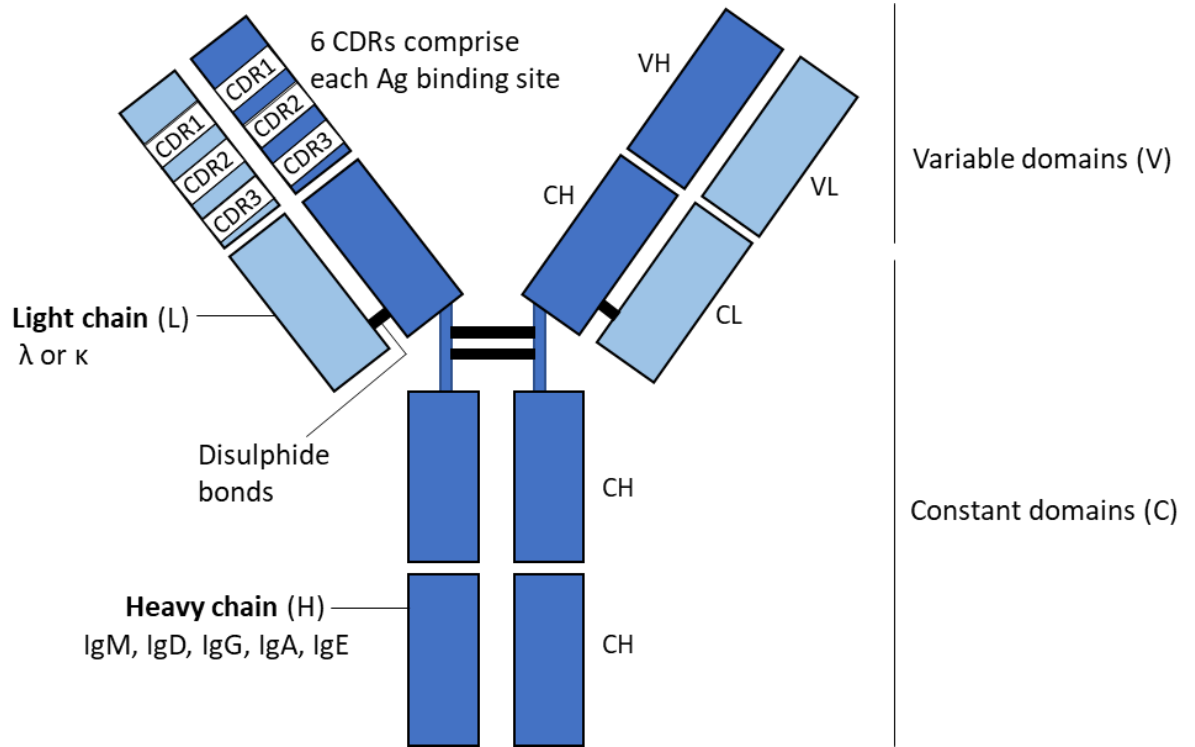


Figure 1.1 Immunoglobulin structure

Immunoglobulins are comprised of two heavy chains (dark blue) and two light chains (light blue). Disulphide bonds (black) connect the heavy and light chains, and the heavy chains to each other. Each light chain contains one variable domain (VL) and one constant domain (CL); each heavy chain contains one variable domain (VH) and three constant domains (CH). Each antigen (Ag) binding site is comprised of six complementarity-determining regions (CDRs), three of which are provided by each of the variable domains of a light and heavy chain. Figure based on Figure 1 from (14).

Naïve B-cells emigrate from the bone marrow and enter secondary lymphoid organs (SLOs) where they are first activated in follicular regions to produce IgM and IgD (1, 13). IgM circulates in the blood and is produced initially upon B-cell activation; IgD proteins derive from the same mRNA transcript as IgM molecules but are produced from alternative splicing of the mRNA (1, 13). Some B cells then enter specific regions called germinal centres where they undergo a process called Ig class switching which requires the recognition of antigen by the BCR, in addition to costimulatory signals from T follicular helper cells (Tfh); Tfh cells surround germinal centres and support isotype switching via engagement of CD40 on B cells by CD40L on T-cells (1, 13). Isotype switching enables the production of IgG, IgA and IgE and relies on alternative splicing of the heavy chain gene regions (1, 13). Meanwhile, during B cell proliferation in germinal centres, another process called affinity maturation increases the binding affinities of antibodies for the antigen; this is driven by somatic hypermutation mediated by an enzyme called activation-induced cytidine deaminase (AID) (1, 13). AID introduces mutations into the IgV domains (1, 13). B cells that acquire mutations which enhance the affinity of their BCR for binding antigen gain a survival advantage, as they process and present antigen to Tfh cells more efficiently, which provides them with more costimulation from Tfh cells (1, 13).

The specific stimulus and cytokine environment within the germinal centre determines which antibody isotypes are produced (1, 13). IgG can be found in blood and tissues and is the most abundant isotype in the body (1, 13). IgA is also a predominant antibody isotype found in mucosal surfaces such as in the gut and respiratory system, while IgE functions to remove parasites and contributes to immune responses that cause allergy and asthma (1, 13). Following B-cell isotype switching and affinity maturation in the germinal centres of SLOs, B cells differentiate into two main subsets: 1) extrafollicular short-lived plasma cells which produce high levels of Ig and migrate to peripheral tissues; 2) memory B cells which express the BCR and secrete no to little Ig and reside in either specific tissues, SLOs or the circulation (1, 13). During secondary infection, memory B-cells respond rapidly, enabling faster production of class-switched Ig molecules that have higher affinity for antigen than in the primary immune response (1, 13).

1.3.2. T Lymphocytes

T-cells each express a T-cell receptor (TCR) which enables recognition of antigen presented in complex with MHC class I or class II proteins (1). As with the BCR, a single TCR recognises a specific antigen (1). The most common TCR is made up of an α and β chain where the α chain is formed from somatic recombination of variable and joining gene segments, and the β chain is formed from somatic recombination of polymorphic variable, diversity and joining gene segments (discussed further in Section 1.3.2.3) (1, 15).

1.3.2.1 CD4 T-cells recognise antigen presented in complex with MHC class II

CD4 T-cells recognise exogenously derived antigen presented by MHC class II molecules (1, 16). A schematic depicting antigen processing and presentation by MHC class II molecules is shown in Figure 1.2, right. MHC II proteins are exclusively expressed by professional antigen-presenting cells (APCs) such as dendritic cells (DCs), macrophages, and B-cells (1, 16). Polymorphic gene regions encode the MHC II proteins: HLA-DR, HLA-DQ and HLA-DP in humans, and H2-A and H2-E in mice (1, 16). Within the endoplasmic reticulum (ER) of APCs, MHC II proteins fold in complex with an invariant chain (Ii) protein (1, 16). This complex is transported to late endosomes, called MHC class II compartments (MIIC) (1, 16). Cathepsin proteases within the MIIC cleave the Ii, leaving a peptide called the class-II associated invariant chain peptide (CLIP) bound to the peptide-binding groove of MHC class II proteins (1, 16). Exogenous proteins are endocytosed by APCs and proteolytically degraded in endosomes which then fuse with the MIIC (1, 16). The MHC II-like molecule HLA-DM is also present within the MIIC; HLA-DM binds to and stabilises MHC II molecules thus enabling CLIP to be released and exogenously derived peptides can bind onto the peptide-binding groove (1, 16). The peptide-MHC complexes are then transported to the cell surface (1, 16).

1.3.2.2 CD8 T-cells recognise antigen presented in complex with MHC class I

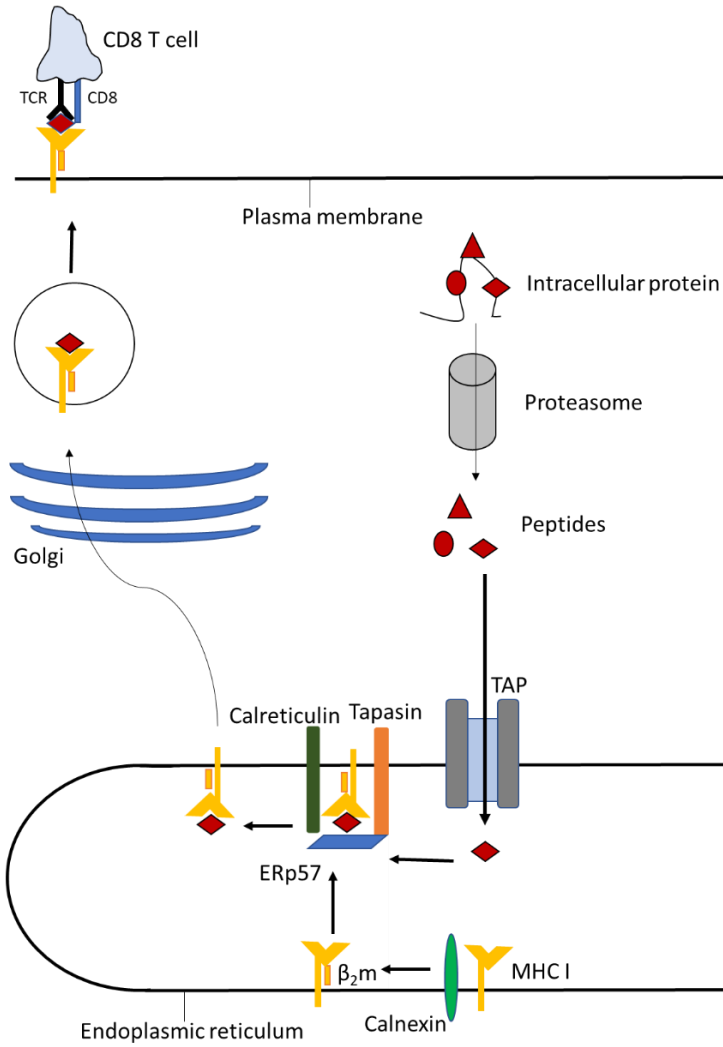
CD8 T-cells recognise antigen presented by MHC class I molecules (1, 16). A schematic depicting antigen processing and presentation by MHC class I molecules is shown in Figure 1.2, left. MHC class I molecules are expressed in all nucleated cells from polymorphic gene regions HLA-A, HLA-B, HLA-C in humans, and H2-K, H2-D, H2-L in mice. Intracellular proteins are degraded by the cytoplasmic proteasome, to form the majority of peptides presented by MHC I molecules (1, 16). There are alternative forms of the proteasome called the immunoproteasome and thymus-specific proteasome which are expressed by immune cells and thymic epithelial cells, respectively (1, 16). During inflammation and elevated IFN γ levels, when there is a larger protein pool, immunoproteasomes are more efficient at protein degradation than constitutive proteasomes (1, 16). In addition to degradation of fully functional proteins, it has been found that 30 to 70% of proteins are degraded before they are fully functional (17, 18). Defective ribosomal products (DRIPs) result from defects in translation or transcription; they are degraded rapidly by the proteasome to prevent damaging protein aggregation (16, 18). Once generated, peptides from the cytoplasm are transported into the ER via the transporter associated with antigen processing (TAP) (1, 16). MHC I heavy chain molecules in the ER membrane are bound by the chaperone molecule calnexin; when the MHC I heavy chain binds to the light chain protein beta-2 microglobulin (β_2M), calnexin dissociates from the MHC I molecule (1, 16). The MHC I- β_2M complex then binds to the peptide loading complex (PLC), which consists of the chaperone proteins calreticulin, tapasin, and ERp57 (1, 16). ERp57 forms a heterodimer with tapasin. Tapasin

associates with and stabilises TAP, while enabling spatial proximity between the MHC I molecule and peptides being transported into the ER (1, 16). Once peptides bind stably to MHC I, the peptide-MHC I complex forms and can be released from the PLC to travel from the ER, via the Golgi to the plasma membrane (1, 16).

DCs can present intracellular peptides to activate CD8 T-cells, however, many viruses are trophic in that they infect certain cell types (19). This means dendritic cells may not be infected, which could limit the induction of anti-viral CD8 T-cell responses (19). Cross presentation is the presentation of endocytosed extracellular peptides on MHC I molecules and enables the activation of CD8 T-cells in response to extracellularly derived peptides (19). There are two main mechanisms by which cross presentation is thought to occur: the cytosolic and vacuolar pathways (19, 20). The cytosolic pathway involves exportation of exogenous antigens from endosomes into the cytoplasm where they are degraded by the proteasome into peptides; peptides are either loaded onto MHC I molecules in the ER or imported into the phagosome by TAP where they encounter MHC I molecules (20, 21). The vacuolar pathway involves proteasome-independent proteolytic degradation of exogenous antigens within phagosomes, followed by peptide loading onto MHC I molecules (20, 22).

Antigen processing for presentation on MHC I molecules results in relatively stable peptide-MHC (pMHC) complexes (16). However, MHC I complexes have been shown to dissociate at the cell surface, leaving MHC I heavy chains at the plasma membrane (23, 24). Free MHC I heavy chains with empty peptide-binding grooves can form new pMHC complexes provided there is a sufficient level of exogenous β_2M and peptides; this enables peptide loading of APCs *in vitro* (25). MHC I heavy chains and complexes are also endocytosed primarily for degradation, however, endocytosed exogenous peptides can bind to a small fraction of MHC I heavy chains within the endosomal compartment and undergo recycling back to the surface (16).

MHC I antigen presentation



MHC II antigen presentation

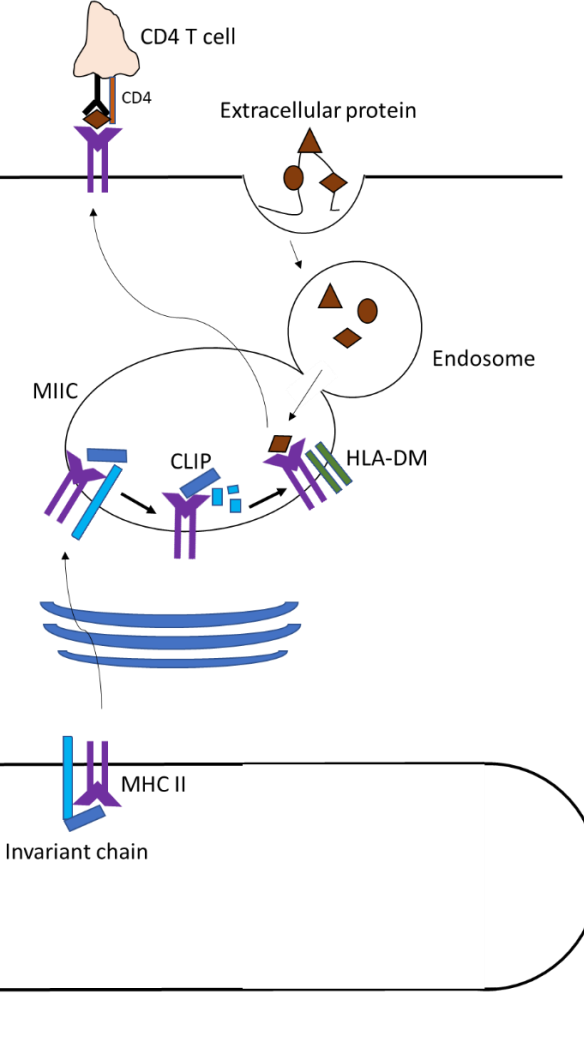


Figure 1.2 MHC I and MHC II antigen presentation pathways

Left) Intracellular proteins are degraded by the proteasome into peptides, which are transported into the endoplasmic reticulum (ER) via the transporter associated with antigen processing (TAP). In the ER, heavy chain MHC I molecules associate with the chaperone calnexin, until β_2 -microglobulin (β_2 M) forms the light chain of MHC I molecules, by binding to the heavy chains. This MHC I complex then associates with the peptide loading complex (PLC), which is made of the chaperone molecules calreticulin, ERp57 and tapasin, which facilitate binding of peptides to MHC I molecules. The peptide-MHC I complexes travel through the Golgi to the cell surface for antigen presentation to CD8 T-cells. **Right)** Extracellular proteins are endocytosed by APCs and degraded in endosomes to form peptides. In the ER, MHC II molecules bind to the invariant chain (Ii) protein and are transported through the Golgi to specialised late endosomes called the MHC class II compartment (MIIC). Here, proteases within the MIIC cleave the Ii, leaving a peptide called the class-II associated invariant chain peptide (CLIP) bound to the peptide-binding groove of MHC class II proteins. Endosomes containing extracellularly-derived peptides fuse with MIIC endosomes and peptides are loaded onto MHC II molecules with the help of HLA-DM proteins. Peptide-MHC II complexes are transported to the cell surface for antigen presentation to CD4 T-cells.

1.3.2.3 $\alpha\beta$ T-cell development

The ultimate goal of T-cell development is the production of mature T-cells that can be activated via their TCRs by non-self-peptides in complex with MHC molecules (1, 26). T-cells originate from multipotent haematopoietic stem cells in the bone marrow that differentiate into lymphoid progenitors and migrate to the thymus (1, 26). Within the thymus, T-cell precursors are called thymocytes and develop into mature T-cells (1, 26). Thymocytes undergo a process called positive selection which ensures they express TCRs with sufficient binding affinity for pMHC complexes in order to induce TCR signalling (1, 26). On the other hand, strongly self-reactive T-cells are prevented from entering the circulation via a process called negative selection (1, 26). Deletion of strongly self-reactive thymocytes is called central tolerance (1, 26). Since all nucleated cells present self-peptides restricted by MHC molecules, central tolerance helps to prevent the induction of autoimmune disease (1, 26). A schematic of T-cell development in the thymus is shown in Figure 1.3.

The thymus is divided into two main regions: the outer cortex and inner medulla. Lymphoid precursors initially emerge from venules at the cortico-medullary junction and migrate through the cortex (1, 26). When they first enter, thymocytes do not express CD8 or CD4 molecules and therefore are called double negative (DN) (1, 26). The TCR is a heterodimer of one α and one β chain; each β chain of the TCR is encoded by variable (V_β) diversity (D_β) and joining (J_β) gene segments, while each TCR α chain is encoded by variable (V_α) and joining (J_α) segments (1, 26). There are four stages of DN thymocytes; in the first stage the DN1 cells have not rearranged the genes encoding the TCR (1, 26). In the second stage, DN2 cells start to rearrange the TCR β -chain genes via somatic recombination which joins D_β and J_β gene segments (1, 26). DN3 thymocytes rearrange V_β to DJ_β gene segments and expressed β chains then assemble with a pre-TCR α chain, forming a pre-TCR (1, 26). The pre-TCRs dimerise and enable ligand-independent pre-TCR signalling (1, 26). This enables the transition of DN3 thymocytes to the highly proliferative DN4 stage where further rearrangement of β -chain genes is halted and thymocytes begin to express both CD8 and CD4 to generate double-positive (DP) thymocytes, which make up the majority of total thymocytes (1, 26). Subsequent rearrangement of V_α and J_α segments produces TCR α chains, giving rise to an $\alpha\beta$ TCR, and proliferation reduces, giving rise to non-blasting DP cells (1, 26). Thymic cortical epithelial cells mediate positive selection by presenting pMHC complexes to the DP thymocytes (1, 26). During positive selection, DP cells that recognise pMHC survive, while those that fail to recognise pMHC die by apoptosis (1, 26). Recognition of peptide in complex with MHC I or MHC II halts T-cell expression of CD4 and CD8 co-receptors, respectively (1, 26). This results in the formation of single-positive thymocytes that migrate down into the medulla and undergo negative selection (1, 26). Negative selection begins in the cortex during positive

selection and continues in the medulla (1, 26). In the medulla, pMHC is presented by DCs, macrophages, and medullary thymic epithelial cells (mTECs); the presentation of self-antigens on MHC molecules by mTECs is enabled by the autoimmune regulator (AIRE), a transcription factor which drives the ectopic expression of a large range of self-antigens (1, 26). Strong binding of the TCR to pMHC causes apoptosis of highly self-reactive thymocytes, while thymocytes with TCRs that bind pMHC with low affinity survive (1, 26). Some thymocytes expressing TCRs that have intermediate affinity for pMHC differentiate into thymic T regulatory cells (Tregs) which express the transcription factor Forkhead Box P3 (FOXP3) and contribute to peripheral tolerance of self-antigens (1, 26). Having survived both positive and negative selection, mature T-cells expressing the sphingosine-1-phosphate receptor (S1PR) emigrate from the thymus via chemotaxis towards elevated sphingosine-1-phosphate (S1P) levels in the blood and lymph (1, 26).

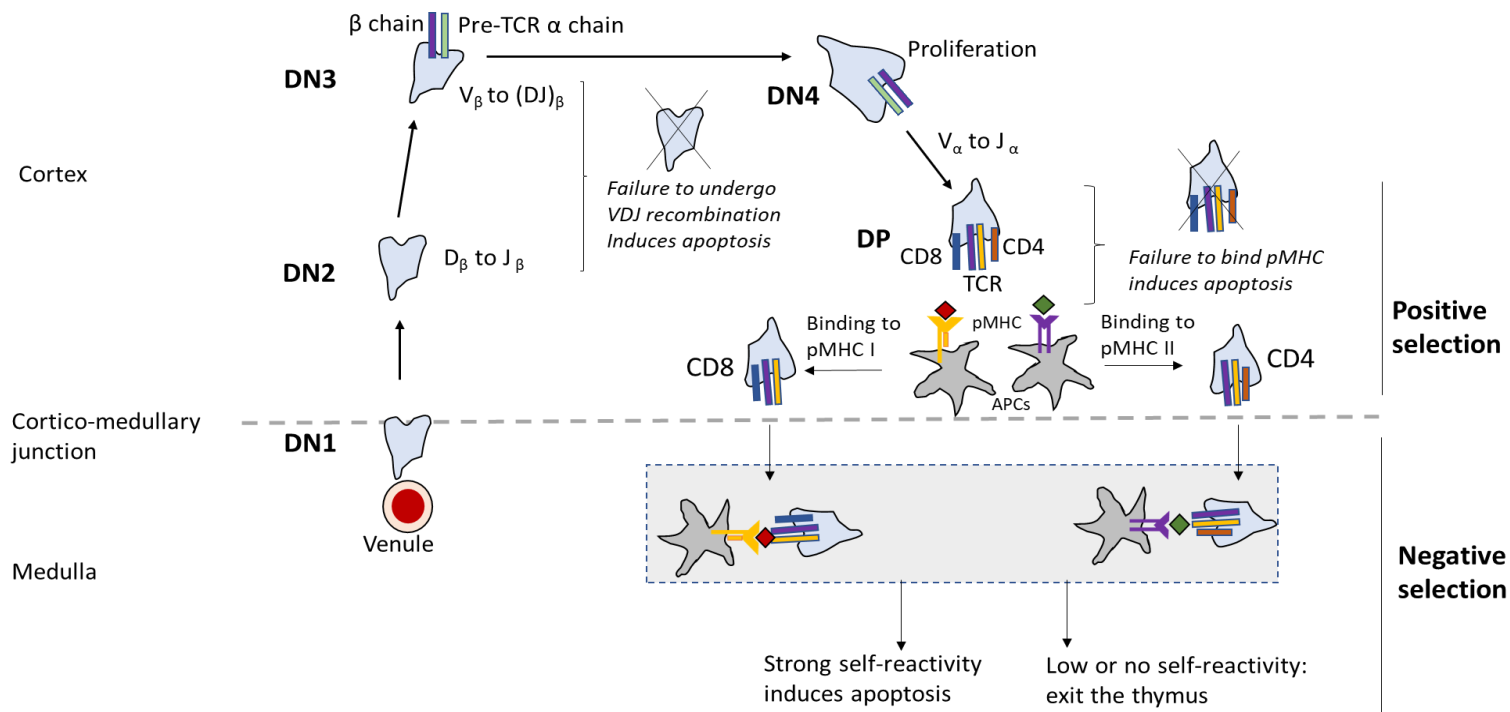


Figure 1.3 Thymic T-cell development

Thymocytes migrate from the bone marrow and enter the thymus via venules near the cortico-medullary junction, which lies between the thymic cortex (above dotted line) and medulla (below dotted line). Thymocytes enter the cortex lacking expression of the TCR and both CD8 and CD4 co-receptors, making them double-negative (DN). DN1 thymocytes migrate to the cortex where they become DN2 thymocytes which undergo somatic recombination to join D_β and J_β gene segments for the TCR β chain. DN3 thymocytes rearrange V_β to $(DJ)_\beta$ segments, producing the β chain, which associates with the pre-TCR α chain. Thymocytes which fail to successfully join VDJ segments undergo apoptosis. Following ligand-independent pre-TCR signalling, DN4 thymocytes proliferate to form double-positive thymocytes which express both the CD8 and CD4 co-receptor and the TCR, following successful joining of V_α to J_α gene segments which enables synthesis of the TCR α chain. During positive selection, thymic cortical epithelial cells present peptide in complex with MHC I and MHC II molecules; DP thymocytes which recognise pMHC are selected to become single-positive thymocytes. Failure to bind pMHC induces apoptosis. Single-positive thymocytes undergo negative selection in the cortex and medulla: thymocytes with TCRs that bind strongly to self-pMHC undergo apoptosis; thymocytes with low or no self-reactivity exit the thymus to form the peripheral T-cell repertoire.

1.3.2.4 *T-cell activation in secondary lymphoid organs*

After exiting the thymus, naïve CD8 and CD4 T-cells enter secondary lymphoid organs (SLOs), such as the spleen and lymph nodes, where they scan DCs for cognate pMHC (27). In the absence of cognate antigen, T-cells egress from the SLOs via the efferent lymphatic vessel and travel through the thoracic duct before returning to the blood for re-circulation (27). Recognition of cognate pMHC by the TCR (Signal 1) in SLOs can either result in T-cell tolerance or the acquisition of effector functions such as proliferation, cytokine secretion and cytotoxic potential (the latter in the case of CD8 T-cells), depending on the strength of Signal 2 (costimulation) and Signal 3 (cytokine signals) which are also required for T-cell activation (28). Signal 2 is comprised of costimulation primarily mediated by CD80/CD86 on DCs binding to the CD28 receptor on T-cells (28). A schematic of how CD28 contributes to TCR signalling (discussed below) is shown in Figure 1.4. CD28 ligation activates phosphatidylinositol-3-kinase (PI3K), which leads to the activation of protein kinase B (Akt) and the nuclear translocation of nuclear factor kappa-light-chain-enhancer of activated B cells (NFκB) which induces pro-survival signalling in T-cells (28). Akt also inhibits cell cycle arrest, helping to drive proliferation and cell survival (28). Additionally, Akt inhibits the kinase glycogen synthase kinase-3 (GSK3) to support nuclear localisation of nuclear factor of activated T-cells (NFAT) which drives IL2 transcription (28). As a result, CD28 costimulation augments signalling required for T-cell activation and insufficient costimulation can induce tolerance (28). While CD28-deficient mice display weakened immune responses to infection, there are several other costimulatory molecules including lymphocyte function associated antigen 1 (LFA1) and inducible T-cell costimulator (ICOS) which can compensate for low levels of CD28 (29-31). Signal 3 is provided by cytokines secreted by DCs and in the local environment which are influenced by the type of infection, which drives the differentiation of T-cells into distinct effector subsets (32, 33). Differentiation occurs during clonal expansion, which is the proliferation of antigen-specific T-cell clones into effector T-cells (32, 33). Most effector T-cells emigrate from SLOs to sites of inflammation, although CD4 follicular helper T-cells (T_{fh} cells) express CXCR5 and migrate to B-cell follicles within SLOs to aid B-cell activation and isotype switching (27).

1.3.2.5 *Proximal T-cell receptor signalling*

As previously discussed, three main signals are required for naïve T-cell activation: TCR ligation by cognate pMHC (signal 1), costimulation through CD28 (signal 2) and cytokine signalling (signal 3) (28). The pathways involved in naïve and effector T-cell activation are very similar, although CD28 costimulation is not necessary for effector T-cell activation (34). A schematic of the signalling pathways downstream of TCR and CD28 ligation is shown in Figure 1.4. The octameric TCR complex includes the αβ TCR heterodimer, and three pairs of CD3 chains: γε, δε and ζζ (28, 35). Ligation of cognate pMHC by the TCR ultimately transmits signals that recruit cytoplasmic adaptor

signalling proteins to form a multi-molecular proximal signalling complex; the resultant spatiotemporal organisation of T-cell signalling intermediates leads to actin polymerisation, calcium signalling, nuclear factor- κ B (NF κ B) signalling and mitogen-activated protein kinase (MAPK) signalling (28, 35). The latter three pathways result in transcriptional changes that support the survival and proliferation of T-cells, including upregulation of interleukin 2 (IL2) and its receptor (IL2R) (28, 35).

pMHC binding of the TCR receptor causes the phosphorylation of tyrosine residues in the CD3 chains by Src tyrosine kinases such as lymphocyte-specific protein tyrosine kinase (Lck) and, to a lesser extent, Fyn (28, 35). Lck associates with CD4 or CD8 co-receptor chains and is recruited near to the TCR complex when the TCR and CD4/CD8 co-receptors bind to cognate pMHC (28, 35). Lck specifically recognises and phosphorylates tyrosine residues within protein domains called immunoreceptor tyrosine activation motifs (ITAMs), which contain two tyrosine residues within conserved amino acid motifs (36). There is one ITAM domain within each CD3 chain of the $\delta\gamma$ and $\delta\epsilon$ pairs that can be phosphorylated, and three ITAMs within each ζ chain, which amounts to a total of 10 ITAMs within the TCR complex (36). Tyrosine phosphorylation within ITAMs of the ζ chains provides a docking site for the tyrosine kinase ζ chain-associated 70kDa tyrosine phosphoprotein (ZAP70) to bind via SH-2 domains (36). Lck can then phosphorylate ZAP-70 at Y493, and activate ZAP70 catalytic activity, enabling autophosphorylation of ZAP70 (28, 35, 36). Activated ZAP70 tyrosine-phosphorylates the transmembrane adaptor protein linker for activation of T-cells (LAT) (28, 35). LAT contains nine tyrosine residues that can be bound by phospholipase C- γ (PLC- γ), growth factor receptor-bound protein 2 (GRB2), inducible tyrosine kinase (Itk), and GRB2-related adapter downstream of Shc (GADS) among other adaptor proteins (28). Another key adaptor protein, Src homology 2 domain containing leukocyte phosphoprotein of 76 kDa (SLP76) can bind to LAT and together they form the scaffold for the formation of a multimolecular complex that organises T-cell signalling intermediates (28, 35). One pathway downstream of TCR signalling is cytoskeletal rearrangement; Vav guanine nucleotide exchange factor 1 (VAV1) binds to SLP76, GADS, LAT and Itk and is activated by Itk (37). VAV1 activates the GTPases Cdc42 and Rac, which in turn activate (WASp family verprolin homologous protein-2) WAVE2 and Wiskott-Aldrich syndrome protein (WASp), respectively (37). WASp and WAVE2 induce actin polymerisation from existing filamentous actin (F-actin) filaments via the actin-related protein 2/3 (Arp2/3) actin nucleation complex (37). Actin remodelling supports the morphological polarisation of the T-cell towards the APC and formation of the immune synapse (discussed further in Section 1.3.2.12) (37). Three other main pathways induce transcription of genes related to effector T-cell function: the calcium pathway, the MAPK pathway and the NF κ B pathway (28, 38, 39). PLC γ 1 is a central protein that binds to LAT and SLP76 to transduce signals down these pathways (Figure 1.4). PLC γ 1 is phosphorylated and activated by Itk. Activated PLC γ 1

hydrolyses phosphatidylinositol 4,5-bisphosphate (PIP₂) into two important molecules for downstream signalling: diacylglycerol (DAG) and inositol 1,4,5- triphosphate (IP₃).

1.3.2.6 Calcium signalling

IP₃ binds IP₃ receptors which act as calcium channels in the ER and opens them, resulting in calcium release from the ER into the cytoplasm (38, 40). This reduced Ca²⁺ concentration in the ER activates the STIM/ORAI1 pathway which results in an influx of Ca²⁺ through Ca²⁺-responsive ORAI1 channels at the plasma membrane (38, 40). The increase in intracellular calcium concentration induces activation of calcineurin, which enables the dephosphorylation of the transcription factor NFAT and subsequent release of NFAT from calcineurin (38, 40, 41). NFAT can then translocate to the nucleus where it cooperates with the transcription factor AP-1 to induce the transcription of genes related to T-cell activation, such as the IL2 gene (38, 40, 41). Thus, intracellular calcium levels during TCR ligation can be an indicator of TCR signal strength; quantification of calcium flux using fluorescent calcium sensors such as Fura-2 can be used experimentally to indicate the strength of TCR proximal signalling upon ligation (42, 43).

1.3.2.7 MAPK signalling

DAG can activate the guanine nucleotide-binding protein Ras and protein kinase C-theta (PKC θ) (39). Initiation of the MAPK cascade by Ras, results in the phosphorylation of the MAPK Erk that leads to the synthesis of Fos protein (39). Fos and phosphorylated Jun protein- which is produced downstream of PKC θ signalling- form heterodimeric AP-1 which induces transcription of IL2 and IL2R (39).

1.3.2.8 NF κ B signalling

Activation of PKC θ by DAG also enables the assembly of a protein complex containing CARMA-1, Bcl10 and MALT1 (39). NF κ B is normally sequestered in the cytoplasm by inhibitor of NF κ B (I κ B) (39). The CARMA-1/Bcl10/MALT1 complex degrades the regulatory subunit of inhibitor of NF κ B kinase (IKK), which allows the degradation of I κ B which usually sequesters NF κ B in the cytoplasm (Figure 1.4) (39). Released NF κ B can enter the nucleus and activate genes related to the function, survival, and homeostasis of T-cells (39).

1.3.2.9 CD28 costimulation augments TCR signalling

Ligation of CD28 by CD80/CD86 on APCs activates phosphatidylinositol-3-kinase (PI3K), which phosphorylates PIP₂ to generate PIP₃ (44). PIP₃ activates Akt which supports the translocation of NF κ B into the nucleus (44). PIP₃ also recruits VAV1 to the IS which supports actin polymerisation (44). Furthermore, Akt inactivates glycogen-synthase kinase 3 (GSK3) which supports the nuclear localisation of NFAT (44). Therefore, CD28 costimulation augments the major TCR signalling pathways.

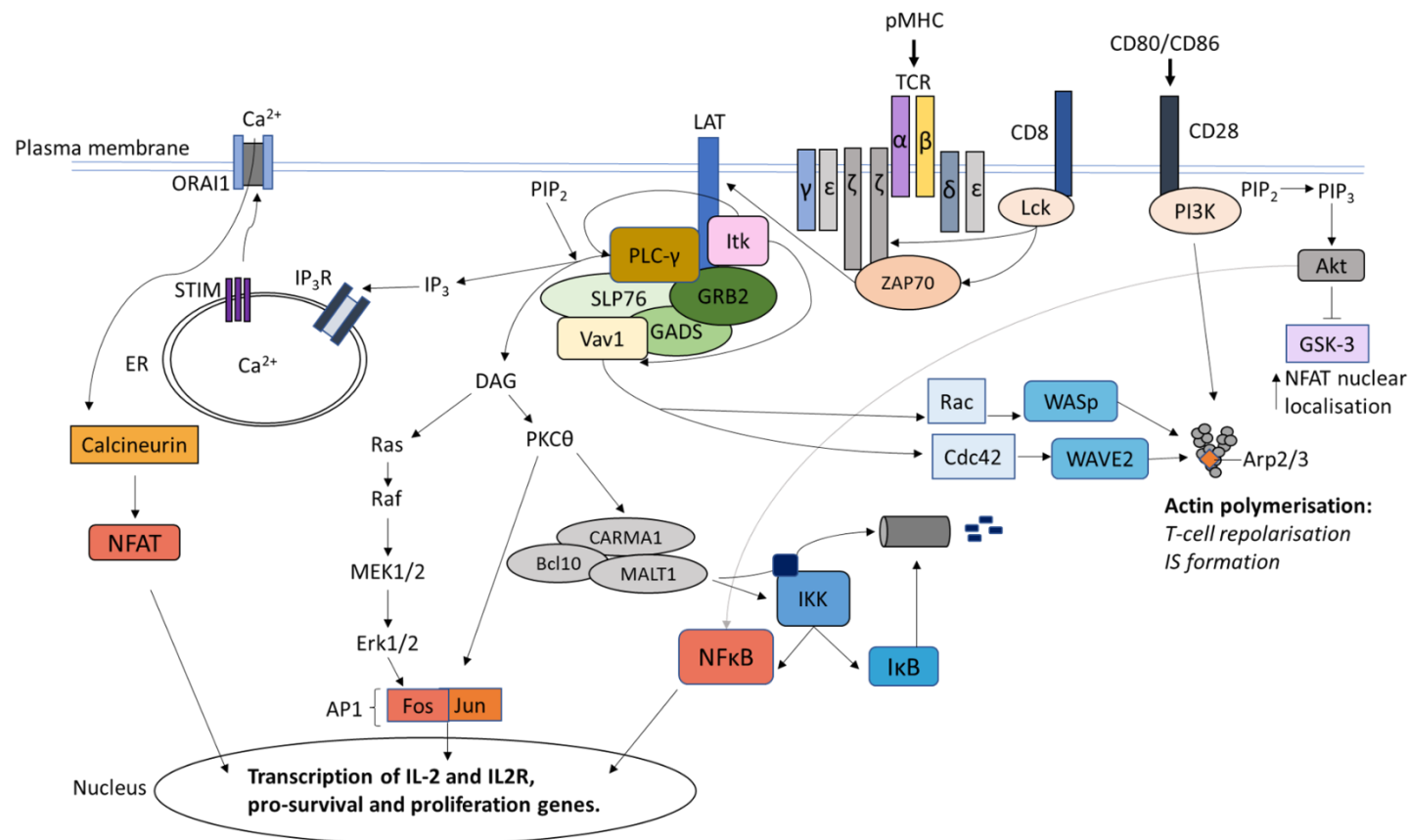


Figure 1.4 TCR signalling and CD28 costimulation

TCR ligation by pMHC induces Lck-mediated phosphorylation of tyrosine residues within the ITAMs in the CD3 chains ($\gamma\epsilon$, $\delta\epsilon$, $\zeta\zeta$) associated with the TCR. Phosphorylation of the ζ chains recruits ZAP70 which is activated by Lck and autophosphorylation. ZAP70 activates LAT which recruits various proximal signalling proteins including Itk, GRB2, PLC- γ , SLP76, VAV1 and GADS. Together LAT and SLP76 form the scaffold for a multimolecular proximal signalling complex. Vav1 recruitment to SLP76, GADS, LAT and Itk enables activation of VAV1 by Itk. VAV1 activates the GTPases Rac and Cdc42, which activate WASp and WAVE2. WASp and WAVE2 initiate actin polymerisation from existing F-actin filaments in cooperation with Arp2/3. Itk also activates PLC- γ which hydrolyses PIP₂ into IP₃ and DAG. IP₃ binds to IP₃R on the ER membrane which acts as calcium channels and open to release Ca²⁺ from the ER into the cytoplasm. This causes aggregation of STIM proteins in the ER membrane, which opens ORAI1

calcium-responsive channels in the plasma membrane. The subsequent influx of extracellular Ca^{2+} activates the phosphatase calcineurin, which dephosphorylates NFAT to enable NFAT nuclear translocation. Meanwhile, DAG activates Ras, which activates Raf, MEK1/2 and ERK1/2, leading to transcription of the transcription factor Fos. DAG also activates PKC θ which leads to activation and of the transcription factor Jun. Jun and Fos dimerise to produce the transcription factor AP1. PKC θ also activates CARMA1/Bcl10/MALT1 to degrade the regulatory subunit of IKK, which enables degradation of I κ B which usually sequesters NF κ B in the cytoplasm. NF κ B then translocates into the nucleus. In the nucleus, NFAT, AP1 and NF κ B induce the transcription of IL2, IL2R, pro-survival and proliferation genes. CD28 ligation by CD80/CD86 activates PI3K, which phosphorylates PIP₂ to form PIP₃. PIP₃ activates Akt, which inactivates GSK-3. Active GSK-3 supports export of NFAT from the nucleus; therefore, Akt activation enhances the nuclear localisation of NFAT. Akt also enhances NF κ B nuclear translocation and recruitment of VAV1 to the IS, promoting actin polymerisation.

1.3.2.10 CD4 T-cell effector function

During activation of naïve CD4 T-cells, the cytokine environment determines their differentiation into one of several major effector T helper (Th) subsets, including: Th1, Th2, Th17, Tfh and Tregs (45, 46). Th1 cells are induced by IL12 and IFN γ and secrete effector cytokines including IFN γ (47, 48). Th1 cells activate macrophages to be more potent killers of intracellular microbes and induce Ig class switching to IgG by B cells (49, 50). Th1 cytokines also support the differentiation of effector CD8 T-cells (51). Th2 cells are induced by IL4, which they secrete along with IL5 and IL13 (45). Th2 cells enhance eosinophil degranulation and induce Ig class switching to IgE by B cells (49). The Th2 response is useful in controlling extracellular parasitic infections such as helminths, while inappropriate Th2 responses cause allergy and asthma (45). Th17 cells are induced by IL6, IL23 and TGF β and produce IL17 and IL22 (45, 52). Th17 cells enhance neutrophil responses and activate epithelia to produce antimicrobial peptides (53, 54). Tregs have been divided into two main subsets: thymic or natural Tregs (tTregs or nTregs) which develop in the thymus and peripheral Tregs (pTregs), which develop extrathymically in the periphery (55). As previously discussed (Section 1.3.1. Tfh cells support Ig isotype switching and affinity maturation within germinal centres, to support the B cell response (13, 45).

While tTregs emerge from the thymus as CD4⁺ Foxp3⁺ CD25^{hi} regulatory cells with immunosuppressive capacity, pTregs develop when conventional CD4⁺ Foxp3⁻ CD25^{lo} T-cells are activated in the presence of the cytokines IL2 and TGF β , which induces transcription of the master transcription factor FOXP3 (55, 56). Currently, Helios and Nrp-1 are the main markers proposed to distinguish between tTregs and pTregs in mice, with tTregs expressing higher levels of both proteins, but they are not conclusive and markers specific to distinct human Treg subsets are unknown (55, 57, 58). Tregs are thought to exert their immunosuppressive effects onto APCs and effector CD4 and CD8 T-cells in both contact-dependent and contact-independent mechanisms. One contact-dependent mechanism involves the binding of the co-inhibitory receptor CTLA-4 on the surface of Tregs to the B7 molecules CD80 and CD86 on APCs; CTLA-4 binds these ligands with higher affinity, outcompeting CD28 on the surface of T-cells, thus limiting CD28-dependent costimulatory signalling (59). CTLA-4 can also pull off CD80 and CD86 from the target cell membrane via transendocytosis, decreasing the availability of these CD28 ligands (60). Another contact-dependent mechanism involves the capture of fragments of the effector T-cell membrane by Tregs via trogocytosis which also decreases CD80 and CD86 availability (61). Tregs also secrete immunosuppressive cytokines such as TGF β and IL10 which inhibit effector T-cell proliferation and cytokine secretion (62). Tregs may also express the ectoenzymes CD39 and CD73 which convert ATP to ADP/AMP, and AMP to adenosine, respectively. Secreted adenosine binds to the A2A adenosine receptor on DCs and effector T-cells causing elevated, suppressive levels of cyclic

adenosine monophosphate (cAMP) (63-65). Tregs also express indoleamine-2,3-deoxygenase (IDO) which catalyses the degradation of tryptophan; depletion of tryptophan in the local environment leads to metabolic stress in nearby effector T-cells (66, 67). Moreover, a product of tryptophan catabolism is the release of kynurenine which can bind to the aryl hydrocarbon receptor (AhR) to induce conversion of Th17 cells to Tregs, increasing the number of Tregs and therefore local immunosuppression (68). The immunosuppressive mechanisms used by Tregs seem to depend on contextual factors such as the disease, anatomical site, and species (62). The suppressive capacity of Tregs are commonly assessed *in vitro* via proliferation assays involving co-culture with effector T-cells and enzyme-linked immunosorbent assays (ELISAs) which assess IL10 and TGF β production (69). Induced Tregs (iTregs) are the closest *in vitro* model of pTregs found *in vivo*. iTregs can be generated *in vitro* by CD3/CD28 antibody or peptide-mediated stimulation of naïve conventional CD4 T-cells in the presence of TGF β and IL2 (70, 71). While Foxp3⁺CD4⁺ Tregs have been found to make up the majority of circulating Tregs *in vivo* in both mice and humans, CD4⁺ Foxp3⁻ Tregs that develop in the periphery have also been described. These include Tr1 and Tr3 Tregs. Tr1 cells are a subset of Treg that primarily secretes IL10 along with TGF β , while Tr3 cells primarily secrete TGF β (72, 73).

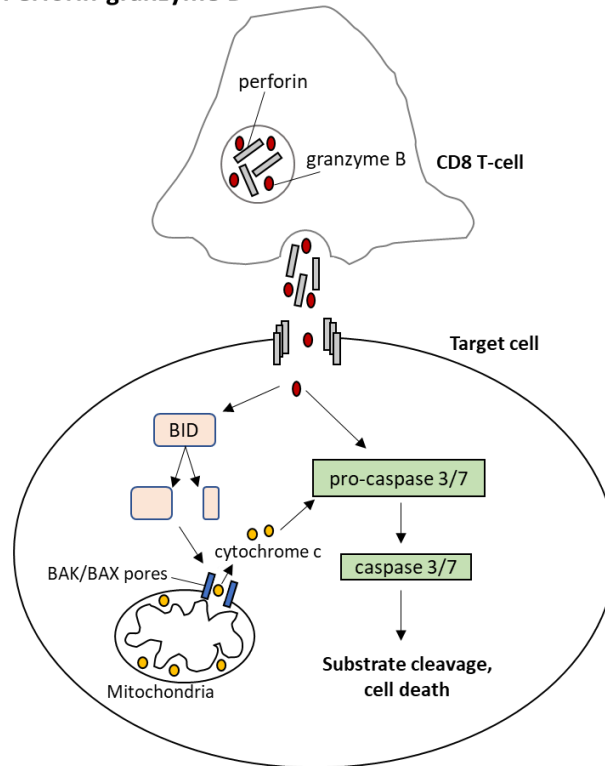
1.3.2.11 CD8 T-cell effector function

Most CD8 T-cells differentiate into cytotoxic T-lymphocytes (CTLs), which have the ability to kill target cells via two main mechanisms: granzyme-perforin and death receptor-ligand mediated apoptosis, the latter of which includes the Fas ligand/Fas (FasL/Fas) pathway (74-76). A schematic of the granzyme-perforin and FasL/Fas pathways is shown in Figure 1.5. Inside lymphoid organs, engagement of the TCR on naïve CD8 T-cells induces a transcriptional program that endows them with effector functions that have cytotoxic potential (77). An important feature of CTLs is the production of cytotoxic granules that are stored in lysosomes (76). Cytotoxic granules contain perforin-1 and granzyme B, among other molecules (78). Perforin-1 is a glycoprotein encoded by the PRF1 gene (79). Upon secretion of the cytotoxic granules by CD8 T-cells, released perforin-1 can polymerise in the target cell membrane to form pores that are 16-22nm in diameter, thus enabling the flow of molecules between the cytoplasm and extracellular space, potentially breaking membrane integrity, though cell death mediated by perforin-1 in the absence *versus* presence of granzymes is less efficient (80, 81). Granzymes are serine proteases; there are 5 granzymes in humans and 10 granzymes in mice (82). Granzyme A and B are found in both species and are the most studied; granzyme B (GzmB) is thought to be the most important for cytolytic killing by CD8 T-cells (82). GzmB is delivered into the target cell cytoplasm through pores formed by perforin-1 and cleaves pro-caspases 3 and 7 to activate their cysteine protease activity, leading to the cleavage of substrates which cause apoptosis (82). GzmB can also directly cleave the proapoptotic factor BH3-interacting domain death agonist (BID) to induce cytochrome c release

from mitochondria, through pores made by polymerised BAK/BAX, that leads to caspase activation and apoptosis (82-84). The degranulating CTL itself is protected from perforin-1 and GzmB via several mechanisms. Perforin-1 requires neutral pH and Ca^{2+} to be active (85, 86). The acidic environment of a lysosome helps to stabilise perforin-1 and maintain it in an inactive form, while the chaperone molecule calreticulin binds to free Ca^{2+} in the lysosome, sequestering it from perforin-1 (87). Cytotoxic granules also contain serglycin, serine protease inhibitor B9 (serpin B9) and cathepsins (88-90). Within the lysosome, serglycin binds to perforin-1, preventing polymerisation and serpins inhibit granzyme enzymatic activity (88, 89). Once perforin-1 is secreted into the immune synapse, the pH is neutral which releases perforin from serglycin and enables pore-formation (85). Cathepsins such as cathepsin B are cysteine proteases present within cytotoxic lysosomes that are transferred to the plasma membrane upon degranulation which coat the cytotoxic CD8 T-cell surface at the IS and protect it from perforin via proteolytic inactivation (90).

Fas is broadly expressed by most cell types and belongs to the death receptor subset of the tumour necrosis factor receptor (TNFR) family. It is a trimeric receptor that aggregates on the cell surface following ligation to FasL (91). FasL is expressed by certain cell types including activated T-cells and NK cells, therefore, these cells can induce Fas-mediated target cell death upon cell contact (92). Upon engagement of Fas on the target cell by FasL on T-cells, aggregation of Fas receptors induces conformational changes that enable recruitment of the adaptor protein Fas-associated death domain (FADD) to Fas via homotypic interactions between death domains (93, 94). FADD then recruits pro-caspase-8 via homotypic binding of death effector domains (DEDs), which leads to proximity-induced conformational changes in pro-caspase 8 that activate its auto-proteolytic ability (95, 96). Activated pro-caspase 8 can cleave itself and form the active caspase 8 (96). Caspase 8 induces apoptosis by directly cleaving caspase 3 and caspase 7 or by cleaving BID to induce the mitochondrial pathway of apoptosis (82, 97). An alternative form of cell death downstream of Fas ligation is necroptosis, a programmed, inflammatory form of cell death that occurs when caspase 8 is inhibited and apoptosis is blocked (98).

Perforin-granzyme B



FasL/Fas

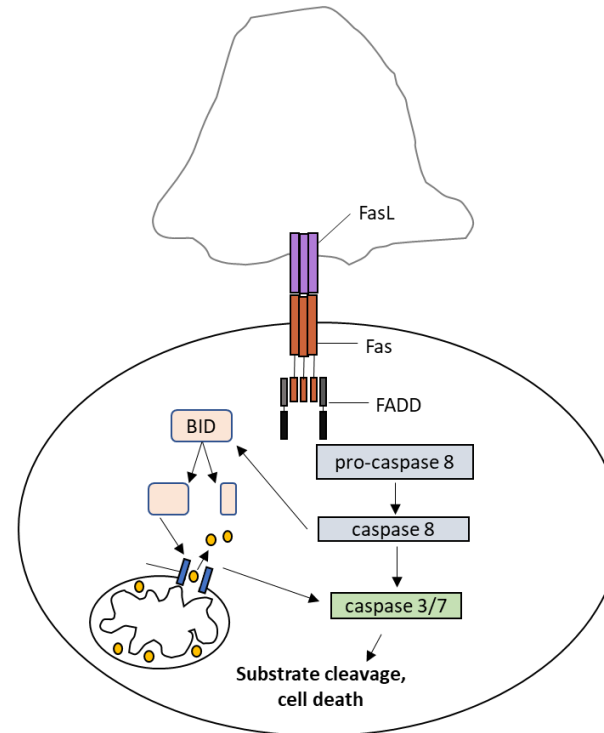


Figure 1.5 CD8 T-cells induce target cell death via two main pathways

CD8 T-cells can induce target cell death via two main pathways: the perforin-granzyme B and the FasL/Fas pathways. **Left)** The perforin-granzyme B pathway involves the exocytosis of cytotoxic granules containing perforin and granzyme B. Perforin polymerises on the target cell membrane to create pores which enable granzyme B delivery into the target cell cytoplasm. Granzyme B can: cleave pro-caspase 3 and 7 to activate their cysteine protease activity or cleave BID to induce the polymerisation of BAK and/or BAX proteins in the mitochondrial membrane. Cytochrome c is released from the mitochondrial intermembrane space and can cleave pro-caspase 3 and 7. Caspase 3 and 7 can cleave multiple substrates to induce cell death. **Right)** FasL on T-cells can bind to Fas on the target cell membrane to induce trimerization of Fas, and the recruitment of FADD via death domains. FADD recruits pro-caspase 8 via death effector domains (DED), leading to caspase 8 auto-cleavage and activation. Caspase 8 can cleave caspase 3 and 7 directly or indirectly through the mitochondrial pathway of apoptosis to induce cell death.

The primary cytokines expressed by effector CD8 T-cells are IFN γ , IL2, and TNF α which are upregulated following TCR stimulation (1). Upregulation of the transcription factors T-box transcription factor (Tbet) and Eomesodermin (Eomes) downstream of TCR and IFN γ receptor (IFN γ R) signalling enable these factors to bind to the promoter of the IFN γ gene to enhance expression (99). Other transcription factors activated downstream of TCR proximal signalling, such as NFAT and NF κ B have also been shown to induce IFN γ transcription (100, 101). As IFN γ upregulation and secretion is a major outcome of TCR stimulation in CD8 T-cells, IFN γ production is widely used as a measure of T-cell activation, commonly measured by ELISA or intracellular antibody staining (102, 103). IFN γ has been shown to induce upregulation of MHC I on target cells to promote antigenic stimulation of CD8 T-cells (104). IFN γ can directly increase CD8 T-cell cytotoxicity, including through granzyme B upregulation (102, 105) and stimulate CD8 T-cell proliferation (106). However, the effects of IFN γ on the T-cell response are diverse and this cytokine can also have negative effects on CD8 T-cell cytotoxicity and proliferation (107, 108). IL2 binds to the trimeric IL2 receptor (IL2R), which is comprised of CD25 the IL2R β and IL2R γ chains, to induce prosurvival and anti-apoptotic signalling (51). IL2 also promotes the generation of short-lived effector T-cells (SLECs) over memory-precursor effector cells (MPECs) and elevates the expression of perforin, granzyme B and IFN γ to support CD8 T-cell effector functions (51). TNF α has both pro-inflammatory and anti-inflammatory effects and has been found to facilitate both killing of tumour cells by CD8 T-cells as well as activation-induced cell death in CD8 T-cells (109, 110). Moreover, it has been found to both enhance tumour infiltration by CD8 T-cells and impair CD8 TIL densities within tumours (111, 112).

Studies have established several types of CD8⁺ regulatory T-cells including CD8⁺CD28⁻ and CD8⁺CD28^{low} subsets (113). The β -chain of the IL2 and IL15 receptor (CD122) has also been used to identify CD8 Tregs (114, 115). While CD8⁺CD28⁻ Tregs are thought to be induced in the periphery, CD8⁺CD28^{low} Tregs have been shown to develop in the thymus, although peripheral induction of these cells is also a possibility (113). In mice, Foxp3 expression by CD8 Tregs is variable while human CD8 Tregs have been found to express Foxp3 (116). Similar to CD4 Tregs, CD8 Tregs secrete IL10 and TGF β to inhibit proliferation of effector T-cells (117-119). CD8 Tregs have also been found to cause down-regulation of CD80 and CD86 on APCs to reduce activation of T-cells (120). Unlike CD4 Tregs, it is not known if CD8 Tregs express CD39 and CD73 to suppress effector CD8 T-cells via adenosine-dependent mechanisms. It is yet to be established whether different types of CD8 Treg subsets perform unique functions and a more specific marker for CD8 Tregs is required to enable deeper understanding of this cell type.

1.3.2.12 Immune synapse stability and T-cell polarisation

Migrating T-cell polarity

Following priming of naïve T-cells and differentiation into effector T-cells, T-cells polarise in order to migrate to sites of infection or tumours and scan for antigen. T-cell polarisation and morphology is regulated by several systems: the actin cytoskeleton, microtubule cytoskeleton, surface proteins, vesicular trafficking and polarity proteins (121). A migrating T-cell has a leading edge, comprised of filopodial ruffles and thin membrane sheet-like protrusions called lamellipodia, which are driven by the polymerisation and branching of actin (121, 122). Behind the leading edge lies a more stable lamella region that forms the mid-body, where myosin II accumulates; from the mid-body to the rear of the T-cell, myosin II organises actin filaments in parallel to the axis of migration and enables the retrograde flow of actomyosin towards the tail-end of the T-cell, called the uropod (123-125). The sliding of actin filaments by myosin II generates cell tension that drives the cell body and uropod forward, enabling amoeboid migration that involves: extension of the leading edge in the direction of movement, weak adhesion of this extension to the surrounding substrate, contraction of the cell body and retraction and detachment of the tail (122, 126). As in other amoeboid cells, there is a diffuse layer of F-actin beneath the plasma membrane in T-cells, called the actin-cortex, which is not anchored via focal contacts and stress fibres towards the substrate (126). T-cells adopt different modes of migration depending on the 2D and 3D environment they are in (122). In 2D environments, T-cell migration has been shown to require integrin-mediated adhesion, however, during scanning for antigen in 3D tissue environments, T-cells have been shown to squeeze through narrow gaps by rearranging their actin cytoskeleton, without the need for integrins- similar phenomena have been observed in neutrophils (122, 127, 128). The microtubule cytoskeleton derives from the microtubule-organising centre (MTOC) which lies within the uropod of a migrating T-cell, behind the nucleus that is located in the mid-body of the cell (129). During T-cell activation, the MTOC translocates to the front of the cell and vesicles containing T-cell effector molecules are transported along polarised microtubules by kinesin and dynein motors (discussed below) (129, 130). Migrating T-cells also show a polarised distribution of surface receptors. Some receptors accumulate at the leading edge of a migrating T-cell, such as LFA-1 and chemokine receptors, while others are transported to the uropod by actomyosin retrograde flow, such as TCRs, CD2, CD43 and CD44 (131-134). Meanwhile, C-terminus phosphorylated ezrin-radixin-moesin (cpERM) adaptor proteins associated with actin also bind to receptors such as intercellular adhesion molecule 1 (ICAM), CD43 and CD44 to maintain them at the rear of the cell (131, 135, 136). Polarity proteins including the partitioning-defective (PAR) proteins, scribbled (Scrib), lethal giant larvae (Lgl) and discs large (Dlg) have also been shown to help maintain T-cell polarity (137).

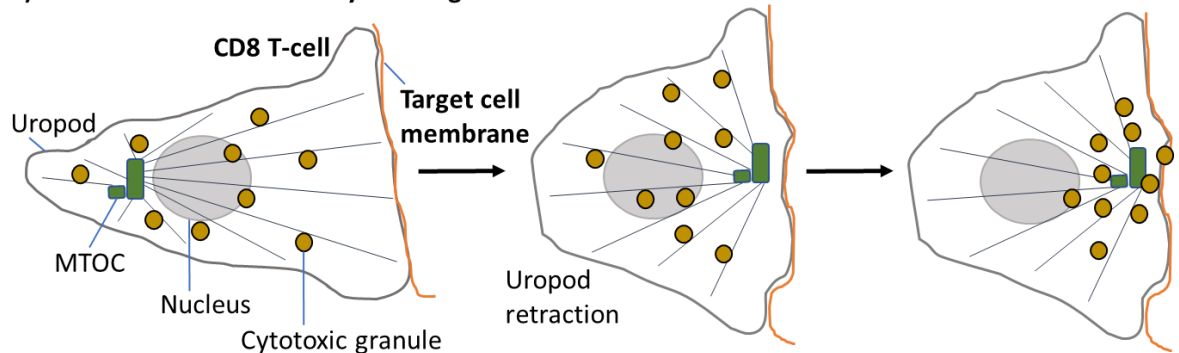
Repolarisation of T-cells upon antigen encounter and the immune synapse

Upon activation of the TCR by cognate antigen, the T-cell stops migrating and repolarises itself towards the APC for optimal T-cell activation and delivery of effector molecules (121). This involves retraction of the uropod, rounding up of the T-cell and MTOC translocation from behind to in front of the nucleus where it is positioned adjacent to the plasma membrane region in contact with the APC (121). Although the direct molecular pathways that induce MTOC repolarisation are unclear, TCR proximal signalling proteins that are associated with actin remodelling including Lck, LAT, SLP76, PKC, VAV1 and CDC42 seem to be important (138, 139). Accordingly, there is evidence that actin and microtubule networks are linked, potentially via adhesion and de-granulation adaptor protein (ADAP) which can bind to both F-actin through vasodilator-stimulated phosphoprotein (VASP), and the MTOC via the microtubule motor protein dynein (140, 141). Once the MTOC has localised adjacent to the interface between the T-cell and the APC, called the immune synapse (IS), it enables the transport of cytotoxic granules, signalling proteins and cytokines to the centre of the IS via dynein (142, 143). A schematic of MTOC translocation during T-cell polarisation towards the target cell is shown in Figure 1.6a. Actin cytoskeletal rearrangements have been shown to be critical for T-cell repolarisation and effector function as inhibition of actin polymerisation abrogated proximal TCR signalling (144) and disrupted T-cell: APC binding (145). TCR signalling leads to actin polymerisation via the activation of the actin-related proteins 2/3 (Arp2/3) complex by two major nucleation-promoting factors (NPFs) called Wiskott-Aldrich syndrome protein (WASp) and WASp family verprolin homologous protein (Wave2) (28, 126). Arp2/3 enables the branching of actin onto pre-existing actin filaments. Following TCR ligation, the multi-molecular proximal signalling complex forms; Vav1 binds to SLP76, GADS, LAT, and Itk, the latter of which activates VAV1 (28, 146). VAV1-dependent activation of the Rho-GTPase Cdc42 enables subsequent activation of WAVE2 (147, 148). Meanwhile, VAV1 also activates the Rho-GTPase Rac1 to activate WASp (148). WASp and WAVE2 promote actin polymerisation from Arp2/3 complexes, causing F-actin accumulation at the IS (148). Additionally, WASp has been shown to couple LFA-1 to the actin cytoskeleton (126).

The IS is an actin-dependent structure which supports T-cell activation and the delivery of cytotoxic granules by CD8 T-cells and has three major concentric regions called supramolecular activation clusters (SMACs): the central region of the IS is called the c-SMAC and is surrounded by peripheral (p-SMAC) and distal (d-SMAC) regions (149). A schematic of the immune synapse is shown in Figure 1.6b. In the mature IS, the c-SMAC contains the TCR and molecules such as CD28, the p-SMAC is rich in adhesive molecules such as LFA-1, providing a ring of strong attachment to the APC underpinned by an F-actin ring, and the outermost d-SMAC contains larger molecules such as the tyrosine phosphatase CD45 (127, 149). F-actin initially forms in the d-SMAC and

continually moves inwards as radial arcs across the p-SMAC where it dynamically accumulates to form a peripheral actin ring, before translocating to c-SMAC where it is disassembled (150-153). TCR and LFA-1 microclusters form distinct patches in the d-SMAC and are pulled by centripetal waves of F-actin towards the c-SMAC (152, 153). Although TCR microclusters and associated signalling molecules initially associate with F-actin via SLP76, Nck and WASp/WAVE in peripheral regions of the IS, these microclusters have been shown to travel into and become concentrated in the c-SMAC in an actin-independent manner (151, 154). Meanwhile, LFA-1 microdomains link to underlying F-actin via linker proteins such as talin (155). The actin-deplete state of the c-SMAC, in addition to a high concentration of proteins at the c-SMAC, excludes LFA-1 clusters from this region (127, 151). The F-actin is depolymerised at the boundary between the p-SMAC and c-SMAC possibly by negative regulators such as cofilin (156), enabling a clear central region at the IS for subsequent delivery of cytotoxic granules by exocytosis, but also delivery of T-cell signalling molecules directly to the c-SMAC. Surface receptors, including the TCR, have also been shown to be degraded following endocytosis from the c-SMAC, or recycled back to the c-SMAC (153). On the opposite end of the T-cell, other molecules including CD43 and CD44 accumulate in a region called the distal-pole complex (127).

a) MTOC translocation and cytotoxic granule secretion



b) The immune synapse

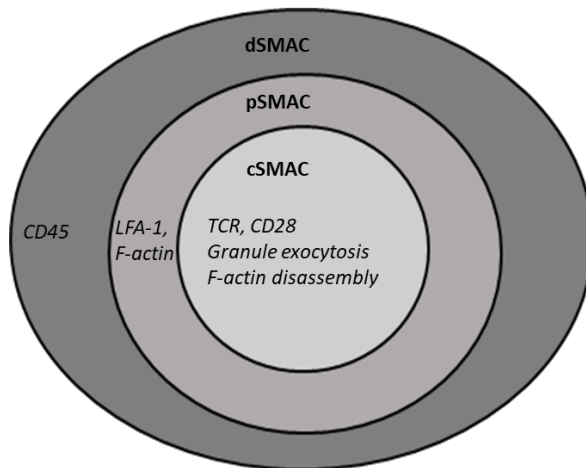


Figure 1.6 MTOC translocation and structure of the immune synapse

a) Upon ligation of the TCR by cognate pMHC on the target cell, T-cells repolarise towards the target cell. This involves retraction of the uropod and translocation of the microtubule organising centre (MTOC) from behind to in front of the nucleus, where it docks behind the immune synapse (IS). In the migrating T-cell, cytotoxic granules are distributed around the cell attached to microtubules. Following MTOC translocation, cytotoxic granules are transported by the microtubule motor protein dynein towards the IS, where cytotoxic molecules are released towards the target cell. **b)** The immune synapse can be divided into three concentric regions called supramolecular activation clusters: the central region is called the central SMAC (cSMAC) and contains the TCR and proximal TCR signalling molecules such as CD28. The peripheral region surrounding the c-SMAC (pSMAC) is rich in F-actin and the integrin LFA-1. The outermost region is called the distal SMAC (dSMAC) and contains larger molecules such as the phosphatase CD45.

1.3.2.13 T-cell tolerance, memory, exhaustion

T-cell tolerance and anergy

Despite central tolerance, which involves the deletion of T-cells that express TCRs with high affinity for self-antigen, T-cells expressing TCRs that bind to self-antigen with low affinity exit the thymus to enter circulation (157). Therefore, peripheral tolerance mechanisms are needed to prevent the activation of self-reactive T-cells in the periphery (157). When T-cells are stimulated by cognate self-antigen in the absence of sufficient costimulation, they adopt a phenotype of decreased effector responses, which is called T-cell tolerance (157). This tolerant state helps to prevent autoimmunity (157). DCs constitutively present self-antigen to T-cells in the absence of inflammation but the lack of PAMPs and DAMPs prevents DCs from undergoing maturation (12). Since immature DCs express low levels of costimulatory ligands and do not secrete inflammatory cytokines, they provide weak Signals 1, 2 and 3 to T-cells, which prevents the acquisition of T-cell effector functions (12). Although the tolerant state can be partially reversed to restore T-cell effector functions, for example, by expanding T-cells *in vitro* in the presence of IL2 and IL15 or under lymphopenic conditions *in vivo*, eventual reversion back to a tolerant state has been shown to occur due to epigenetic programming (157, 158). Both CD4 and CD8 Tregs also contribute to peripheral tolerance by suppressing the priming and activation of T-cells through various mechanisms (discussed in Sections 2.3.2.9 and 2.3.2.10). Anergy is often used to describe the non-responsive T-cell state resulting from *in vitro* stimulation of naïve T-cells, in the absence of costimulation (157). T-cell anergy and tolerance share functional and transcriptional phenotypes but also have differences, due to the distinct ways they are induced.

T-cell memory

During an acute pathogenic infection, naïve T-cells first encounter antigen in secondary lymphoid organs (SLOs) and proliferate over ~1 week, giving rise to 1) effector T-cells that function to eliminate the pathogen over ~1-2 weeks and 2) a smaller pool of memory T-cells which survive long-term (159). Once the pathogen has been eradicated, the immune response diminishes in order to prevent tissue damage; 90-95% of antigen-specific T-cells undergo apoptosis (160). This leaves behind memory T-cells which have the potential to rapidly respond to antigen upon secondary infection, eradicating the pathogen before the host displays symptoms of disease (77, 159, 160). Memory T-cells can be divided into 2 major subsets: central-memory (T_{CM}) and effector-memory (T_{EM}) T-cells (77, 160, 161). T_{CM} cells express high levels of the IL-7 receptor (CD127), C-C chemokine receptor 7 (CCR7) and L-selectin/CD62L (77, 160, 161). In contrast, T_{EM} cells express low levels of CD127, CD62L, and are deficient in CCR7 (77, 160, 161). CD127 expression enables IL-7-driven homeostatic proliferation of T_{CM} cells to maintain the memory pool (77, 160, 161). The CCR7 ligands CCL19 and CCL21 are produced by SLOs, therefore T_{CM} cells home to SLOs; this homing is also mediated by CD62L which binds to its ligands on high endothelial

venules (HEVs), facilitating transmigration of T_{CM} cells into SLOs (77, 160, 161). T_{EM} cells, which are similar in function to T-effector (T_E) cells, preferentially circulate in peripheral tissues as they express low levels of these SLO homing molecules (77, 160, 161). While T_{CM} respond to antigens by proliferating to produce T_{EM} cells, T_{EM} cells respond by carrying out cytolytic or cytokine-secreting effector functions at the site of infection (77, 160, 161). T-cell memory has a half-life of ~8-15 years, therefore, immunological memory can last for decades (161). The antigen and cytokine milieu affect the ratio of the transcription factors Tbet and Eomes within a T-cell (99). In turn, these transcription factors are important drivers of T-cell fate, with a higher and lower Tbet:Eomes ratio translating into an effector or memory phenotype, respectively (99).

T-cell exhaustion

T-cell exhaustion occurs during chronic infection or cancer, as a result of chronic antigenic stimulation of T-cells. T-cell exhaustion mechanisms evolved to limit damage from long-term inflammation in healthy tissue, as they diminish T-cell effector responses; however, in the tumour setting, exhaustion of T-cells limits their anti-tumour potential. Under chronic stimulation, exhausted T-cells develop from memory precursor effector cells (MPECs) which inhibits the formation of the memory T-cell pool (162, 163).

CD8 T-cell exhaustion was first described in a model of chronic lymphocytic choriomeningitis (LCMV) infection, where virus-specific CD8 T-cells lost the ability to secrete IFN- γ and kill viral targets in a CD4 T-cell dependent manner (164). The CD8 T-cell exhaustion phenotype develops progressively, starting with a loss of proliferative capacity and IL2 production (165-167). Later stages of exhaustion development involve partial loss or lack in the ability to produce IFN- γ and to degranulate (166, 167). The most severe stage of exhaustion leads to the deletion of tumour or virus-specific T-cells (167). Several factors determine the severity of T-cell exhaustion. The availability of viral epitopes influences epitope-specific T-cell exhaustion, with higher epitope presentation accelerating exhaustion development (166). Accordingly, higher viral load and longer duration of infection heighten the exhausted phenotype. Moreover, IL10 and TGF β are cytokines that have been shown to promote exhaustion during chronic LCMV infection. Reduced CD4 T-cell help and a higher expression level of more inhibitory receptors also augments the T-cell exhaustion phenotype (167). While T-cell exhaustion has been primarily studied in chronic viral infections, chronic antigen persistence in tumour development leads to T-cell populations with similar phenotypes.

Originally, the reduced effector functions of exhausted CD8 T-cells were thought to have solely negative effects on viral and tumour clearance, but accumulating data has demonstrated that exhausted T-cell populations may be epigenetically specialised to effectively limit tumour and

viral growth over long time periods, with minimal immunopathology (168-170). There is recent epigenetic and transcriptomic evidence that exhausted CD8 T-cells from chronic viral infection may develop from distinct populations of effector T-cells *versus* classical effector T-cells or memory precursor T-cells, suggesting that exhausted T-cells may form a distinct lineage evolved to protect the host from otherwise damaging full-blown effector T-cell responses to chronic antigen (169). It has also been broadly accepted that terminally differentiated exhausted T-cell populations express the transcription factor T-cell factor 1 (TCF1) and the coinhibitory receptors programmed cell death 1 (PD1) and T-cell immunoglobulin and mucin domain-containing protein 3 (TIM3) (171). These PD1⁺ TIM3⁺ GzmB⁺ CD8 T-cell populations, which have effector functions, develop from TCF1⁺ PD1⁺ TIM3⁻ GzmB⁻ T-cell precursors which display a stem cell-like, self-renewing capacity (172, 173). TCF1 is also expressed by central memory cells and is thought to drive the proliferative and self-renewal capacity of the precursor population (168, 173-176). It has been shown that TCF1⁺ PD1⁺ TIM3⁻ T-cell precursors are responsible for an expansion of tumour-specific T-cells in response to PD1 blockade, suggesting that PD1 blockade does not simply reverse the exhausted state of T-cells, but induces proliferation of the precursor subset and expands the population of terminally differentiated T-cells which mediate tumour control (172). This suggests that targeting the terminally exhausted TCF1⁺ PD1⁺ TIM3⁺ CD8 TIL subset to enhance the effector functions of this population could further enhance tumour control in combination with PD1 blockade. It is unknown whether blockade of TIM3 on CD8 TILs directly improves tumour-specific CD8 T-cell effector functions, including cytotoxicity, or if this occurs indirectly through other cell types. Thus, it is of interest to further establish the cell types and contexts necessary for therapeutic efficacy of PD1 and TIM3 blockade.

The transcriptional pathways that regulate T-cell exhaustion are still being revealed but some transcription factors have been identified. While effector T-cells express higher levels of Tbet and less Eomes and memory T-cells express higher Eomes levels and less Tbet, chronic stimulation drives T-cells to express even higher levels of Eomes *versus* memory cells, to promote the exhausted phenotype (177). The transcription factors Tox and NFAT are also implicated in the development of exhaustion (178, 179).

Coinhibitory receptors

T-cell exhaustion is partially mediated by the upregulation of multiple co-inhibitory receptors TIM3, PD1, lymphocyte activation gene-3 (LAG3), cytotoxic T-lymphocyte associated protein-4 (CTLA4), T-cell immunoglobulin and ITIM domain (TIGIT) and carcinoembryonic antigen-related cell adhesion molecule 1 (CEACAM1), which belong to the immunoglobulin superfamily of co-receptors and inhibit TCR signalling (163). While coinhibitory receptor expression is associated with T-cell exhaustion, coinhibitory receptors are also expressed on T-cells with intact cytotoxicity

and cytokine production. Many coinhibitory receptors such as PD1, CTLA4 and CEACAM1 are normally upregulated following CD8 T-cell activation and counteract costimulatory signals to produce a balanced T-cell response (180). Under chronic antigen stimulation, however, coinhibitory receptors are strongly upregulated and maintained on the surface of CD8 T-cells to support exhaustion development (163). Recently, the coordinated upregulation of coinhibitory receptors in a tumour setting has been found to result from IL27 signalling through the IL27 receptor (IL27R) on T-cells (181, 182). Downstream of IL27R ligation, upregulation of the transcription factors Prdm1 and c-Maf were found to induce the expression of a gene module encoding PD1, LAG3, TIM3, TIGIT and IL10 in CD8 TILs from murine melanoma (181, 182). The expression of these coinhibitory receptors was almost absent in CD8 TILs from double-knockout mice that did not express Prdm1 and c-Maf in T-cells (181, 182). Moreover, TILs from these double-knockout mice produced higher levels of IFN γ , TNF, proliferated more and this was associated with reduced tumour growth (181, 182).

Programmed cell death 1 (PD1)

Programmed cell death 1 (PD1) is a transmembrane protein comprised of an extracellular IgV domain, transmembrane domain and a cytoplasmic tail which contains an immunoreceptor tyrosine-based inhibitory motif (ITIM) and immunoreceptor tyrosine-based switch motif (ITSM). ITIMs and ITSMs are conserved amino acid motifs which contain tyrosine residues that are phosphorylated downstream of receptor ligation. Phosphorylated ITSMs and ITIMs recruit phosphatases to the IS. Thus, these inhibitory motifs counteract ITAMs, which recruit kinases to the IS. PD1 is upregulated following TCR stimulation and regulates effector, memory and exhausted T-cell responses; it is also expressed by B cells and myeloid cells. Following PD1 ligation on T-cells by its primary ligand PDL1, which is expressed by APCs and peripheral tissues, the ITIM and ITSM domains are bound by the Src homology region 2 domain-containing phosphatase 2 (SHP2). SHP1 can also bind to the ITSM motif, however it is unclear what role SHP1 plays in PD1 signalling as SHP2, but not SHP1, has been shown to associate with PD1 at the immune synapse to dephosphorylate proximal T-cell signalling proteins (183, 184). Supporting the suppressive role of PD1 signalling, PDL1 is often upregulated by tumour tissues to escape the antitumour T-cell response and a higher expression of PDL1 in human tumour samples is associated with a worse prognosis (185, 186). In our lab, PD1 was found to regulate T-cell polarisation and the stability of the immune synapse with tumour targets: PD1 blockade treatment of tumour-bearing mice *in vivo* partially restored T-cell polarisation and immune synapse stability of isolated CD8 TILs *in vitro* (187). However, PD1 blockade of TILs *in vitro* decreased the IS stability suggesting that PD1 engagement over a timescale of days rather than hours was required for the suppressive effect.

Cytotoxic T-lymphocyte associated protein 4 (CTLA4)

Cytotoxic T-lymphocyte associated protein 4 (CTLA4) is comprised of an extracellular IgV domain, transmembrane domain and a cytoplasmic tail; in naïve T-cells, CTLA4 is stored within intracellular vesicles and becomes transiently expressed on T-cells following TCR stimulation, with a peak expression level 48-72h post-stimulation (188). Unlike PD1, the CTLA4 cytoplasmic tail does not contain classical ITIM or ITSM motifs, but contains two tyrosine motifs one of which enables binding of PI3K, SHP2, PP2A and AP1 and AP2. CTLA4 helps to regulate T-cell priming in lymphoid organs by limiting the access of CD28 on T-cells to its ligands CD80 and CD86 on APCs; CTLA4 competitively binds to the CD28 ligands with higher affinity than CD28, restricting CD28-mediated costimulation. CTLA4 can also bind to CD28 ligands and pull them out of the APC surface via transendocytosis, reducing ligation of CD28. Accordingly, CTLA-deficient mice develop severe autoimmune disease that leads to death. CTLA4 has also been shown to promote T-cell motility to prevent stable contact between T cells and APCs and is constitutively expressed by Tregs (189). Moreover, CTLA4 binding to ligands on DCs has been shown to induce a tolerogenic DC phenotype characterised by IL10 secretion and expression of indoleamine-2,3-dioxygenase (IDO), an enzyme which depletes tryptophan from the environment and suppresses T-cell proliferation (190).

Lymphocyte activation gene-3 (LAG3)

Lymphocyte activation gene-3 (LAG3) is structurally similar to CD4 and consists of four extracellular IgG domains, a transmembrane domain and a cytoplasmic tail that contains a KIEELE motif thought to be required for inhibitory signalling (191-193). LAG3 is upregulated following T-cell stimulation, constitutively expressed by Tregs and is also found on a subset of NK cells (194, 195). LAG3 was found to bind MHC II, which suggested it competitively inhibits CD4 binding. However, recent evidence suggests this is not a primary mechanism by which LAG3 regulates T-cells; LAG3 fusion protein inhibited CD4 and MHC II binding only when the TCR was not ligated, while another study found no evidence for LAG3-mediated inhibition of the CD4 and MHC II interaction (191, 192). Other ligands for LAG3- which has four glycosylation sites- have been identified including: galectin 3, liver sinusoidal endothelial cell lectin (LSECTin) and fibrinogen-like protein 1 (FGL1) (196, 197). Upon ligand binding, it is unknown how an inhibitory signal through LAG3 is transmitted as there is conflicting data on the importance of the KIEELE motif (193, 198).

T-cell immunoglobulin and ITIM domain (TIGIT)

T-cell immunoglobulin and ITIM domain (TIGIT) contains an IgV extracellular domain, transmembrane domain and a cytoplasmic tail that contains an ITIM and immunoglobulin tail tyrosine (ITT)-like motif (199, 200). TIGIT is expressed by activated T-cells and NK cells (199-201). TIGIT signalling studies in NK cells have shown that TIGIT ligation by its ligand CD155 induces

tyrosine phosphorylation of the cytoplasmic tail which recruits SHP1 to inhibit PI3K, MAPK and NF κ B signalling (201, 202). In T-cells, this has been shown to inhibit T-cell activation and proliferation in addition to downregulation of TCR α , CD3 ϵ and PLC γ (203). TIGIT signalling also induces upregulation of molecules such as IL7R and IL15R, and anti-apoptotic molecules to maintain survival of exhausted T-cells (203). *In vitro*, the costimulatory receptor CD226 competes with TIGIT for binding CD155, however, TIGIT binds with greater affinity to their shared ligands. It is unknown to what degree this competitive inhibition of CD226 costimulation plays a role *in vivo*.

T-cell immunoglobulin and mucin domain-containing protein 3 (TIM3)

(expression, appraisal of putative ligands, function)

T-cell immunoglobulin and mucin domain-containing protein 3 (TIM3) was first discovered as a cell surface marker for IFN γ -producing CD4 Th1 and cytotoxic CD8 T-cells (204), although it has since been found expressed on Tregs, NK cells, macrophages and DCs (205-211). TIM3 belongs to the TIM family of genes including TIM1, TIM3 and TIM4 on chromosome 5 in humans and TIM1-8 on chromosome 11 in mice (212, 213). The TIM3 gene family belongs to the wider immunoglobulin superfamily (213). Murine TIM3 is 281 amino acids long, while human TIM3 is 302 amino acids long (204). Both murine and human TIM3 have an extracellular domain comprised of an N-terminal immunoglobulin variable-region-like domain and a mucin domain rich in serine and threonine residues (214). This is followed by a stalk domain, a transmembrane domain and cytoplasmic tail which contains six tyrosine residues (214). Human TIM3 (hTIM3) is 63% identical to murine TIM3 (mTIM3), and the cytoplasmic domain shares 77% identity (214). The TIM3 cytoplasmic tail does not contain ITIMs or ITSMs (214). Instead, two of the 6 tyrosine residues in the TIM3 cytoplasmic tail are thought to be critical for TIM3 signalling (Tyr 256 and 263 in mTIM3, and Tyr 265 and 272 in hTIM3) (215-217). TIM3 is encoded by seven exons and in mice, but not humans, alternative splicing can produce a soluble form of TIM3 lacking the mucin and transmembrane domains (218). In humans, a disintegrin and metalloprotease (ADAM) enzymes can cleave TIM3 at the stalk region, separating the extracellular domain from the transmembrane region to generate soluble TIM3 (219). Cleavage seems to require an intact cytoplasmic domain, suggesting it occurs downstream of TIM3 signalling, but the role of soluble TIM3 is unknown (219). The IgV domain of TIM3 is comprised of two anti-parallel β sheets, linked via a disulfide bridge between cysteine residues (220). Four other cysteine residues are linked by two additional disulfide bridges in the IgV domain and a cleft is formed between CC' and FG' loops which is where the putative TIM3 ligands phosphatidylserine, CEACAM1, and HMGB1 are thought to bind (discussed below) (220).

Inhibitory signalling upon TIM3 ligation

Although the mechanisms of TIM3 inhibitory signalling have yet to be fully defined, the primary mechanism proposed for TIM3 inhibitory signalling involves phosphorylation of the TIM3 cytoplasmic tail by Src kinases including Itk at the Y265 and Y263 residues upon TIM3 ligation, followed by dissociation of the HLA-B-associated transcript 3 (BAT3) from the TIM3 cytoplasmic tail, which is thought to enable the Src kinase Fyn to bind to the same site of the tail (215-217). A schematic of signalling downstream of TIM3 is shown in Figure 1.7. Firstly, BAT3, bound to TIM3, is proposed to maintain a pool of active Lck at the immune synapse, which promotes TCR proximal signalling; dissociation of BAT3 from the TIM3 tail therefore reduces the local availability of active Lck at the IS (215, 221). Accordingly, BAT3 and active Lck (with the Y394 phosphorylation) were co-immunoprecipitated following overexpression in 293T cells, while the interaction of BAT3 and Lck was abrogated using a TIM3 agonist antibody (215). Meanwhile, the inactive form of Lck (with the Y505 phosphorylation) did not bind to BAT3 (215). Additionally, BAT3 mRNA levels were less than half in TIM3⁺PD1⁺ versus TIM3⁻PD1⁺ TILs from CT26 colorectal carcinomas, associating TIM3 upregulation with reduced BAT3 expression, although the mechanism was not elucidated (215). Secondly, Fyn has been shown to activate membrane-anchored phosphoprotein associated with glycosphingolipid-enriched microdomains (PAG) which recruits the tyrosine kinase Csk to the immune synapse in lipid rafts containing Lck, enabling the deactivation of Lck via inhibitory phosphorylation at the Y505 of Lck (222). Thus, by maintaining Fyn at the IS, TIM3 may support deactivation of Lck, although this mechanism has yet to be demonstrated. Together, these possible mechanisms suggest that TIM3 can suppress TCR proximal signalling processes, by inducing inhibitory signalling that centres on Lck. Notably, while ligation of TIM3 is thought to be required for TIM3 inhibitory signalling, the relevant TIM3 binding partners have yet to be confirmed.

TIM3 ligands

Galectin-9

Galectin-9 is a C-type lectin that comprises two carbohydrate recognition domains (CRDs) joined by a flexible linker (223). Each CRD contains an arginine residue which is important for binding to glycosylated regions on TIM3, although the exact binding site on TIM3 is unclear (220, 224). Galectin-9 is predicted to bind to oxygen (O) and nitrogen (N)-linked glycans in the TIM3 mucin and stalk domains, while it could also bind to N-linked glycosylation sites on the TIM3 IgV domain that is on the opposite side to the FG-CC' cleft, a binding site for other TIM3 ligands (220). Galectin-9 is primarily expressed in the thymus, lymph nodes, spleen and bone marrow, but also on epithelial and endothelial cells, fibroblasts and myocytes (225). Galectin-9 expression levels are

generally reduced in tumours compared to normal tissue, suggesting downregulation of galectin-9 supports tumour growth despite its association with inducing suppression of T-cells via TIM3 (223). Low or absent galectin-9 expression levels in a variety of human tumour lines including renal, melanoma, lung and breast cells has been reported (226). Accordingly, galectin-9 ligation of its binding partners has been found to induce apoptosis of melanoma and leukaemia cell lines (227). Galectin-9 is reported to have antimetastatic potential by enhancing cancer cell aggregation and reducing cell adhesion to the ECM (228-230). Furthermore, upregulation of galectin-9 has been associated with cell cycle arrest, while loss of galectin-9 by cancer cells gives them a proliferative advantage (223). Nevertheless, it is likely that the context of galectin-9 expression will determine the overall effect of galectin-9 expression on tumour cell growth, as increased levels of galectin-9 have been found on leukaemia and colorectal cell lines (226). Additionally, variable levels of galectin-9 have been found to be expressed on ovarian tumour cell lines depending on the tumour subtype (226). Galectin-9 is found on the cell surface but is also highly secreted; soluble levels of galectin-9 have been positively correlated with increased tumour progression, while intratumoural levels have been found to have less effect on disease progression (223).

Galectin-9 was first reported to bind TIM3 using transient transfection of Chinese hamster ovary (CHO) cells to induce intracellular (but not cell surface) expression of galectin-9, and intracellular staining using TIM3-Ig (224). Upon binding to TIM3, galectin-9 has been found to cause dissociation of BAT3 and active Lck protein from the TIM3 cytoplasmic tail, leading to dampening of T-cell proximal signalling by reducing the local pool of active Lck at the IS (215). In support of Bat3 and TIM3 as binding partners, BAT3 bound to the cytoplasmic tail of mTIM3 using a yeast 2-hybrid approach, while mTIM3 and BAT3 were co-immunoprecipitated from EL4 T-cell lymphoma cells (215). Ligation of TIM3 by galectin-9 induced tyrosine phosphorylation of the TIM3 cytoplasmic tail via Itk at the murine TIM3 (mTIM3) tyrosine 256, which caused dissociation of BAT3 from the TIM3 cytoplasmic tail due to the topographical change (215). In support of a stimulatory role for BAT3, BAT3 overexpression enhanced IFN γ and IL2 secretion of MOG-specific Th1 T-cells isolated following adoptive transfer into Rag $^{-/-}$ mice (215). Following galectin-9 treatment *in vitro*, BAT3 overexpression by Th1 T-cells decreased cell death (215). Thus, BAT3 was indicated to protect Th1 T-cells from apoptosis that could result from galectin-9 binding to TIM3. Another study confirmed the pro-apoptotic role of galectin-9 binding to TIM3, as the addition of galectin-9 to TIM3 $^{+}$ CD8 TILs *in vitro* enhanced apoptosis, while TIM3 blockade partially reversed this effect (231). IFN γ production by T-cells is also regulated via TIM3 ligation by galectin-9 and galectin-9 was found to interact with TIM3 to decrease the abundance of CD44 hi CD62 lo T-cells suggesting it reduces the formation of memory T-cells (232). In contrast to other findings, a study

using TIM3-Ig and galectin-9 in *in vitro* binding assays found that galectin-9 did not bind to TIM3 (233).

Phosphatidylserine (PtdSer)

Phosphatidylserine (PtdSer) is a phospholipid that is usually located on the inner leaflet of the plasma membrane but becomes exposed on the outer leaflet in apoptotic cells, enabling the recognition and engulfment of apoptotic bodies by phagocytes (234, 235). TIM3 was shown to bind to PtdSer in its FG-CC' cleft, a property shared by other TIM family members (236). Through binding to PtdSer, TIM1 and TIM4 have been shown to enhance the phagocytosis of apoptotic cells *in vitro* by fibroblasts although it has not been demonstrated *in vivo* (212, 237). Similarly, fibroblastic cells expressing TIM3 phagocytosed apoptotic cells via PtdSer, although T-cells expressing TIM3 did not display phagocytic capacity (236). As failure to clear apoptotic bodies is associated with autoimmunity, TIM protein engagement of PtdSer may play a role in maintaining peripheral tolerance (212, 238). One study has revealed that TIM3 on CD8⁺ DCs facilitated the uptake and presentation of antigens from apoptotic cells and confirmed that TIM3 can bind to PtdSer, however, the direct role of PtdSer and TIM3 interactions in mediating antigen uptake and cross presentation was unclear (208). Overall, more studies are required to confirm the functional effects of TIM3: PtdSer interactions on both T-cells and DCs.

High-mobility group protein B1 (HMGB1)

HMGB1 is released from dying cells and acts as a danger signal, by forming complexes with nucleic acids which trigger receptor for advanced glycation end products (RAGE) and Toll-like receptors (TLRs) 2 and 4 on DCs and macrophages (239). This induces the release of proinflammatory cytokines such as TNF and IL-6 and promotes DC maturation, thereby supporting T-cell activation (239-241). In a MC38 murine colon carcinoma model, TIM3 was found to bind to HMGB1 and impaired HMGB1-mediated nucleic acid uptake by DCs, which limited DC activation (242). The chemotherapeutic drug cisplatin has been shown to increase the release of HMGB1 from dying tumour cells (243); TIM3 blockade was found to enhance the anti-tumour response to cisplatin therapy (242). Moreover, since the TIM3 blocking antibody used in the study (RMT3-23) is known to block the FGCC' cleft of TIM3, this suggested that HMGB1 binds at a site in this cleft which overlaps with the PtdSer and CEACAM1 binding sites (242, 244). Notably, anti-galectin 9 and annexin V administration into tumour-bearing mice did not alter the effect of TIM3 blockade, suggesting that HMGB1 could bind to TIM3 independent of PtdSer and galectin-9 (242). However, subsequent binding studies failed to recapitulate an interaction between HMGB1 and TIM3 (244). Further studies are needed to investigate whether HMGB1 is a TIM3 ligand and whether targeting of the TIM3/HMGB1 axis could work well in combination with other chemotherapeutic agents.

CEACAM1 (carcinoembryonic antigen related adhesion molecule-1)

CEACAM1 is the most recently proposed TIM3 ligand (245). Alternative splicing of the CEACAM1 mRNA transcript generates nine transmembrane and three secreted CEACAM1 isoforms each comprised of one N-terminal IgV domain followed by up to three extracellular constant Ig domains (245). Transmembrane CEACAM1 isoforms have either short (S) or long (L) cytoplasmic domains, the latter of which contains two ITIM motifs that can transmit inhibitory signalling (245). CEACAM1 is expressed by activated T-cells, DCs, macrophages, NK cells, and epithelial tumour cells (245). Activated T-cells predominantly express CEACAM1-L isoforms, except for intestinal T-cells which express more CEACAM1-S than CEACAM1-L (245). While all CEACAM1-L isoforms have an N-terminal Ig domain that is thought to bind the FG-CC' cleft of TIM3, similar to phosphatidylserine and HMGB1, it is unknown whether the number of extracellular constant Ig domains affects signalling downstream of CEACAM1-L isoforms (245). CEACAM1-4L is the most abundant long isoform expressed by T-cells and has three extracellular constant Ig domains (245). As CEACAM1 has multiple N-linked glycosylation sites along the extracellular domains but not in the FG-CC' cleft, it has been suggested that galectin-9 (which binds N and O-linked glycans) can bridge CEACAM1 and TIM3 to facilitate their binding (246).

Similar to galectin-9, binding of CEACAM1 *in trans* to mTIM3 using a mCEACAM1 NFc fusion protein has been shown to induce BAT3 dissociation from the TIM3 cytoplasmic tail; CEACAM1 coexpression *in cis* with TIM3 was required for BAT3 dissociation from TIM3, as BAT3 dissociation occurred in TIM3^{Tg} mice (which overexpressed TIM3 on T-cells) but not TIM3^{Tg}CEACAM1^{-/-} T-cells (which overexpressed TIM3 but lacked CEACAM1 on T-cells) (221). CEACAM1 has also been proposed to promote TIM3 surface expression via *in cis* interactions, as CD4 T-cells from tolerization-resistant CEACAM1^{-/-} but not tolerised WT mice lacked TIM3 expression after *Staphylococcus aureus* enterotoxin B (SEB) administration (221). Moreover, cotransfection of CEACAM1 and TIM3 into Jurkat T-cells enhanced the percentage of TIM3⁺ T-cells compared to transfection with TIM3 alone (221, 247). In support of binding *in cis* between TIM3 and CEACAM1, following transfection of hTIM3 and hCEACAM1 into HEK293T cells, TIM3 and CEACAM1 co-immunoprecipitated; mutation of amino acids in the IgV domains that were predicted to enable binding abrogated the co-immunoprecipitation (221). CEACAM1 has been proposed to bind TIM3 on early stage post-activated primary human CD8 T-cells to inhibit restimulation-induced cell death (RICD), as T-cells expressed high levels of both receptors during clonal expansion, while TIM3 blockade, TIM3 knockdown or CEACAM1 knockdown using small interfering RNA (siRNA) increased cell death following anti-CD3 restimulation (247). CEACAM1 is coexpressed with TIM3 on TILs that have exhaustion phenotypes such as low IL2 and IFN γ secretion and low proliferative capacity (221, 248, 249). *In vivo* tumour studies have associated CEACAM1 and TIM3 coexpression with T-cell suppression by measuring the cytokine production and proliferation of TILs *ex vivo*,

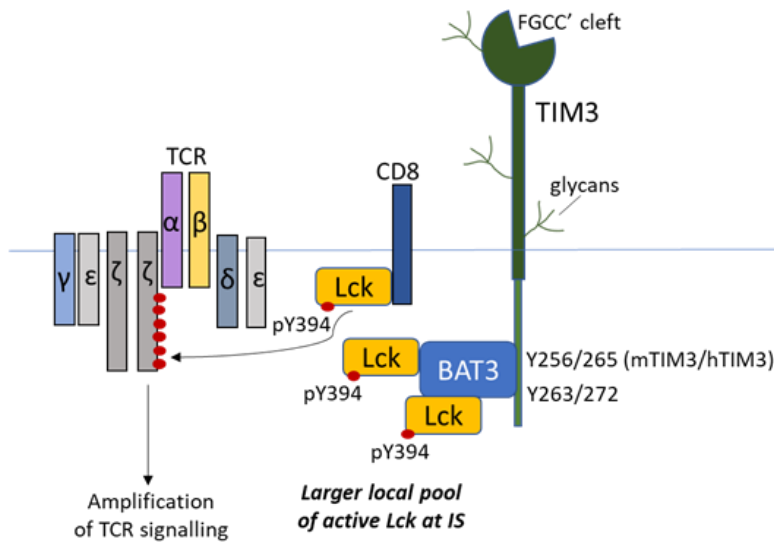
however, there is no evidence that CEACAM1 and TIM3 directly coregulate killing of tumour cells by cytotoxic CD8 T-cells, as the role of other cell types cannot be excluded in the *in vivo* experiments conducted (248, 249). In addition to CD4 and CD8 T-cells, both CEACAM1 and TIM3 are expressed by NK cells and myeloid cells including DCs, macrophages and neutrophils (205, 207-209, 242, 250-254). One study has reported that CEACAM1 and TIM3 do not interact to alter NF κ B, NFAT or AP1 translocation to the nucleus, while confirming inhibitory signalling on these pathways from both receptors alone (255). More evidence is needed to determine whether CEACAM1 can directly bind to TIM3 as a ligand, *in cis* and *in trans*, and whether these receptors can directly coregulate killing of tumour cells by cytotoxic CD8 T-cells, in the absence of other cell types. Such knowledge will aid the development of cancer therapies that effectively target these receptors to enhance the anti-tumour CD8 T-cell response.

TIM3 costimulatory signalling

Although the majority of data indicates an inhibitory role for TIM3, under certain contexts TIM3 has been found to exhibit costimulatory signalling. A schematic of signalling downstream of TIM3 is shown in Figure 1.7. The primary mechanism proposed to mediate TIM3 costimulation is the binding of BAT3 to the cytoplasmic tail of unligated TIM3, which maintains a pool of active Lck at the IS, supporting TCR proximal signalling (215, 221, 256). In the first study to describe an activating role for TIM3, transient ectopic expression of both murine and human TIM3 on Jurkat cells promoted NFAT/AP-1 and NF κ B signalling- this was dependent upon the three most C-terminal tyrosines in the cytoplasmic tail (216). Doxycycline-induced TIM3 expression on Jurkat T-cells also enhanced IL2 production and a higher frequency of T-cells produced IFN γ when T-cells expressed full-length TIM3 (flTIM3) compared to T-cells that lacked the five most C-terminal tyrosines (216). Furthermore, antibody ligation of TIM3 roughly halved the production of IFN γ secreted by anti-CD3 stimulated murine T-cells that overexpressed TIM3, suggesting that the antibody inhibited costimulation via TIM3, although whether the antibody clone used (5D12) is antagonistic (as claimed by the authors) or agonistic is unclear (216). Costimulatory TIM3 signalling has been proposed to accelerate restimulation-induced cell death (RICD) in late-stage primary human CD8 T-cells, as siRNA-mediated knockdown of TIM3 decreased RICD and was associated with reduced phosphorylation of tyrosines in whole T-cell lysates and reduced expression of the proapoptotic proteins BIM and FASL (247). Following acute LCMV infection, TIM3 enhanced the development of short-lived effector cells (SLECs) over memory precursor effector T-cells (MPECs) in the antigen-specific CD8 T-cell pool (257). Moreover, overexpression of TIM3 enhanced phosphorylation of the ribosomal component S6 which is downstream of Akt/TOR signalling and increased the T-cell response to restimulation according to p26 and CD69 expression (258). Therefore, these data suggested that TIM3 costimulation could contribute to the depletion of the memory T-cell pool seen in chronic infection and tumour settings (162, 259,

260). Overall, more studies are needed to identify the contextual factors that induce costimulatory *versus* coinhibitory signalling downstream of TIM3.

TIM3 costimulatory signalling



TIM3 coinhibitory signalling

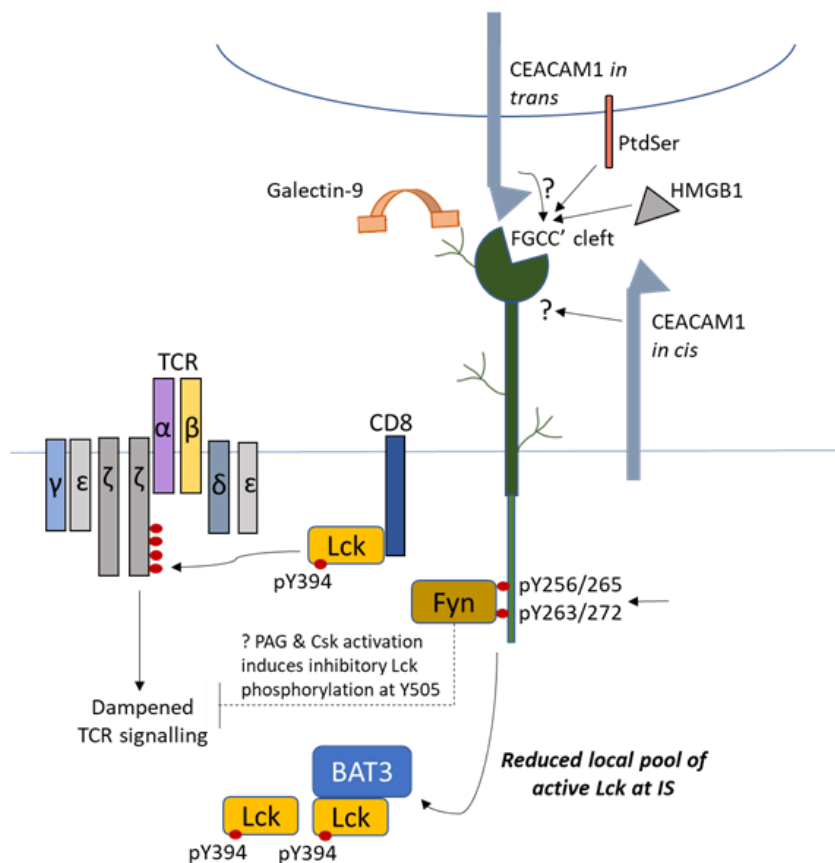


Figure 1.7 Inhibitory and costimulatory TIM3 signalling

Top) Costimulatory signalling downstream of unligated TIM3 is thought to result from the recruitment of HLA-B-associated transcript 3 (BAT3) to the residues 252-270 in the TIM3 cytoplasmic tail, which includes the two key tyrosine residues, Y256/265 and Y263/272 in mice/humans. BAT3 binds to active forms of Lck which are phosphorylated at Y394, maintaining a pool of active Lck at the IS, which promotes TCR signalling. **Bottom)** Ligation of TIM3 in the FGCC' cleft by CEACAM1 *in cis* or *in trans*, HMGB1 or PtdSer, or binding of galectin-9 to N- or O-linked

glycans in the TIM3 IgV, mucin or stalk domains, induces phosphorylation of Y256/265 and Y263/272. This causes dissociation of BAT3 from the TIM3 tail, which reduces the local pool of active Lck at the IS, dampening TCR signalling. In another proposed mechanism for TIM3 coinhibitory signalling, Fyn is known to activate the transmembrane protein phosphoprotein associated with glycosphingolipid-enriched microdomains (PAG), which activates Csk to induce inhibitory phosphorylation of Lck at Y505.

1.4 Cancer

Cancer is a group of more than 200 different diseases caused by the uncontrolled proliferation of cells. In the multi-step process of transformation, normal cells acquire multiple genomic mutations which often endow the resultant neoplastic cells with one or more of the hallmarks of cancer, first posited by Hanahan and Weinberg (261). These include the ability to sustain proliferative signalling, evade growth suppressors, invade and metastasise, resist apoptosis, replicate limitlessly and induce angiogenesis (261). More recently, two further hallmarks of cancer have emerged: reprogrammed metabolism and evasion of immune destruction (262). Treatments have and continue to be developed that target any aspects of these hallmarks and are often most effective in combination regimes (261, 262).

Clinically, two major staging systems are used to define the anatomic nature of cancer. The Tumour, Node, Metastasis (TNM) system describes the size of the tumour, whether it has spread to lymph nodes, and if it has metastasised to distant organs (263). Based on the TNM system, cancers can be categorised into four stages of increasing severity: Stage I where the cancer is small and contained at the primary site of tumour initiation, Stage II involves a larger tumour that in some cases has spread to nearby lymph nodes, Stage III involves invasion of nearby tissues or lymph nodes, while Stage 4 includes metastasis to one or more distant organs (263). Dependent on the tumour stage and type, multiple therapeutic approaches may be appropriate, including the core pillars of cancer therapy which include: surgery for excisable tumours (45% of cancer patients), the non-specific destruction of dividing cells by chemotherapy (28% of patients) and radiotherapy (27% of patients) (Cancer Research UK, 2014). While fifty years ago, 24% of cancer patients survived for 10 years, by 2010, this had doubled due to advances in cancer therapy (Cancer Research UK, 2014). However, due to the heterogeneity of cancer cell populations within tumours, tumours often develop resistance to therapies. For example, increased cancer cell invasiveness into peritumoral normal tissue provides tumour access to intact blood supplies, thus enabling tumour resistance to anti-angiogenic drugs (264), or cancer cells gain tyrosine kinase oncogene mutations which alter the kinase domain, enabling them to escape small molecule tyrosine kinase inhibitors (265).

1.5 Cancer Immunotherapy

1.5.1. Tumour immunosurveillance and immunoediting

A key emerging hallmark of cancer is the ability of tumours to escape the anti-tumour immune response. The concept that the immune system can detect antigenic differences between transformed and healthy cells to eliminate cancer cells was first proposed over 50 years ago and was termed immunosurveillance (266). It has become clear that the immune system plays many

roles during tumorigenesis depending on the timing of its response (262, 267). While in early stages chronic inflammation can promote malignant transformation, later on, the immune response can control tumour growth and shape the immunogenicity of tumours (262, 267). The interactions between cancer and the immune system are now referred to as immunoediting, which is divided into three distinct phases: Elimination, Equilibrium and Escape (268, 269). During the Elimination phase, newly transformed cells display distinct antigenic profiles that differentiate them from normal tissue and enable their elimination by immune cells (268, 269). However, tumour cells with mutations that enable them to resist immune attack can survive and replicate until the second phase, Equilibrium, is reached (268, 269). During this phase, tumour growth is dynamically balanced by the immune system's attempts to control it (268, 269). During this phase, the genetic instability of tumour cells enables them to gradually adapt to better escape immune control (268, 269). Meanwhile, the immune system can alter its response to counteract the evolving tumour (268, 269). Eventually, either the tumour is destroyed by the immune system, or the Escape phase is reached, wherein the immune system can no longer control the tumour, allowing it to grow (268, 269).

1.5.2. Tumour immunosurveillance by T-cells

Effective cancer immunosurveillance by T-cells, which prevents the outgrowth of tumours, requires a number of steps to occur, including: release of tumour-associated antigens by dying cancer cells, antigen uptake by and maturation of dendritic cells (DCs), the successful priming and activation of T-cells by APCs in lymph nodes, trafficking of T-cells to the tumour site through blood vessels, extravasation of the T-cells into the tumour and finally the recognition and killing of cancer cells by T-cells (270). As CD8 T-cell mediated killing of cancer cells releases more cancer cell antigens, this process has been called the 'cancer-immunity cycle', because an effective anti-tumour T-cell response positively feedbacks onto itself (270). Disruption of any of these steps occurs in cancer patients and is often mediated by the excessive activation of inhibitory molecules which enables tumours to escape CD8 T-cell cytotoxicity. The aim of T-cell targeting immunotherapies is to identify which of these steps are inhibiting the revolution of the cancer-immunity cycle in a given patient and administer treatments to facilitate those steps to occur.

1.5.2.1 Steps 1, 2 and 3: Uptake of tumour antigens by DCs for priming of T-cells

Cancer cell mutations lead to the expression of tumour antigens which enable T-cells to distinguish them from normal tissue, these include tumour-associated antigens (TAA) that are often tissue-specific, overexpressed on tumour cells and can be found at lower levels on non-tumour cells (270). TAAs also include cancer/testis antigens usually expressed during embryogenesis in germ cells but found expressed on tumours, such as melanoma-associated antigen 1 (MAGE1), the first TAA identified in melanoma (270). Tumour-specific antigens (TSAs)

are non-self, neoantigens found solely on tumour cells. DCs are critical for the induction of T-cell immunity and can be divided into two broad classes: conventional DCs (cDCs) and plasmacytoid DCs (pDCs) (12, 271). pDCs sense viral RNA and DNA, produce type I interferons and are less involved with priming naïve tumour-specific T-cells compared to cDCs (12). cDCs can be divided into two subtypes: cDC1s, which primarily activate CD8 T-cells by cross-presentation of exogenous antigens via MHCI and prime Th1 cells, while cDC2s activate CD4 T-cells by presentation of internalised antigens via MHCII (12). cDC1s have been shown to be essential for rejection of immunogenic tumours, while vaccination with TAA-pulsed cDC1s limits tumour growth (272). DCs in the periphery uptake and process tumour antigens at tumour sites, meanwhile, dying tumour cells release DAMPs that can bind to pattern recognition receptors such as TLRs on DCs to induce the maturation of immature DCs to mature DCs (271). During maturation, DCs switch to a phenotype highly conducive for subsequent T-cell priming in TDLNs; they upregulate MHC molecules, CD40, CD80 and CD86 costimulatory molecules, and migrate to nearby lymphoid organs (273). In tumour-draining lymph nodes (TDLNs), DCs cross-present epitopes of tumour antigens on MHC I molecules to CD8 T-cells; if the DCs are sufficiently mature they provide strong costimulation and cytokine signals that enable effective T-cell priming (12, 273). Frequently, however, cancer cells adapt to reduce the availability of antigen and DAMPs to prevent DC maturation (12, 273). DC maturation can also be prevented by soluble mediators such as transforming growth factor beta (TGF- β), IL10, lactic acid and vascular endothelial growth factor (VEGF) that are common in the TME (273). Moreover, such TME factors can induce DCs to express immunosuppressive factors including arginase I, indoleamine 2,3-deoxygenase (IDO), IL10 and TGF β which further suppresses activation of DCs and T-cells (274-276). Tregs and myeloid-derived suppressor cells (MDSCs) in the TDLN can secrete tolerising cytokines during antigen presentation to induce CD8 T-cell tolerance of tumour antigens (273). In a murine mammary carcinoma model, TIM3 has been shown to limit CXCL9 expression by CD103⁺ cDC1s and thus limit granzyme B expression by CD8 T-cells (206). Though the mechanism is unclear, TIM3 blockade synergised with paclitaxel chemotherapy to reduce tumour growth, but this effect was abrogated in the absence of CD103⁺ DCs or CD8 T-cells suggesting that TIM3 might regulate T-cell priming by tumour antigens (206).

1.5.2.2 Step 4 and 5: T-cell trafficking and infiltration of tumours

In contrast to the effective trafficking of T-cells to sites of infection, CD8 T-cells often show limited infiltration of tumours. T-cell trafficking is regulated by selectins, chemokines and integrins which enable migration to the site of inflammation and subsequent extravasation into the tissue (270). In tumours, however, mismatching of chemokine-chemokine receptors on CD8 T-cells and tumours, downregulation of integrin and selectin ligands by tumours, as well as abnormal vasculature restrict T-cell homing and infiltration of tumours (270). For example, the chemokine

receptor CXCR3 is expressed by TILs in melanoma, colorectal and breast tumours (277-279). It was shown that the expression of CXCL9 and CXCL10 (CXCR3 ligands) by melanoma metastases positively correlated with the trafficking of CD8 T-cells to those tumour sites (278). Moreover, several studies have demonstrated that the upregulation of CXCL9 and CXCL10 in murine solid tumours enhanced the infiltration of CXCR3⁺ CD8 T-cells into tumours to inhibit growth (280-282). However, tumours can downregulate IFN- γ -inducible CXCR3 ligands to limit the recruitment T-cells (278, 279). Meanwhile, in tumour vasculature, pericytes attach loosely to endothelial cells, causing vessel leakiness which disrupts blood flow and T-cell trafficking into tumours. Moreover, high levels of VEGF in tumours cause endothelial cells to downregulate expression of adhesion molecules including ICAM-1, vascular cell adhesion protein 1 (VCAM-1) and CD34, which usually bind to their T-cell-expressed ligands LFA-1, very late antigen 4 (VLA-4) and L-selectin, respectively, thus inhibiting T-cell rolling and extravasation (283-285). Accordingly, VEGF and VEGFR antibodies have been shown to help reverse this state of 'EC anergy', thus enhancing T-cell trafficking into tumours (286). Furthermore, normalisation of tumour vasculature by targeting TNF to angiogenic blood vessels using the peptide RGR (ligand for platelet-derived growth factor receptor β) have been shown to enhance T-cell infiltration of tumours and overall survival (287).

1.5.2.3 Steps 6 and 7: Recognition and killing of cancer cells by T-cells

It is well established that TILs have defects in cytotoxicity, cytokine secretion and proliferation (288, 289). These functional defects have been linked to tumour-induced inhibitory signalling in T-cells, often induced via ligation of coinhibitory receptors, which are commonly upregulated by TILs. Furthermore, there is evidence that defects in the cytoskeletal polarisation of T-cells can induce suppression of T-cell cytotoxicity.

Defective T-cell cytoskeletal rearrangements and polarisation in TILs

Studies have revealed that TILs display impaired cytoskeletal rearrangements including disrupted actin remodelling and impaired translocation of the MTOC from behind the nucleus to the IS, leading to inhibition of lytic granule release (130, 290). Suppressed cytolytic function in TILs has also been associated with: a reduced frequency of cell couple formation between T-cells and tumour targets; less spreading of the T-cell onto the APC- as measured by the width to length ratio in conjugated T-cells- and a reduced duration of cell coupling (291). F-actin accumulation at the IS is critical for T-cell activation; in support of the idea that impaired F-actin formation can inhibit TIL functions, non-lytic TILs showed impaired localisation of F-actin to the interface with APCs, compared to lytic TILs (290). Moreover, another study revealed that during coculture of follicular lymphoma cells with TILs from human patients *versus* healthy donor T-cells, a lower frequency of TILs formed cell couples with tumour targets (292). This was associated with reduced F-actin accumulation at the IS in TILs compared to either healthy donor T-cells or T-cells from the

peripheral blood of cancer patients (292). TILs also showed impaired recruitment of cytoskeletal signalling proteins, including LFA-1 and filamin-A, to the IS (292). Defects in the recruitment of cytoskeletal signalling proteins to the IS and reduced cell coupling frequencies were also associated with T-cells that conjugated with CLL *versus* healthy B cells, while T-cells from CLL patients *versus* healthy donors also showed decreased cell coupling frequencies and F-actin accumulation at the IS (293). These defects were shown to be reversed using treatment with lenalidomide, a drug which promotes anti-tumour T-cell responses and provides clinical benefit in patients with B-cell lymphomas, highlighting the therapeutic potential for drugs that target the cytoskeleton of TILs (294). Additionally, it was shown that PDL1 expressed by CLL B cells suppressed F-actin formation at the IS and that PDL1 blockade could partially reverse this suppressive effect (295). In this study, impaired F-actin accumulation was associated with reduced levels of activated RhoA, Rac1 and Cdc42 (295). Similarly, our lab has previously found that, compared to control T-cells cultured *in vitro*, TILs displayed defective cell coupling with tumour targets, less stable interfaces with cell couples, and failed to clear F-actin from the centre of the IS *in vitro* (187). As TIL cytotoxicity was suppressed compared to control TILs, such dysregulated F-actin remodelling likely disrupted the exocytosis of cytotoxic granules from the centre of the IS (187). Moreover, PD1 was upregulated on TILs *versus* T-cells cultured *in vitro* and partially contributed to inhibition of interface stability and cytotoxicity, as PD1 blockade treatment *in vivo* partially restored cytotoxicity, interface stability in cell couples and F-actin clearance from the IS (187). Overall, further identification of receptors and their ligands which modulate cell couple formation, interface stability and F-actin accumulation at the interface between CD8 T-cells and tumour targets will help to identify ways to overcome these mechanisms of TIL suppression.

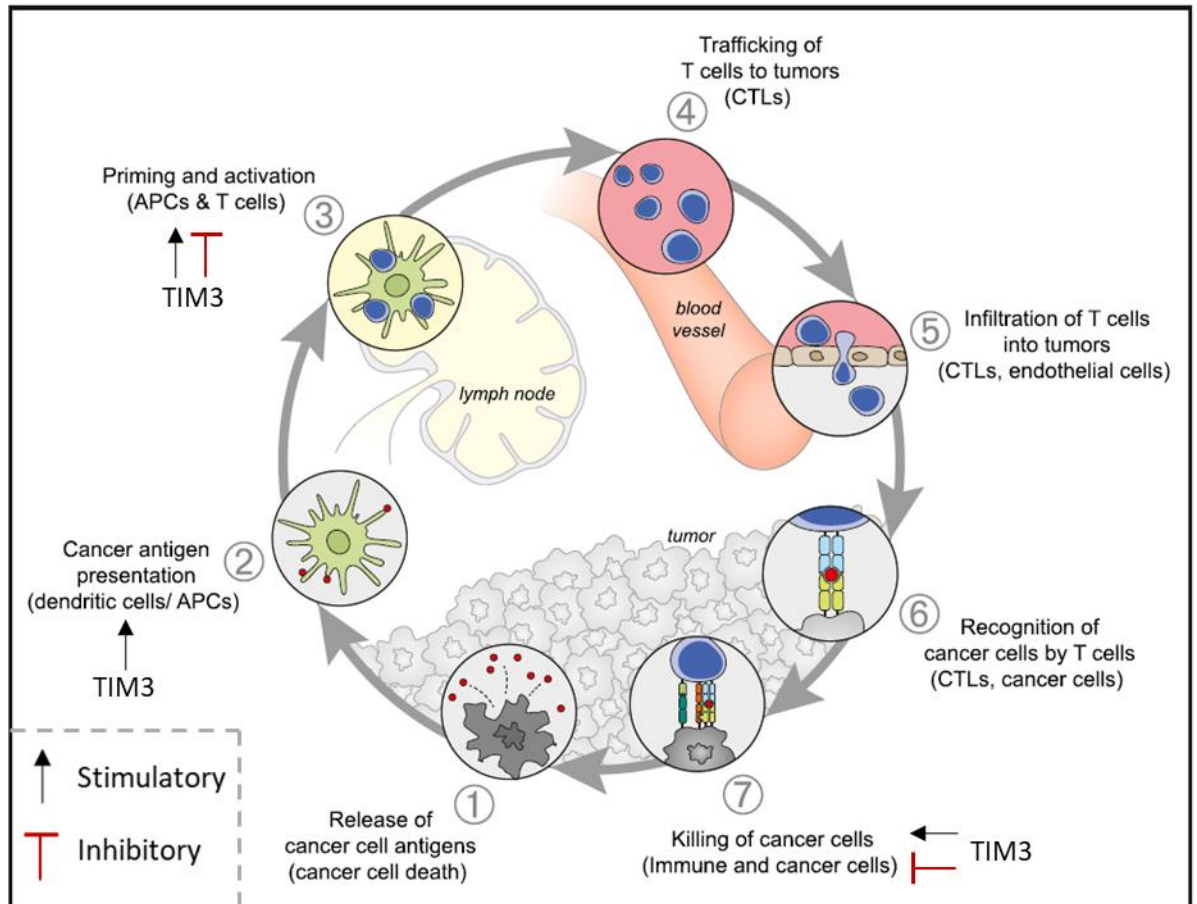


Figure 1.8 The cancer-immunity cycle

An effective anti-tumour CD8 T-cell response reinforces itself in a process called the cancer-immunity cycle (117). In step 1, tumour cell death releases tumour antigens. In step 2, antigens are taken up and processed by dendritic cells. TIM3 has been shown to enhance cross-presentation and phagocytosis of apoptotic cells by dendritic cells, through interactions with phosphatidylserine (208). Dendritic cells migrate to the tumour draining lymph nodes where they present antigen to and activate naïve CD8 T-cells in step 3. TIM3 has been found to both stimulate and inhibit T-cell activation, direct or indirectly by reducing proinflammatory cytokine production by natural killer cells and macrophages. In steps 4 and 5, effector CD8 T-cells leave the lymph nodes and migrate to and infiltrate tumour sites. In step 6 and 7, CD8 T-cells recognise cognate tumour antigen and kill tumour cells, releasing more tumour antigens and driving step 1 of the cancer-immunity cycle. Figure taken from (270).

1.5.3. The tumour microenvironment (TME)

In the solid tumour microenvironment (TME), heterogeneous cancer cell and cancer stem cell (CSC) populations are surrounded by stromal cells such as adipocytes, endothelial cells and perivascular cells (296). Other components of the TME include adaptive and innate immune cells such as myeloid derived suppressor cells (MDSCs) and cancer-associated fibroblasts (CAFs), which are the main secretors of extracellular matrix (ECM) components that form a dynamic supportive mesh of a tumour (296). Many components of the TME suppress anti-tumour CD8 T-cell responses.

Cancer associated fibroblasts (CAFs) and the extracellular matrix (ECM)

In normal organs, fibroblasts both deposit and restructure ECM to support the organ parenchyma and play a major role in wound healing upon tissue injury (296). Activation of fibroblasts in tumours can cause them to differentiate into myofibroblasts that express smooth muscle actin, resemble mesenchymal progenitors, and make up a large proportion of the CAF population (296, 297). Crosstalk between tumour cells and fibroblasts often occurs via other cell types, such as the recruitment of TGF β -secreting macrophages via platelet-derived growth factor secreted by cancer cells, which supports fibroblast activation population (296, 297). In tumours, CAFs remodel the ECM via proteinases such as matrix metalloproteinases (MMPs), which can cleave growth factors such as VEGF from the ECM to promote angiogenesis population (296, 297). CAFs also cross-link collagen and elastin fibres (298) and upregulate ECM synthesis to support tumour growth by altering interstitial scaffolding and signalling population (296, 297). As a result, tumours are stiffer than surrounding normal tissue and this stiffness has been shown to regulate cancer cell phenotype; in a murine mammary carcinoma model, lower collagen crosslinking was associated with reduced tumour incidence population (296, 297). Fibroblasts also lay down the basement membrane which is a specialised form of ECM surrounding the basal surface of epithelial cells and is composed of collagen IV, laminins, entactin/nidogen and proteoglycans population (296, 297). The basement membrane is breached by cancer cells during invasion and metastases. CAFs have also been shown to promote cancer cell proliferation, inflammation and tumour invasiveness. By increasing the density of ECM, CAFs can physically inhibit CD8 T-cell infiltration into the tumour-cell-rich regions, leading to the accumulation of T-cells in stromal tumour regions which have a lower density of fibronectin and collagen fibres (299). In this way, CAFs prevent CD8 T-cells from directly contacting and killing tumour cells. Moreover, ECM deposition by CAFs can reduce the diffusion of oxygen into the tumour, while the resultant hypoxia can enhance the secretion of VEGF by CAFs (300). VEGF can downregulate the expression of ICAM1 and VCAM1 by endothelial cells, thus suppressing integrin-dependent T-cell extravasation into the tumour (301). Moreover, CAFs secrete TGF β which can inhibit T-cell infiltration into the tumour and the therapeutic efficacy of coinhibitory receptors blockade (302, 303).

Cancer-associated adipocytes (CAAs)

Adipocytes are fat-storage cells which have been shown to secrete proangiogenic adipokines such as leptin, as well as vascular endothelial growth factor (VEGF) which can suppress T-cell infiltration and support tumour angiogenesis (301). Cancer-associated adipocytes (CAA) have also been shown to support tumour growth by acting as a supply of metabolites and fatty acids (304). Enhanced expression of collagen VI by CAAs has been shown to enhance tumour growth, by activating Akt in cancer cells (305).

Cells of the tumour vasculature

Tumours recruit vasculature during a stage called the angiogenic switch via members of the VEGF family and fibroblast growth factor 2 (FGF-2) which recruit perivascular cells or endothelial precursor cells from the bone marrow (306, 307). Tumour blood vessels tend to be irregular, and leaky with dead ends. The leakiness results from a loose association of perivascular cells with the endothelial cells and causes high tumour interstitial pressure (306). As discussed previously, tumour vasculature can prevent the trafficking of T-cells into tumours (Section 1.3.2.2).

Myeloid derived suppressor cells (MDSCs)

MDSCs are a suppressive group of immature myeloid cells that have been blocked from differentiating into macrophages, DCs or granulocytes by factors in the TME (308, 309). In tumours, MDSCs are activated by factors such as IFN γ and TGF β to inhibit natural killer cells, B cells, DCs and T-cells as well as inducing Tregs (308, 309). They have also been shown to enhance cancer cell invasion and metastasis (308, 309). T-cell suppression by MDSCs is associated with metabolism of L-arginine by the enzymes iNOS and arginase (308). L-arginine catabolism depletes the availability of arginine within tumours, inhibiting T-cell proliferation via decreasing the CD3 ζ chain expression and preventing cyclin D2 and CDK4 upregulation (308). NO, generated by iNOS, has also been shown to induce T-cell apoptosis (308). Moreover, reactive oxygen species (ROS) and peroxynitrite derived from MDSCs have been shown to abrogate antigen-specific stimulation of T-cells via nitration of the TCR and CD8 co-receptor (310).

Tumour associated macrophages (TAMs)

Macrophages within tumours are referred to as tumour-associated macrophages (TAMs). Classically, circulating monocytes give rise to macrophages that can be broadly grouped into two major subsets which lie at opposite ends of a polarisation continuum. M1 macrophages are polarised by Th1 cytokines, such as IFN- γ , TNF- α and IL-12, produce ROS and can clear microbes and cancer cells (296). M2 macrophages are polarised by Th2 cytokines such as IL-4 and IL-13, can kill parasites and are involved with tissue remodelling (296). Macrophages can change phenotype upon external signals; in the often Th2 polarised TME (311), TAMs have a phenotype that is closer

to M2 than M1 macrophages (312). TAMs have been shown to suppress T-cell cytotoxicity via recruitment of Tregs and depletion of L-arginine via arginase I, similar to MDSCs (313). TAMs can also directly support tumour growth, invasion, angiogenesis, and metastasis through secretion of growth factors, ECM-degrading enzymes and angiogenic factors (296).

TIM3 regulation of myeloid cells

TIM3 is expressed by myeloid cells including DCs, macrophages and NK cells, although data are limited on how TIM3 regulates these cells and how this may contribute to immunosuppression in the TME. In a murine model of breast cancer, TIM3 blockade treatment induced CXCL9 upregulation by DCs which indirectly improved the anti-tumour response to paclitaxel chemotherapy, by enhancing granzyme B expression in CD8 T-cells (206). TIM3 on murine CD8⁺ DCs has been found to bind to PtdSer, which facilitated phagocytosis of apoptotic cells and enabled cross-presentation (208). TIM3 antibody blockade treatment *in vivo* inhibited phagocytosis and cross-presentation of antigens from dying cells and was associated with autoantibody production (208). This provided evidence that TIM3 on CD8⁺ DCs induces tolerance in autoreactive CD8 T-cells, which can regulate adaptive immune responses to prevent autoimmunity. Thus, TIM3 on DCs may also induce tolerance in tumour-specific T-cells. In macrophages, TIM3 was found to inhibit the TLR-dependent response, as siRNA knockdown of TIM3 in TLR-stimulated monocytes and macrophages enhanced the expression of TLRs (250). Moreover, TIM3 overexpression on macrophages downregulated the expression of proinflammatory cytokines such as TNF α , IL-12 and IFN γ and reduced colitis induced in a murine model (251). Therefore, TIM3 on macrophages may also suppress the tumour-specific T-cell response. Furthermore, TIM3 was upregulated on NK cells isolated from the blood of melanoma patients *versus* healthy donors and TIM3 blockade enhanced the proliferation, IFN γ -production and cytotoxicity of NK cells from melanoma patients *in vitro* (253). Similarly, a higher level of TIM3 on peripheral NK cells was associated with poorer prognosis in patients with lung adenocarcinoma, while TIM3 blockade treatment enhanced the IFN γ production and cytotoxicity of NK cells *in vitro* (210). The regulatory role of TIM3 on myeloid cells highlights the need to identify how TIM3 regulates different cell types in the TME *in vivo* and which cellular targets primarily mediate the therapeutic effects of TIM3 blockade.

1.5.4. Checkpoint blockade therapies

PD1 and CTLA4 blockade are FDA-approved cancer therapies

The FDA-approval of CTLA4 antibody blockade in 2011 provided a major breakthrough in cancer immunotherapy (314). Ipilimumab has been shown to improve survival in a variety of tumour types including melanoma, renal cell carcinoma and non-small cell lung cancer in comparison to chemotherapy (315). However, generally only 10-20% of patients benefit from this treatment, while often more 30% of patients experience grade 3 or 4 immune-related adverse events (irAEs), which result from hyperactive immune responses (315). The therapeutic effect of CTLA4 blockade primarily results from enhanced priming of T-cells in TDLN or tertiary lymphoid structures (TLS), due to blocking of the CTLA4-mediated disruption of CD28-dependent T-cell costimulation (316). Depletion of Tregs has also been shown to contribute to therapeutic effect of CTLA4 blockade (317). Furthermore, CTLA4 blockade enables T-cells with lower affinity TCRs to activate in response to cognate antigen, which can explain reports of a broader TCR repertoire in the periphery following blockade (318). A wider TCR repertoire has been associated with enhanced T-cell responses to tumour-associated or tumour-specific antigens but also with more autoimmunity (318).

PD1 blockade was FDA-approved in 2014 and was previously thought to act primarily in inflammatory tumour sites to directly restore effector functions of exhausted TILs by blocking the inhibitory signals induced following PD1 ligation by tumour-expressed PDL1. A larger proportion of patients with advanced melanoma showed objective responses to anti-PD1 treatment nivolumab (30%) *versus* chemotherapy (10%); nivolumab treatment was also associated with reduced toxicity *versus* chemotherapy and commonly around 10% of patients treated with PD1 blockade experience grade 3 or 4 irAEs (319). Notably, mounting evidence supports the idea that PD1 blockade does not directly reverse the exhaustion of TILs. More recently, PD1 blockade during a chronic viral infection has been associated with the proliferation of a TCF1⁺ PD1⁺ CXCR5⁺ TIM3⁻ stem-cell-like subset of exhausted cells, which differentiated into a TCF1⁻ PD1⁺ CXCR5⁻ TIM3⁺ exhausted population (169, 173). In tumours, a similar subset of TCF1⁺ PD1⁺ TIM3^{hi} CD8 T-cells with proliferative and self-renewal capacity has been shown to generate TCF1⁻ PD1⁺ TIM3^{lo} CD8 T-cells and mediate tumour control and response to PD1 blockade (172, 320). The therapeutic effect of PD1 blockade has also been associated with the infiltration of new T-cell clones into the TME from extratumoural sites (321). PD1 blockade is also thought to mediate therapeutic effect by regulating T-cell priming in the lymph nodes, as CD28 was shown to be dephosphorylated following therapy and was shown to be necessary to enhance the effector function CD8 T-cells (183, 322). In the Wülfing lab, PD1 blockade failed to enhance the cytotoxicity of TILs *ex vivo*

despite reducing tumour growth *in vivo*, suggesting indirect mechanisms enhanced the anti-tumour T-cell response to have therapeutic effect in this model (187).

Immune-related adverse events (irAEs) limit checkpoint blockade

A major limitation to immune checkpoint blockade is the incidence of Grade 3 and 4 toxicities such as colitis, skin inflammation, nephritis, pneumonitis and myocarditis (315). In a phase III trial Grade 3 and 4 toxicities occurred in ~30% of patients receiving CTLA4 blockade treatment compared to ~16% of patients that received PD1 blockade (323). While co-blockade of CTLA4 and PD1 is associated with an enhanced therapeutic effect it is also associated with an increased incidence of irAEs (55%) (323). The increased incidence of autoimmune side effects in CTLA4 compared to PD1 blockade is thought to arise from the systemic increase in T-cell priming and subsequent expansion of autoreactive T-cells resulting from CTLA4 treatment, whereas PD1 upregulation by T-cells is more localised to the tumour site (315).

Blockade of alternative checkpoints may reduce irAEs

There is a huge effort to identify further immune checkpoints that can be coupled with PD1 blockade instead of CTLA4 blockade and reduce treatment side effects. TIM3 and LAG3 are promising targets as they have been shown to be specifically upregulated in inflammatory sites such as the TME *versus* the periphery (231, 276). TIM3 has been shown to be primarily expressed on TILs in cancer patients rather than in peripheral T-cells. Moreover, TIM3 deficient mice do not display severe autoimmunity, unlike PD1 and CTLA4-deficient mice (324). Overall, the evidence suggests that targeting TIM3 in combination with other checkpoints (such as PD1) could enable therapeutic synergy while causing less autoimmune side effects, compared to treatment regimens that use co-blockade of CTLA4 and PD1.

TIM3 blockade

In preclinical studies, TIM3 blockade has shown promising results in combination with PD1/PDL1 blockade. Although TIM3 blockade had no effect alone on tumour growth, TIM3 blockade synergistically inhibited the growth of CT26 colorectal murine tumours combined with PDL1 blockade, causing tumour regression in half of the treated mice (325). The average tumour size in combination treated mice was less than a third of the tumour size in mice that received either treatment alone after three weeks; this effect of combined treatment was associated with enhanced IFN γ secretion by isolated TILs (325). In B16F10, MC38 and CT26 MCA-induced tumour models TIM3 blockade synergised with anti-PD1 in a manner dependent on CD8 T-cell-derived IFN γ and CD4 T-cells (326). In a mouse model of acute myelogenous leukaemia, co-blockade of PDL1 (using anti-PDL1 antibody) and TIM3 (using a fusion protein of the mTIM3 extracellular domain fused to the human IgG1 Fc tail) caused a significant reduction in tumour burden and

longer survival time that was more effective than either alone (327). In the Renca murine tumour model, TIM3 upregulation was associated with resistance to blockade of the adenosine 2a receptor (A2aR) and co-blockade of the adenosine 2a receptor (A2aR) and TIM3 *in vivo* synergised to suppress tumour growth and reduce relapse frequencies in mice that responded to treatment (328). In samples from lung cancer patients CD4 and CD8 TILs that had bound to PD1 blocking antibody upregulated TIM3, corroborating findings that TIM3 was upregulated in response to PD1 blockade treatment in murine models of lung cancer (329). Moreover, in samples from head and neck cancer patients, PD1 blockade of PD1⁺TIM3⁺ TILs was associated with activation of the PI3K/Akt/mTOR pathway which induced upregulation of TIM3, while TIM3 expression on TILs was associated with resistance to IFN γ and TNF α upregulation following PD1-blockade *in vitro* (330). Importantly, it is currently unclear whether the therapeutic effects of TIM3 blockade *in vivo* result from direct reversal of tumour-induced suppression of CD8 T-cells, or if other cell types indirectly enhance the anti-tumour CD8 T-cell response. Understanding the relevant cell types targeted by TIM3 blockade will be critical to improving the administration of this treatment.

Given the therapeutic benefits of TIM3 blockade in preclinical models, phase I/II clinical trials are ongoing to assess the effect of this treatment in human cancer patients, primarily in combination with PD1 blockade, with one trial involving a bispecific antibody that targets both receptors (246, 331). These clinical trials are primarily focused on treatment of solid tumour patients and limited results are currently available. In an interim report of a phase I study of TIM3 blockade monotherapy and combination with PDL1 blockade, no dose-limiting toxicities were observed and tumour regression was observed in 2/23 patients treated with anti-TIM3 (LY3321367) monotherapy (332). In patients with solid tumours treated with the TIM3 blockade antibody MBG453 (reported to block the PtdSer binding site) in combination with PD1 blockade, 4 partial responses occurred out of 86, but there was no measured benefit of TIM3 blockade alone (333). Again, no dose-limiting toxicities of TIM3 blockade were observed and further dosage expansion is being investigated (333). These results provide evidence that TIM3 can be used in combination with PD1 and result in less toxicity versus CTLA4 and PD1 combination therapies, but further data are required to assess the therapeutic efficacy *in vivo*. Compared to preclinical murine studies, the data so far suggest a reduced efficacy of TIM3 in the clinical setting, making it important to further investigate which contextual factors determine an inhibitory *versus* stimulatory role for TIM3 on T-cells. Further mechanistic knowledge of TIM3 signalling will help to identify which patients might benefit most from TIM3 blockade and which pathways could be targeted to enhance the therapeutic potential of TIM3 blockade.

1.5.5. Adoptive T-cell transfer therapies benefit from checkpoint blockade

The adoptive transfer of *in vitro*-activated tumour-specific CD8 T-cell populations into cancer patients circumvents the requirement for T-cell priming in cancer patients (334). Adoptive T-cell transfer (ATT) can involve the infusion of: 1) native tumour-specific T-cells derived from patient blood samples, 2) T-cells genetically engineered to have a tumour-specific TCR or 3) the infusion of T-cells genetically engineered to express chimeric antigen receptors (CAR) (334).

T-cells can be expanded from PBMC or tumour tissue and assayed for specificity to patient tumour tissue for subsequent infusion of activated and expanded tumour-specific T-cells back into the patient (334). Such an approach has had remarkable results in the treatment of melanoma patients wherein 50-70% of patients in a trial showed objective responses to therapy with almost no severe toxicity (335-337). However, in other cases, self-reactive T-cell clones in the infused populations can cause severe autoimmune side effects (334). To help avoid autoimmunity, T-cells isolated from patient blood can be transfected to express a neoantigen-specific TCR and expanded *in vitro* (334). However, the efficacy of this approach is limited by the need to identify suitable neoantigens and downregulation of MHC I molecules by tumour cells (334). Another ATT approach uses CAR T-cells which recognise antigens independent of MHC presentation, which helps to overcome downregulation of MHC I molecules by tumour cells as an escape mechanism (334). The most effective CARs are the second-generation CARs which comprise an antigen-binding domain, which is a single chain similar to the variable region of an antibody, a hinge region, a transmembrane domain and two intracellular domains required for T-cell proximal signalling: for example, a costimulatory domain from a costimulatory receptor such as CD28, and a CD3 ζ domain (334). Two CD19-specific CARs are FDA-approved for the treatment of B cell lymphomas (334, 338, 339). However, the efficacy of CARs against solid tumours is limited by the need to identify tumour-specific antigens, ineffective T-cell trafficking to tumours, ineffective penetration of tumours by T-cells, as well as the immunosuppression of T-cell effector functions.

Notably, adoptively transferred T-cells often upregulate coinhibitory receptors upon chronic antigen stimulation within the TME, making the combination of checkpoint blockade and ATT a promising strategy. In preclinical studies, the trafficking of adoptively transferred T-cells to the tumour site was enhanced in combination with PD1 blockade and increased tumour regression (340). Moreover, CTLA4 blockade was shown to enhance the persistence of adoptively transferred MART1-specific T-cells in patients with metastatic melanoma (341). In a murine model of melanoma, combination therapy with PD1 and CTLA4 blockade also enhanced the therapeutic outcome of ATT (342). Thus, the improvement of new checkpoint blockade therapies, such as TIM3 blockade, can support the development of improved regimens for ATT therapies.

1.5.6. 3D models of the immune response to solid tumours

Tumour monolayer models have provided important insights into cancer signalling pathways, however, it has become clear that 2D models lack physiological relevance compared to 3D *in vivo* tumours. Owing to their 3D architecture, *in vivo* solid tumours contain metabolite gradients and different mechanotransductive stimuli compared to flat layers of cells. In a spheroid, diffusion gradients of molecules such as oxygen and glucose form between the spheroid surface and inner layers where cells are furthest from the surrounding culture medium (343-350). Lower pH in the spheroid core can also result from enhanced glycolysis at the centre of spheroids (350). These gradients often induce necrosis at the centre of spheroids, which mimic areas of necrosis in tumours *in vivo*; this is thought to partially account for the increased physiological relevance of 3D tumour models (344, 346, 348, 349, 351, 352). Necrotic tumour regions have been found to modulate tumour growth and immunosuppression within the TME and a higher extent of necrosis is associated with higher grades of tumour, an impaired cytotoxic potential of tumour-specific CD8 T-cells and a higher T classification as well as metastases (353-357). Therefore, the *in vitro* growth of cancer cells into compact 3D clusters, called tumour spheroids, is an increasingly popular method to study solid tumours in a more physiologically relevant setting. 3D tumour models also carry advantages compared to *in vivo* models, as they are less variable, less costly, reduce animal-usage and enable faster experimental execution (358).

Cancer cells cultured in 3D versus 2D have transcriptomic, proteomic and phenotypic differences associated with increased physiological relevance

Using CRISPR for genome-wide screening of lung tumour spheroids and monolayers in parallel, it was found that the phenotypes of cells from 3D *versus* 2D culture more closely modelled *in vivo* tumour xenograft phenotypes (359). Additionally, the genes with stronger phenotypic effects upon knockout in 3D- *versus* 2D- cultured cells were enriched for common lung cancer mutations in patients (359). 3D organoids of renal cell carcinoma (RCC) tissue from patients expressed higher levels of the RCC biomarkers carbonic anhydrase 9 and vimentin compared to 2D cultured cells (360). Moreover, the cells in 3D but not 2D culture retained the lipid-rich morphology of cells from RCC tumours, indicating that 3D *versus* 2D culture better recapitulates both the morphology and transcriptome of cancer cells (360). Human breast cancer cells grown in 2D *versus* 3D showed differences in the expression of the human epidermal growth factor receptors 2 and 3 (HER2 and HER3) (361). While HER2 and HER3 heterodimers were expressed on monolayer cells, HER2 homodimers were only expressed on cells grown in 3D, while the formation of heterodimers was reduced in spheroid cells (361). The homodimerization of HER2 resulted in downregulation of Akt and enhanced levels of activated MAPK; reduced Akt activation resultant from 3D *versus* 2D culture was recapitulated in several other cell lines (361). This suggested that the altered architecture of cancer cell growth in 3D *versus* 2D can affect protein localisation at the cell

surface, with consequences for receptor-induced cellular signalling. Additionally, treatment of cells with the HER2 blocking antibody Herceptin more effectively inhibited the proliferation of cells grown in 3D *versus* 2D, demonstrating how such differences can affect therapeutic responses (361). In support of the notion that a 3D *versus* 2D culture method can alter cellular responses to treatments, the optimal ratio of the chemotherapeutic agents doxorubicin and resveratrol used for combined treatment of human pancreatic tumour cells differed between a spheroid and monolayer model (362). In further support of differences between 2D and 3D cultured cells, human breast cancer cell lines grown in 3D using Matrigel enabled malignant and non-malignant cells to be more easily distinguished compared to growth in 2D, where the differences were less apparent. In 3D culture, malignant cells formed disorganised, proliferative colonies whereas non-malignant cells were organised and growth arrested (363). Several other studies have demonstrated that cancer cells have significantly different transcriptomes and proteomes in 3D *versus* 2D culture, which often confer distinct responses to chemotherapies (364-369).

Culture of cancer cells in 3D *versus* 2D suppresses the tumour-specific T-cell response

In clinical studies of tumour vaccines, which involve injection of tumour-associated antigens (TAAs) along with adjuvant, a very small fraction of patients that are classified as immunised, according to the effective killing of monolayers by isolated vaccine-induced TAA-specific T-cells, actually show clinical responses (370, 371). This provides evidence that T-cell cytotoxicity against monolayers is not an accurate readout for predicting clinical efficacy of T-cell-targeted treatments. Although there are few studies directly comparing the T-cell response to 3D *versus* 2D tumour targets, there is accumulating evidence that the cytotoxic CD8 T-cell response to 3D *versus* 2D targets is less effective. The downregulation of heat shock protein 70 (hsp70) was associated with reduced antigen presentation in lung tumour spheroids *versus* monolayers (372). Downregulation of hsp70 reduced the capacity of cancer cells to induce a tumour-specific CD8 T-cell response, as measured by the secretion of IFN γ and TNF α (372). As hsp70 is a chaperone protein which facilitates the trafficking of peptides for presentation on MHC I molecules, this 3D model revealed a possible immune evasion mechanism used by *in vivo* tumours (373). Other studies showed that the expression of the HLA-A0201-restricted tumour-associated antigen MART-1/Melan-A was decreased in 3D- *versus* 2D-cultured melanoma cells and this inhibited the antigen-specific CD8 T-cell response (374, 375). Melan-A/MART1 transcript levels were 6-fold lower in cells grown in 3D *versus* 2D, while HLA-A0201 expression was also reduced 3-fold in 3D *versus* 2D culture (374). During a 3-24h coinubation, 2D melanoma targets could induce IFN γ secretion by CD8 T-cells, but 3D targets could not (374). These findings suggested that simply growing tumour cells in 3D *versus* 2D induces transcriptomic changes that can suppress the tumour-specific CD8 T-cell response. Furthermore, human melanoma cells grown in 3D were shown to secrete higher levels of lactic acid *versus* monolayers, which increased the suppression

of tumour-specific CD8 T-cells (375). In support of this finding, another study reported that human melanoma cells grown in 3D secreted high levels of lactic acid which inhibited the secretion of IL2 and IFN γ by tumour-specific CD8 T-cells (350, 375). Unlike naïve T-cells, activated T-cells rely heavily on glycolysis rather than oxidative phosphorylation, which enables glycolytic intermediates to be fed into the pentose-phosphate pathway for the enhanced production of nucleic acids, amino acids and lipids (376, 377). This reliance on glycolysis causes lactic acid accumulation within T-cells which can suppress effector functions (378). In this study, T-cell suppression was attributed to the defective export of intracellular lactic acid from T-cells by the monocarboxylate transporter-1 (MCT-1) which relies on a higher intracellular *versus* extracellular lactic acid concentration to function (350). Indicating that this mechanism may be physiologically relevant, the concentration of lactate in cancer patient serum positively correlated with tumour burden (350). Overall, as *in vivo* tumours are three-dimensional, these findings suggest that 3D *in vitro* tumour models may offer more relevant insights into immunotherapeutic mechanisms *versus in vitro* 2D models. Furthermore, such data suggests that studying the signalling of coinhibitory receptors such as TIM3 using 2D tumour models alone may not fully recapitulate signalling pathways present *in vivo*. Moreover, differences in the regulation of the T-cell response between 2D and 3D models could provide a tool to understand the environmental requirements for signalling pathways induced by coinhibitory receptors.

3D tumour models aid the identification of novel combination immunotherapies

In vitro tumour spheroid models have been used to identify novel combination treatments for cancer that have demonstrated therapeutic efficacy *in vivo*. In tumour-stroma heterotypic spheroids which secreted high levels of CXCL12, blockade of the CXCL12/CXCR4 axis using the molecule NOXA12 enhanced T-cell infiltration into the spheroids (379). In the same model PD1 blockade synergised with CXCL12 blockade to enhance T-cell activation, as measured by NFAT transcription, which increased spheroid death (379). Demonstrating physiological relevance of spheroid models, this *in vitro* finding was validated *in vivo* using the murine CT26 colorectal cancer model; PD1 blockade alone slightly reduced tumour growth but combination with NOXA12 blockade significantly reduced tumour growth (379). Using an *in vitro* MC38 murine colorectal cancer spheroid system, another study identified that CDK4/6 inhibitors could synergise with PD1 blockade to enhance T-cell-mediated anti-tumour immunity (380). Inhibition of CDK4/6 enhanced the secretion of Th1 cytokines including CXCL9, CXCL10 and IFN γ by spheroids (380). As these cytokines are known to enhance the infiltration and activation of T-cells into tumours, the authors combined inhibition of CDK4/6 with PD1 blockade, which resulted in enhanced spheroid death *versus* either treatment alone (380). This finding was corroborated in an *in vivo* MC38 murine model of colorectal cancer where co-blockade: reduced tumour growth *versus* single treatments; increased the levels of CXCL9 and CXCL10 in tumour tissue; enhanced IFN γ production in CD8 T-

cells (380). Importantly, the synergistic effect was lost upon depletion of either CD4 or CD8 T-cells suggesting that T-cells were required for the therapeutic effect (380). Overall, these data suggest that *in vitro* spheroid systems are useful tools to identify novel anti-tumour combination treatments that have efficacy *in vivo*.

1.5.7. The RencaHA + CL4 T-cell Model

The murine renal carcinoma model used by our lab involves two main components: 1) Renca cells that express the viral antigen haemagglutinin (HA) derived from the influenza virus and therefore the dominant 9-amino-acid long H-2K^d-restricted epitope (518-526, IYSTVASSL, denoted as HA^{pep}); 2) HA^{pep}-specific Clone 4 (CL4) CD8⁺ T-cells derived from TCR-transgenic CL4 mice. This model of the neoantigen-specific CD8 T-cell response will be referred to as the RencaHA/CL4 T-cell model.

A schematic of the RencaHA/CL4 T-cell model is shown in Figure 1.9. Previous studies in the lab have investigated the immunosuppression of CL4 T-cells within the TME of murine Renca tumours using two Renca models in parallel: 1) *in vitro* monolayer cultures of Renca wildtype (RencaWT) cells which do not endogenously express HA, but have been exogenously peptide-pulsed with HA^{pep} to form 2D targets for CL4 T-cells; 2) *in vivo* subcutaneous tumours which are each grown from the injection of 1 million RencaHA cells into the dorsal neck region of BALB/c recipient mice (381, 382). The adoptive transfer of primed, cytotoxic CL4 CD8 T-cells into tumour-bearing mice followed by the harvest of tumours 96h later has enabled the isolation of CL4 TILs (187, 328). Previously in our lab, CL4 TILs have been characterised for functional and phenotypic changes resulting from exposure to the immunosuppressive RencaHA TME, including the assessment of: coinhibitory receptor expression, cytotoxicity using 2D microscopic assays and T-cell polarisation and cell coupling abilities, as well as F-actin accumulation at the IS, via widefield imaging of T-cells coincubated with monolayer Renca cells (187, 328).

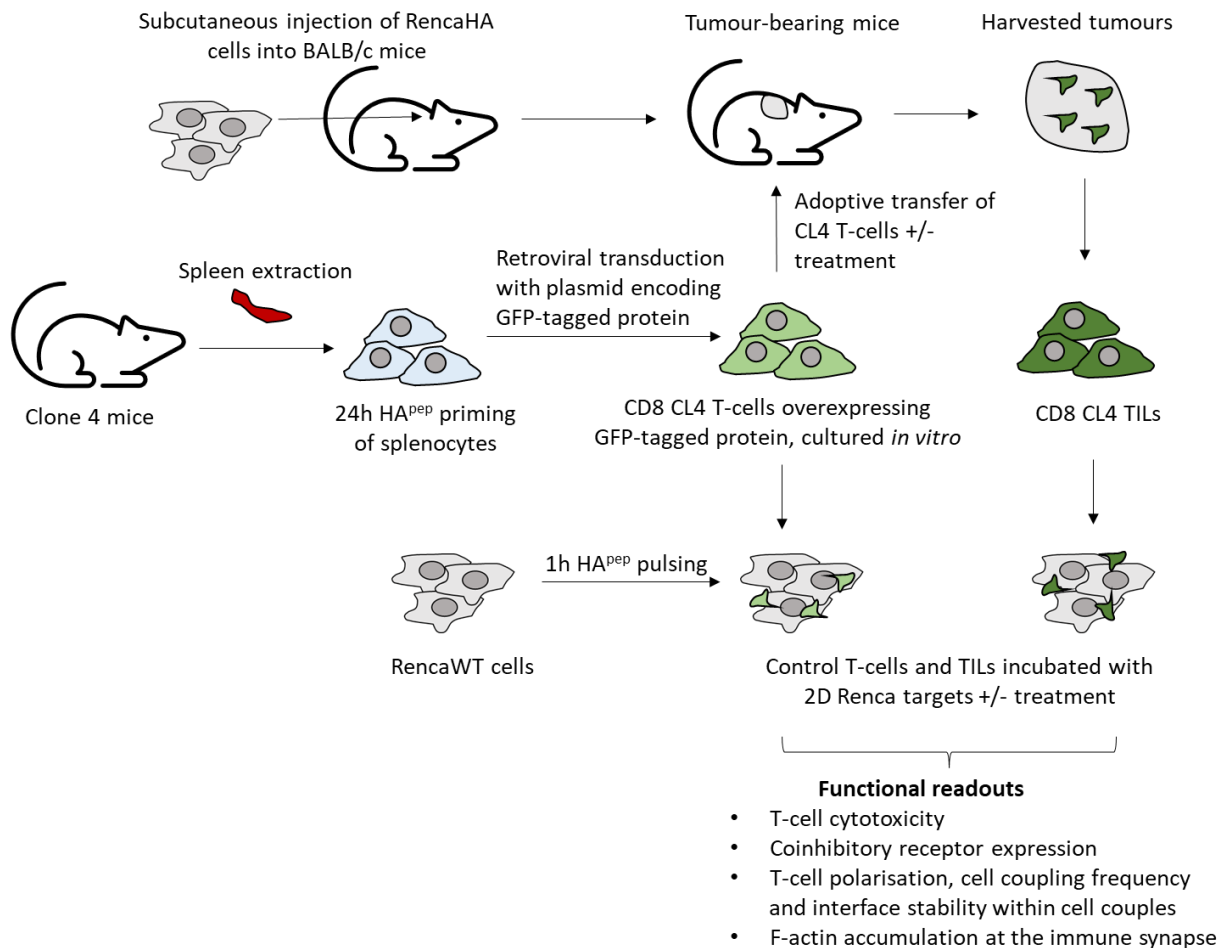


Figure 1.9 The RencaHA and CL4 CD8 T-cell model

For tumour growth, 10^6 RencaHA cells are injected subcutaneously into the dorsal neck of each BALB/c mouse. For adoptive T-cell transfer experiments, splenocytes are harvested from Clone 4 mice and primed with a 9-amino-acid long H-2K^d-restricted epitope from influenza virus (518-526 IYSTVASSL) which is denoted as HA^{pep}. Following peptide priming, CL4 CD8 T-cells proliferate, enabling retroviral transduction of T-cells using plasmids encoding a GFP-tagged protein of interest, for example, F-tractin, a small F-actin binding peptide. GFP-positive T-cells are sorted by flow cytometry and adoptively transferred into tumour-bearing mice, meanwhile, a population of GFP-positive T-cells are maintained in culture *in vitro*. On the day of functional assays, tumours are harvested and CD8 CL4 tumour-infiltrating lymphocytes (TILs) are extracted. Meanwhile, Renca wild-type (RencaWT) cells are peptide-pulsed with HA^{pep} for 1h. Upon plating with peptide-pulsed RencaWT 2D targets, TILs and control T-cells, which have not encountered the RencaHA TME, can be characterised for various functional readouts including: cytotoxicity; the ability of T-cells to polarise and form cell couples tumour targets; the interface stability within cell couples; F-actin accumulation at the immune synapse (IS). The expression of coinhibitory receptors by TILs and control T-cells can also be measured.

1.5.8. Immunosuppression in the Renca tumour microenvironment

It was previously shown that exposure to the Renca TME inhibited CL4 TIL cytotoxicity, MTOC translocation, cell coupling abilities and calcium signalling compared to T-cells that were primed and cultured *in vitro* (187). Furthermore, compared to T-cells cultured *in vitro*, TILs displayed defective polarisation towards Renca targets and failed to clear F-actin from the centre of the IS *in vitro*, which is likely to disrupt the exocytosis of cytotoxic granules (187). PD1, which was upregulated on TILs *versus* T-cells cultured *in vitro*, partially contributed to inhibition of interface stability and cytotoxicity, as PD1 blockade treatment *in vivo* partially restored cytotoxicity, interface stability and F-actin clearance from the IS (187). Another study revealed that TIM3 was upregulated in response to blockade of the adenosine A2a receptor (A2aR) and co-blockade of A2aR and TIM3 synergised to reduce tumour growth and protect from tumour relapse (328). Furthermore, A2aR and TIM3 co-blockade *in vivo* improved interface stability between CL4 TILs and targets *in vitro*, as measured by the frequency of TILs that displayed interface-destabilising translocation away from the initial site of cell coupling (328). Co-blockade also enhanced the cytotoxicity of TILs *in vitro* (328). Notably, TIM3 was expressed by ~50% of TILs, and coexpressed with the putative TIM3 ligand CEACAM1 on 41% of TILs, indicating the importance of TIM3 signalling in this model. Overall, TIM3 contributes to immunosuppression in the Renca TME and TIM3 blockade has therapeutic effect, therefore, the RencaHA/CL4 T-cell model is well-suited to study how TIM3 regulates the tumour-specific T-cell response.

Accordingly, it is of interest to identify whether the therapeutic effects of TIM3 blockade result from direct regulation of the tumour-specific CD8 T-cell response *in vivo* or whether other cell types indirectly mediate the therapeutic efficacy, as this is currently unclear. Although *in vivo* murine models are highly physiologically relevant to tumours in cancer patients, they involve high variability and multiple cell types which may indirectly modulate CD8 T-cell function. This makes it difficult to investigate the direct mechanisms by which TIM3 regulates CD8 T-cells *in vivo*.

Meanwhile, 2D tumour models are highly useful for studying TIM3 signalling mechanisms but lack physiological relevance. Development of an *in vitro* 3D RencaHA/CL4 model would provide a more physiologically relevant tool to dissect if and how TIM3 and the putative TIM3 ligand CEACAM1 may directly regulate the tumour-specific CD8 T-cell response.

1.6 Hypothesis and aims of this project

Hypothesis: TIM3 signalling differs in tumour-specific CD8 T-cells between 2D and 3D tumour models.

To test this hypothesis, the aims of this project are:

Chapter 3

- To develop and characterise a RencaHA spheroid model that can be used to investigate immunosuppression of the tumour-specific CL4 CD8 T-cell response.
- To develop a 3D microscopic cytotoxicity assay and image analysis method that enables the quantification of interactions between T-cells and tumour spheroids.

Chapter 4

- To investigate if TIM3 signalling in tumour-specific CD8 T-cells differs between a 2D and 3D tumour environment.
- To establish if TIM3 blockade can directly modulate tumour-specific CD8 T-cell cytotoxicity in the Renca model, in the absence of other cell types.
- To investigate whether TIM3 on CD8 T-cells modulates steps required for the delivery of cytotoxic granules into target cells, including: cell couple formation between T-cells and tumour cells, morphological polarisation of T-cells during cell couple formation and interface stability within cell couples.

Chapter 5

- To investigate if CEACAM1 *in cis* (on the same T-cell as TIM3) and *in trans* (on Renca cells) directly coregulates tumour-specific CD8 T-cell cytotoxicity together with TIM3, in the absence of other cell types and how this differs between 2D and 3D tumour environments.
- To investigate whether CEACAM1 *in trans*, expressed on RencaHA cells, and TIM3 on CD8 T-cells coregulate steps required for the delivery of cytotoxic granules into target cells including: the morphological polarisation of T-cells during cell couple formation and interface stability within cell couples.

Chapter 2 Methods

2.1 Mice

TCR-transgenic, BALB/c, Clone 4^{+/-} mice were bred at the University of Bristol Animal Services Unit. Mice were genotyped using blood samples taken from the tail vein in blood buffer. Blood samples were stained using anti-mouse V β 8.1 (eBioscience, KJ16-133, FITC) and anti-mouse CD8a (Biolegend, 53-6.7, APC) to identify Clone 4⁺ mice, which were humanely culled to harvest the spleen as a source of CL4 CD8⁺ T-cells.

2.2 Media and Reagents

2.2.1. Vanilla and IL-2 medium

For culture of Renca cells in 2D and 3D, vanilla medium comprised of 89% RPMI + L-Glutamine (Gibco), 10% FBS (Thermo Fisher Scientific), 1% PenStrep (Gibco) and 0.04% β -mercaptoethanol (Gibco). For culture of T-cells, IL-2 medium was made by supplementation of vanilla medium with 50U/ml recombinant human IL-2 (National Institute of Health/NCI BRB Preclinical Repository).

2.2.2. Fluorobrite vanilla medium

For 2D and 3D microscopic cytotoxicity assays, Fluorobrite vanilla medium comprised 88% Fluorobrite DMEM (Thermo Fisher Scientific), 10% FBS (Thermo Fisher Scientific), 1% L-glutamine (Gibco), 1% PenStrep (Gibco) and 0.04% β -mercaptoethanol.

2.2.3. Phoenix Medium

Incomplete Phoenix medium contained 88% DMEM (Gibco), 10% FBS (Hyclone), 1% PenStrep (Gibco), 1% MEM Non-Essential Amino Acids (Gibco). Addition of 300 μ g/ml hygromycin and 1 μ g/ml diphtheria toxin to Incomplete Phoenix medium produced Complete Phoenix medium for long term culture of Phoenix cells.

2.2.4. Chloroquine

4.1mg/ml chloroquine solution was produced by dissolving chloroquine phosphate powder (Sigma-Aldrich) into sterile filtered distilled water to aid calcium phosphate transfection of Phoenix cells.

2.2.5. Imaging Buffer, FACS/MACS buffer

Imaging buffer comprised of PBS (Gibco) without calcium or magnesium plus 10% FBS (Thermo Fisher Scientific) supplemented with 1mM CaCl₂ (Sigma), 500 μ M MgCl₂ (Sigma). FACS buffer for running stained T-cell and Renca samples and MACS buffer for isolation of polyclonal CD8⁺ T-cells

comprised 97.6% PBS (Gibco) without calcium or magnesium, 2% FBS (Thermo Fisher Scientific) and 0.4% 2mM EDTA (Sigma).

2.3 Cloning

Vector NTI software (Thermo Fisher Scientific) was used to design PCR primers for the amplification of the desired insert from a donor plasmid (to add CEACAM1 to pIRES-hygromycin resistance-tdTomato or pGC-TIM3-GFP plasmids; to add tdTomato to the pIRES-hygromycin-resistance plasmid) and the addition of new sequences such as the P2A ribosome-skipping sequence or the caspase 8 and granzyme B (GzmB) fluorescent sensor sequences, these sequences were as previously described (97, 383, 384). Restriction enzyme digests were used to generate complementary ends in recipient linearised vectors that could ligate with insert fragments. This enabled the generation of the pIRES-hygromycin-resistance-tdTomato, pIRES-hygromycin-resistance-CEACAM1-tdTomato, pGC-CEACAM1-P2A-TIM3-GFP and the pIRES-hygromycin-resistance-tdTomato-Caspase8/GzmB plasmids.

2.4 Cell line maintenance

2.4.1. Renca cells

Murine RencaWT and RencaHA cell lines were cultured in 25ml or 75ml vented flasks containing 5ml or 10ml of vanilla medium, respectively. Hygromycin (250µg/ml) was added as a selective antibiotic to flasks containing RencaWT/HA lines that expressed the fluorophores mCherry or tdTomato (RencaWT^{mCh}, RencaWT^{tdT} and RencaHA^{tdT}, RencaHA^{Casp8}, Renca^{GzmB}). Geneticin (100µg) was added as a selective antibiotic to the RencaHA^{tdT}, RencaHA^{Casp8} and Renca^{GzmB} cell lines to maintain the expression of a plasmid which encoded haemagglutinin from the influenza strain A/PR8. To keep cells at <80% confluence, cells were passaged every 48h: cells were washed in 10ml PBS prior to addition of 2ml of 0.05% Trypsin and 0.05% EDTA (Sigma), and incubation of the cells at 37 degrees Celsius for 3 minutes. The flask was then tapped to encourage detachment of cells from the flask bottom, which was confirmed using a light microscope. Cells were transferred into 15ml or 50ml falcon tubes using 5ml of vanilla medium and centrifuged at 200 xg for 3 minutes. Cell pellets were resuspended in vanilla medium for re-plating.

2.4.1.1 Lipofectamine transfection of RencaHA lines to express tdTomato

The RencaHA^{tdT} and RencaWT^{tdT} cell lines were generated by transfection of the RencaHA and RencaWT lines with a plasmid encoding the tdTomato fluorophore and hygromycin phosphotransferase- which confers hygromycin resistance- using lipofectamine 2000 (Thermo Fisher Scientific) and the manufacturer's protocol. The cells were grown for a week in hygromycin and geneticin before tdTomato-positive cells were FACS sorted and cultured.

2.4.2. Phoenix cells

A schematic of retroviral transduction of CL4 T-cells using the ecotropic Phoenix retroviral packaging cell line is shown in Figure 2.1. Phoenix cells were cultured in 60 x 15mm Primaria coated cell culture dishes (Falcon) in Complete Phoenix medium. Cells were passaged by removal of Complete Phoenix medium and addition of 1ml 0.02% EDTA (Sigma) to cover the plate bottom and incubated for 1 minute at 37 degrees Celsius. Cells were detached from the plate bottom by gentle tapping and collected using 5ml DMEM and transferred to a falcon tube for centrifugation at 200 xg for 3 minutes. For continuous culture, 600,000 cells were added per plate in 6ml of Complete Phoenix medium. For retroviral production, phoenix cells were plated in Incomplete Phoenix medium and cultured for 72h, before splitting at a 1:2 ratio on day 1, 24h before the day of transfection on day 2.

2.4.2.1 *Transfection of phoenix cells, transduction of T-cells, isolation of GFP⁺ T-cells*

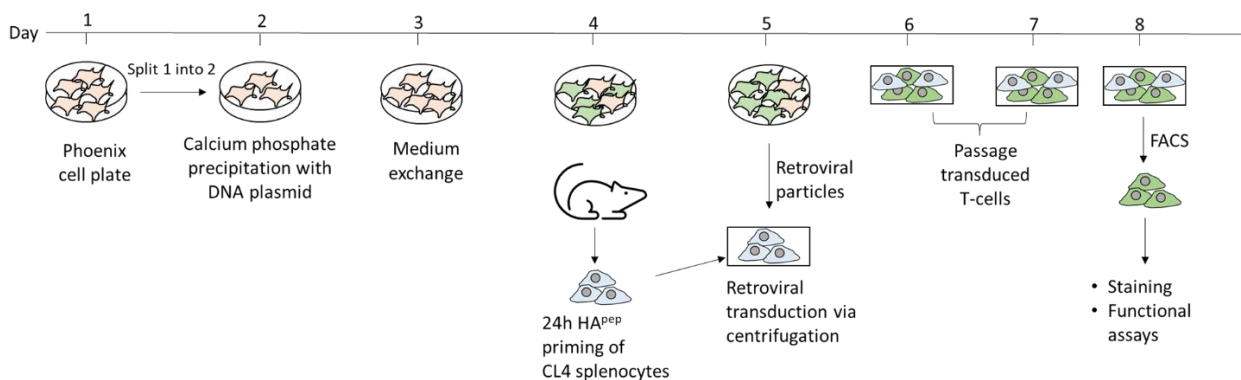
The Phoenix cell line can be transfected with DNA plasmids containing a gene of interest to generate retroviral particles that can transduce T-cells. Following retroviral transduction, T-cells that overexpress a T-cell signalling protein can be cultured. Phoenix cells were transfected with plasmids encoding the GFP-tagged gene of interest (e.g. TIM3-GFP) using calcium phosphate precipitation. Firstly, 25µl chloroquine was added to each phoenix cell plate and incubated at 37 degrees Celsius. Meanwhile, two solutions were made using the following for one phoenix plate: Solution A contained 2µl 1M NaOH and 500µl HEPES Buffered Saline (HBS); Solution B contained 500µl distilled H₂O and 10µl of the DNA plasmid to be transfected at a concentration of >1000ng/µl. 62µl 2M CaCl₂ was then added dropwise to Solution B, forming a visible precipitate. Using a stripette, Solution A was bubbled, while Solution B was added dropwise to Solution A. The solution was then added at 1ml per phoenix plate that had been pre-incubated with chloroquine. The plates were returned to the incubator for 37 degrees Celsius. 16-20h later on day 3, the phoenix medium was exchanged with fresh Incomplete Phoenix medium and left for 48h until day 5, when the Phoenix plate supernatant (containing retroviral particles) was harvested into falcon tubes and centrifuged at 200 xg for 3 minutes to pellet any phoenix cells. The supernatant was used for retroviral transduction of T-cells that had been peptide primed for 24h in the mixed splenocyte reaction (see section 1.3.3). On day 5, primed T-cells were collected from wells and washed 4 times in RPMI via centrifugation at 200 xg for 3 minutes. Phoenix cell supernatant was used to resuspend cell pellets at a concentration of 1ml phoenix cell supernatant/well of splenocyte cells, and 1ml of this cell solution was added to each well of a flat-bottomed 24 well plate (Corning). Protamine sulphate was added to wells at 8µg/ml and plates were sealed with parafilm prior to centrifugation at 200xg for 2h at 32 degrees Celsius. The supernatant of each well was removed without disturbing the cells and replaced with 2ml IL-2 medium per well, in which cells were resuspended before being cultured at 37 degrees Celsius. From day 6-7, cells

were passaged every 12h to maintain them at 90% confluency. On day 8, successfully transduced GFP⁺ CL4 T-cells were isolated via fluorescent activated cell sorting (FACS) (Supplementary Figure 1.1).

2.4.3. Mixed splenocyte reaction: priming of CL4 T-cells

On day 4, splenocytes were harvested from a CL4 mouse spleen, by mashing the spleen with a 5ml syringe plunger through a 40µm cell strainer into a 50ml falcon tube, using 50ml RPMI + L-Glutamine (Gibco) to wash through the cells several times. Cells were centrifuged at 200 xg for 3 minutes, the supernatant discarded and the cell pellet resuspended in 1ml ammonium-chloride-potassium (ACK) lysis buffer (Gibco) for 3 minutes to lyse red blood cells. The cells were quenched using 40ml RPMI + L-Glutamine (Gibco) and centrifuged at 200 xg for 3 minutes. The cell pellet was resuspended in vanilla medium at a density of 5 x 10⁶ cells/ml. 1µl of the peptide IYSTVASSL (HA^{PEP}) from the influenza haemagglutinin protein (A/PR/8/H1N1) was added to each well and then 1ml of the cell suspension was plated in each well of a flat bottomed 24 well plate (Corning) for priming of T-cells for 24h.

Figure 2.1 Retroviral transduction of CL4 T-cells using the ecotropic Phoenix packaging cell line



2.4.4. Priming and culture of polyclonal CD8 T-cells

A flat-bottomed 48-well plate was coated using 10 µg/ml anti-CD3 antibody (BioXcell) diluted in PBS at 4 degrees Celsius overnight, and then the wells were washed twice using PBS. Polyclonal CD8 T-cells were harvested from a BALB/c mouse spleen, which had been mashed through a 40 µm cell strainer. Following red blood cell lysis using ACK lysis buffer (Gibco) splenocytes were centrifuged at 200 xg for 4 minutes, the supernatant discarded, and the cell pellet was resuspended in 450 µl MACS buffer and 50 µl anti-CD8α microbeads (Miltenyi) prior to incubation at 4 degrees Celsius for 15 minutes. Cells were washed by centrifugation at 200 xg for 5 minutes in 50 ml MACS buffer in a falcon tube, the supernatant discarded, and the cell pellet resuspended in 6 ml MACS buffer. The cells were then passed through a LS-column held within a MACS magnet (Miltenyi) and then 9 ml of MACS buffer was used to wash the magnet. 6 ml of MACS buffer was then added to the LS-column and was forced through the column using the plunger into a falcon

tube, to isolate the CD8 polyclonal T-cells. The polyclonal CD8 T-cells were counted and then added to the wells of the plate at 5×10^6 cells per well. Anti-CD28 antibody (BioXcell) was added to each well for a final concentration of 1 $\mu\text{g}/\text{ml}$; T-cells were activated for 24 h (in parallel with peptide-priming of CL4 T-cells on day 4 of Figure 2.1). Polyclonal T-cells were then cultured identically to CL4 T-cells until the 3D microscopic cytotoxicity assay on day 8.

2.5 Spheroids

2.5.1. Spheroid culture

On day 0 single RencaHA^{tdT} cells were mixed into Matrigel (Corning, growth factor reduced, phenol red free) at a concentration of 8 cells/ μl and 50 μl Matrigel was plated per well, in a 24-well plate. Matrigel domes were solidified according to the manufacturer's protocol and 2ml of Renca vanilla medium was added per well for spheroid growth over 10 days. From day 0 to 7, 1ml Renca medium was exchanged every 48 hours and from day 8 to 9, every 12h.

2.5.2. Haematoxylin and Eosin staining of spheroids

A plate of spheroids was harvested from Matrigel on day 10 of spheroid growth for processing and haematoxylin and eosin (H&E) staining. Renca vanilla medium was aspirated from the wells and 1ml PBS was gently added per well and aspirated to wash the wells without disruption of the Matrigel domes. 1ml of Cell Recovery Solution (Corning) was added to each well and the plate was incubated at 4 degrees Celsius for 1h. Solution and spheroids were collected from each well using a Pasteur pipette and transferred to a 15ml falcon tube for centrifugation at 80 xg for 2mins. Supernatant was discarded and spheroids were washed twice by topping up the falcon tube with 10ml PBS (Gibco) via centrifugation at 80 xg for 2mins. Dissociated spheroids were then mixed into luke-warm 4% Agarose (VWR) and the agarose was left to set at room temperature in a few wells of a 24-well plate. The agarose pieces were removed from the plate wells using a small spatula and the embedded spheroids were transferred to 10ml 10% neutral buffered formalin (Sigma-Aldrich) in a bijoux tube and incubated at room temperature overnight. The next day, the agarose-embedded spheroids were transferred to 70% ethanol. The spheroids were paraffin embedded and then sectioned using a microtome to form 5 μm width sections and placed onto Superfrost slides (VWR). Slides were de-waxed in xylene for 30 minutes. Sections were rehydrated in a series of ethanol solutions for 10 minutes each: 100%, 90%, 80%, 70% and then submerged in deionised water for 10 minutes. Haematoxylin nuclear stain was added to slides for 3 minutes and then rinsed off using deionised water, then washed for 5 minutes in tap water. Slides were then rapidly dipped in 3% hydrochloric acid in 95% ethanol 10 times, before rinsing slides in tap water for 2 minutes and deionised water for 2 minutes. Slides were stained with eosin for 30 seconds and then washed 3 times in 95% ethanol for 5 minutes per wash and then 3 times in 100%

ethanol for 5 minutes. Lastly, sections were incubated in xylene three times for 15 minutes, and coverslips were mounted onto the sections using Vectashield Antifade Mounting Medium (Vector laboratories). Sections were imaged using a widefield microscope.

2.5.3. Hypoxia staining of spheroids

Spheroids were stained using the Hypoxprobe Kit (100mg pimonidazole HCl plus 1.0ml of 4.3.11.3 mouse monoclonal antibody (mAb)). Two plates of 10-day-old spheroids were grown as described in Section 2.5.1. on day 10 of spheroid growth, one spheroid plate was placed in a hypoxic incubator (2% O₂). The other plate was kept in a normoxic incubator (18.6% O₂). Spheroids were incubated overnight for 16h. The next day, pimonidazole HCl (PimHCl) was dissolved in serum-free medium and added to wells in both plates, immediately after each other, for a final concentration of 170µM PimHCl (the spheroid plate in the hypoxic incubator was not removed hypoxic conditions). After a 2h incubation, spheroid domes were washed, without dome disruption, twice with 1ml PBS per well to remove residual medium. Spheroids were then dissociated and isolated from Matrigel domes as described in Section 2.5.2. Spheroids from each plate were added to luke-warm 4% agarose (Sigma-Aldrich) in separate wells of a 96-well plate to set. Agarose blocks were retrieved from wells and added to 10ml 10% neutral buffered formalin (Sigma-Aldrich), inside bijoux tubes, for fixation overnight. The next day, spheroids were transferred into 70% ethanol for up to 3 days. Spheroids were paraffin-embedded and sectioned at a width of 5µm with a microtome and placed onto Superfrost Slides (VWR). For staining of spheroids to detect hypoxic cells with the 4.3.11.3 mouse mAb, slides were first de-waxed in Histo-Clear (VWR) for 30 minutes. Slides were then rehydrated in a series of ethanol solutions: 10 minutes in each of 100%, 90%, 80% 70% ethanol, followed by 10 minutes in deionised water. Next, slides were incubated at 90 degrees Celsius for 10 minutes in 10mM citrate buffer (pH 6.0), followed by two washes for 5 minutes each in PBS. Excess liquid was tapped off and removed around the sections with a tissue. Using a the ImmEdge Hydrophobic Barrier Pen (Vector Laboratories), a hydrophobic boundary was drawn around each section. Sections were blocked with 2.5% Normal Horse Serum Blocking Solution (Vector Laboratories), followed by 3 washes in PBS for 5 minutes each. A solution containing 0.1% bovine serum albumin (BSA) in PBS was used to dilute the primary mouse mAb stock solution with a dilution factor of 1/50 (vol/vol). 100µl of the working primary mAb solution was added to each section and incubated for 4 degrees Celsius overnight. For a negative control, sections were incubated with purified mouse IgG1 kappa isotype control antibody (Thermo Fisher Scientific). Slides were washed three times with PBS for 5 minutes each, while the secondary antibody (rat anti-mouse IgG1 Secondary Antibody, FITC (eBioscience)) container was spun down for 10,000 xg for 10 minutes at 4 degrees Celsius. Secondary antibody was diluted in 1% BSA in PBS with a dilution factor of 1/2000 (vol/vol) and added to sections for a 45-minute incubation. Slides were washed in PBS, 3 times for 5 minutes each. The second wash was done on top of a

shaker. Hoescht 33342 (Thermo Fisher Scientific) was diluted 1/5000 (vol/vol) and added to each section for 10 minutes. Coverslips were mounted onto sections using ProLong Gold Antifade Mountant (Invitrogen), according to the manufacturer's protocol. Sections were imaged using a confocal microscope.

2.5.4. Viability staining of spheroids

Spheroids were grown as previously described (Section 2.5.1. viability dye (Thermo Fisher Scientific) in Fluorobrite vanilla medium was added to each well of spheroids for 1.5h. Fluorobrite medium was then replaced with serum-free Fluorobrite vanilla medium with 1.5 μ M DRAQ7. CellTrace™ Calcein Violet AM (Thermo Fisher Scientific) was diluted in serum-free Fluorobrite vanilla medium and added to wells at a final concentration of 1 μ M, for a 30-minute incubation. Mid-sections of spheroids, defined by the z-plane of their widest diameter, were immediately imaged using a confocal microscope.

2.6 Flow cytometry staining

2.6.1. T-cell staining

CL4 T-cells were collected from culture into a falcon tube, which was topped up with PBS and centrifuged at 200 xg for 4 minutes. The cell pellet was resuspended in PBS at a concentration of 1 x 10⁶ cells/ml. 1.5 x 10⁶ cells for each staining condition were added to separate polystyrene FACS tubes (Corning). Cells were spun down and each pellet was resuspended in 100 μ l of PBS per 1x10⁶ cells, containing 1 μ l of Zombie Near Infrared™ Fixable Viability Kit reagent (Biolegend) per 100 μ l. Cells were incubated at room temperature in the dark for 15 minutes. 3ml FACS buffer was used to wash the cells in each tube via centrifugation at 250 xg for 4 minutes. The pellets were resuspended in 50 μ l FACS buffer containing 1 μ l Purified Rat Anti-Mouse CD16/CD32 Fc block (BD Pharmingen) per tube and incubated at 4 degrees Celsius for 15 minutes. Antibodies, diluted in FACS buffer, were added to each tube at the required concentration and incubated for 30 minutes on ice in the dark. 3ml FACS buffer was added to each tube and cells were centrifuged at 250 xg for 4 minutes. Cell pellets were resuspended in 3ml FACS and centrifuged at 250 xg for 4 minutes to remove residual antibody. Cell pellets were then fixed in paraformaldehyde and run through a BD LSRFortessa X-20 Flow Cytometer (BD Biosciences). Data were analysed using Flowjo analysis software version 7.10.1 (BD Biosciences).

2.6.2. Renca staining

2D Renca monolayers were detached from cells by washing flasks with PBS and then incubating cells for 5 minutes at room temperature in 10ml Accutase solution (Sigma-Aldrich) per 75ml flask. Detached cells were centrifuged at 200 xg for 3 minutes and the cell pellet was resuspended in PBS, followed by another centrifugation to wash cells. Cell pellets were then resuspended at a

concentration of 1×10^6 per 100 μ l of PBS. Meanwhile, 3D Renca spheroids were dissociated from Matrigel as previously described (Section 2.5.2. and then mashed through a 70 μ m pore size strainer (Thermo Fisher Scientific) to generate a single cell suspension. The 3D-cultured Renca cells were centrifuged at 200 xg for 3 minutes and the cell pellet was resuspended in PBS, followed by another centrifugation to wash cells. Cell pellets were then resuspended in an identical manner to the 2D-cultured cells. Renca cells from 2D and 3D culture were then divided into separate polystyrene tubes (Corning) and stained following the same protocol as for T-cell staining (2.6.1).

2.6.3. Antibody table

Marker	Clone	Fluorophore	Application	Manufacturer	Dilution/ concentration
TIM3	B8.2C1.2	PE	FC	Biolegend	2 µg/ml
CEACAM1	CC1	APC	FC	Biolegend	2 µg/ml
Galectin-9	RG9-35	BV421	FC	BD Bioscience	2 µg/ml
MHC-I	SF1-1.1	Pacific Blue	FC	Biolegend	5 µg/ml
Hypoxyprobe primary mouse mAb	4.3.11.3	N/A	IHC	Hypoxyprobe	60 µg/ml
IgG kappa mouse isotype control	P3.6.2.8.1	N/A	IHC	Thermo Fisher Scientific	20 µg/ml
Rat anti-mouse IgG1 Secondary Antibody	M1-14D12	FITC	IHC	eBioscience	0.1 µg/ml
TIM3	RMT3-23	N/A	Blockade	BioXcell <i>In Vivo</i> mAb	10 µg/ml
Isotype for TIM3 blockade	Rat IgG2a, 2A3	N/A	Blockade control	BioXcell <i>In Vivo</i> mAb	10 µg/ml
Anti-CD3	145-2C11	N/A	T-cell priming	BioXcell <i>In Vivo</i> mAb	10 µg/ml
Anti-CD28	37.51	N/A	T-cell priming	BioXcell <i>In Vivo</i> mAb	1 µg/ml

2.7 Microscopic cytotoxicity assays

2.7.1. 2D microscopic cytotoxicity assay

Transduced GFP⁺ CL4 T-cells were isolated via fluorescent activated cell sorting (FACS) (Supplementary Figure 1.1) and then incubated in IL-2 medium at 37 degrees Celsius. Meanwhile, RencaHA^{tdT} or RencaWT^{tdT} cells were peptide-pulsed for 1 h at 37 degrees Celsius with 2 µg/ml HA^{pep} or left unpulsed, except where peptide pulsing concentration was titrated, as stated. Renca cells were washed twice using 10 ml PBS and centrifugation at 200 xg for 3 minutes. Renca cell pellets were resuspended in Fluorobrite medium at a concentration of 10,000 pulsed Renca cells per 50 µl. 10,000 cells were plated into each well of a 384-well Black, Optically Clear Bottom, ViewPlate (PerkinElmer) and the plate was incubated at 37 degrees Celsius for 4 h to enable cells to attach to the well-bottoms and spread. Sorted CL4 T-cells were resuspended in Fluorobrite medium at a concentration of 10,000 cells per 50 µl, and 10,000 CL4 T-cells were added to each

well of the assay plate (apart from control wells with Renca cells only where 50 μ l Fluorobrite medium was added). 4 replicate wells were plated for each condition. For TIM3 blockade treatment, T-cells were pre-incubated with 10 μ g/ml TIM3 blockade antibody (RMT3-23) for 1 h and 10 μ g/ml TIM3 blockade antibody was present in the relevant wells during the entire assay period. Assay plates were immediately placed into the Incucyte™ Live Cell Analysis System (Essen Bioscience) and images were taken using the phase contrast and red channels using 1600 ms exposure time and a 15 minute time interval for 18 h, by the end of which all target cells had been killed as determined by visual assessment.

2.7.1.1 Analysis

The total red object (target cell) area per well ($\mu\text{m}^2/\text{well}$) was quantified at each time point using the in-built Incucyte™ ZOOM 2018a software (Essen Bioscience). For the 4 replicate wells of each condition, an average target cell area per well was quantified at each time point. This data was exported to Excel, where the average red object area at each timepoint, for each condition, was first normalised to the red object area at the 2h timepoint. A rolling average was calculated for each condition across every 3 subsequent timepoints. The rolling average of red object areas across all timepoints for each condition were plotted in line graphs in Excel to identify the timepoint at which a decrease in target cell area initiated. A 6 h period from the point at which killing initiated was then used for further analysis. Using the raw average red object areas during that 6 h time period of T-cell killing, the red object areas at each time point were normalised to the target area at the initial timepoint. As before, a rolling average was calculated for every 3 subsequent timepoints. Then the SLOPE function in excel was used to calculate the rate of killing per hour in each condition. The rate of killing in conditions containing T-cells were normalised to a control condition where T-cells were not present to rule out T-cell-independent Renca death.

2.7.2. 3D microscopic cytotoxicity assay

10-day-old spheroids were grown as described above in Section 2.5.1. On the day of the assay, transduced GFP⁺ CL4 T-cells were isolated via fluorescent activated cell sorting (FACS) (Supplementary Figure 1.1) and then incubated in IL-2 medium at 37 degrees Celsius; 200,000 T-cells were sorted per well of spheroids in the final assay plate, and then incubated separate wells of a 96-well plate. Spheroids were dissociated using incubation with 600 μ l Cell Recovery Solution per well (Corning), for 1 h at 4 degrees Celsius. Dissociated spheroids from each plate of spheroids (if more than 1 plate was used) were then collected from wells using a Pasteur pipette and transferred to separate 15 ml falcon tubes. Falcon tubes were topped up with PBS and centrifuged at 80 xg for 2 minutes to spin down spheroids to the bottom of the tube. The supernatant was discarded and spheroids were washed again in 10 ml PBS. The supernatant was discarded and spheroids in each tube were resuspended in 1 ml of vanilla medium containing

2 μ g/ml HA^{PEP} for peptide loading. Spheroids from each tube were transferred to a well of a 24-well plate for incubation at 37 degrees Celsius for 1 h, as this minimised spheroid aggregation during peptide-pulsing. During peptide-pulsing of spheroids, TIM3 blockade antibody, isotype control antibody or no treatment was added to the relevant wells of the T-cells in the 96-well plate and incubated at 37 degrees Celsius for 1 h. Following peptide-pulsing, spheroids were collected into a 15 ml falcon tube and washed in 10 ml PBS via centrifugation at 80 xg for 2 minutes. Supernatant was discarded and 10 ml PBS was used to wash again via centrifugation at 80 xg for 2 minutes. After supernatant was discarded by tipping the falcon tubes upside down, 200 μ l of residual buffer was left in the falcon tube with the spheroids- if less than this volume was left, PBS was added to reach 200 μ l. This volume was divided by the number of wells from the original spheroid plate (typically 8-10 wells) to calculate the volume of the spheroid solution that would contain 400 spheroids. Meanwhile, T-cells treated with TIM3 blockade, isotype control antibody, or no treatment, were collected from the 96-well plate into 1.5 ml eppendorfs and centrifuged at 300 xg for 4 minutes in a tabletop centrifuge. The supernatant was aspirated using a pipette to leave eppendorfs containing each containing a T-cell pellet at the bottom. In most experiments, 400 spheroids were then added to the relevant eppendorfs and mixed with the T-cell pellet (containing 200,000 T-cells) and spheroids and T-cells were coincubated for 15 minutes at room temperature. In the experiment displayed in Figure 4.1, T-cells were first mixed with Matrigel at a concentration of 200,000 T-cells per 50 μ l Matrigel, and then 400 spheroids were subsequently added to the Matrigel and T-cells. Either way, 50 μ l Matrigel containing spheroids and T-cells was then pipetted in the centre of each well-bottom of a chilled glass-bottom 24-well plate Eppendorf Cell Imaging Plate. Matrigel domes were set at 37 degrees Celsius for 10 minutes. 1 ml Fluorobrite medium containing 1.5 μ M DRAQ7 viability dye (Thermo Fisher Scientific) and 10 μ g/ml TIM3 blocking antibody (if appropriate) was then added to each well of the plate. Spheroids and T-cells were imaged using a Leica SP8 AOBS confocal microscope with a 10x HC PL Fluotar lens (numerical aperture (NA) = 0.3) and LASX version 3.7 software, which was set up for sequential excitation of tdTomato and GFP, then DRAQ7 fluorophores. Brightfield images were also acquired. For each condition, the first 3-6 spheroids that appeared in the field of view with diameters of 200-250 μ m were imaged. A 'mark and find' was set up to automatically image the set positions over the course of 12h, every 2h. Each spheroid was imaged with a z-step of 3 μ m from a few planes above the surface of the spheroid to a few planes below the mid-section of the spheroid, as determined by the z-plane with the widest diameter. Imaging excess planes either side of the spheroid mid-section and upper surface prevented loss of sample coverage due to occasional z-drift throughout the imaging period.

2.7.2.1 Analysis

To obtain measurements of spheroid-infiltrating T-lymphocyte (SIL) number, SIL volumes, spheroid total volume (included the hollow core), spheroid tdTomato⁺ volume (excluded the hollow core), spheroid sphericity (how closely the spheroid shapes were to a perfect sphere), SIL infiltration depth (the shortest distance between a SIL's edge and the outer surface of a spheroid) and the pathlength of T-cell tracks over time, raw data was pre-processed and semi-automatically analysed using Step 1 and Step 2, respectively, of a custom Cancer Segmentation macro developed in collaboration with Dr Stephen Cross of the Wolfson Bioimaging Facility using the Fiji image analysis plugin MIA (v0.9.26) and its MIA_MATLAB (v1.1.1) package, which can be found on Github through Zenodo at <http://doi.org/10.5281/zenodo.2656513> and <http://doi.org/10.5281/zenodo.4769615>, respectively (385). In step 1, the brightfield channel was used to check the field of view contained a spheroid, T-cells and no abnormal material debris and the tdTomato channel was used to manually mark the mid-point of each spheroid in the z-stack and remove excess planes either side of the spheroid surface or mid-point, which generated cropped z-stacks of half-spheroids. In step 2, the z-stacks of half-spheroids were mirrored in the z-axis and then concatenated to produce pseudo-whole spheroids, as this facilitated subsequent spheroid sphericity and volume measurements. The separate channels from the concatenated stacks were extracted to enable the analysis of objects (T-cells, live and dead cancer regions) which were detected in distinct channels. For the spheroid (tdTomato) channel, background noise was removed from images using a 2D Gaussian filter (sigma = 2 pixels). Images were binarised using the Otsu automatic threshold and image segmentation was applied using MorphoLibJ to perform connected-components labelling to create objects in 3D – each spheroid object is comprised of pixels connected to each other in 3D (386). Ellipsoid fitting using the BoneJ plugin for sphericity measurements. Spheroid objects smaller than a user-defined threshold (kept constant for all data analysis at $1 \times 10^6 \mu\text{m}^3$) could be removed to ensure detection of the primary spheroid in the field of view and avoid detection of spheroid fragments or parts of adjacent spheroids that were on the edges of the field of view. Spheroid volumes excluding the hollow core were measured based on the tdTomato⁺ volumes, using spatially calibrated units. To enable detection of whole-spheroid volumes, including the hollow core, an alpha shape was fit to each spheroid object using MATLAB; an alpha shape enclosed objects to smooth out holes or small bumps on the surface. For alpha shape implementation to spheroid objects, an alpha radius of 150.0 was used. To avoid any adjacent spheroids becoming detected a distance-based watershed transformation was applied. 3D ellipsoids were fit to spheroid objects in order to enable sphericity measurements. For the T-cell channel (GFP) background noise was removed using a 2D Gaussian filter (sigma = 2 pixels). These channels were binarised using the Triangle threshold. A distance-based watershed transformation was used to detect T-cells and distinguish adjacent T-

cells from each other. Connected-components labelling was used to detect 3D T-cell objects using MorphoLibJ (386). The BoneJ plugin was used to conduct ellipsoid fitting which enabled the measurement of T-cell volumes. T-cell objects with volumes smaller than a user-defined threshold ($250\mu\text{m}^3$ was used) were removed to remove debris or highly auto-fluorescent spheroid cells from further analysis. Each T-cell object was related to the closest spheroid object; to be related (that is, for a T-cell to be classified as infiltrating the spheroid) the centre of the T-cell object had to overlap with the spheroid, within the same time frame. The centre of T-cell and spheroid objects were related to each other via spatial overlap- this enabled the determination of the distance of a T-cell from the spheroid surface; these values were output as increasingly positive when the T-cell is further from the spheroid surface and increasingly negative if they are further inside the spheroid surface. The longest chord (length) of a T-cell was measured as the longest possible line between two ends of the surface of the same T-cell. CL4 T-cell objects were tracked through timeframes using the Munkres Assignment Algorithm (<https://hbase.apache.org/>), which calculated the distance from each T-cell in one time frame, to the same T-cell in the next time frame, to determine cell tracks that minimised the distances of object-object relations, using a maximum linking distance of $50\mu\text{m}$. Dead spheroid regions were detected in the DRAQ7 channel. A 2D median filter was used to remove background fluorescence. The image was binarised using the Otsu threshold. The volume of dead spheroid regions was measured using MorphoLibJ to perform connected-components labelling to create objects in 3D. Each dead spheroid object was related to the closest spheroid object (which was detected in the tdTomato channel); to be related, the centre of objects had to overlap in the same time frame.

2.8 Imaging calcium signalling, T-cell polarisation and interface stability

2.8.1. Calcium imaging

1×10^6 RencaHAtdT target cells were HA^{pep}-pulsed or left unpulsed, as previously described (Section 2.7.1. 200,000 sorted CL4 T-cells per condition were incubated in $2\mu\text{M}$ Fura-2 AM (Molecular Probes) diluted in imaging buffer, at 25 degrees Celsius, for 30 minutes, in the dark in 1.5ml eppendorf tubes. T-cells were washed twice in 1ml serum-free imaging buffer via centrifugation at 300 xg for 4 minutes in a table-top centrifuge. Each pellet of T-cells was resuspended in $20\mu\text{l}$ imaging buffer. RencaHA^{tdT} cells were resuspended in imaging buffer at a concentration of 5,000 cells per $10\mu\text{l}$. $50\mu\text{l}$ of imaging buffer per well was added to wells of a glass-bottomed 384-well optical imaging plate (Brooks Life Science systems). Imaging was conducted at 37 degrees Celsius using a Leica DM IRBE-based wide-field system with a Sutter DG5 illumination and a Photometrics Coolsnap HQ2 camera. For each imaging run, $5\mu\text{l}$ of the CL4 T-cell suspension (40,000 T-cells) was first pipetted onto the bottom of the well containing $50\mu\text{l}$ imaging buffer and CL4 T-cells were allowed to settle. The plate was placed on the microscope

stage and then 10 μ l of the RencaHA^{tdT} cell suspension was added to the top of the well. When RencaHA^{tdT} cells began to reach the cell bottom, an imaging period of 15 minutes was initiated with a time-interval of 10 seconds. At each timepoint, a differential interference contrast (DIC) bright-field image, and two fluorescent images were taken using excitation wavelengths of 340 nm and 380 nm, using a 40x oil objective lens (NA = 1.25). Images were analysed using Fiji image analysis software. Background fluorescence from the field of view was subtracted and the images from the 340 nm channel were divided by the images from the 380 nm channel to obtain images that displayed a ratio of the fluorescent intensities. These fluorescent intensities were then multiplied by 100 to fit the 8-bit display scale for further analysis. Using Fiji, differential interference contrast (DIC) images were used as a reference to identify the coordinates of cell couples; using the 340/380 image, the fluorescent intensity within the centre of a T-cell within a cell couple was measured every 10 seconds from 60 seconds before the initial contact between the T-cell and the target cell, up to 360 seconds later.

2.8.2. Analysis of coupling frequencies and T-cell morphological polarisation

Fiji was used to analyse T-cell coupling abilities, morphological polarisation and interface stability.

By analysing the DIC reference images obtained from the live-cell imaging described in Section 2.8.1. T-cells which contacted a RencaHA^{tdT} target cell with lamellipodia were manually analysed to determine if they subsequently formed a cell couple with the target cell within 30 seconds (3 time-frames) after initial cell contact, which involves spreading of the T-cell onto the Renca cell. Cell coupling frequencies were calculated as follows: *number of T-cells that formed cell couples following initial contact with target cells/ number of T-cells that did not form cell couples following initial contact with a target cell*. Cell couple formation was defined as the initial time point where the interface was at its maximal diameter, or two time-frames after initial cell contact, whichever occurred first. The lengths and widths of T-cells in cell couples were measured using a line-measurement in Fiji, every 1 minute from initial cell couple formation, up to 3 minutes after cell couple formation. The length/width ratio was calculated to quantify the morphological polarisation of T-cells between conditions.

2.8.3. Analysis of T-cell interface stability

Using the same DIC live cell imaging data as above, T-cells were manually analysed for the formation and time-of-onset of off-interface-lamellipodia (OIL) during cell coupling. OIL were defined as small membrane protrusions that moved away from the interface rather than towards the interface, as previously described (187). The percentage of OIL in cell couples was calculated as:

*(the number of T-cells that formed OIL/the number of T-cells that did not form OIL) *100*. The initial time-of-onset of OIL in T-cells within each condition was averaged for further statistical analysis.

2.9 Statistical tests

Normality of data distributions were tested using the SPSS Explore function and visually assessed using the Shapiro-Wilk test, histograms, normal Q-Q plots and box-plots. Where data were moderately positively skewed, a square-root (SQRT) transformation was applied and re-assessed for normality. Where SQRT transformation did not sufficiently transform data to normality, strongly positively skewed data were log-transformed (LG10) and re-assessed for normality. Student's t-tests, One-Way and Two-Way ANOVAs were conducted using GraphPad Prism version 6.0 software. Tukey's test was used for multiple comparisons.

Chapter 3 Development of a tumour spheroid model

3.1 Introduction

Improving checkpoint blockade and adoptive T-cell transfer (ATT) solid cancer therapies

Checkpoint blockade therapies, which block T-cell coinhibitory receptor: ligand interactions such as PD-1/PDL-1 blockade, have been FDA-approved for treatment of advanced stage cancers including melanoma and NSCLC, but they are only effective in around 10-30% of patients (387). Notably, single blockade treatments can lead to immune escape of solid cancers via upregulation of alternative checkpoint receptor ligands (326, 329). Thus, it is important to identify additional checkpoints, such as TIM3, that can be targeted in combination with PD-1/PDL-1 blockade. TIM-3 and PD-1 co-blockade has shown therapeutic synergy in preclinical and clinical trials, but with variable efficacy (325, 327, 332). Importantly, the mechanisms by which TIM3 regulates the anti-tumour CD8 T-cell response are largely unknown, and in some cases TIM3 has been shown to mediate stimulatory as well as inhibitory T-cell signalling. Furthermore, adoptive T-cell therapy (ATT) has shown promising potential as a treatment for advanced cancer patients and involves the infusion of a population of activated tumour-specific CD8 T-cells with high cytotoxic potential into the patient. However, adoptively transferred T-cells, like endogenous T-cells, encounter many barriers within the tumour microenvironment (TME) of solid tumours, which limits their ability to both infiltrate and kill tumours. Chronic activation leads to T-cell exhaustion, meanwhile, immunosuppressive factors- such as checkpoint receptor ligands- are often highly upregulated by tumour cells, preventing an effective anti-tumour response by adoptively transferred T-cells (388). Importantly, checkpoint blockade therapies are a promising way to improve the efficacy of ATT. Therefore, the elucidation of mechanisms by which T-cell co-receptors such as TIM-3 modulate TIL effector functions is important in order to improve the efficacy of both ATT and checkpoint blockade therapies. However, studying these mechanisms *in vivo* is complicated by the high number of variables that interact in complex networks. In contrast, *in vitro* tumour spheroid models offer a reductionist system to dissect the direct interactions between tumour cells and T-cells in a physiologically relevant 3D context.

The RencaHA/CL4 T-cell model

The RencaHA/CL4 T-cell model of ATT used by our lab involves two main components: 1) Renca cells that express the viral antigen haemagglutinin (HA) derived from the influenza virus and therefore the dominant 9-amino-acid long H-2K^d-restricted epitope (HA^{pep}), 2) HA^{pep}-specific Clone 4 (CL4) CD8 T-cells derived from TCR-transgenic CL4 mice. Previous studies in the lab, which have investigated the immunosuppression of CL4 T-cells within the TME of murine Renca tumours, have used two main Renca models: *in vitro* monolayer cultures of Renca wildtype (RencaWT) cells

that have been exogenously peptide-pulsed with HA^{pep} to form 2D targets expressing the cognate antigen of CL4 T-cells, in parallel with *in vivo* subcutaneous tumours which are each grown from the injection of 1 million RencaHA cells into the dorsal neck region of Balb/c recipient mice (381, 382). These *in vivo* RencaHA tumours have formed 3D targets for CL4 T-cells adoptively transferred into tumour-bearing mice (381, 382).

2D and 3D *in vitro* and *in vivo* solid cancer models

While monolayer cultures have proven to be incredibly useful for establishing basic principles of cancer signalling and genetics, it is well recognised that the culture of cancer cells as a flat sheet upon tissue culture plastic is considerably different to the *in vivo* context where cancer cells grow in 3D. One increasingly popular method to study cancer is the use of *in vitro* and *ex vivo* 3D models, which carry benefits in comparison to both 2D and *in vivo* tumour models. The multicellular tumour spheroids (MCTS) model is the most well-established way to culture cancer cells *in vitro* in 3D and was first developed in the 1970s to investigate radiotherapy-resistance mechanisms of cancer (389). It typically involves the culture of cancer cell lines in nonadherent wells to induce formation of well-rounded compact clusters of cancer cells, but can also involve growth of cells in synthetic or natural hydrogel scaffolds, such as polyethylene glycol (PEG)-based scaffolds and Matrigel (MG), respectively (390).

Over the past five decades MCTS have been used to investigate cancer's responsiveness to therapeutics including chemotherapy and less frequently, immunotherapy (361, 362, 364, 367, 369, 375, 379, 380, 391). MCTS more faithfully recapitulate important aspects of the TME compared to 2D cultures including cell-cell and cell-ECM adhesions in x-y-z planes, in addition to gradients of nutrients such as glucose, oxygen, pH and metabolites, owing to the 3D architecture (344-348). A spheroid is comprised of multiple concentric cell layers that increase in distance from the surrounding culture medium towards the spheroid centre, resulting in diffusion gradients of molecules from the centre to the spheroid surface (392). These chemical gradients often result in central necrotic regions that resemble the central necrosis commonly found in tumours *in vivo* (344, 346, 348, 349, 351-353, 393). Necrotic tumour cells have been found to be important modulators of tumour progression and immunosuppression, with an increasing extent of tumour necrosis being associated with higher grades of tumour, an impaired cytotoxic ability of tumour-specific CD8 T-cells, and increased tumour T classification and metastases (353-357).

Clearly, *in vivo* murine models represent a more physiologically relevant model of human cancer *versus in vitro* models, but in comparison to *in vivo* tumour models, MCTS models are less costly, less variable, require less animal-usage, and enable faster experimental execution compared to *in vivo* models. While the most simplistic MCTS involve the growth of cancer cells alone, further

elements of the TME can be added to the system in a highly controlled manner; heterotypic MCTS have been developed that contain cancer, stromal and immune cells (394, 395).

This chapter describes the development and characterisation of a MCTS scaffold-embedded 3D Renca model (using the hydrogel Matrigel), which subsequently enabled us to identify mechanisms of TIM3-mediated T-cell suppression, alongside the 2D Renca model (discussed in later chapters). Overall, the 3D Renca model can aid the improvement of both checkpoint blockade therapies and ATT as a cancer therapeutic.

In this chapter, the following aims are addressed:

- 1) To generate a RencaHA cell line expressing the red fluorophore tdTomato (RencaHA^{tdT}) and establish if RencaHA^{tdT} cells can be grown into MCTS (referred to as spheroids from now on), therefore providing an *in vitro* 3D model of RencaHA tumours, amenable to 3D imaging by confocal and 2-photon microscopy.
- 2) To determine the growth dynamics of RencaHA^{tdT} spheroids, in order to determine the age of RencaHA^{tdT} spheroids with a growth profile most relevant to *in vivo* RencaHA tumours. To determine how spheroid culture can be integrated with the timeline for CL4 T-cell culture for the development of a 3D microscopic cytotoxicity assay, which can enable assessment of tumour-specific killing of Renca spheroids by CL4 T-cells.
- 3) To determine the viability profile of RencaHA^{tdT} spheroids, in order to see if RencaHA^{tdT} spheroids recapitulate dead regions that are commonly found in *in vivo* tumours, including RencaHA tumours.
- 4) Determination of whether RencaHA^{tdT} spheroids should be HA^{pep}-pulsed for use in 3D microscopic cytotoxicity assays, by looking at how HA^{pep}-pulsing regulates the time before onset of killing by CL4 T-cells.
- 5) To establish a method for image analysis of spheroids and T-cell imaging data in order to enable quantification of: T-cell infiltration of spheroids, T-cell-dependent changes in spheroid viability and the dimensions of T-cells and spheroids.
- 6) To determine the spheroid: T-cell ratio for optimal image analysis and efficacy of data from 3D microscopic cytotoxicity assays.
- 7) To determine whether cognate antigen specificity of spheroid-infiltrating T-lymphocytes (SILs) impacts on spheroid death and/or the spatiotemporal dynamics of SIL infiltration and in doing so determine the suitability of the 'RencaHA^{tdT} spheroid + T-cell' model to study tumour-specific CD8 T-cell responses.

3.2 Results

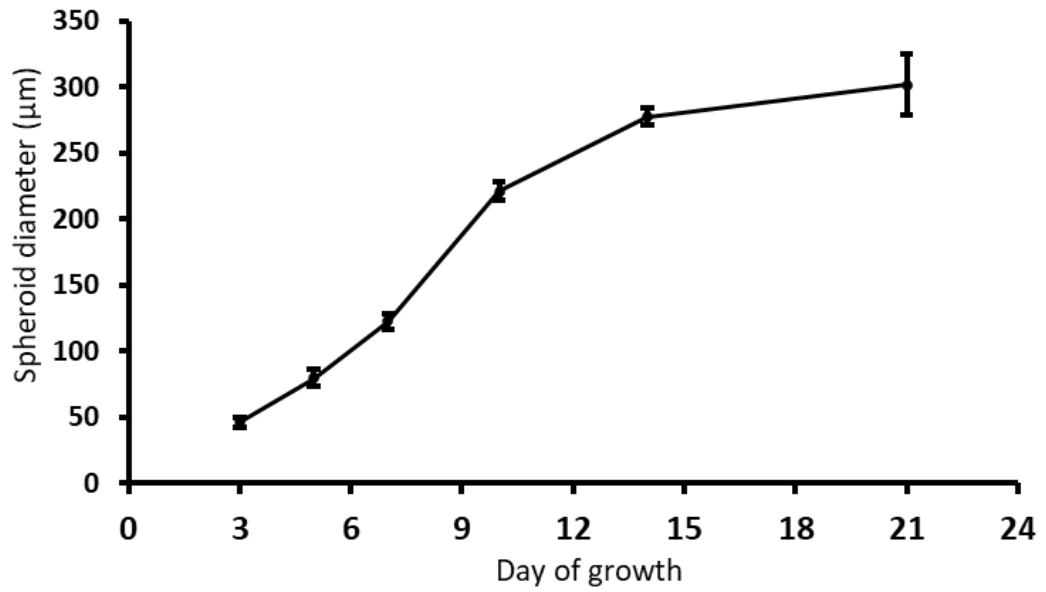
3.2.1. RencaHA^{tdT} spheroid growth over time

MCTS growth curves have been shown to be cell line-dependent but have been commonly modelled using variations of the Gompertz equation, as have the growth curves of *in vivo* tumours (351, 364, 396). There is often an initially exponential phase of spheroid growth, followed by a slower phase of growth that eventually reaches a plateau phase in which the maximal spheroid size has been reached. This spheroid size limit is likely due to diffusion limits of oxygen and/or nutrients, and the development of an expanding necrotic core which is thought to release growth-inhibitory toxic molecules (343, 352, 392).

RencaHA cells were transfected to express the red fluorophore tdTomato, to generate RencaHA^{tdT} cells. RencaHA^{tdT} cells successfully grew into spherical compact spheroids upon seeding into Matrigel (MG) (cells were seeded on Day 0). To establish the day of culture that spheroids should be used for functional assays with CL4 T-cells, spheroid diameters were measured over time; the mean spheroid diameter increased exponentially from Day 0 to 10, from 46 μ m to 221 μ m, approximately doubling every 3 days (Figure 3.1a, b). The mean spheroid diameter increased at a reduced rate from day 10, reaching 277 μ m on day 14 (Figure 3.1a, b). From days 14-21 there was a plateau phase of spheroid growth, the mean spheroid diameter reached 301 μ m by day 21 (Figure 3.1a, b).

10-day-old RencaHA^{tdT} spheroids were deemed most suitable for future spheroid assays because this timepoint would give the largest spheroids that were still in a highly proliferative phase and exhibited a dead core which was likely to be necrotic (discussed later), making them relevant to *in vivo* Renca tumours. Therefore, an experimental timeline was designed that enabled integration of spheroid and CL4 T-cell culture to conduct microscopic cytotoxicity assays using activated CL4 T-cells with 10-day-old spheroids (Figure 3.2).

a)



b)

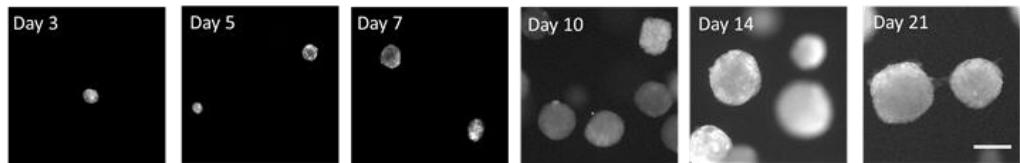


Figure 3.1. RencaHA^{tdT} spheroid growth over time.

Single RencaHA^{tdT} cells were seeded into Matrigel at a density of 400 cells per 50µl Matrigel dome/well for spheroid growth and imaged at the relevant timepoints using a confocal or widefield microscope. **a)** Spheroid diameters over the course of their growth from Day 3 to 21 where the day of seeding single cells to form spheroids was Day 0. **b)** Brightfield images of spheroids on different days of spheroid growth. n=6-28 spheroids per timepoint, from 3 independent repeats. Error bars show mean \pm SEM.

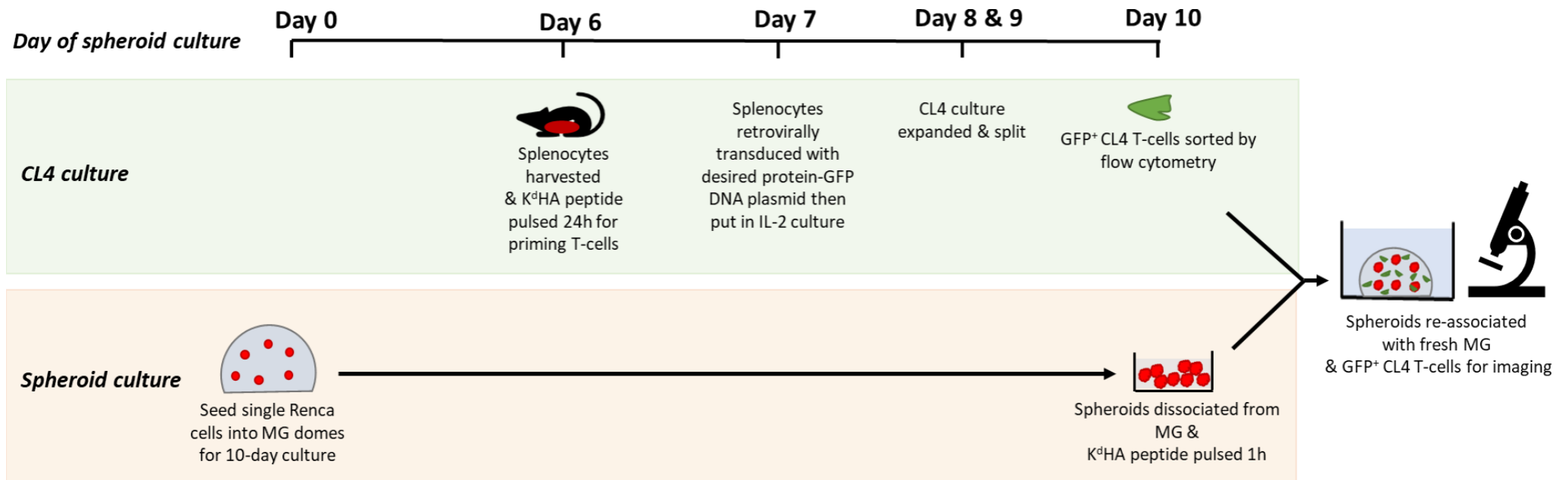


Figure 3.2. Schematic to show integration of Renca spheroid and T-cell culture timelines.

Bottom panel) Single cell suspensions of Renca cells were seeded on Day 0 at a density of 400 cells per 50 μ l Matrigel dome/well into 24-well plates and grown for 10 days with half-medium exchange every other day from Day 0-7, and every 12 hours on Day 8-9. **Top panel)** On Day 6 of spheroid culture, a spleen is harvested from a CL4 mouse and the splenocytes are pulsed with HA^{pep} peptide for 24h to prime CL4 T-cells. Splenocytes are then retrovirally transduced with a desired protein-GFP DNA plasmid and cultured in IL-2 until Day 10 when they are sorted by flow cytometry to obtain GFP⁺ T-cells. **Both panels)** On Day 10, spheroids are dissociated from the MG and HA^{pep} peptide pulsed for 1h, prior to assembly with GFP⁺ CL4 T-cells into fresh Matrigel; they are then ready for imaging using confocal or 2-photon microscopy.

3.2.2. The viability profile of RencaHA^{tdT} MCTS

It was of interest to characterise the viability profile of 10-day-old RencaHA^{tdT} spheroids, because the central necrosis commonly found in spheroids is thought to be partially responsible for the increased physiological relevance of 3D *versus* 2D models (351, 353, 354, 356, 357). Haemotoxylin and eosin staining of spheroids showed that the spheroids had an intact periphery of viable cells surrounding a hollow dead core (Figure 3.3a, left panel). This dead core was confirmed by staining live spheroids with DRAQ7 viability dye which labels dead cells, and Calcein Violet-AM dye which labels live cells (Figure 3.3a, centre panel). The fluorescent intensity distributions of the DRAQ7 and Calcein Violet-AM dyes differed significantly, with a relatively low mean DRAQ7 fluorescent intensity at the spheroid edge, which increased towards the centre of the spheroid (Figure 3.3b, top panel). Meanwhile, there was a relatively high mean fluorescent intensity of Calcein Violet at the spheroid edge which decreased towards the centre of the spheroid (Figure 3.3b, top panel).

Furthermore, mean tdTomato fluorescence of the RencaHA^{tdT} spheroids was high in the intact periphery of spheroids, but low in the DRAQ7⁺ dead centre (Figure 3.3a, right panel). As expected, the distribution of mean fluorescent intensity of the DRAQ7 and tdTomato fluorescence differed significantly from each other towards the edge and centre of the spheroid. (Figure 3.3b, bottom panel).

3.2.3. RencaHA^{tdT} spheroids do not display hypoxia

Hypoxia has been described to contribute to necrosis at the spheroid core, and is normally found in spheroids that have reached $\geq \sim 500 \mu\text{m}$ in diameter (352). Oxygen deprivation leading to decreased viability has, however, been described in spheroids $\geq 200 \mu\text{m}$ (397, 398). To determine whether RencaHA^{tdT} spheroids were hypoxic, spheroids were stained with Hypoxyprobe. 10-day-old spheroids did not display hypoxia, and therefore the dead core was unlikely to be a result of oxygen deprivation *per se* (Figure 3.4), though this did not rule out that oxygen deprivation contributed to central death, as low oxygen levels have been described to increase cancer cell sensitivity to deprivation of other factors such as glucose and amino acids, or low pH. Although these not investigated, any of the latter factors may be responsible for the observed central death of RencaHA^{tdT} spheroids.

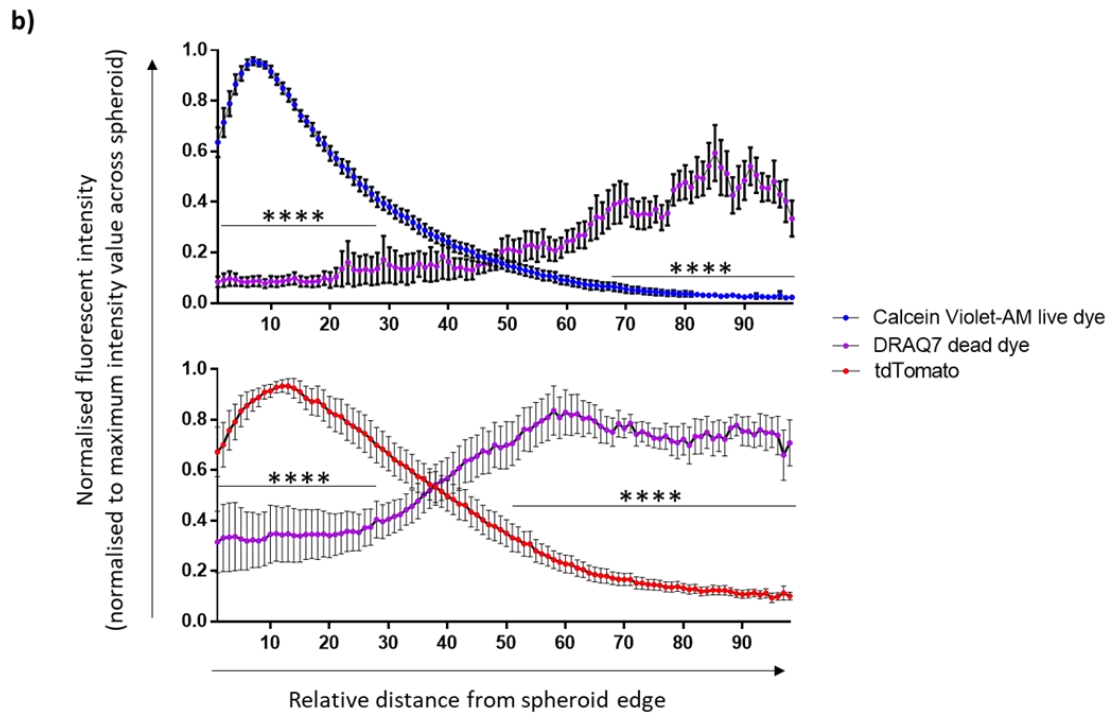
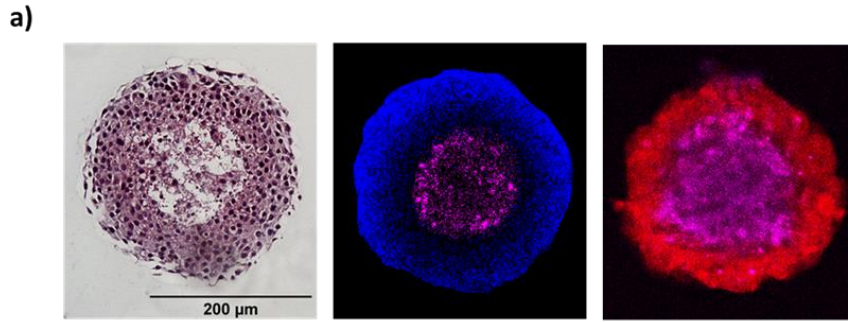


Figure 3.3. 10-day-old spheroids exhibited a dead core.

10-day old RencaHA^{tdT} spheroids were: fixed and paraffin-embedded, and then sectioned for H&E staining, or stained with viability dyes DRAQ7 and Calcein Violet-AM. **a)** The left panel shows a representative mid-section of an H&E-stained spheroid which displays the dead hollow core at the spheroid centre. The centre panel is a representative mid-section of a spheroid showing viability dye staining by Calcein Violet-AM in blue (live cells) and DRAQ7 in purple (dead cells). The right panel shows a representative spheroid mid-section showing the endogenous tdTomato fluorescence of the spheroid and staining with DRAQ7. **b)** The top panel shows the fluorescent intensity profile (mean gray value) of Calcein Violet-AM and DRAQ7 at distances from the spheroid edge towards the spheroid centre, left to right. The bottom panel shows the fluorescent intensity profile of tdTomato and DRAQ7 across the spheroid radius. For data shown in each of the top and bottom panels, n=6-10 spheroids from 2 independent repeats; data analysed to compare DRAQ7 and tdTomato fluorescent distributions across spheroids were acquired from 2 experimental repeats executed prior to a separate set of 2 independent repeats which included Calcein Violet-AM that were analysed for comparison of Calcein Violet-AM and DRAQ7 distributions. Means across the spheroid radius were compared using a 2-Way ANOVA and Sidak's multiple comparisons test. Error bars show mean \pm SEM.

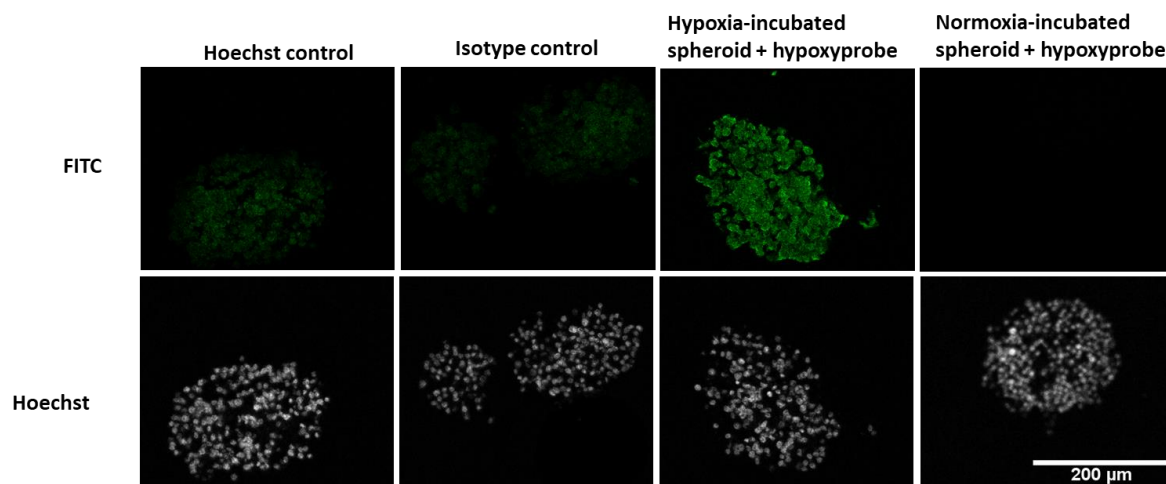


Figure 3.4. 10-day-old spheroids did not display hypoxia.

Spheroids were incubated in hypoxic or normoxic incubators for a total of 16h and incubated with pimonidazole hydrochloride (HCl) for the last 2h before fixation and paraffin embedment. In hypoxic but not normoxic cells, pimonidazole HCl is reduced to form protein adducts that can be detected using the Hypoxyprobe primary antibody. Representative images of spheroid mid-sections are shown: the first 3 columns, from left to right, are spheroids that were incubated under hypoxic conditions and stained with either: Hoechst only, an isotype control primary antibody, and the Hypoxyprobe primary antibody. Primary antibody staining was detected using a FITC-labelled secondary detection antibody. The top row shows FITC fluorescence, while the bottom row shows the nuclear Hoechst staining of the same sections. The right-most column shows a spheroid incubated under normoxic conditions, which did not display hypoxia.

3.2.4. HA^{pep}-pulsed *versus* unpulsed RencaHA^{tdT} target cells induced increased IFN γ secretion and comparable cytotoxic function by CL4 T-cells, while decreasing the time taken for target cell death to initiate

We hypothesised that HA^{pep}-peptide pulsing Renca cells might reduce the time taken for T-cells to kill Renca cells, enabling microscopic cytotoxicity assays to have a shorter imaging period. Thus, we investigated the effect of pulsing Renca targets with HA^{pep} on the time before the onset of measurable T-cell killing and the rate of killing by CL4 T-cells.

To achieve this, a 2D microscopic cytotoxicity assay was used; the primary readout of this assay was the rate of killing by T-cells. A 6h window of initial T-cell killing, starting at the onset of target cell area decrease, was used to calculate the percentage decrease in target cell area per hour. Representative examples of this temporal window are indicated by dotted red lines in Figure 3.5b. In this 2D microscopic cytotoxicity assay, a decrease in target cell area is associated with T-cell killing while a target area increase represents Renca growth- which occurs in the absence of T-cells.

The effect of peptide pulsing RencaHA^{tdT} target cells was investigated by plating CL4 T-cells with 2 μ g/ml HA^{pep}-pulsed or unpulsed RencaHA^{tdT} target cells in the 2D microscopic cytotoxicity assay. The mean rate of CL4 T-cell-mediated killing of pulsed and unpulsed RencaHA^{tdT} targets did not differ significantly (Figure 3.5a).

Importantly, we found that it took a significantly longer mean time (~2h longer) before the unpulsed *versus* pulsed RencaHA^{tdT} target areas began to decrease (Figure 3.5c); the mean pulsed and unpulsed RencaHA^{tdT} target areas, normalised to the target areas at 2h, are shown over the duration of the assay (Figure 3.5b). In order to confirm that pulsing RencaHA^{tdT} targets enhanced the activation of T-cells, thus reducing the time before onset of the target area decrease, we established the level of IFN γ secreted by CL4 T-cells during the 2D cytotoxicity assays using ELISA. T-cells secreted a significantly higher mean level of IFN γ when cocultured with pulsed *versus* unpulsed RencaHA^{tdT} target cells, indicating the enhanced activation of T-cells as a result of peptide pulsing (Figure 3.5d).

We also confirmed that T-cell-mediated killing of Renca cells was antigen-specific within this assay; RencaWT^{mCh} cells were exogenously pulsed with a range of HA^{pep} concentrations from 0.00002-2 μ g/ml. A reduced concentration of HA^{pep} peptide pulsing was associated with a reduced rate of killing, between peptide pulsing concentrations of 0.00002-0.02 μ g/ml, confirming antigen dependence of the killing (Figure 3.6). The data also suggested that peptide pulsing Renca cells with \geq 0.02 μ g/ml HA^{pep} saturated the MHCI H-2K^d molecules at the surface of Renca cells, since there was no corresponding enhancement of killing rate at these higher peptide pulsing concentrations (Figure 3.6).

Additionally, we indirectly investigated the relative level of HA^{pep} expressed by RencaHA^{tdT} compared to RencaWT^{mCh} cells, which has not been previously determined by the lab, due to the lack of a suitable anti-HA^{pep} antibody. The mean rate of killing of unpulsed RencaHA^{tdT} target cells was comparable to the mean rate of CL4 T-cell killing of 0.002µg/ml HA^{pep}-pulsed RencaWT^{mCh} target cells, which indicated that the level of HA^{pep} endogenously expressed by unpulsed RencaHA^{tdT} cells was lower than the expression level of HA^{pep} on 0.02-2µg/ml HA^{pep}-pulsed RencaWT^{mCh} target cells (Figure 3.6).

However, since other data (Figure 3.5a) showed that the killing of pulsed *versus* unpulsed RencaHA^{tdT} targets did not differ, it is likely that HA^{pep}-independent factors resulted in different rates of killing of the 0.02-2 µg/ml pulsed RencaWT^{mCh} and unpulsed RencaHA^{tdT} cell lines.

Overall, the time taken for killing to initiate was longer against unpulsed *versus* 2µg/ml HA^{pep}-pulsed RencaHA^{tdT} targets, while the rate of killing did not differ, therefore, pulsed RencaHA^{tdT} targets were used for subsequent 2D and 3D microscopic cytotoxicity assays, except where indicated.

Notably, previous *in vitro* 2D microscopic cytotoxicity assays in the lab have used 2µg/ml HA^{pep}-pulsed RencaWT^{mCh} target cells as a model of RencaHA tumour cells *in vivo*. Together, the above findings suggested that ligands for T-cell coinhibitory or costimulatory receptors may be differentially expressed by RencaWT^{mCh} *versus* RencaHA^{tdT} cells, as maximally pulsed RencaWT^{mCh}, but not maximally pulsed RencaHA^{tdT} cells, induced a higher rate of CL4 T-cell killing *versus* unpulsed RencaHA^{tdT} cells. For example, intercellular adhesion molecule-1 (ICAM-1) could be more highly expressed on RencaWT^{mCh} *versus* RencaHA^{tdT} cells; ICAM-1 expression by Renca cells has been shown to provide important co-stimulation to naïve CL4 cells, which results in elevation of IFN γ secretion. Thus, increased ICAM-1 expression by the RencaWT^{mCh} *versus* RencaHA^{tdT} cell line could have increased the activation of engaged effector CL4 T-cells, reducing the dependence of CL4 T-cells on HA^{pep} availability (399). Possible differences in the RencaWT and RencaHA lines will be important to establish for future experiments and for the interpretation of past findings, which used these cell lines interchangeably.

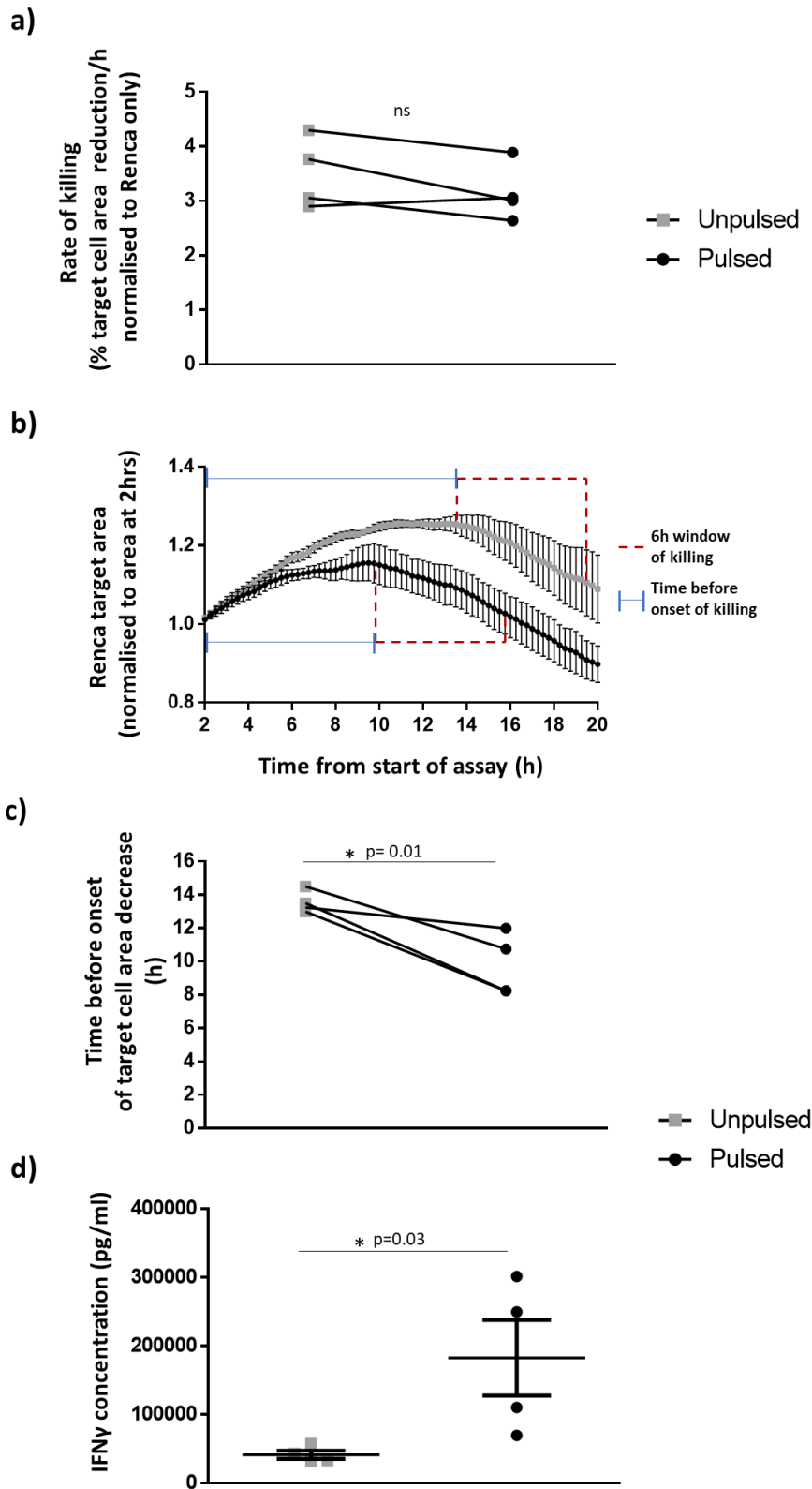


Figure 3.5. The HA^{pep} expression level of unpulsed RencaHA^{tdT} cells was not sufficiently different from RencaHA^{tdT} 2 μ g/ml HA^{pep}-pulsed targets to alter the rate of CL4 killing during a 2D microscopic killing assay, but did lead to lower IFN γ production by the CL4. The time before RencaHA^{tdT} target cells were killed by CL4 was reduced when target cells were HA^{pep}-pulsed *versus* unpulsed.

RencaHA^{tdT} cells were pulsed with 2 μ g/ml HA^{pep} or left unpulsed and plated as target monolayers in the 2D microscopic cytotoxicity assay which used the IncucyteTM Live Cell analysis system. **a)** 2 μ g/ml HA^{pep} pulsed and unpulsed RencaHA^{tdT} cells were plated as target cells with CL4 T-cells for

2D microscopic cytotoxicity assays. Each point shows the mean rate of killing from one of four independent repeats. Lines connect data from the same independent repeat. Means were compared using a one-tailed, paired t-test. ns= non-significant p-value. **b)** The change in unpulsed and pulsed RencaHA^{tdT} target areas, normalised to the target areas at 2h, over the duration of a 2D microscopic cytotoxicity assay is shown. Error bars show mean \pm SEM from four independent repeats. Red dotted lines indicate the 6h window of T-cell killing that is used to calculate the rate of killing by T-cells. Blue solid lines indicate the time period before onset of target area decrease. **c)** The time taken before the onset of target area decrease is plotted for unpulsed and pulsed RencaHA^{tdT} target cells. **d)** Each point shows the mean IFN γ concentration in the supernatant from the 2D microscopic cytotoxicity assay wells, from three replicate wells of an ELISA, from a total of 4 independent repeats. For all graphs, each point represents the mean from an individual repeat, out of four independent repeats. Lines connect data from the same independent repeat. Means were compared using a one-tailed paired t-test.

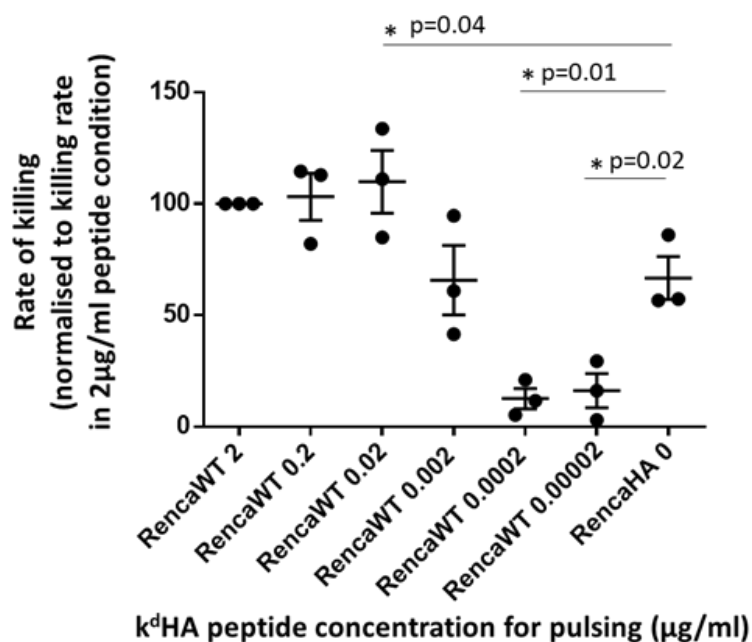


Figure 3.6. The rate of CL4 killing was comparable between RencaHA^{tdT} unpulsed and 0.002 µg/ml HA^{pep}-pulsed RencaWT^{tdT} targets during a 2D microscopic killing assay.

RencaWT^{mCh} cells which had been pulsed with varying concentrations of HA^{pep}, and unpulsed RencaHA^{tdT} cells were plated as monolayer target cells in the 2D microscopic cytotoxicity assay, which used the IncucyteTM Live Cell analysis system, for assessment of CL4 T-cell cytotoxicity. Each point shows the mean from one of three independent repeats. Error bars show mean ± SEM. The mean rate of killing of the RencaHA^{tdT} target was compared to all other means using One-Way ANOVA, with Dunnett's test. Non-significant p-values are not shown. Error bars show mean ± SEM. Means were compared using a one-tailed paired t-test.

3.2.5. Development of RencaHA cell lines that express fluorescent sensors for Caspase 8 and Granzyme B activity to enable determination of T-cell cytotoxicity pathways.

Another aspect of the *in vitro* RencaHA/CL4 model that has not been defined is the mechanism of Renca cell death initiated upon CL4 coinubation. Therefore, we transfected the RencaHA cell line with DNA plasmids encoding fluorescent sensors of caspase 8 and granzyme b (GzmB) activity to generate the RencaHA^{Casp8} and RencaHA^{GzmB} cell lines, using a previously described cloning method (97, 383). These lines can be used in combination to determine the extent of CL4 T-cell-dependent Renca cell death that is induced by the GzmB or the FasL/Fas pathways, which induce cell death through activation of caspase 3/7 and caspase 8, respectively. When the active enzyme enters or is activated within the Renca cell, it cleaves a protein sequence located within a linker sequence in the fluorescent probe. As this linker joins the fluorophore tdTomato to a nuclear exit signal, enzyme activity causes tdTomato fluorescence to translocate from an exclusively cytoplasmic location to both a nuclear and cytoplasmic location (Figure 3.7a).

To confirm that the GzmB probe worked correctly, RencaHA^{GzmB} cells were plated with CL4 T-cells at a range of effector: target ratios. Increasing the effector: target ratio increased the percentage of cells that displayed a cytoplasmic-to-nuclear translocation event (using manual analysis) indicating that the probe correctly sensed T-cell-dependent GzmB activity within the Renca cells. In future, staining Renca nuclei using Hoechst would enable automated detection of these events (not included here). Furthermore, to confirm that the caspase 8 probe worked correctly, we hypothesised that we could induce Fas-mediated RencaHA^{Casp8} cell death using the agonistic anti-Fas antibody (clone Jo2). However, the anti-Fas antibody did not initiate Renca cell death at a range of concentrations from 2-2000ng/ml. This corroborated a previous study in which the antibody only initiated Renca cell death in the presence of IFN- γ (400). Therefore, addition of IFN- γ to the RencaHA^{Casp8} cells during the 2D microscopic cytotoxicity assay could enable verification of the caspase 8 fluorescent probe.

Overall, RencaHA^{Casp8} and RencaHA^{GzmB} cell lines were created that are suitable for future determination of Renca cell death pathways initiated by CL4 T-cells (though further verification of the RencaHA^{Casp8} line is required). These cell lines can also enable improved verification of T-cell mediated cell death in future 3D microscopic cytotoxicity assays, alongside DRAQ7 viability staining.

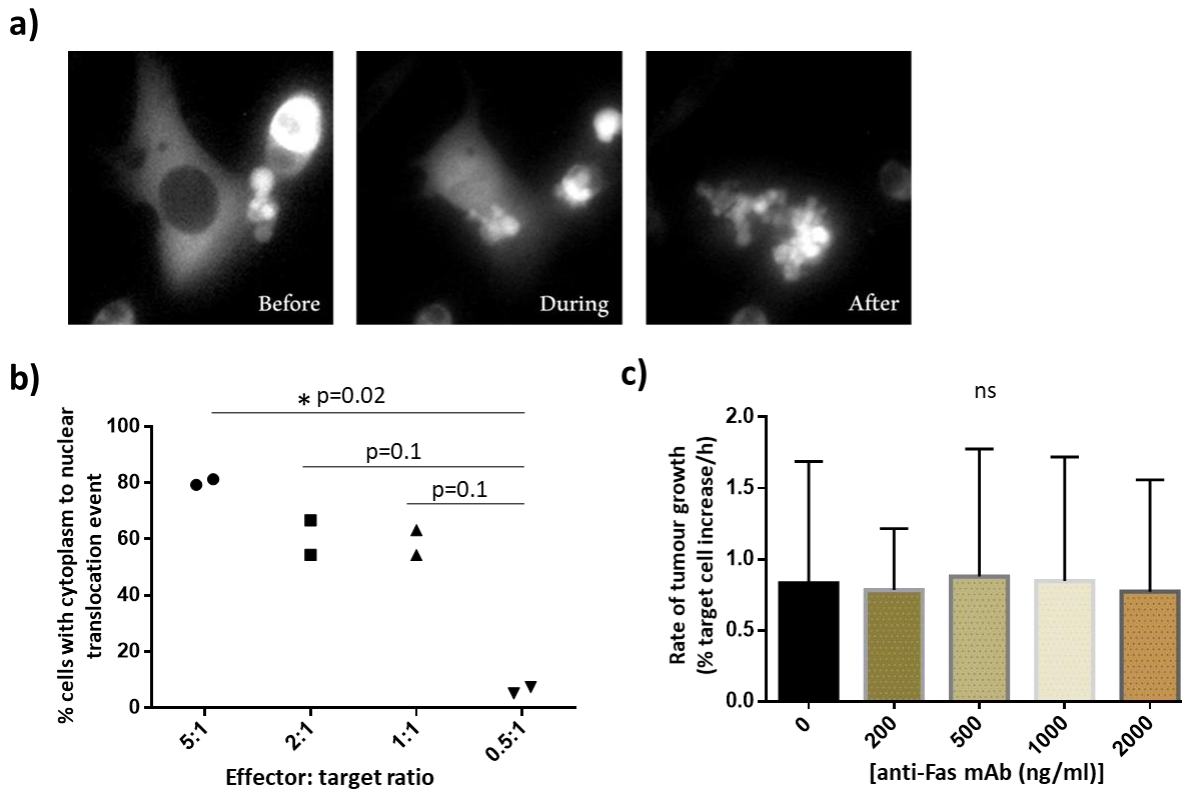


Figure 3.7 RencaHA lines expressing fluorescent sensors for granzyme B (RencaHA^{GzmB}) and caspase 8 (RencaHA^{Casp8}) activity were generated and enabled measurement of T-cell-dependent apoptosis; Renca cells were susceptible to GzmB-mediated apoptosis in the presence of T-cells but were unaffected by Fas-FasL dependent death in the absence of T-cells. **a) Representative timelapse images of Renca cells plated in the 2D microscopic cytotoxicity assay show the localisation of the fluorescent sensors before (left panel, cytoplasmic) and during (middle panel, cytoplasmic and nuclear) delivery of the T-cell cytotoxic granules. The right panel shows subsequent apoptotic blebbing of the dying Renca cell. Images were acquired using the Incucyte with an acquisition interval of five minutes. **b)** CL4 T-cells were plated with RencaHA^{GzmB} target cells at a range of effector: target ratios and the percentage of cells displaying cytoplasmic-to-nuclear translocation of the fluorescent sensors was measured manually using Fiji software. Data are from two independent repeats. Means were compared using One-Way ANOVA matched by repeat. **c)** RencaHA^{Casp8} target cells were incubated with various concentrations of anti-Fas Jo2 antibody to assess the sensitivity of Renca cells to the Fas-FasL dependent death pathway (no RencaHA^{Casp8} cell death was detected). Data are from three independent repeats, error bars show mean \pm SEM. Means were compared using One-Way ANOVA matched by repeat.**

3.2.6. Development of an image analysis 'Cancer segmentation' macro enabled the measurement of various SIL and spheroid spatiotemporal parameters.

We decided to use an imaging period of 2-12h post-plating T-cells with spheroids, in the 3D microscopic cytotoxicity assay, which would enable a 2h window to set up the microscope, assign the imaging positions and troubleshoot any microscope issues. This imaging period also enabled us to use the facility microscope in off-peak hours when microscope demand was lowest. In order to reduce the time taken to acquire images from each spheroid, half-spheroids were imaged as representative samples of spheroids; the half-way point of a spheroid was determined as the z-plane at which the spheroid diameter was widest.

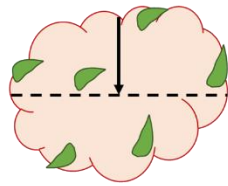
To measure the sphericity and volume of the spheroids it was substantially easier to automate the analysis of whole spheroids *versus* half-spheroids, therefore, using Fiji image analysis software, half-spheroid images were mirrored in the x-y axes for further analyses. (Figure 3.8, step 1 and 2). Using a 'Cancer segmentation' macro that was developed with Dr Stephen Cross using Matlab and Fiji software, the following measurements could be output from the analysis: T-cell number, T-cell volumes, spheroid total volume (included the hollow core), spheroid tdTomato⁺ volume (excluded the hollow core), spheroid sphericity (how closely the spheroid shapes were to a perfect sphere), SIL infiltration depth (the shortest distance between a SIL's edge and the outer surface of a spheroid) and the pathlength of T-cell tracks over time- useful if the image acquisition time intervals were sufficiently short to enable tracking of individual T-cells.

The SIL density of a spheroid was calculated using the SIL number divided by the spheroid tdTomato⁺ volume (as the dead core would not be a region of T-cell mediated killing) and gave a readout of changes in SIL migration/adherence to the spheroids. SIL surface density was calculated where spheroid shapes differed substantially between groups (which would cause different surface area: volume ratios); this was calculated using the SIL number divided by the spheroid surface area (Chapter 5). The spheroid total volume was used to compare the initial spheroid dimensions between groups to determine if spheroid dimensions may have influenced any differences between groups. T-cell volume measurements were systematically overestimated due to the imaging setup and analysis; a compromise was made between resolution, the imaging acquisition length at each timepoint and laser power/photobleaching in order to image samples at a reasonable speed, with sufficient resolution and minimal photobleaching. With the pixel x-y and z-interval resolutions of 1.10 μm and 3 μm , respectively, the chosen image segmentation algorithms enabled consistent detection of T-cells but systematically increased the measured volume of T-cells. Accordingly, a single pixel increase in all axes around a T-cell object translated to a more substantially enhanced volume due to the small size of these objects. (The analysis is discussed in more detail in Chapter 2.) Nevertheless, useful information could be obtained from

relative T-cell volumes- the relative extent of T-cell blasting- between groups. SIL infiltration depth gave information on how deeply SILs migrated into the spheroids and the pathlength of T-cell tracks could give an estimate of motility (where time intervals were sufficiently short), with longer tracks being associated with higher motility. The macro provided the ability to measure T-cells in the entire field of view (SILs in contact with and outside spheroids), or only SILs (in contact with spheroids). In future analyses, which aim to characterise SIL behaviour, it can be assumed that SIL measurements, rather than all T-cell measurements are discussed.

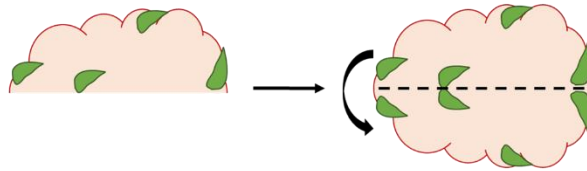
The analysis also output 'outline' files which enabled visualisation of how T-cell and spheroid objects were detected. Outline files facilitated manual assessment and adaptation of image segmentation thresholds in order to improve object detection where required. In these output files, dead spheroid volume (shown in purple) was outlined in blue, total spheroid (red tdTomato⁺ volume including hollow core) was outlined in green and SIL objects (shown in green) were outlined in white (Figure 3.8, step 3). tdTomato⁺ volumes (excluding the hollow core) were outlined in orange- the hollow core is not visible in Figure 3.8 step 3, as it shows a z-projected image, but can be seen in Figure 3.9b. A time course of up to 12h post-plating provided sufficient time to see SIL infiltration and spheroid death as shown in the representative z-projected images of a spheroid over time (Figure 3.8, step 3).

1. Image acquisition



Imaged half a spheroid as representative sample of a spheroid, with z-interval of 3 μm

2. Image pre-processing for analysis



Mirrored half the spheroid in x-y axes to produce a whole spheroid which facilitated measurement of sphericity (how close to a perfect sphere the spheroid was).

3. Image analysis: detection of spheroid and SIL objects

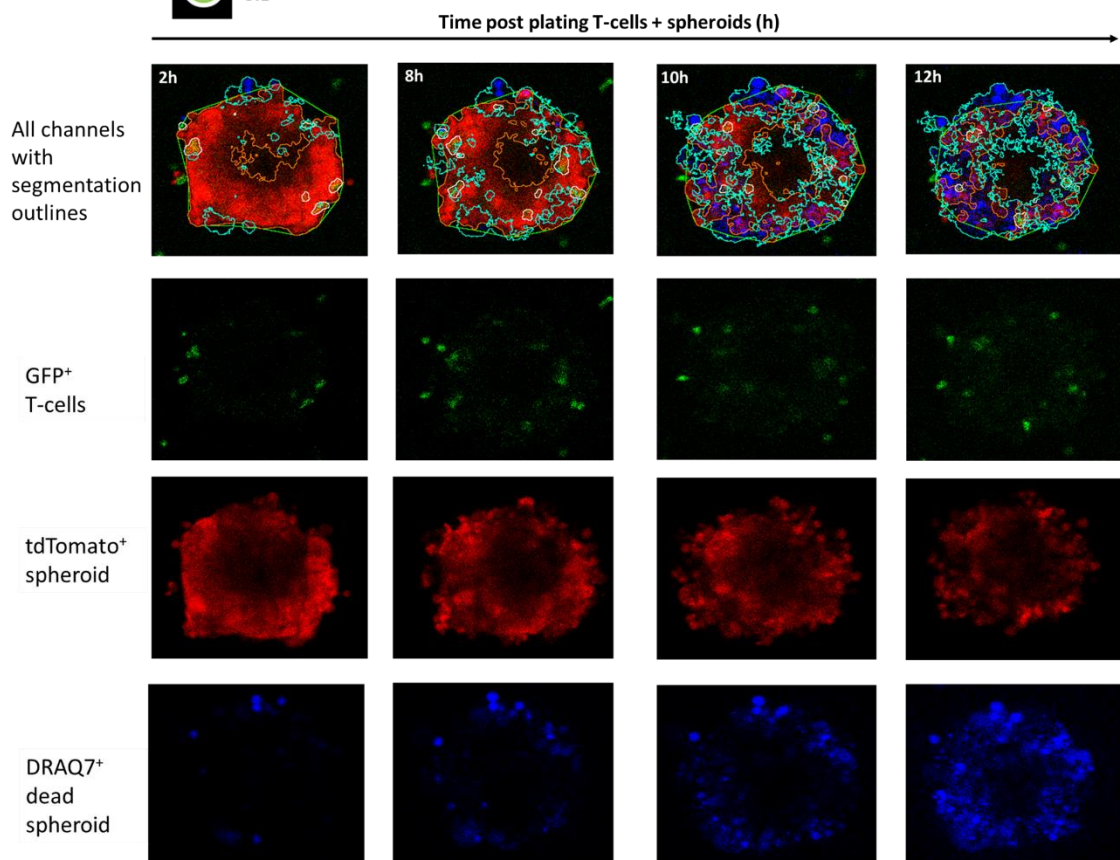
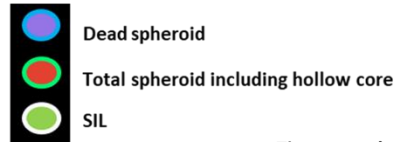


Figure 3.8. Schematic to show strategy for imaging and image analysis.

Step 1) Half-spheroids were imaged as representative samples of whole spheroids, with a z-interval of 3 μm , using confocal microscopy. **2)** Half-spheroids were pre-processed for further analysis: spheroids were mirrored in the x-y axes using Fiji image analysis software. This facilitated automated measurements of sphericity – which is substantially easier to execute on whole spheroids compared to half-spheroids. **3)** Image analysis using a tailored ‘Cancer Segmentation’ macro enabled detection of dead spheroid volume (outlined in bright blue), total spheroid volume including the hollow core (outlined in green), and SILs (outlined in white). Representative images of a single mid-section plane of a spheroid when 200,000 T-cells were plated per well of spheroids; an increase in dead spheroid volume can be seen during an imaging period of 2 to 12 hours. Notably, as a consequence of the initial mirroring of half spheroids into whole spheroids, measurements output by the automated analysis, including SIL density, tdTomato⁺ spheroid volume and dead spheroid volume, are doubled for all spheroids analysed.

3.2.7. Adding high numbers of T-cells per well of RencaHA^{tdT} spheroids can limit the efficacy of image analysis to identify individual SILs

To decide the number of T-cells to add to each well of ~400 spheroids, several factors were considered, including: the numbers of transduced T-cells that could reliably be available on the day of the assay, the time taken to sort the desired cells by flow cytometry and the ability to segment and identify single SILs in the spheroid imaging data. To address the latter factor, a titration of the number of T-cells to add to each well of spheroids was conducted by adding 100,000, 200,000 or 500,000 T-cells per well. These T-cells were retrovirally transduced to overexpress Ftractin-GFP, a small peptide that binds to filamentous actin (F-actin) and can label T-cells green without causing any functional effects. The efficacy of automated image segmentation to identify SILs between the 100,000, 200,000 and 500,000 T-cell groups was important to consider; in the 500,000 T-cell group there were cases of ineffective detection of individual SILs, wherein multiple SILs were grouped as one SIL object (Figure 3.9a, right panel). Adding 500,000 T-cells per well would also make it harder to identify if independent variables were increasing SIL density, because the baseline untreated SIL density had the potential to cover the entire spheroid surface. Therefore, 500,000 T-cells per well would be unsuitable for the 3D microscopic cytotoxicity assay.

3.2.8. Increasing the number of T-cells added per well of RencaHA^{tdT} spheroids increases SIL density but has no significant impact on spheroid death, infiltration depth or SIL volume

It was hypothesised that adding more T-cells to each well of spheroids would increase SIL density and spheroid death, with unknown effects on SIL infiltration depth or SIL blast morphology. As expected, it was found that the mean SIL density was increased when 500,000 *versus* 200,000 or 100,000 T-cells, and this increase was significant at 6, 8 and 12h post-plating T-cells and spheroids (Figure 3.10a). This is despite the mean SIL density of the 500,000 T-cell per well group likely being an underestimate in some cases due to suboptimal object detection, as previously discussed. Mean SIL density was also significantly higher when there were 200,000 T-cells *versus* 100,000 T-cells per well at 10 and 12h post-plating (Figure 3.10a). Surprisingly, there were no significant differences in mean spheroid death at any timepoints between the three groups; while there was an increased mean spheroid death in the 200,000 *versus* 100,000 T-cells per well groups in two of the three independent repeats, adding 500,000 T-cells per well consistently did not lead to increased mean spheroid death *versus* either the 100,000 or 200,000 T-cell groups (Figure 3.10b).

To explain this latter finding, it is possible that immunosuppressive metabolic competition between cells could have been increased in the 500,000 T-cell group, therefore limiting T-cell cytotoxicity in this context. High competition between cells for nutrients such as glucose and amino acids has been described in tumours, and is known to have immunosuppressive effects on TILs (401). There were also no significant differences in mean SIL volume, which is a measure of T-cell blasting and activation, between the 100,000, 200,000 and 500,000 T-cell groups and the slight trend of increased mean SIL volume in the 500,000 T-cell group could be accounted for by the suboptimal image segmentation of SILs in this group as a result of high SIL densities at the spheroid surface, as previously discussed (Figure 3.10c). There were also no biologically meaningful differences in mean SIL infiltration depths across all timepoints; SILs remained on the spheroid surface in all groups (Figure 3.10d).

Based on these findings, 200,000 T-cells per well of spheroids were used for future 3D microscopic cytotoxicity assays, because it enabled more SILs to be studied *versus* using 100,000 T-cells per well, but also did not have the image segmentation limitations of the 500,000 T-cell per well group.

3.2.9. DRAQ7 stains dead cells at the RencaHA^{tdT} spheroid surface and not the dead core of spheroids in the presence of T-cells

Additionally, within all groups and timepoints, DRAQ7 labelled Renca cells on the outer edge of the spheroids but not the dead core in the presence of T-cells (Figure 3.9b), suggesting that the ongoing death at the spheroid surface in the presence of T-cells resulted in consumption of the dye at the spheroid surface and prevented diffusion of the dye deeper into the spheroid centre. In order to adapt the 3D microscopic cytotoxicity assay analysis to this finding, we compared the increase in spheroid death over the time course, normalised to the first timepoint of 2h, across all groups. This helped to ensure that the extent of DRAQ7⁺ staining present before the first assay timepoint did not affect the measurements of spheroid death over time (in all assays spheroids in the absence of T-cells were used as controls to measure the baseline level of T-cell-independent spheroid death).

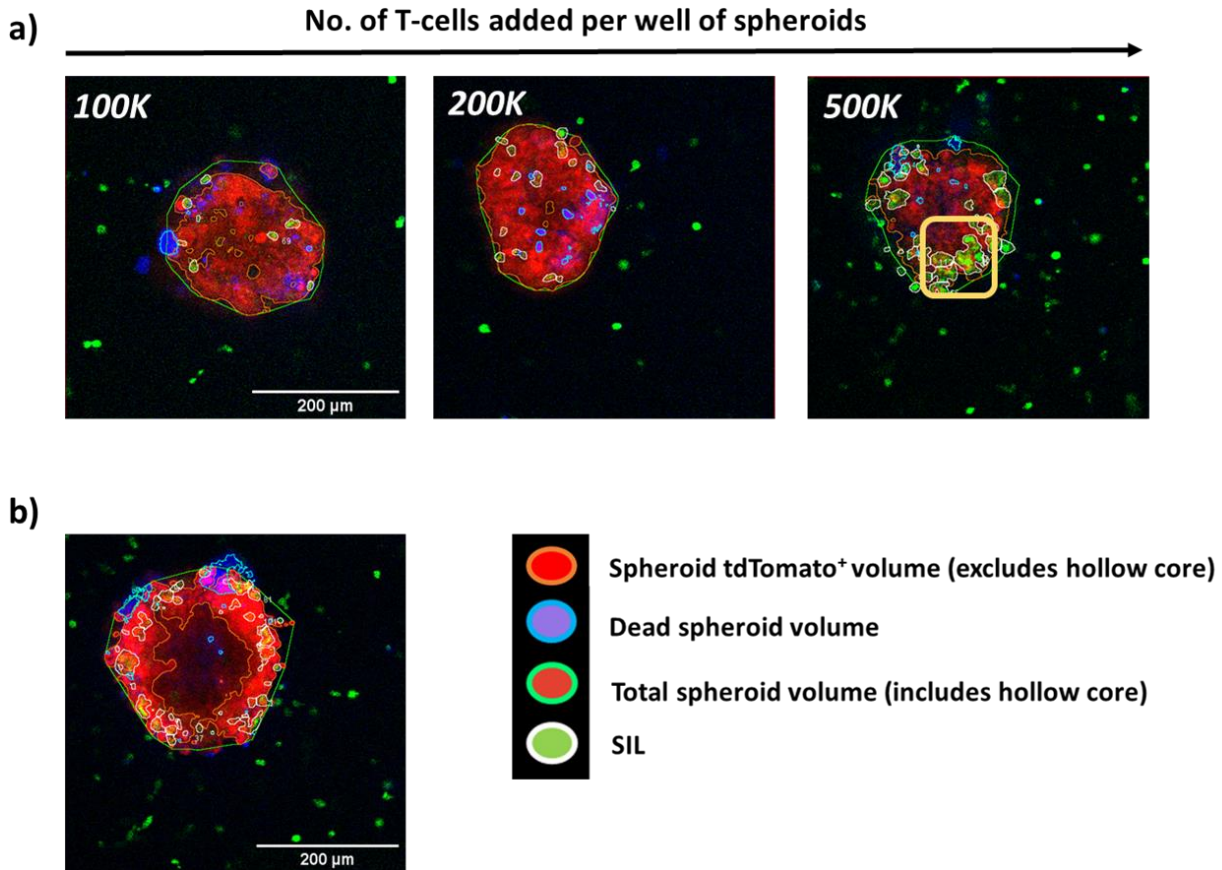


Figure 3.9. Incubation of 500, 000 T-cells per well of spheroids resulted in SIL densities that reduced the efficacy of image segmentation to identify individual SILs, DRAQ7 did not stain the dead core of spheroids when T-cells are present.

RencaHA^{tdT} spheroids were incubated with 100,000, 200,000 or 500,000 CL4 T-cells, transfected to overexpress Ftractin-GFP, per well. **a)** Representative images of a z-plane at the surface of spheroids when 100,000 (left), 200,000 (middle) and 500,000 (right) T-cells are plated per well of spheroids, from the 4h timepoint. The yellow box highlights that when 500,000 T-cells are plated per well multicellular rather than single SIL objects can be detected due to limits in image segmentation. **b)** Representative image showing the lack of DRAQ7 (blue) staining in the centre of spheroids co-incubated with T-cells.

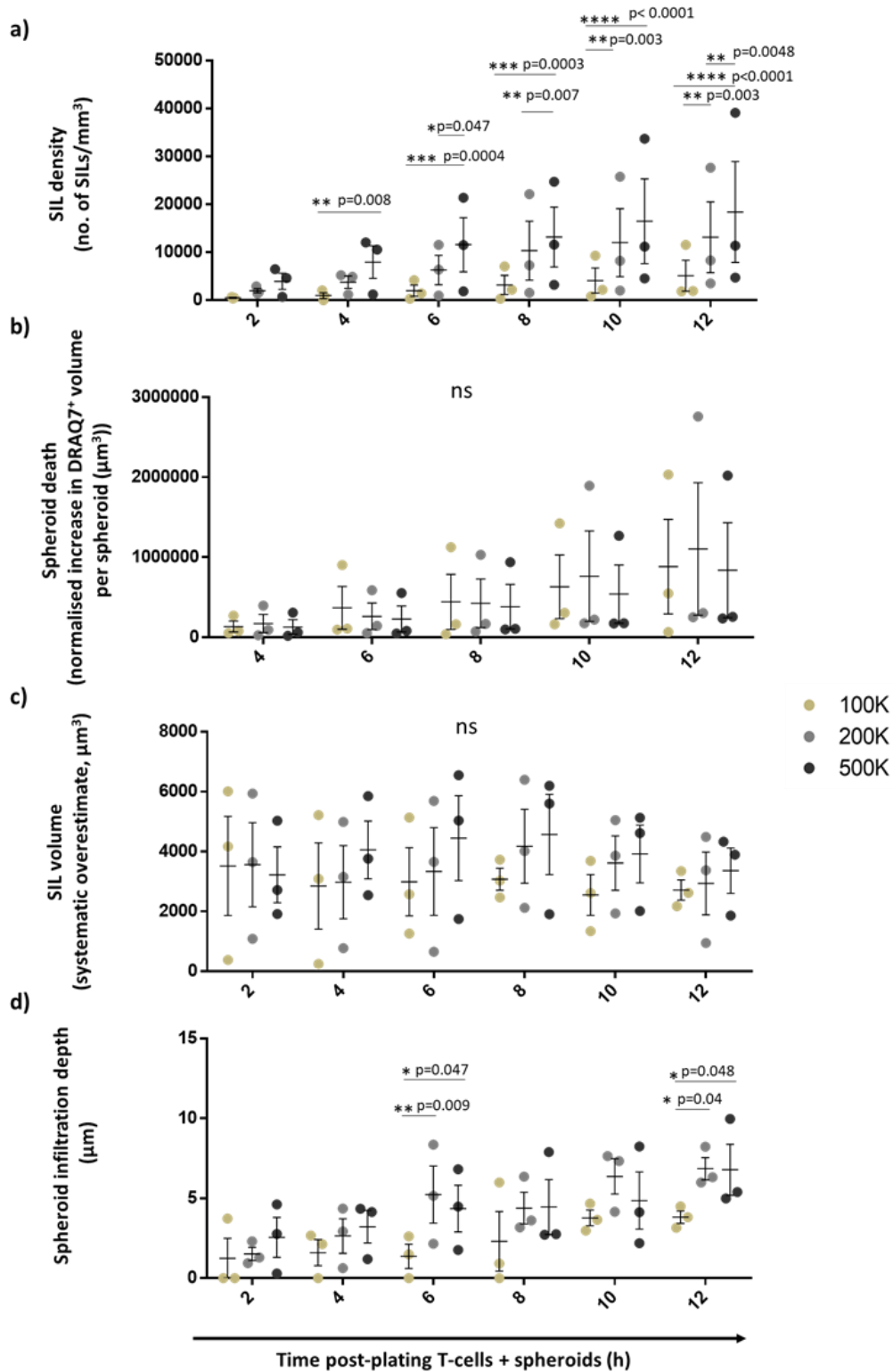


Figure 3.10. Titration of CL4 T-cell number per well of RencaHA^{tdT} spheroids.

Spheroids were plated with 100,000, 200,000 or 500,000 CL4 T-cells per well for 12h and imaged every 2h using a confocal microscope. The mean **a)** SIL density **b)** spheroid death **c)** SIL volume **d)** SIL infiltration depth in spheroids plated with 100,000, 200,000 and 500,000 T-cells per well of spheroids over the imaging period. In **b)** Spheroid dead volume at each timepoint is normalised to the initial dead volume at 2h. Error bars show mean ± SEM and individual points represent the mean for an independent repeat out of 3 independent repeats. n= 3 spheroids per group, per repeat. In all cases, means were compared using Two-Way ANOVA, matched by repeat and timepoint. Non-significant p-values are not shown on graphs with significant p-values. For graphs without significant p-values, ns= non-significant differences across all groups.

3.2.10. T-cells kill RencaHA^{tdT} spheroids from the outside-in

The mean infiltration depth of SILs across all timepoints ranged from 0-10 μ m as shown in Figure 3.10d, suggesting that SILs were only at the edge of the spheroids. Since the SILs would be a heterogeneous population, to further investigate whether any SILs were infiltrating deeply into the spheroid, the distribution of SIL infiltration depths in a spheroid was investigated. It was found that the majority of SILs were at the very surface of the spheroid with a mean of 72% of total SILs at a 0 μ m depth, while some SILs were at a slightly higher infiltration depth of up to 32 μ m from the spheroid surface (Figure 3.11a, b); this was unlikely to mean that CL4 SILs had penetrated between Renca cell layers, since the diameter of a Renca cell which is adhered to a plastic flask is up to ~50 μ m as observed under the light microscope.

By looking at the DRAQ7 and tdTomato fluorescence intensity profiles across spheroids incubated with 200,000 T-cells per well, it was evident that the mean relative DRAQ7 fluorescence intensity was highest at the spheroid edge and decreased towards the spheroid centre when T-cells were present (Figure 3.11c, top panel). This supported the previous observation that DRAQ7 did not stain the dead core of spheroids when T-cells were present (Figure 3.9b), likely due to high consumption of the dye at the spheroid surface which prevented diffusion of DRAQ7 into the spheroid core (previously discussed). As expected, the DRAQ7 fluorescent intensity profile across a spheroid radius differed significantly depending on whether T-cells were absent or present, with the fluorescent intensity increasing and decreasing towards the spheroid centre in the absence and presence of T-cells, respectively. (Figure 3.11c, bottom panel). The tdTomato fluorescent intensity profile was the same with spheroids incubated with or without T-cells (Figure 3.11c, top panel), suggesting that in a timescale of hours tdTomato fluorescence is not lost when RencaHA^{tdT} cells have been killed (Figure 3.3b, bottom panel). This corroborated previous findings that endogenously expressed fluorescent proteins can remain stable to emit signals even once fluorophore-expressing cells have died (402, 403).

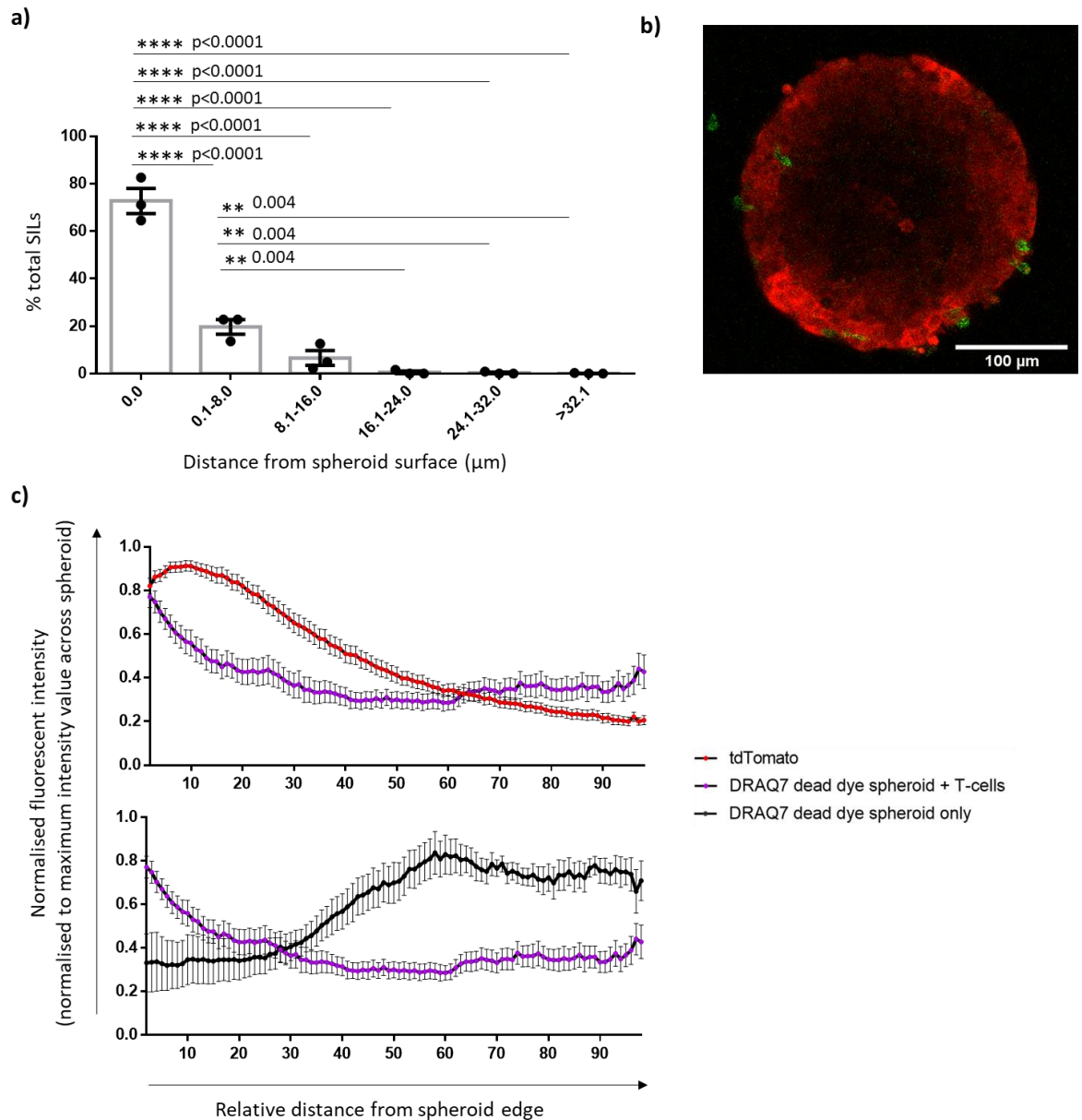


Figure 3.11. CL4 SILs killed RencaHA^{tdT} spheroids outside-in.

Spheroids were plated with 200,000 CL4 T-cells per well and incubated for 12h in the 3D microscopic cytotoxicity assay. **a)** The percentage of total SILs per spheroid at a range of infiltration depths is shown. Error bars show mean \pm SEM. Means were compared using One-Way ANOVA, matched by repeats. Non-significant p-values are not shown. **b)** A representative spheroid mid-section showing tdTomato⁺ spheroid volume (red) and SIL infiltration (green). **c, top panel)** Fluorescent intensity profiles across the spheroid radius of tdTomato (red) and DRAQ7 (purple). **c, bottom panel)** Fluorescent intensity profiles across the spheroid radius of DRAQ7 in the presence (purple) and absence (black) of T-cells. n=6 and 16 spheroids for the group with and without T-cells, respectively from 2-4 independent repeats.

3.2.11. 2 μ M CTV can be used to stain T-cells with limited toxicity

It was then of interest to establish whether our model could be used to study aspects of the antigen-specific rather than non-specific T-cell response, because an antigen-specific response enables ATT therapeutic efficacy in our *in vivo* murine model and is critical for effective anti-tumour immunity. In order to determine if the spheroid death induced by CL4 T-cells required antigen-specificity (in the 3D microscopic cytotoxicity assay), a method was developed for imaging non-HA^{pep}-specific polyclonal CD8 T-cells, CL4 T-cells, spheroids, and spheroid death within the same samples.

First, Cell Trace Violet (CTV) and Carboxyfluorescein succinimidyl ester (CFSE) were titrated as candidate dyes for staining T-cells, using the 2D microscopic cytotoxicity assay as a readout of dye-mediated T-cell suppression. CFSE suppressed T-cell cytotoxicity at increasing concentrations, causing a significant reduction in mean killing rate at a concentration of 1 μ M, compared to DMSO control (Figure 3.12, higher panel). On the other hand, CTV was less cytotoxic and caused significant suppression of T-cell killing at higher dye concentrations than CFSE, of 3 and 5 μ M. The data indicated a slight suppression of T-cells at lower CTV concentrations of 1-2 μ M *versus* the DMSO control, but there was little difference in CTV toxicity between dye concentrations of 1 and 2 μ M (Figure 3.12, lower panel). CTV staining of T-cells enabled quadro-colour imaging alongside GFP, tdTomato (spheroids) and DRAQ7 (dead dye) fluorophores, because it uses the ultraviolet channel. To ensure a strong fluorescent signal during imaging while minimising toxic effects of the dye, a concentration of 2 μ M CTV was used to stain T-cells for subsequent experiments that investigated antigen-specific *versus* non-antigen-specific SIL responses. Nevertheless, since 2 μ M CTV showed a slight suppressive effect on T-cell killing *versus* the DMSO control, both CL4 T-cells and polyclonal CD8 T-cells were stained with CTV in order to minimise differences between these groups. In order to differentiate between CL4 T-cells and polyclonal T-cells, CL4 T-cells but not polyclonal T-cells were retrovirally transduced to express Ftractin-GFP, a small peptide that binds to filamentous actin (F-actin) and can label T-cells green without causing any functional effects. Therefore, CTV⁺ polyclonal and CTV⁺GFP⁺ CL4 T-cells could be differentiated within the 3D microscopic cytotoxicity assay using green fluorescence.

a)

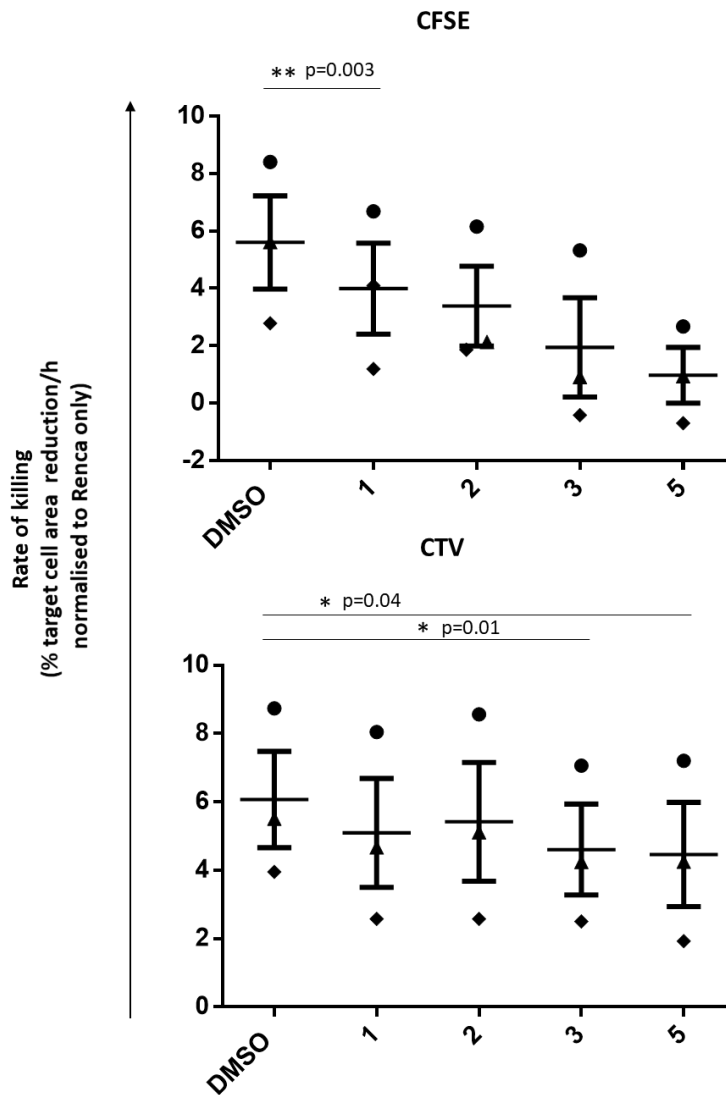


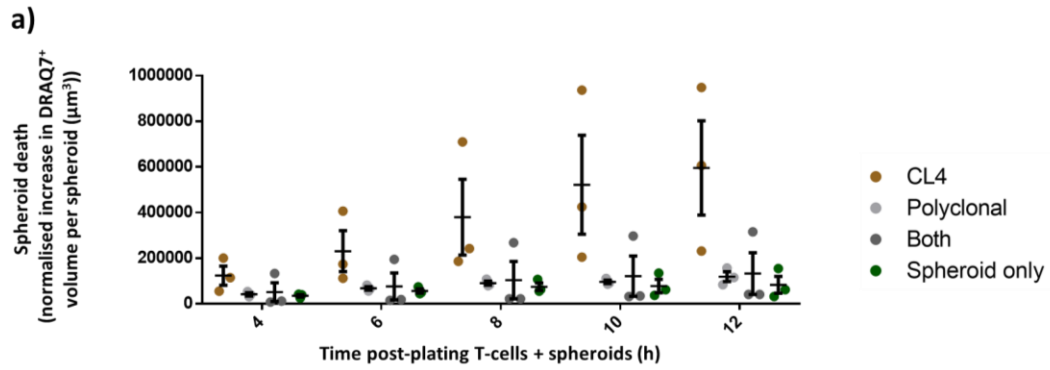
Figure 3.12. Titration of CFSE and CTV for staining T-cells.

The rate of T-cell killing of 2µg/ml HA^{pep}-pulsed RencaHA^{tdT} targets was used to assess the toxicity of dyes CFSE and CTV for staining T-cells, at a range of dye concentrations using the 2D microscopic cytotoxicity assay, imaged using the Incucyte™ Live Cell analysis system. Error bars show mean ± SEM and individual points represent the mean from an independent repeat out of 3 independent repeats. Means were compared to the DMSO control group using One-Way ANOVA with Dunnett's test; within each graph, data points with the same shape represent values taken from the same independent repeat – despite high variability in the cytotoxicity of T-cells between independent repeats, increased dye concentration has a similar effect on the rate of killing within each independent repeat, likely accounting for the statistically significant results calculated. Non-significant p-values are not shown.

3.2.12. HA^{pep}-specific CL4 T-cells but not polyclonal CD8 T-cells significantly kill spheroids

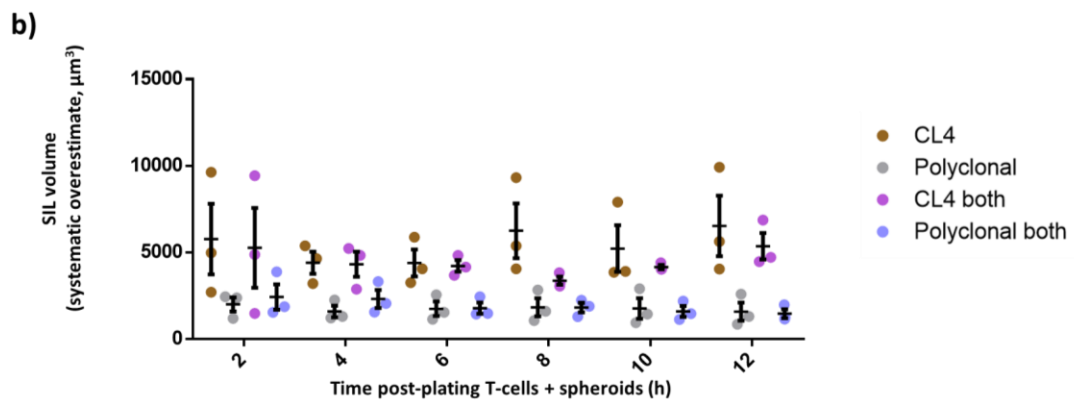
To establish whether the spheroid model could be used to recapitulate the antigen-specific nature of anti-tumour T-cell responses, each well of spheroids was incubated with 200,000 CL4 T-cells, 200,000 polyclonal T-cells, or 200,000 of both CL4 and polyclonal cells (400,000 T-cells total per well). From here on, these groups will be referred to as 'CL4', 'Polyclonal' and 'Both', respectively. The mean DRAQ7⁺ volume per spheroid was significantly higher in the 'CL4' group than all other groups at 8, 10 and 12 hours post-plating T-cells with spheroids (Figure 3.13a, left table). Moreover, there was a significant increase in the DRAQ7⁺ volume per spheroid (compared to the DRAQ7⁺ spheroid volume at 4h) in the 'CL4' group by 8h, while there was no significant increase in the DRAQ7⁺ volume per spheroid in the Polyclonal, 'Both' or 'Spheroid only' groups up to 12 hours post-plating T-cells with spheroids (Figure 3.13a, right table).

It was surprising that the presence of polyclonal T-cells inhibited the cytotoxic function of CL4 SILs in the 'Both' group. Thus, the volume of CL4 and polyclonal T-cells across all groups containing T-cells were compared as an indication of metabolic activity and therefore activation status. As previously mentioned, T-cell volume measurements are systematically overestimated due to limits of the analysis but can give useful information about relative T-cell volumes between groups. Interestingly, CL4 T-cells had a higher volume than polyclonal T-cells in the 'CL4' and 'Both' groups, suggesting that CL4 T-cells had a similarly blasted morphology in these groups, despite having a suppressed cytotoxic function in the presence of polyclonal T-cells (Figure 3.13b). The 'Both' group also differed from the 'CL4' group in that it contained 400,000 T-cells in total per well of spheroids, *versus* 200,000 per well in the 'CL4' group. Previous findings suggested that 500,000 T-cells per well of spheroids limited the cytotoxic function of the CL4 T-cells, potentially due to enhanced metabolic competition. However, according to that previous data, T-cell mediated spheroid death would be limited to a similar level as plating 200,000 T-cells per well (Figure 3.10b). In this data, the reduced rather than equivalent level of T-cell cytotoxicity in the 'Both' group compared to the 'CL4' group suggested that polyclonal T-cells released soluble mediators that actively suppressed CL4 T-cell cytotoxicity and/or polyclonal T-cells sterically hindered CL4 T-cell access to the spheroid surface (Figure 3.13a).



Spheroid death, comparisons between groups	4	6	8	10	12
CL4 vs Polyclonal	ns	ns	0.001 **	<0.0001 ****	<0.0001 ****
CL4 vs Both	ns	ns	0.002 **	<0.0001 ****	<0.0001 ****
CL4 vs Spheroid only	ns	ns	0.0006 ***	<0.0001 ****	<0.0001 ****
Polyclonal vs Both	ns	ns	ns	ns	ns
Polyclonal vs Spheroid only	ns	ns	ns	ns	ns
Both vs Spheroid only	ns	ns	ns	ns	ns

Spheroid death over time, comparisons within each group	6	8	10	12
CL4	ns	0.003 **	<0.0001 ****	<0.0001 ****
Polyclonal	ns	ns	ns	ns
Both	ns	ns	ns	ns
Spheroid only	ns	ns	ns	ns



SIL volume, comparisons between groups	2	4	6	8	10	12
CL4 vs Polyclonal	0.0003 ***	0.008 **	0.01 *	<0.0001 ****	0.0009 ***	<0.0001 ****
CL4 vs CL4 Both	ns	ns	ns	ns	ns	ns
CL4 vs Polyclonal Both	0.001 **	ns	0.02 *	<0.0001 ****	0.0005 ***	<0.0001 ****
Polyclonal vs CL4 Both	0.002 **	0.01 *	0.01 *	ns	0.02 *	0.0003 ***
Polyclonal vs Polyclonal both	ns	ns	ns	ns	ns	ns
CL4 both vs polyclonal both	0.007 **	ns	0.02 *	ns	0.02 *	0.0002 ***

Figure 3.13. CL4 but not polyclonal CD8 SILs killed HA^{pep}-pulsed RencaHA^{tdT} spheroids, polyclonal CD8 T-cells suppressed the cytotoxicity of CL4 T-cells and CL4 T-cells displayed a more blasted morphology than polyclonal T-cells.

a) Spheroid DRAQ7⁺ dead volume over the duration of a 3D microscopy cytotoxicity assay when spheroids were plated with 200,000 CL4 T-cells ('CL4' group), 200,000 polyclonal CD8 T-cells ('Polyclonal' group), 200,000 of each of CL4 and polyclonal ('Both' group) or with no T-cells added

(Spheroid only group). Spheroid DRAQ7⁺ dead volume at each timepoint was normalised to the initial dead volume at 2h. The top panel indicates whether there was significant death over time within each group, means were compared to the mean at 4h within each group, using Two-Way ANOVA and Dunnett's test, matched by repeat and timepoint. The bottom panel indicates any significant differences between groups at each time point, means were compared at each time point using a Two-Way Anova, matched by repeat and timepoint. **b)** SIL volume over time during the 12h imaging period- SIL volume is systematically overestimated due to limits of the analysis but can still show relative differences between groups. For all graphs, error bars show Mean \pm SEM. For all graphs, each point represents the mean for an independent repeat, out of 3 independent repeats. n=2-6 spheroids per group, per repeat. Means were compared at each timepoint using Two-way ANOVA, matched by repeat and timepoint. Non-significant differences are not shown.

3.2.13. CL4 T-cells increase polyclonal SIL density when plated into the same well of spheroids

It was of interest to see if antigen-specificity had any effect on the density of SILs across groups, therefore whether differences in SIL density were contributing to differences in spheroid death. Moreover, it was of interest to see if steric hindrance of CL4 T-cells by polyclonal T-cells could be a mechanism of CL4 T-cell suppression in the 'Both' group. By 6h post-plating T-cells with spheroids, there was a significantly higher mean density of polyclonal SILs in the 'Both' *versus* the 'Polyclonal' group (Figure 3.14a). Meanwhile, the mean density of CL4 SILs was the same in the CL4 and 'Both' groups across all timepoints (Figure 3.14a). This data suggested that the presence of CL4 T-cells in the 'Both' group enhanced the density of polyclonal SILs, but that the density of CL4 SILs was unaffected by the presence of polyclonal cells. Moreover, it suggests that CL4 SILs were not limited by polyclonal T-cells in accessing the spheroid surface. Importantly the data also supports the notion that there was a difference in CL4 SIL cytotoxicity rather than density between the CL4 *versus* Polyclonal and 'Both' groups.

It was hypothesised that the increase in polyclonal SIL density in the 'Both' group could be due to increased motility of polyclonal T-cells. A higher motility of the T-cells could have enabled more frequent random interactions of T-cells with the spheroids and therefore an increased SIL density. A time-interval of 30 minutes was used for image acquisitions over the time-course, which was a short enough time interval to track T-cells (both SILs and T-cells near but not within spheroids) between timepoints, though it did not capture the entire pathlengths, which were later observed to follow a 'zig-zag' type path using an image acquisition interval of 5 minutes (data not shown). Nevertheless, it was clear that T-cells embedded within Matrigel often did not migrate very far; T-cells migrating towards and attaching to spheroids over the assay were often very close (<50 μm) to spheroids at the start of imaging. Regardless of this limitation, using this T-cell tracking method, it was found that polyclonal T-cells had a longer mean pathlength than CL4 T-cells but that the mean pathlength of polyclonal T-cells in the 'Both' group did not differ from the mean pathlength of polyclonal T-cells in the 'Polyclonal' group (Figure 3.14b). Therefore, CL4 T-cells were less motile than polyclonal T-cells, while the difference in polyclonal SIL density in the 'Both' *versus* 'Polyclonal' group was unlikely to result from increased motility.

To rule out whether differences between the groups could be due to differences in spheroid dimensions spheroid volume and sphericity (spheroid shapes relative to a sphere) between groups was compared. Mean spheroid volume did not significantly differ between groups (Figure 3.15a), and neither did mean spheroid sphericity (Figure 3.15b). This supports the idea that differences between groups are due to the antigen-specificity of the T-cells and not a result of variations in spheroid dimensions between groups.

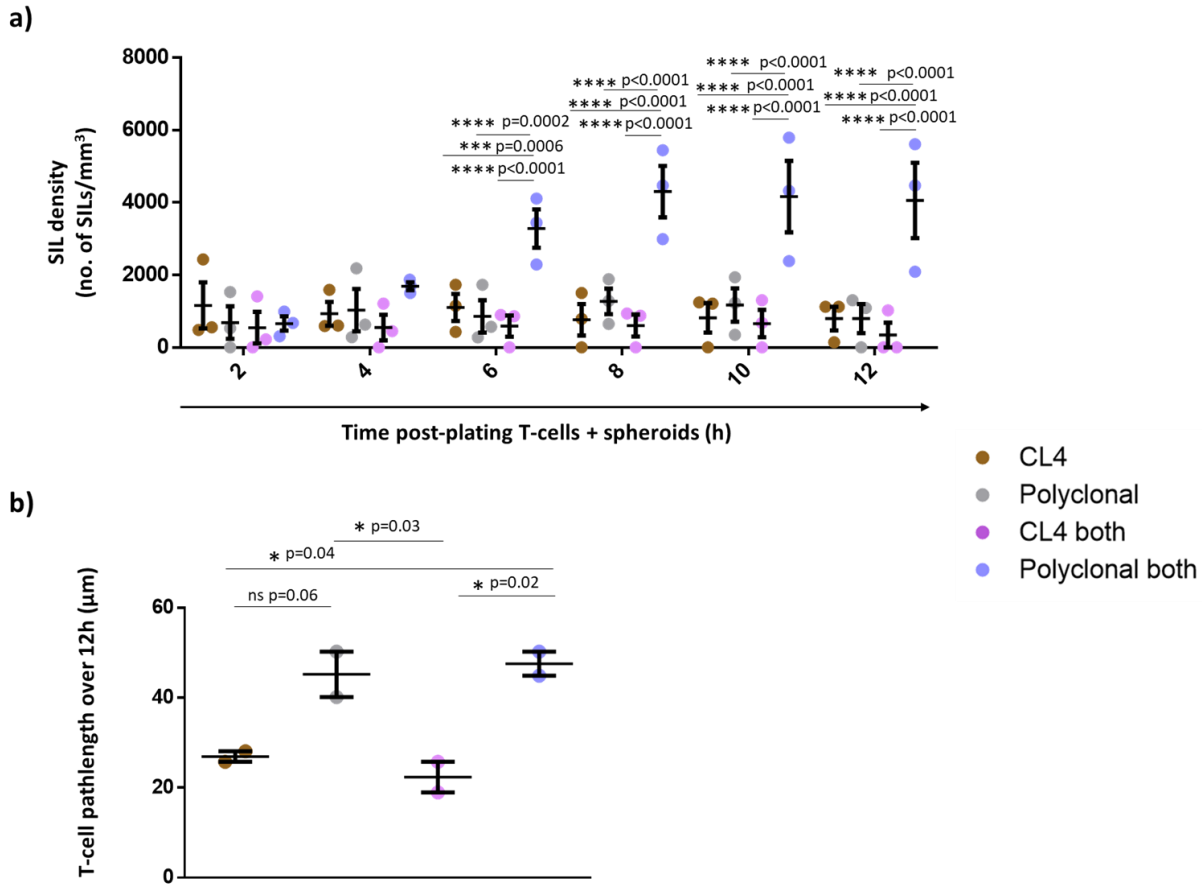


Figure 3.14. The presence of CL4 T-cells increased polyclonal CD8 SIL density, while polyclonal CD8 cells displayed higher motility versus CL4 T-cells.

a) SIL density over the course of a 3D microscopic cytotoxicity assay is shown for polyclonal and CL4 T-cells in the CL4, Polyclonal and ‘Both’ groups. CL4 both = CL4 SILs within the ‘Both’ group. Polyclonal both = polyclonal SILs within the ‘Both’ group. Means were compared using a Two-Way ANOVA, matched by repeat and timepoint. Data are from 3 independent repeats. Non-significant differences are not shown. **b)** T-cell pathlengths were estimated by tracking individual T-cells across timepoints (30-minute time intervals) using the Hungarian algorithm with a maximum linking distance of 50 µm. Each point represents the mean for an individual repeat out of two total independent repeats. n=2-6 spheroids per group, per repeat. ns=non-significant difference. For all graphs error bars show Mean ± SEM.

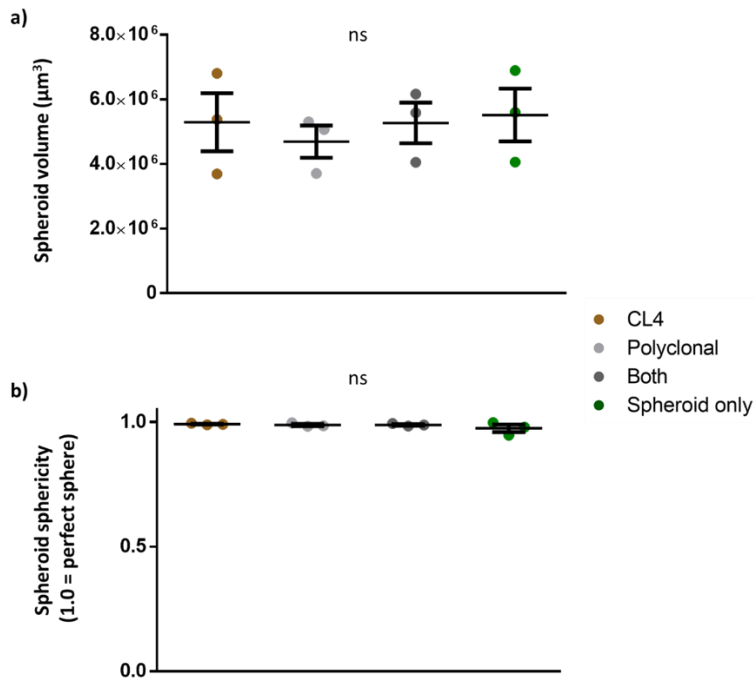


Figure 3.15. Spheroid volume and shape were homogeneous between CL4, polyclonal, both CL4 + polyclonal and spheroid only groups.

a) Spheroid volume across CL4, Polyclonal, 'Both' and Spheroid only groups at 2h post-plating for the 3D microscopic cytotoxicity assay. **b)** Spheroid sphericity (how well spheroid shapes fit a perfect sphere) across groups at 2h post-plating; a value of 1.0 indicates a perfect sphere. Error bars show Mean ± SEM. Each individual point represents a mean of 3 independent repeats. n=2-6 spheroids per group, per repeat. Means were compared using a One-Way ANOVA, matched by repeat. For all graphs, ns= non-significant p-values across all comparisons.

3.2.14. RencaWT^{tdT} and RencaHA^{tdT} spheroids are differentially infiltrated by CL4 T-cells

Another way to investigate the effect of antigen-specificity on T-cell interactions with Renca spheroids was to carry out a 3D imaging cytotoxicity assay using CL4 T-cells incubated with spheroids in the absence or presence of cognate antigen expression, therefore spheroids grown from RencaWT^{tdT} and RencaHA^{tdT} cells were used to achieve these groups. Pulsing spheroids with 2µg/ml HA^{pep} loaded HA^{pep} onto the surface of RencaWT^{tdT} spheroids (pulsed RencaWT^{tdT} spheroids), or increased the level of HA^{pep} on the surface of RencaHA^{tdT} spheroids (pulsed RencaHA^{tdT} spheroids). For this experiment, images were taken at the endpoint of 12h post-plating of T-cells with spheroids using a 2-photon-microscope. Unfortunately, DRAQ7 was not included in these experiments, therefore spheroid death was not measured.

As before, the SIL infiltration depths were not biologically meaningful as the SILs did not infiltrate beyond spheroid surfaces (Figure 3.16b). There was a slight increase in mean SIL density, volume, and elongation (as measured by the length of the longitudinal axis of a SIL) in the pulsed RencaWT^{tdT} spheroids *versus* the unpulsed RencaWT^{tdT} spheroids (Figure 3.16a-d, leftmost graphs). (The SIL longitudinal axis is the longest axis of the SIL and is an indicator of how elongated the SIL is- a more elongated morphology has been associated with increased cell motility.) These infiltration data suggested that antigen specificity slightly increased the SIL density and blasting of T-cells, corroborating the notion that antigen specificity enhanced T-cell activation in this model (Figure 3.13b). Meanwhile, there were no significant differences in SIL density, depth, volume or elongation between the pulsed and unpulsed RencaHA^{tdT} spheroids, suggesting that the level of HA^{pep} endogenously expressed by RencaHA spheroids is not sufficiently different to the HA^{pep} level expressed by pulsed RencaHA spheroids to impact on these parameters of SIL infiltration.

Irrespective of peptide pulsing, there were general differences between SILs in RencaWT^{tdT} and RencaHA^{tdT} spheroids. Interestingly, the RencaHA^{tdT} spheroids displayed an enhanced SIL density compared to the RencaWT^{tdT} spheroids, with a significant increase in mean SIL density between the unpulsed RencaHA^{tdT} and unpulsed RencaWT^{tdT} spheroids (Figure 3.16a). There was also an increase in mean SIL volume in the RencaHA^{tdT} spheroids *versus* the RencaWT^{tdT} spheroids, with a significantly increased mean SIL volume in the unpulsed RencaHA^{tdT} spheroids compared to the pulsed RencaWT^{tdT} spheroids (Figure 3.16c). Moreover, there was a slightly increased mean length of SILs in the RencaHA^{tdT} *versus* RencaWT^{tdT} spheroids, with a significant increase in mean SIL length in the unpulsed RencaHA^{tdT} spheroids *versus* the unpulsed RencaWT^{tdT} spheroids (Figure 3.16d). In summary, this data suggests that CL4 T-cells differentially infiltrate RencaHA^{tdT} spheroids compared to RencaWT^{tdT} spheroids. As pulsing RencaHA^{tdT} or RencaWT^{tdT} spheroids should saturate cell surface H-2K^d molecules, factors other than HA^{pep} peptide expression levels are likely to regulate the differences seen herein, in corroboration with earlier data that indicated there were non-HA^{pep} differences between the RencaHA^{tdT} and RencaWT^{mCh} cell lines. For example, differential expression by Renca of ICAM-1 or ligands for other costimulatory or coinhibitory receptors, could account for the differences in T-cell infiltration of these two cell lines, as previously discussed (Section 1.2.4).

To rule out whether differences between the spheroid groups could be due to differences in spheroid dimensions, spheroid volume and sphericity was compared between groups. Mean spheroid volume did not significantly differ between groups (Figure 3.17a), and neither did mean spheroid 'sphericity', which as previously mentioned, is a measure of spheroid shape- how closely

spheroids match the shape of a perfect sphere (Figure 3.17b). Therefore, spheroid dimensions were not accountable for the differences in SIL infiltration observed.

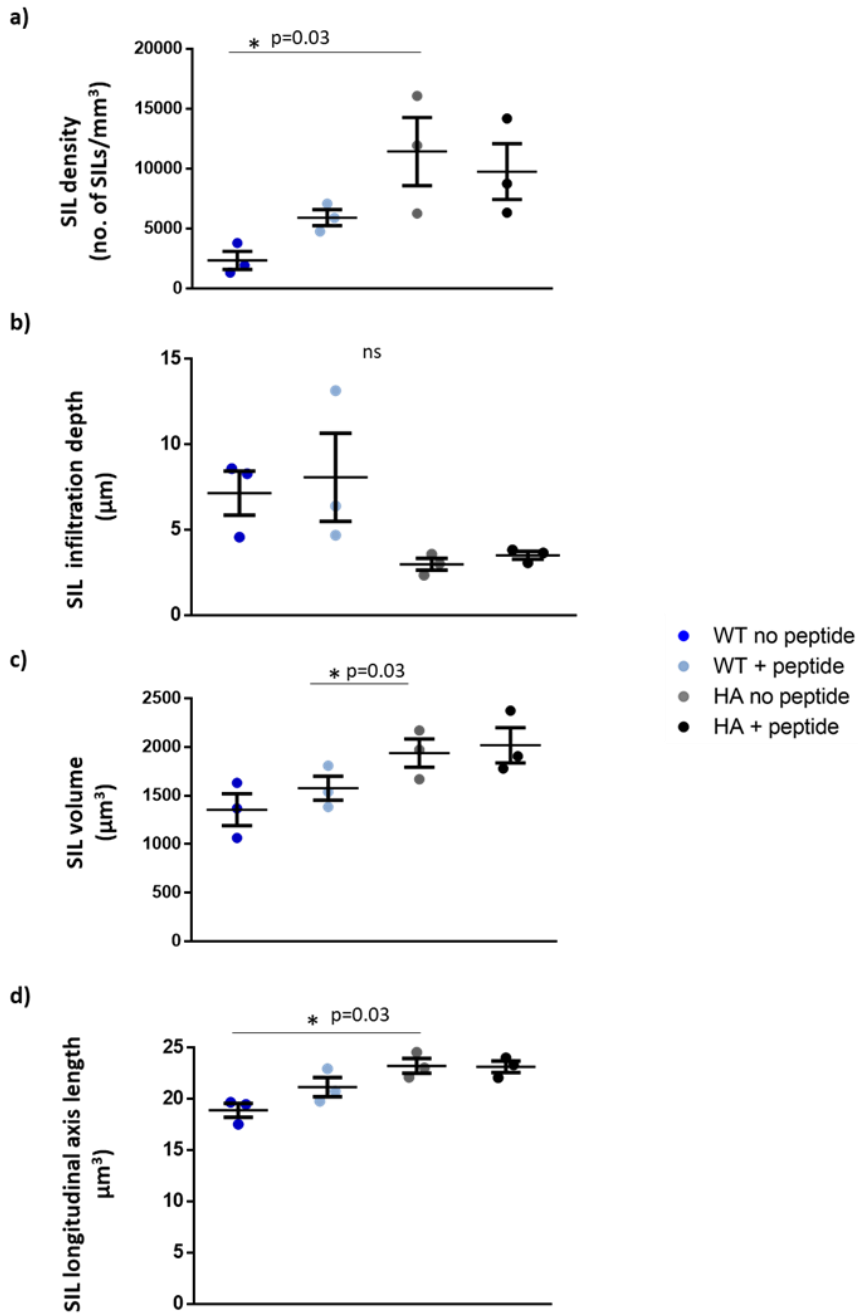


Figure 3.16. CL4 SILs differentially infiltrated RencaWT^{tdT} and RencaHA^{tdT} spheroids by 12h post plating T-cells + spheroids.

RencaWT^{tdT} and RencaHA^{tdT} spheroids were either HA^{pep} pulsed (+ peptide) or unpulsed (no peptide) and incubated with CL4 T-cells. Images were acquired at 12h post-plating using a 2-photon microscope. **a)** SIL density **b)** SIL infiltration depth **c)** SIL volume **d)** SIL length is shown between all groups. For all graphs error bars show mean ± SEM. Means were compared using One-Way ANOVA, with matched repeats. Each point represents a mean value from one independent repeat out of 3 independent repeats. n=8-12 spheroids per group per repeat. Non-significant p-values are not shown in graphs with significant p-values, in **b)** ns indicates non-significant p-values across all comparisons.

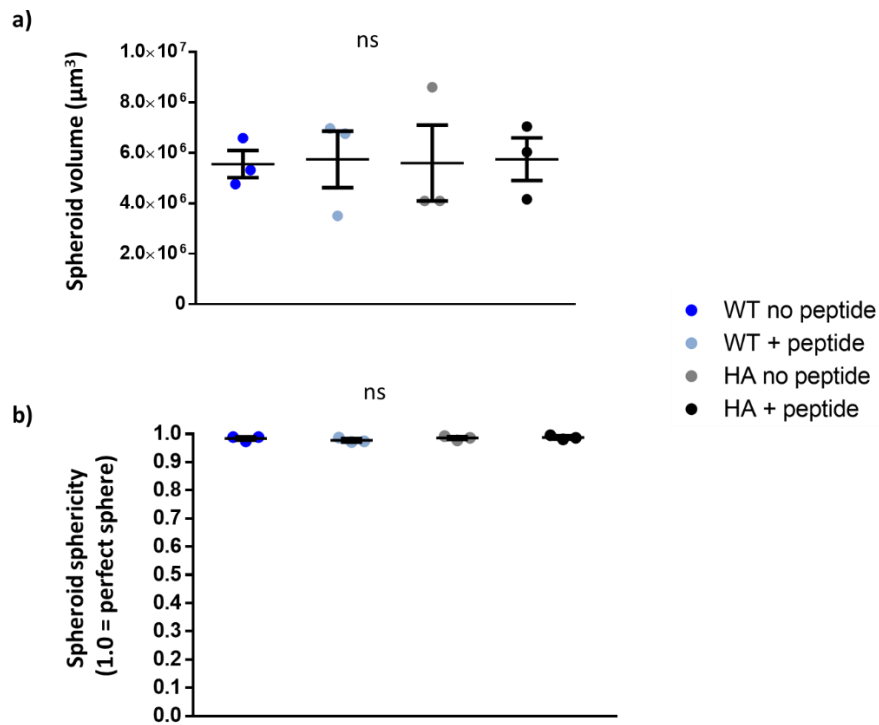


Figure 3.17. Spheroid volume and shape was homogenous between RencaWT^{tdT} and RencaHA^{tdT} spheroids that were used to assess the role of antigen specificity.

RencaWT^{tdT} and RencaHA^{tdT} spheroids were either HA^{pep} pulsed (+ peptide) or unpulsed (no peptide) and incubated with CL4 T-cells. Images were acquired at 2h post-plating using a 2-photon microscope. **a)** Spheroid volume across spheroid groups **b)** Spheroid sphericity (how well spheroid shapes fit a perfect sphere) across spheroid groups at 2h post-plating; a value of 1.0 indicates a perfect sphere. Error bars show Mean ± SEM. Each individual point represents a mean out of 3 independent repeats. Means were compared using a One-Way ANOVA, matched by repeat. n=8-12 spheroids per group, per repeat. For all graphs, ns= non-significant p-values across all comparisons.

3.3 Discussion

Cancer cell culture in a 3D *versus* 2D environment provides an increased physiological relevance to *in vivo* tumours. Gradients of oxygen, nutrients, pH and proliferation are absent in 2D culture, but are typically recapitulated in spheroids (343-345, 348, 392, 404-406). The decreased immunogenicity of tumour spheroids compared to monolayer cancer cells (370, 372, 375, 407-409), and the higher similarity of gene expression profiles between spheroids and tumour xenografts *versus* monolayers have proven spheroids to be a useful intermediate model between 2D and *in vivo* cancer models (359, 365, 366, 368). Our lab has previously utilised an *in vitro* 2D Renca model to study mechanisms of immunosuppression within Renca tumours *in vivo*. The development of a 3D Renca spheroid model can provide an additional *in vitro* tool to investigate the tumour specific CD8 T-cell response, which carries benefits *versus* both Renca monolayer and *in vivo* models.

3.3.1. Generation of a RencaHA^{tdT} cell line enabled growth of Renca tumour spheroids that were amenable to 3D imaging, using Matrigel as a scaffold

In this Chapter, an *in vitro* tumour spheroid model of Renca tumours was developed using the natural hydrogel Matrigel, which acted as an ECM-based scaffold to support spheroid growth. The RencaHA^{tdT} and RencaWT^{tdT} lines produced herein expressed the red fluorophore tdTomato (^{tdT}), making them well-suited for imaging of Renca spheroids in 3D using confocal microscopy. Additionally, the RencaHA^{tdT} cell line is suitable for future investigation of *in vivo* RencaHA^{tdT} tumours via 2-photon-imaging, as freshly harvested *ex vivo* RencaHA^{tdT} tumours could be imaged to visualise Renca cells and GFP⁺ infiltrating CL4 T-cells at the tumour periphery (data not shown). Different cancer cell lines show a range of amenability to culture as multicellular tumour spheroids (MCTS), and it was not known which MCTS culture method would best enable 3D culture of Renca cells (364, 390). Previously in our lab, culture of Renca cells in non-adherent conditions, which forces cell aggregation, has been attempted to form Renca spheroids. These methods formed rugged, irregular cell aggregates that did not resemble the highly compact smooth-surfaced structure of *in vivo* Renca tumours (data not shown). In contrast, seeding and proliferation of single RencaHA^{tdT} cells into Matrigel produced compact, smooth-surfaced spheroids with high sphericity. Although this latter method resulted in a single clone becoming one spheroid, imaging of several spheroids over several repeats includes a range of clones that will be represented within each group. Furthermore, it is not known which clones of the *in vitro* RencaHA population contribute most to the formation of tumours *in vivo*, so the question of how accurately RencaHA^{tdT} spheroids represented the genetic heterogeneity of *in vivo* RencaHA tumours can only be answered with further transcriptomic sequencing and proteomic data. Despite this caveat, the embedment of single RencaHA^{tdT} cells into Matrigel enabled us to easily gain a third dimension within our *in vitro*

Renca model, a feature which has proven to be incredibly important for improving the translatability of *in vitro* results to *in vivo* systems (370, 371, 407).

RencaHA^{tdT} spheroids grew in three phases, firstly, an exponential phase, secondly, a phase of slower growth, and thirdly, a plateau phase. The kinetics of RencaHA^{tdT} spheroid growth matched that of many tumour spheroid models and seemed to fit the shape of a Gompertzian curve which has been widely used as a basis to model the growth of both MCTS and *in vivo* tumours (351, 396, 405). The maximum spheroid diameter of ~300 µm observed was on the lower end of maximum spheroid sizes, with many MCTS reaching >500 µm in diameter (410). The size-limit of RencaHA^{tdT} spheroids was likely regulated by several factors including the number of spheroids grown per unit of medium, a stationary set up with manual exchange *versus* a constant flow of culture medium and cell-line intrinsic proliferation rates. Therefore, alternative culture methods would likely alter the maximum spheroid size attained by RencaHA^{tdT} spheroids.

3.3.2. RencaHA^{tdT} spheroids display a central dead core surrounded by a viable rim of cells

It is widely described that the central core of MCTS becomes necrotic in a size-dependent manner, and the increased similarity of MCTS to *in vivo* tumours has been partially attributed to the central necrosis (344, 345, 348, 349, 351, 405, 406). Although the type of cell death was not elucidated, in order to investigate if there was a dead core at the centre of RencaHA^{tdT} spheroids, viability dyes were used. Calcein Violet-AM was used to label live cells, and DRAQ7- a photostable dye which does not affect cancer cell viability or proliferation in long term assays- was used to label dead cells (411). 10-day-old Renca tumour spheroids, which were used in subsequent functional assays, had a viable rim of cells with a dead centre. Although Calcein AM dyes have been commonly used to stain MCTS, it cannot be ruled out that the distribution of Calcein Violet-AM fluorescent intensity was due to diffusion limits of the dye rather than decreasing viability towards the spheroid centre (392). The DRAQ7 fluorescent intensity profile gave a more convincing picture of viability distribution across the spheroid because there was a low fluorescent intensity at the spheroid edge which increased towards the spheroid centre, suggesting that diffusion limits did not prevent the ability of DRAQ7 to penetrate spheroids (in the absence of T-cells). In summary, RencaHA^{tdT} spheroids had a central dead core, surrounded by a viable rim of cells which makes up ~33-50% of the spheroid diameter. This aligns with reported distributions of viability within spheroids, where the viable rim has been reported to make up ~30-60% of the spheroid diameter (344, 351).

3.3.3. 10-day-old RencaHA^{tdT} spheroids do not display hypoxia

Hypoxia has been the most common explanation for the development of central necrosis in MCTS, due to limited diffusion of oxygen to cells furthest from the cell medium (344, 352, 355). 10-day old spheroids did not display hypoxia and therefore it was unlikely that oxygen-deprivation was the reason for the dead core *per se*. However, it is possible that the entire hypoxic regions of the

spheroids had undergone necrosis, in which case the Hypoxyprobe reagent would not be metabolised by dead cells as has been previously described (412, 413). In the case of RencaHA^{tdT} spheroids however, this is unlikely, as in spheroids with central necrosis resulting from hypoxia, there is usually a hypoxic region around the hollow core (412, 414). On the other hand, lower central glucose concentrations as spheroids increase in size could be an important factor in the development of RencaHA^{tdT} dead cores. Cancer cells are known to be highly glycolytic, often shifting their metabolism to produce ATP via glycolysis rather than the more efficient process of oxidative phosphorylation, even in the presence of oxygen (415). This enables cancer cells to divert molecules down the pentose-phosphate pathway for synthesis of nucleotides and lipids, thus providing the building blocks for rapid cell proliferation (415). Accordingly, low glucose concentrations at the centre of spheroids are an important determinant of central necrosis in MCTS (343, 344, 347, 348, 406). Transfer of spheroids into glucose-deficient medium has been shown to reduce the time before onset of central necrosis, while growth of spheroids in medium with low glucose concentrations has been shown to induce formation of necrotic cores, while high-glucose concentrations did not (348, 406). Thus, though it was not assessed herein, glucose deprivation could have contributed to the dead core of RencaHA^{tdT} spheroids. In fact, it has been shown that spheroids grown under low oxygen concentrations are more sensitive to a decrease in glucose concentrations and vice versa, suggesting that multiple factors interact dynamically to regulate the size of the necrotic core (344). Lastly, it is likely that other factors such as availability of amino acids, pH and toxic products released from central necrosis were also factors which contributed to spheroid death (351).

3.3.4. The time of onset of CL4 T-cell killing is faster in the presence of 2µg/ml HA^{pep}-pulsed *versus* unpulsed RencaHA^{tdT} cells, but HA^{pep}-pulsing does not change the rate of killing

In order to optimise the practicality of 2D and 3D microscopic cytotoxicity assays, we hypothesised that peptide pulsing RencaHA^{tdT} targets would decrease the time before the onset of T-cell-dependent killing, enabling shorter imaging periods. Therefore, we assessed the effect of HA^{pep}-pulsing on the time before target cell death onset and the rate of killing by CL4 T-cells, using the 2D microscopic cytotoxicity assay. Firstly, we confirmed that cognate antigen was required for CL4 T-cell killing of monolayer Renca target cells in the 2D microscopic cytotoxicity assay. Secondly, the time period before the onset of target cell area decrease was significantly longer when T-cells were plated with unpulsed *versus* pulsed RencaHA^{tdT} targets; the rate of killing in the 6h time period after killing initiated, however, did not differ between pulsed and unpulsed targets. As a result, we decided to pulse targets with 2 µg/ml HA^{pep} in future cytotoxicity assays (except where noted), reducing the time and cost of imaging.

The delayed killing of unpulsed *versus* pulsed targets has a few possible explanations. CD8 T-cells are long-known to be serial killers, with the ability to transiently engage their TCR with peptide-MHC (pMHC) on a given target cell, before disengaging and binding to a new pMHC (416). Moreover, it has been shown that antigen-dose sensing in lymph nodes by the TCR can shorten the time taken for naïve T-cells to activate when more antigen is available (417). Furthermore, higher pMHC level on target cells has been found to increase the probability of a TCR ligating a new pMHC in a manner likely dependent upon positive TCR-signalling feedback mechanisms (418). Accordingly, in the context of serial triggering, the same total strength of T-cell stimulation would take longer to occur when CL4 T-cells encountered a weaker peptide stimulus. Upon reaching a threshold level of activation, the T-cells could then kill unpulsed and pulsed targets at comparable rates, as observed. Our lab has observed that CL4 T-cells binding to unpulsed *versus* pulsed Renca cells displayed a reduced calcium flux, supporting the idea that a longer period of serial triggering is necessary to activate T-cell killing of unpulsed *versus* pulsed targets (data not shown). Furthermore, confirming the enhanced activation of CL4 T-cells during coincubation with peptide-pulsed *versus* unpulsed RencaHA^{tdT} targets, the level of IFN γ secreted by CL4 T-cells in the presence of pulsed *versus* unpulsed RencaHA^{tdT} cells was significantly higher. Nevertheless, other explanations for the delayed onset of T-cell killing under lower peptide stimulus conditions include: T-cells binding to targets that expressed less cognate antigen delivered weaker or a reduced frequency of lytic hits (granules containing less cytotoxic molecules or less frequent degranulation events, respectively); T-cells binding unpulsed *versus* pulsed targets may have been less motile thus moving more slowly between target cells and taking longer to deliver sufficient Fas-FasL or granule-mediated cytotoxic signals per target cell, delaying induction of apoptosis.

3.3.5. An image analysis macro was developed to quantify spatiotemporal parameters of CL4 T-cell: spheroid interactions and 200,000 CL4 T-cells per well of spheroids provided a suitable effector: target ratio for 3D microscopic cytotoxicity assays.

An image analysis 'Cancer segmentation' macro was developed that enabled quantitation of the following spatiotemporal parameters in data from 3D microscopic cytotoxicity assays: T-cell number, T-cell volume, spheroid total volume (included the hollow core), spheroid tdTomato⁺ volume (excluded the hollow core), spheroid sphericity (how closely the spheroid shapes matched a perfect sphere), SIL infiltration depth (the minimal distance between a SIL's edge and the outer surface of a spheroid) and the pathlength of T-cell tracks over time. Using this macro, we determined the optimal T-cell: spheroid ratio for execution of 3D microscopic cytotoxicity assays. We found that increasing the number of CL4 T-cells per well of spheroids increased SIL densities but did not have a significant impact on spheroid death (though spheroid death did non-significantly increase when plating 200,000 *versus* 100,000 T-cells per well). The data suggested that metabolic competition between cells may have been higher in the 500,000 (highest) T-cell group, as spheroid

death did not increase compared to plating 200,000 T-cells, despite a higher SIL density (previously discussed). Importantly, due to image segmentation limitations when plating 500,000 T-cells per well, 200,000 T-cells per well were used for future 3D cytotoxicity imaging assays; plating 200,000 T-cells also provided enhanced SIL densities and spheroid death compared to 100,000 CL4 T-cells per well.

3.3.6. SILs did not penetrate deeply into RencaHA^{tdT} spheroids, but killed at the spheroid surface

As expected, the majority of SILs were found at the surface of the spheroids and were unlikely to be migrating through Renca cell layers; this poor, slow infiltration of spheroids by immune competent cells has been commonly observed in melanoma MCTS and metastases (375, 419). Furthermore, the DRAQ7 fluorescent intensity profile showed high DRAQ7⁺ staining at the edge of spheroids where the T-cells were located and a reduced intensity towards the centre of the spheroid, indicating T-cell-dependent killing and demonstrating that DRAQ7 did not stain the dead core of spheroids in the presence of T-cells. Relevant to this, in an *in vivo* model of ATT similar to the system used by our lab, intravital imaging revealed that tumour-specific CTLs (cytotoxic T-lymphocytes) killed subcutaneous tumours from the periphery towards the centre in the first 'early phase', 3-4 days post-ATT, but that in a later phase at 5-6 days post-ATT the CTLs had distributed evenly throughout the tumour (420). Thus, the Renca spheroid model may recapitulate the 'early phase' of RencaHA subcutaneous tumour infiltration by CL4 T-cells and the outside-in dynamic of subcutaneous tumour death caused by tumour-specific T-cells *in vivo*.

3.3.7. T-cell killing of RencaHA^{tdT} spheroids during 3D microscopic cytotoxicity assays is dependent on the presence of cognate antigen

Having determined that CL4 T-cells caused spheroid death to occur in an outside-in manner, we used a 3D microscopic cytotoxicity assay to confirm that spheroid death resulted from an antigen-specific T-cell response. For the 3D microscopic cytotoxicity assay, four groups were included within the experiment: 'Polyclonal', 'CL4', 'Both' and 'Spheroid only'. The 'Polyclonal' and 'CL4' groups each contained 200,000 T-cells (of the respective T-cell types) per well of spheroids, while the 'Both' group contained 200,000 of both T-cell types within the same well so that differences between T-cell types could be detected within the same spheroids. Spheroid death was significantly higher within the 'CL4' group compared to all other groups at later timepoints. Moreover, spheroid death increased significantly in the 'CL4' group, while significant spheroid death did not develop in the 'Polyclonal', 'Both' or 'Spheroid only' groups over the entire imaging period. These findings corroborated existing *in vivo* data which has shown that antigen specificity is important for tumour-killing by T-cells; a study using chimeric tumours made of both EG7 and EG4 tumour cells which did and did not express the cognate antigen for OVA-specific OT-I CD8 T-cells, respectively, has shown that OT-I T-cell transfer leads to clearance of EG7 but not EG4 tumour regions (421). The results of

that study also suggested that the T-cell-mediated tumour death following adoptive transfer was largely contact-dependent and not due to a non-specific innate response or bystander effects (421). In further support of our findings, and the requirement for tumour-specificity during tumour-killing by CD8 T-cells, another study that utilised the EG7/EG4 model with OT-I T-cells showed that the density of OTI tumour-infiltrating lymphocytes (TILs) was similar in both EG4 and EG7 tumours which were grown on opposite flanks of the same mouse, but that there was regression and apoptosis in the EG7 tumours only (422). Intriguingly, the 'Both' group did not display spheroid death despite there being 200,000 CL4 T-cells per well, suggesting that 'Polyclonal' T-cells suppressed the cytotoxic potential of CL4 T-cells. Previous data indicated that plating 500,000 T-cells per well caused suppression of T-cells, possibly via increased metabolic competition due to higher T-cell numbers (previously discussed). However, in that experiment, spheroid death was not lower but similar in the 500,000 T-cell group *versus* the 200,000 T-cell group, suggesting that polyclonal T-cells were actively suppressing CL4 T-cells either by steric hindrance at the spheroid surface and/or by releasing suppressive soluble mediators. Larger T-cell volume has been linked to a heightened T-cell activation status, while more suppressed T-cells have smaller cell sizes (423). Therefore, to determine if CL4 T-cells were suppressed by polyclonal T-cells, we assessed T-cell volumes. Interestingly, the volume of CL4 T-cells in the 'CL4' and 'Both' groups were higher than the volumes of polyclonal T-cells in the 'Polyclonal' and 'Both' groups, suggesting that the CL4 T-cells were more metabolically active than the polyclonal T-cells regardless of the presence of polyclonal T-cells. These findings align with a study which showed that OT-I TILs extracted from cognate-antigen-expressing EG7 tumours were larger than OT-I TILs from EG4 tumours that do not express the cognate OVA-antigen (422). Therefore, the Renca spheroid model both recapitulated antigen-specific killing by tumour-specific CTLs and the effects of tumour-derived cognate antigen on T-cell size. Thus, if the polyclonal T-cells suppressed the cytotoxic potential of CL4 T-cells via a suppressive soluble mediator, this was not evident via a decrease in CL4 T-cell volumes.

We hypothesised that steric hindrance of CL4 T-cells by polyclonal T-cells could be responsible for the reduced cytotoxicity of CL4 T-cells in the presence of polyclonal T-cells, therefore, densities across all groups were compared. Interestingly, the SIL density of polyclonal T-cells was higher in the 'Both' group *versus* all other groups, while the CL4 SIL density across all groups did not differ. Firstly, this data suggested that polyclonal T-cells were unlikely to have suppressed CL4 T-cells via steric hindrance. Instead, polyclonal T-cells may have released suppressive soluble mediators, such as adenosine or IL-10, to suppress CL4 cytotoxicity, however, due to time constraints, this was not investigated. Secondly, these findings are at odds with *in vivo* data which has shown that the presence of tumour-expressed cognate antigen increases antigen-specific TIL densities. A longer cocubation of T-cells with spheroids may be required in order to see a similar dynamic to *in vivo*, as an increased cognate-antigen-dependent *versus* non-specific accumulation of transferred TILs

has been found to require a timescale of days (420). The increased polyclonal SIL density in the 'Both' group could be explained by an increase in the polyclonal T-cell motility within the 'Both' group compared to all other groups; in this case, increased motility of polyclonal T-cells may have increased the frequency of T-cells adhering to spheroids and therefore the SIL density. However, polyclonal T-cells had significantly longer estimated pathlengths than CL4 T-cells, regardless of CL4 T-cells being in the same wells, suggesting that the presence of CL4 T-cells within the same wells did not alter polyclonal T-cell motility. Additionally, this finding suggested that recognition of cognate antigen reduced CL4 T-cell motility. This corroborates an intravital imaging study, wherein the velocities of adoptively transferred TILs were found to be around half in tumours that expressed *versus* lacked cognate antigen during an early phase of 3-4 days post-ATT (420). Notably, this data highlighted that T-cells which eventually bound to spheroids were often located very close (<50 μm) to the spheroids at the start of the 3D microscopic cytotoxicity assay. Therefore, T-cell motility was greatly limited by the Matrigel they were embedded in, making the model unsuitable for studying physiologically relevant T-cell migration, which is a caveat of this system. Nevertheless, our SIL density data indicated that CL4 T-cells may have secreted a factor which enhanced the homing or adherence of polyclonal T-cells to spheroids. Supporting this notion, an *in vivo* study demonstrated that the presence of tumour-specific TILs enhanced the infiltration of polyclonal TILs towards the tumour centre; without the tumour-specific TILs, polyclonal TILs remained at the tumour periphery (420). Due to time restraints, we were unable to elucidate the possible CL4 T-cell-derived factor responsible.

Overall, our findings demonstrated that the 3D microscopic cytotoxicity assay was suitable for studying the tumour-specific CL4 T-cell response to RencaHA^{tdT} spheroids, which could enable subsequent investigation into mechanisms of tumour immunosuppression.

Additionally, we used another approach to determine how cognate antigen affected CL4 T-cell interactions with Renca spheroids; we investigated CL4 T-cell interactions with RencaHA^{tdT} and RencaWT^{tdT} spheroids, which do and do not express endogenous cognate antigen, respectively. Moreover, we utilised exogenous HA^{pep}-pulsing to provide an additional increase in HA^{pep} expression levels on these cell lines. Unfortunately, DRAQ7 dye was not included in these experiments, therefore we only measured parameters of infiltration. Although non-significant, the pulsed *versus* unpulsed RencaWT^{tdT} spheroids showed an increase in SIL density, SIL volume and SIL length. This increased recruitment and blasting of SILs indicated that antigen specificity increased the activation of T-cells, corroborating previous findings using CL4 and polyclonal T-cells against pulsed RencaHA^{tdT} targets (previously discussed). Moreover, pulsed *versus* unpulsed RencaHA^{tdT} spheroids showed no difference in SIL density, SIL volume or SIL length, which indicated that any differences in the HA^{pep} expression level on these spheroids did not alter these parameters of SIL

activation or infiltration dynamics. These experiments supported evidence that there were HA^{pep}-independent differences between the RencaWT and RencaHA lines within the 3D model, as previous data (from the 2D microscopic cytotoxicity assay) had suggested (Section 1.2.4). It was found that between RencaHA^{tdT} and RencaWT^{tdT} spheroids, there were non-significant but consistent differences in SIL density, SIL volume and SIL length even when both lines were maximally peptide loaded, supporting the notion that these cell lines differ beyond HA^{pep} expression levels. This was not further investigated but is important to note for future work, and in the interpretation of previous findings using this model, which used peptide-loaded RencaWT monolayers to model *in vivo* Renca tumours.

3.3.8. Conclusion

In conclusion, the 'RencaHA^{tdT} MCTS + CL4 T-cell' model, in combination with the 3D microscopic cytotoxicity assay and image analysis approach developed herein, enabled spatiotemporal parameters of the tumour-specific CD8 T-cell response to be quantified. This tool is used in later chapters to investigate the mechanisms by which the receptors TIM3 and CEACAM1 may directly suppress tumour-specific CD8 T-cells, with the larger purpose of identifying ways to improve the efficacy of anti-tumour CD8 T-cell responses and the therapeutic potential of ATT against solid cancers.

Chapter 4 Divergent TIM3 signalling in the 2D and 3D

RencaHA/CL4 models

4.1 Introduction

Whether TIM3 has stimulatory and/or inhibitory effects in T-cells has been debated, although the balance sits in favour of an inhibitory role (216, 424-427). TIM3 is highly conserved between mice and humans, with six tyrosine residues in its cytoplasmic tail, one of which is proximal to the transmembrane domain and five more C-terminal tyrosines. Irrespective of whether TIM3 is a positive or negative regulator of T-cells, the tyrosine residues at Y265/Y256 and Y272/Y263 in human/mice, respectively, are the most critical in mediating the functional effects of TIM3.

TIM3 signalling: stimulatory or inhibitory

Unligated Tim3 is thought to induce stimulatory signalling via BAT3, which binds to the TIM3 cytoplasmic tail and maintains a pool of active Lck at the immune synapse (IS), promoting TCR proximal signalling (215). Stimulatory roles of TIM3 to enhance NFAT, AP-1, NFκB signalling and IL-2 production were first found in a transient transfection system and an inducible system for ectopic TIM3 expression using Jurkat cells and the murine form of TIM3 (mTIM3) (216). In the same study, overexpression of TIM3 enhanced the IFNγ production of CD3-stimulated murine CD4 T-cells, while addition of a TIM3-targeting antibody largely inhibited the promotion of IFNγ by these T-cells, although whether the antibody clone used (5D12) is antagonistic or agonistic is unclear (216). Furthermore, TIM3 was found to promote both proximal TCR signalling and the expression of proapoptotic proteins in late-stage primary human CD8 effector T-cells, suggesting that in this context, TIM3 supported stimulatory signalling to accelerate restimulation-induced cell death (RICD) (247). Moreover, ectopic TIM3 expression in CD8 T cells enhanced the expression of pS6, which is downstream of Akt/mTOR signalling and these cells responded more strongly to restimulation according to the expression of pS6 and the early T-cell activation marker CD69 (257). Further supporting a stimulatory role for TIM3, fewer TIM3 KO *versus* WT CD8 T-cells responded to restimulation *in vitro* or rechallenge with antigen *in vivo* (257). Following acute LCMV infection, TIM3 KO mice had fewer short-lived effector T-cells (SLECs) and more memory precursor effector T-cells (MPECs) in the antigen-specific CD8 T-cell pool compared to WT mice and TIM3 ectopic expression enhanced the number of KLRG1⁺ SLECs over MPECs (257). This suggested that TIM3 promoted T cell activation to support development of SLECs over MPECs, indicating that TIM3 supports the depletion of the memory pool in chronic infection settings (257, 428).

Upon TIM3 ligation, tyrosine phosphorylation of Y256 on mTIM3 by Itk was found to cause BAT3 dissociation from the TIM3 cytoplasmic tail, which is proposed to enable the Src kinase FYN to bind at the same region of the tail, enriching FYN at the IS (215, 216). The current evidence suggests that any of FYN, Lck as well as Itk can phosphorylate both Y256 and Y263 upon TIM3 ligation to induce signalling (215, 216). FYN is known to activate PAG which recruits the tyrosine kinase Csk, leading to inactivation of Lck via inhibitory phosphorylation at Y505 on Lck, therefore the recruitment of FYN to the TIM3 tail is thought to play a role in suppression of proximal TCR signalling downstream of TIM3 (222, 429). Inhibitory effects of human TIM3 (hTIM3) were shown using Jurkat cell lines stably transfected with hTIM3, or primary human CD8 T cell populations, which expressed high endogenous levels of TIM3 following PMA/ionomycin stimulation (424). In this study, TIM3 was found to reduce IL-2 production, NFκB and NFAT activity, in direct contrast to previous findings (424). Moreover, in primary CD8 T-cells it was found that TIM3 localised to the IS in lipid rafts and upon conjugation with SEB-loaded B-cells, TIM3 failed to bind to and was excluded from areas enriched for active Lck (426). Upon binding to Galectin-9, (which is composed of two carbohydrate recognition domains joined by a flexible linker), TIM3 was found to colocalise with the phosphatases CD45 and CD148 indicating that Galectin-9 could bind and bring together TIM3 and these phosphatases (426). Overall, this study provided evidence that TIM3 localised to the IS where it could directly modulate proximal signalling processes, including deactivation of Lck via recruitment of CD45 which can dephosphorylate Lck (426). This can inhibit proximal TCR signalling as phosphorylation of Y394 of Lck is required for activation and downstream stimulatory phosphorylation of the CD3ζ chain and ZAP-70. This study also provided evidence that TIM3 regulates the stability of the IS because ligated TIM3 disrupted IS stability, as measured by CD3 enrichment at the IS, while TIM3 blockade enhanced IS stability (426). Another study found an inhibitory effect of TIM3 on T-cell metabolism in Jurkat cells; TIM3 reduced glucose consumption by T-cells with or without PMA/ionomycin stimulation, but did not affect mitochondrial DNA content, membrane potential or ROS production, suggesting the reduced glucose uptake was not counteracted by enhanced oxidative phosphorylation (427). Additionally, TIM3 overexpression caused a significant reduction in the mRNA expression levels of the Glut1 glucose transporter with no effects on Glut2, 3, or 4 transcription levels (427).

TIM3 as a negative regulator of T-cells *in vivo*

The vast majority of *in vivo* data indicates that TIM3 is a negative regulator of T-cells. TIM3, when coexpressed with PD-1, is a marker of the most exhausted TILs (430). Furthermore, TIM3 blockade in addition to PD-1/PDL-1 blockade in pre-clinical trials has been shown to enhance anti-tumour immunity and reduce tumour growth (325, 430). Notably, TIM3 is expressed by a range of cell types including Foxp3⁺ Tregs, CD4 and CD8 T-cells, macrophages, DCs and NK cells. Thus, it is

unclear whether TIM3 blockade therapies act directly on tumour-specific CD8 T-cells to improve anti-tumour immunity, or if other cell types such as DCs indirectly mediate the therapeutic effects. Accordingly, in a murine model of breast cancer, TIM3 blockade improved the response to paclitaxel chemotherapy by enhancement of granzyme B expression by CD8 T-cells; the effect in T-cells was dependent upon DCs that expressed elevated levels of CXCL9 following treatment (206). Additionally, in this study, TIM3 was primarily expressed by myeloid cells in human and murine tumours, suggesting that in some cases TIM3 blockade therapy acts mainly upon the innate immune compartment (206). Furthermore, in several solid tumour types, the majority of tumour-infiltrating CD4⁺ Tregs were TIM3⁺; TIM3⁺ Tregs were found to be twice as immunosuppressive *versus* TIM3⁻ Tregs (431). Notably, double blockade of TIM3 and PD-1 *in vivo* caused downregulation of Treg suppressive molecules including LAG-3, perforin and PD-1 (431). Double blockade also enhanced the function though not the frequency of the TIM3⁺PD1⁺ TILs (431). As the TIM3⁺ Tregs were present in the tumour prior to the development of the TIM3⁺PD1⁺ CD8 population, Tregs were proposed to support exhaustion development in CD8 TILs. Moreover, diphtheria toxin-induced depletion of Tregs synergised with TIM3 blockade to reduce tumour burden in a CD8 and CD4-T-cell dependent manner (431). Thus, Tregs were critical in the development of TIM3⁺PD1⁺ TILs and were a key cellular target of TIM3 blockade. Furthermore, there is limited evidence that TIM3 blockade directly reverses the suppression of TIM3⁺ CD8 T-cells. One study showed that the cytotoxic killing of HIV-infected CD4 T-cells by virus-specific CD8 T-cells, obtained from HIV-infected individuals, was enhanced by TIM3 blockade (432). As a possible mechanism, TIM3 blockade enhanced perforin release and degranulation, as measured by CD107a expression (432). In support of this mechanism, TIM3 has been found to suppress perforin and GzmB expression in unconventional gamma-delta ($\gamma\delta$) T-cells to reduce their cytotoxicity (433). Nevertheless, it has yet to be demonstrated that TIM3 blockade can directly reverse the suppression of tumour-specific CD8 T-cell cytotoxicity, in the absence of other cell types. In summary, there is a need to establish whether the cytotoxic potential of tumour-specific CD8 T-cells can be directly modulated by TIM3 blockade and to what extent different cell types indirectly or directly mediate the therapeutic effects of TIM3 blockade.

Rationale: using the 2D and 3D Renca models to study TIM3 as a regulator of CD8 T-cells

In vitro studies into TIM3 signalling in T-cells have primarily utilised 2D systems with Jurkat T-cell lines or primary T-cells with readouts of transcription factor activity or cytokine production. Moreover, studies on TIM3 signalling and function using *in vivo* systems are highly physiologically relevant *versus* 2D systems, but are subject to many confounding factors, such as the presence of other cell types and higher inter-subject variability. It is important to clarify the effect of TIM3 signalling on the anti-tumour cytotoxicity of CD8 T-cells in the context of developing TIM3-

targeted cancer therapies, as cytotoxic CD8 T-cells are key mediators of tumour death. Furthermore, it is important to determine how well our knowledge of TIM3 signalling in T-cells- mainly elucidated in 2D systems- can translate to TIM3 signalling *in vivo*. Context-dependent alterations in TIM3 signalling are unclear but important to understand for the development and use of TIM3-targeting therapies. Compared to the Renca 2D model previously used by this lab, the 3D Renca system enables us to study T-cell: Renca interactions in an environment with more physiologically relevant metabolite access and mechanotransductory stimuli which have been shown to alter cellular signalling pathways, the cellular transcriptome and proteome. Identification of differences in TIM3 signalling between the 2D and 3D systems can also provide a future tool by which to find unknown interaction partners in the TIM3 signalling network. Furthermore, the effects of TIM3 on T-cell polarisation, T-cell coupling to targets and morphological interface stability have not been described, therefore it is of interest to investigate if TIM3 regulates these aspects of the anti-tumour CD8 T-cell response. In the 2D Renca model, our lab has previously described three functional readouts related to T-cell interactions with Renca cells: 1) the ability of T-cells to form cell couples with Renca cells following first contact, 2) the morphological polarisation of the T-cell and 3) the stability of the cellular interface within these cell couples, as measured by the development of off-interface lamellipodia (OIL). All of these steps are critical for effective delivery of T-cell cytotoxic molecules into the target cell. A greater ability of T-cells to form cell couples with target cells upon first contact increases the frequency of T-cells well-positioned to deliver the lytic hit, meanwhile, more effective T-cell polarisation (a more rounded morphology) is associated with stronger calcium signalling and effective MTOC translocation to the interface for cytotoxic granule release (434-436). Lastly, higher stability of the interface within the cell couple enables more efficient delivery of cytotoxic molecules into the target cell. Lamellipodia are membrane protrusions that enable T-cells to adhere to their targets, as they stretch towards the target cell to stabilise the interface. OIL, however, have no productive effect on T-cell killing of tumour cells, because they move away from the target cell and destabilise the interface. Our lab has previously shown that a higher frequency of OIL and a faster onset of OIL are associated with increased T-cell dysfunction; TIM3-mediated modulation of these parameters could constitute a novel mechanism by which this receptor modulates the tumour-specific CD8 T-cell response (187, 437, 438).

In this chapter, the following aims are addressed:

- 1) To identify if TIM3 acts as an inhibitory or stimulatory receptor in tumour-specific CD8 T-cells and whether this differs between 2D and 3D Renca tumour models using: microscopic cytotoxicity assays, IFN γ ELISA, imaging of calcium signalling and analysis of T-cell: tumour cell coupling frequencies.
- 2) To determine whether any stimulatory and/or inhibitory effects of TIM3 as a receptor are mediated via the TIM3 cytoplasmic tail in both 2D and 3D tumour models using: microscopic cytotoxicity assays, IFN γ ELISA, imaging of calcium signalling and analysis of T-cell: tumour cell coupling frequencies.
- 3) To determine if TIM3 alters tumour-specific CD8 T-cell polarisation or the ability of T-cells to form a stable interface upon cell coupling to Renca tumour targets, in 2D, using microscopic assessment of: T-cell morphology during cell coupling and interface stability as measured by presentation of off-interface lamellipodia.
- 4) To determine if the TIM3 cytoplasmic tail mediates any effects of TIM3 on tumour-specific CD8 T-cell polarisation or the ability of T-cells to form a stable interface upon cell coupling to Renca tumour targets, using: T-cell morphology during cell coupling and interface stability as measured by presentation of off-interface lamellipodia.

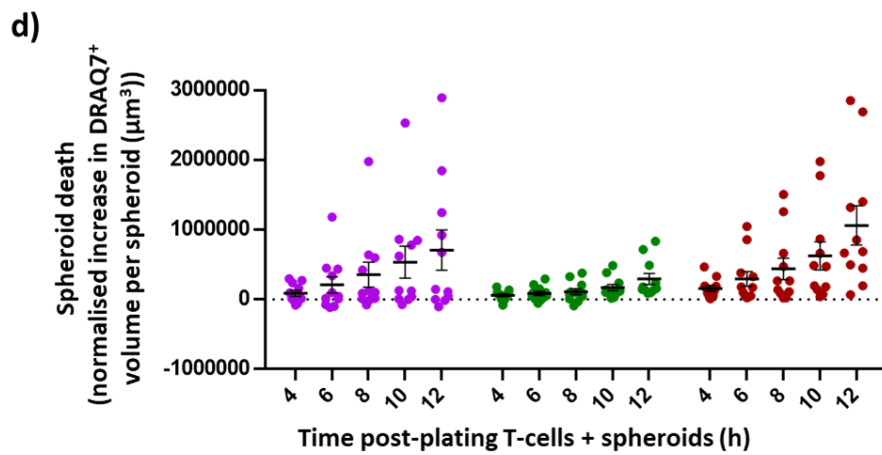
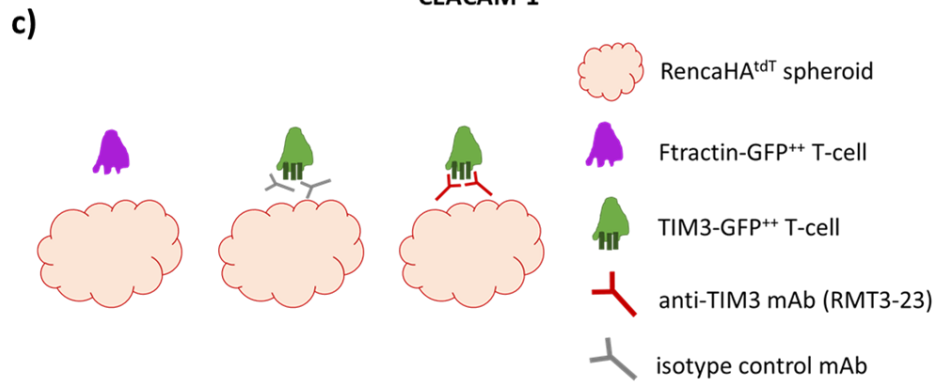
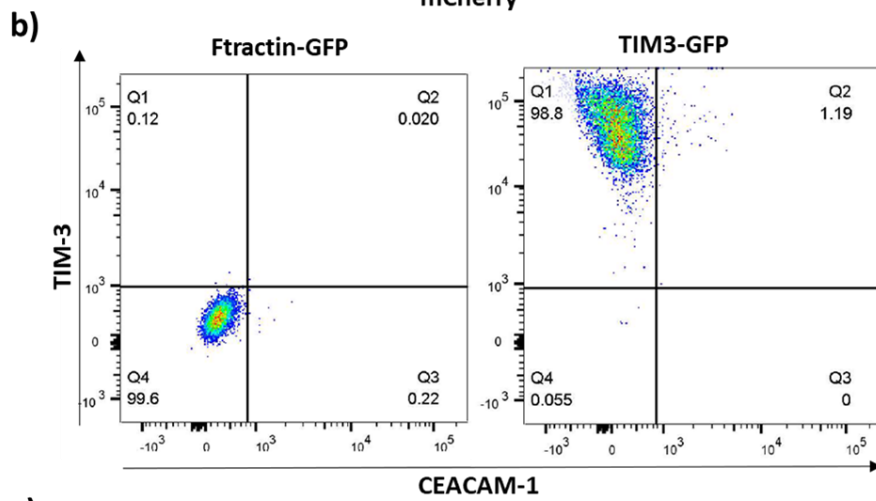
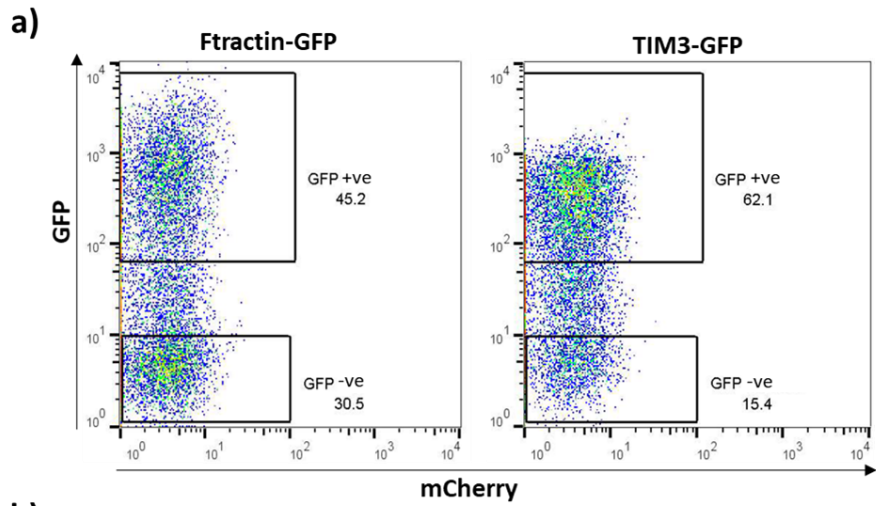
4.2 Results

4.2.1. TIM3 overexpression suppresses CL4 CD8 T-cell killing in 3D and is reversible via acute anti-TIM3 blockade.

CL4 CD8 T-cells were retrovirally transduced to overexpress GFP-tagged TIM3 or Ftractin (TIM3-GFP⁺⁺ or Ftractin-GFP⁺⁺ CL4). The gating strategy used to isolate live, single CL4 T-cells is shown in Supplementary Figure 8.1. GFP-positive T-cells could be detected on the day of cell sorting by flow cytometry, three days post-transduction; cells found between the 'GFP-positive' and 'GFP-negative' gates expressed low levels of GFP, but sorting for cells from the manually defined 'GFP-positive' gate helps to enable a more consistent level of GFP-positivity across different conditions and repeats (Figure 4.1a). The 'GFP-negative gate' was manually created during sorting around the cell population with lower fluorescent intensity on the GFP axis. GFP-positive gate is assigned as CEACAM1 and TIM3 expression on TIM3-GFP⁺⁺ and Ftractin-GFP⁺⁺ was assessed, as it has been reported that CEACAM1 supports TIM3 surface expression on T-cells via intracellular interactions (221). Ftractin-GFP⁺⁺ T-cells did not express detectable levels of TIM3 or CEACAM1, while TIM3-GFP⁺⁺ T-cells overexpressed TIM3 and TIM3 overexpression had no effect on CEACAM1 expression (Figure 4.1b). GFP-sorted cells were plated in a 3D microscopic cytotoxicity assay with RencaHA^{tdT} spheroids ± anti-TIM3 mAb (Figure 4.1c). TIM3 blockade treatment in all experiments in this project involved 1h pre-incubation of T-cells with the anti-TIM3 mAb, in addition to TIM3 blockade treatment throughout the assay. The mean normalised increase in DRAQ7⁺ volume per spheroid was significantly higher in the Ftractin-GFP⁺⁺ CL4 control group *versus* the TIM3-GFP⁺⁺ CL4 group (Figure 4.1d graph and top table). Acute treatment of anti-TIM3 blockade to the TIM3-GFP⁺⁺ T-cells (1h prior to and during the assay) reversed the suppressive effect of TIM3 on the CL4 T-cells (Figure 4.1d graph and top table). The mean DRAQ7⁺ volume per spheroid was significantly higher in the TIM3-GFP⁺⁺ + anti-TIM3 blockade group *versus* the Ftractin-GFP⁺⁺ group at 12h, suggesting that TIM3 overexpression enhanced cytotoxicity in the absence of TIM3 ligation (Figure 4.1d graph and top table).

Ftractin-GFP⁺⁺ CL4 and TIM3-GFP⁺⁺ CL4 treated with anti-TIM3 blockade, caused a significant increase in DRAQ7⁺ spheroid dead volume (compared to the spheroid death at 4h) by 8 and 10h post-plating of T-cells with spheroids, respectively (Figure 4.1d graph and bottom table). In contrast, the TIM3-GFP⁺⁺ CL4 did not cause a significant increase in DRAQ7⁺ spheroid dead volume at any timepoint (Figure 4.1d graph and bottom table). To establish if TIM3 overexpression suppressed the cytotoxicity of CL4 T-cells, possible confounding factors were assessed for differences between groups. No significant differences in SIL density (Figure 4.2a), spheroid volumes (Figure 4.2b) or spheroid shapes (Figure 4.2c) were found between treatment groups,

suggesting that TIM3 overexpression and acute blockade directly altered the cytotoxic capacity of TIM3⁺⁺ T-cells.



- Ftractin-GFP⁺
- TIM3-GFP⁺ + isotype control mAb
- TIM3-GFP⁺ + anti-TIM3 mAb

	<i>Time (h)</i>				
<i>Spheroid death, comparisons between groups</i>	4	6	8	10	12
Ftractin-GFP ⁺⁺ vs TIM3-GFP ⁺⁺ + isotype control mAb	ns	ns	ns	0.004 **	0.0009 ***
Ftractin-GFP ⁺⁺ vs TIM3-GFP ⁺⁺ + anti-TIM3 mAb	ns	ns	ns	Ns	0.005 **
TIM3-GFP ⁺⁺ + isotype control mAb vs TIM3-GFP ⁺⁺ + anti-TIM3 mAb	ns	ns	0.01 *	0.0002 ***	<0.0001 ****

	<i>Time (h)</i>			
<i>Spheroid death over time, comparisons within each group</i>	6	8	10	12
Ftractin-GFP ⁺⁺	ns	ns	0.0005 ***	<0.0001 ****
TIM3-GFP ⁺⁺	ns	ns	ns	ns
TIM3-GFP ⁺⁺ + anti-TIM3 mAb	ns	0.04 *	0.0002 ***	<0.0001 ****

Figure 4.1 TIM3-GFP overexpression suppressed CL4 T-cell cytotoxicity and was reversed by acute incubation with TIM3 blocking antibody in the 3D microscopic cytotoxicity assay.

a) CL4 T-cells were retrovirally transduced to overexpress Ftractin-GFP or TIM3-GFP; representative flow cytometry dot plots show the GFP-based sorting gate for transduced T-cells used in subsequent 2D and 3D cytotoxicity assays. **b)** Representative dot plots show the TIM3 and CEACAM1 cell surface expression by GFP-positive CD8 T-cells transduced to overexpress Ftractin-GFP and TIM3-GFP*. **c)** CL4 T-cells that overexpressed Ftractin-GFP or TIM3-GFP plus anti-TIM3 mAb or isotype control mAb, were coincubated with 2µg/ml K^dHA pulsed RencaHA^{tdT} spheroids in the 3D microscopic cytotoxicity assay. **d)** Spheroid death over the duration of a 3D microscopy cytotoxicity assay when spheroids were plated with 200,000 CL4 T-cells per well, which overexpressed Ftractin-GFP or TIM3-GFP ± blocking anti-TIM3 mAb. Spheroid dead volume at each timepoint was normalised to the initial dead volume at 2h and then to the average dead volume of the Spheroid only group, to subtract any background death. **Top panel)** indicates significant differences between groups at each time point, means were compared using a Two-Way ANOVA, matched by repeat and timepoint. **Bottom panel)** indicates whether there was significant death over time within each group, means were compared to the mean at 4h within each group, using Two-Way ANOVA and Dunnett's test, matched by repeat and timepoint. Individual points represent the mean from an independent repeat from a total of eleven independent repeats, with 3-6 spheroids per group. Error bars show mean ± SEM. *Data in **b)** was acquired by Hanin Alamir from the Wülfing lab.

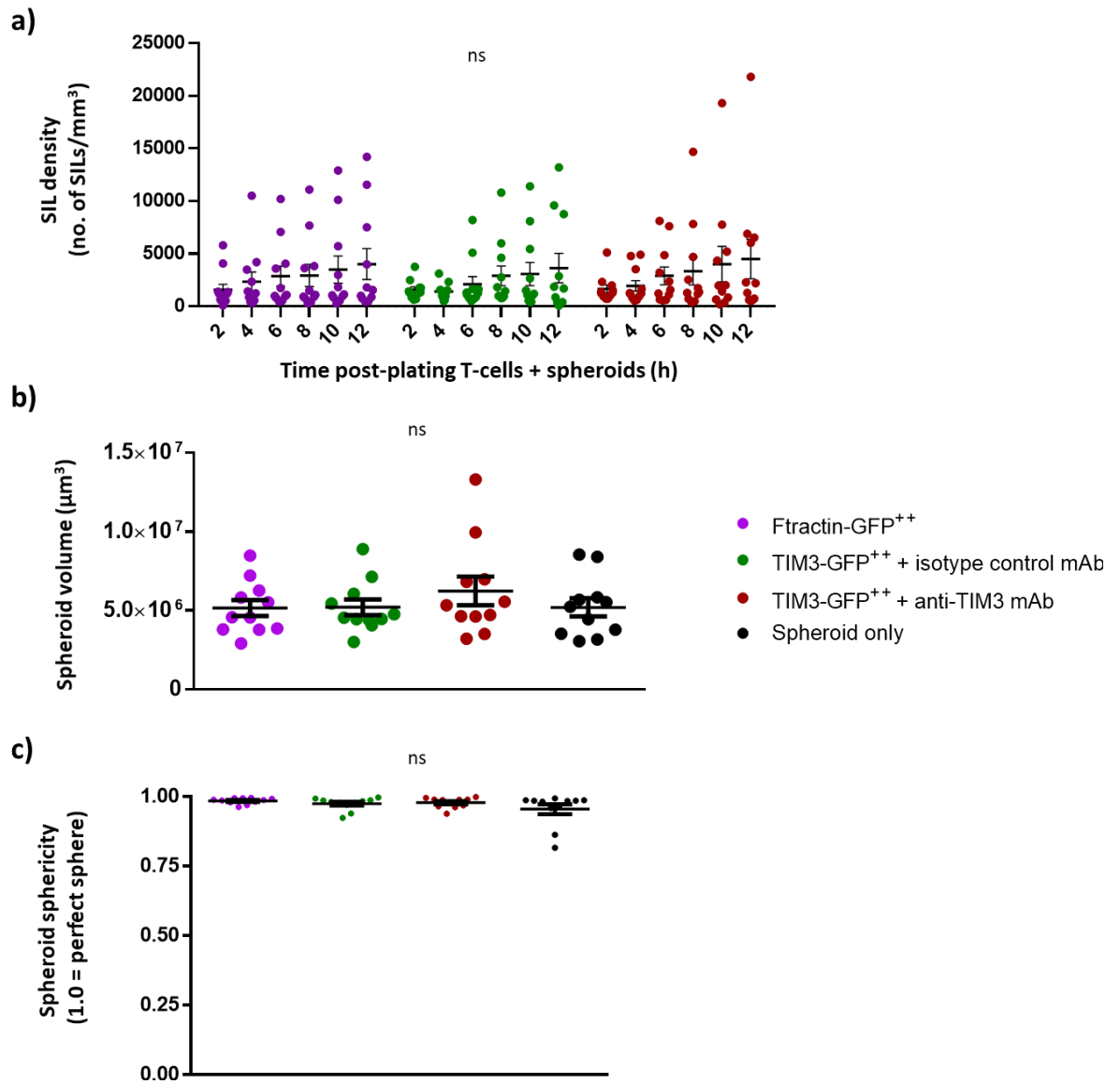


Figure 4.2 Differences in SIL density and spheroid dimensions did not account for differences in cytotoxicity resulting from TIM3 overexpression.

a) SIL density over the course of a 3D microscopic cytotoxicity assay is shown for Ftractin-GFP and TIM3-GFP ± anti-TIM3 groups. **b)** Spheroid volume across Spheroid only, Ftractin-GFP and TIM3-GFP ± anti-TIM3 groups at 2h post-plating for the 3D microscopic cytotoxicity assay. **c)** Spheroid sphericity (how well spheroid shapes fit a perfect sphere) across groups at 2h post-plating; a value of 1.0 indicates a perfect sphere. Each individual point represents a mean of 11 independent repeats. $n = 2-6$ spheroids per group, per repeat. Means were compared using a One-Way ANOVA, matched by repeat. For all graphs, error bars show mean ± SEM and ns = non-significant p-values across all comparisons.

4.2.2. The TIM3 cytoplasmic tail mediates the suppressive effect of TIM3 overexpression on CL4 CD8 T-cell killing in 3D that is reversible by acute TIM3 blockade

It was of interest to determine if the TIM3 cytoplasmic tail mediated the inhibitory effects of TIM3 overexpression in the 3D system. CL4 CD8 T-cells were retrovirally transduced to overexpress full-length TIM3 or truncated TIM3 which lacked the cytoplasmic tail (TIM3-GFP⁺⁺ or TIM3-GFP^{cyt-ve++} CL4) and plated in a 3D microscopic cytotoxicity assay with RencaHA^{tdT} spheroids. The mean normalised increase in DRAQ7⁺ volume per spheroid was significantly higher in the TIM3^{cyt-ve}-GFP⁺⁺ ± anti-TIM3 mAb blockade and TIM3-GFP⁺⁺ + anti-TIM3 mAb groups *versus* the TIM3-GFP⁺⁺ group at 8, 10 and 12h. As there was no effect of acute TIM3 blockade on TIM3^{cyt-ve} T-cells, the suppressive role of TIM3 seemed to require the TIM3 cytoplasmic tail (Figure 4.3, top).

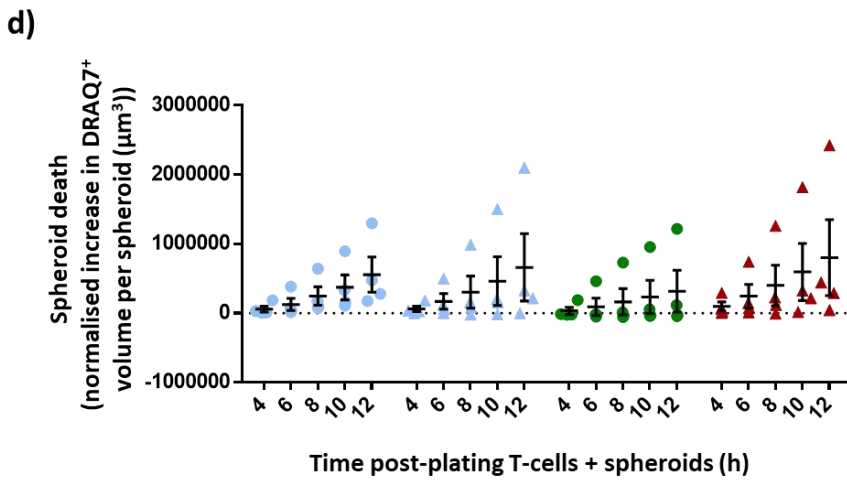
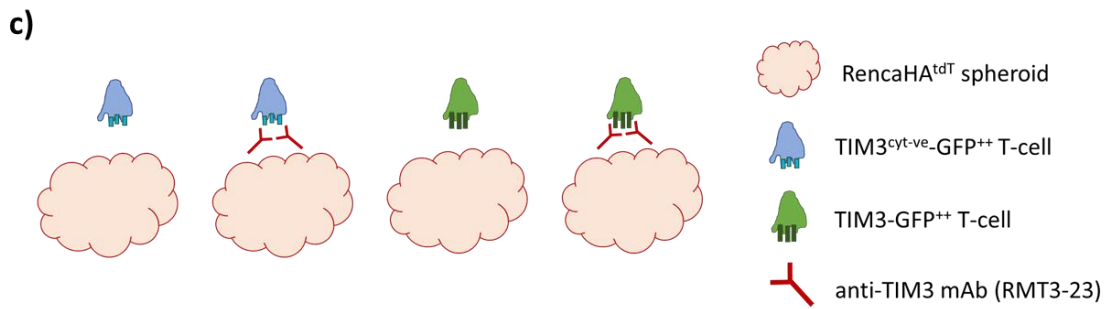
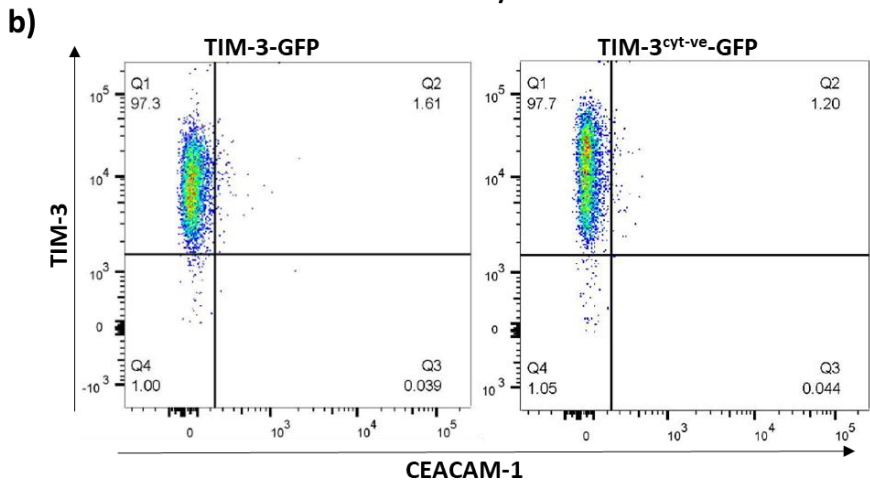
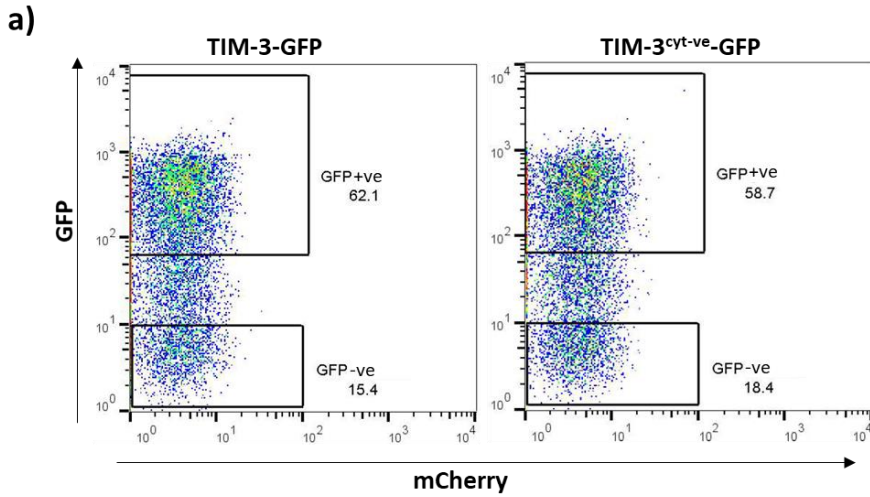
Interestingly, in one of the four independent repeats, across all groups, the T-cell dependent spheroid death is substantially higher than in the three other repeats. In this repeat with higher spheroid death, there was no suppressive effect of TIM3 overexpression, suggesting that T-cells with higher cytotoxicity may be more resistant to TIM3 mediated inhibition. This was not investigated further due to time constraints but would be of interest in future work. Nevertheless, TIM3-GFP⁺⁺ + anti-TIM3 mAb and TIM3^{cyt-ve}-GFP⁺⁺ ± anti-TIM3 mAb T-cells caused a significant increase in DRAQ7⁺ spheroid dead volume (compared to the spheroid death at 4h) at 6h and 8h, respectively, while TIM3-GFP⁺⁺ T-cells caused a significant increase in DRAQ7⁺ spheroid dead volume death at a later timepoint of 10h (Figure 4.3, bottom).

To establish if the TIM3 cytoplasmic tail was responsible for TIM3-mediated suppression of CL4 T-cell cytotoxicity, possible confounding factors were assessed for differences between groups. Interestingly, at several timepoints the SIL density was higher in the TIM3^{cyt-ve}-GFP groups *versus* the TIM3-GFP⁺⁺ groups (Figure 4.4a). This could be due to a difference in the set-up in these experiments (and future 3D microscopic cytotoxicity assays) *versus* previous data; in this and future 3D microscopic cytotoxicity assays, spheroids and T-cells were co-incubated for 15 minutes prior to addition of Matrigel (MG), whereas in the initial experiments, spheroids and MG were mixed prior to addition of T-cells. This updated set-up procedure could make inter-group differences in the efficiency of T-cell attachment to spheroids more evident. No significant differences in spheroid volumes (Figure 4.4b) or spheroid shapes (Figure 4.4c) were found between treatment groups.

As the SIL density differed between groups, normalisation of spheroid dead volumes to the level of SIL density enabled determination of whether the TIM3 cytoplasmic tail reduced the killing ability per cell. We found that normalisation of the spheroid dead volumes to the infiltration factor (which is proportional to the SIL density) did not significantly affect the differences between groups (Figure 4.5, top). The time at which significant spheroid death developed

remained the same for all groups before and after normalisation to the infiltration factor, except in the TIM3-GFP⁺⁺ group, where density-normalised death was delayed to the 12h timepoint (Figure 4.5, bottom).

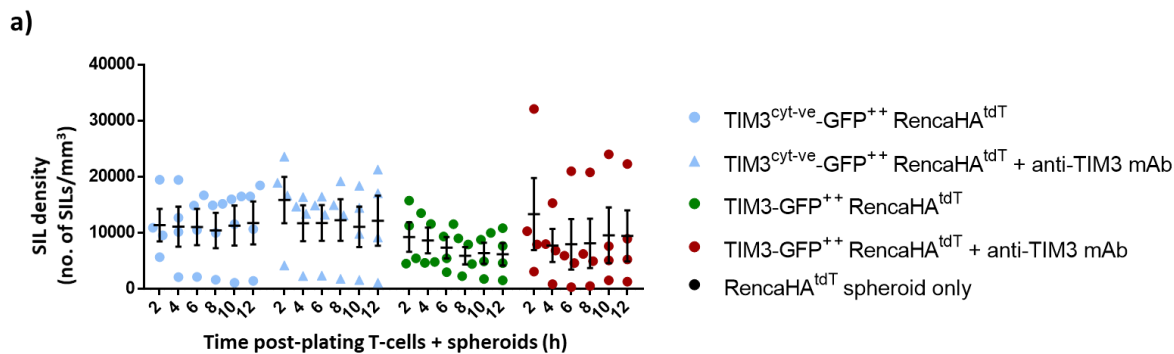
Overall, the data suggests that the TIM3 cytoplasmic tail was responsible for the inhibitory effect of TIM3 overexpression on CL4 T-cells in the 3D Renca model.



<i>Spheroid death, comparisons between groups</i>	4	6	8	10	12
TIM3 ^{cyt-ve} -GFP ⁺⁺ vs TIM3 ^{cyt-ve} -GFP ⁺⁺ + anti-TIM3 mAb	ns	ns	ns	ns	ns
TIM3 ^{cyt-ve} -GFP ⁺⁺ vs TIM3-GFP ⁺⁺	ns	ns	0.0003 ***	<0.0001 ****	<0.0001 ****
TIM3 ^{cyt-ve} -GFP ⁺⁺ vs TIM3-GFP ⁺⁺ + anti-TIM3 mAb	ns	ns	ns	ns	ns
TIM3 ^{cyt-ve} -GFP ⁺⁺ + anti-TIM3 mAb vs TIM3-GFP ⁺⁺	ns	0.007 **	0.002 **	0.0006 ***	<0.0001 ****
TIM3 ^{cyt-ve} -GFP ⁺⁺ + anti-TIM3 mAb vs TIM3-GFP ⁺⁺ + anti-TIM3 mAb	ns	ns	ns	ns	ns
TIM3-GFP ⁺⁺ vs TIM3-GFP ⁺⁺ + anti-TIM3 mAb	ns	0.0002 ***	<0.0001 ****	<0.0001 ****	<0.0001 ****

<i>Spheroid death over time, comparisons within each group</i>	6	8	10	12
TIM3 ^{cyt-ve} -GFP ⁺⁺	ns	0.0002 ***	<0.0001 ****	<0.0001 ****
TIM3 ^{cyt-ve} -GFP ⁺⁺ + anti-TIM3 mAb	ns	0.002 **	<0.0001 ****	<0.0001 ****
TIM3-GFP ⁺⁺	ns	ns	0.03	0.002 **
TIM3-GFP ⁺⁺ + anti-TIM3 mAb	0.03 *	0.0005 ***	<0.0001 ****	<0.0001 ****

Figure 4.3 The TIM3 cytoplasmic tail mediated the suppressive effect of TIM3-GFP overexpression in 3D by inhibition of spheroid death and delaying the onset of spheroid death. **a)** CL4 T-cells were retrovirally transduced to overexpress full length TIM3-GFP or TIM3^{cyt-ve}-GFP* which lacked the TIM3 cytoplasmic domain; representative flow cytometry dot plots show the GFP-based sorting gate for transduced T-cells used in subsequent 2D and 3D cytotoxicity assays. **b)** Representative dot plots show the comparable TIM3 and CEACAM1 cell surface expression by GFP-positive CD8 T-cells transduced to overexpress TIM3-GFP and TIM3^{cyt-ve}-GFP. **c)** Spheroid death over the duration of a 3D microscopy cytotoxicity assay when spheroids were plated with 200,000 CL4 T-cells per well, which overexpressed TIM3^{cyt-ve}-GFP (the extracellular domain of TIM3) or full-length TIM3-GFP ± anti-TIM3 mAb. **d)** Spheroid dead volume at each timepoint was normalised to the initial dead volume at 2h and then to the average dead volume of the Spheroid only group. **Top panel)** indicates significant differences between groups at each time point, means were compared by Two-Way ANOVA, matched by repeat and timepoint. Means are of log-transformed data, due to positive skew. **Bottom panel)** indicates whether there was significant death over time within each group, means were compared to the mean at 4h within each group, using Two-Way ANOVA and Dunnett's test, matched by repeat and timepoint. For all graphs individual points represent a mean of four independent repeats, with 2-4 spheroids per group. Error bars show mean ± SEM. *TIM3^{cyt-ve}-GFP construct was cloned and data in **b)** was acquired by Hanin Alamir from the Wülfing lab.



SIL density	2	4	6	8	10	12
TIM3 ^{cyt-ve} -GFP ⁺ vs TIM3 ^{cyt-ve} -GFP ⁺ + anti-TIM3 mAb	0.04 *	ns	ns	ns	ns	ns
TIM3 ^{cyt-ve} -GFP ⁺ vs TIM3-GFP ⁺	ns	ns	ns	0.02 *	0.01 *	0.003 **
TIM3 ^{cyt-ve} -GFP ⁺ vs TIM3-GFP ⁺ + anti-TIM3 mAb	ns	0.05 *	ns	ns	ns	ns
TIM3 ^{cyt-ve} -GFP ⁺ + anti-TIM3 mAb vs TIM3-GFP ⁺	0.0003 ***	ns	0.02 *	0.0005 ***	0.01 *	0.001 **
TIM3 ^{cyt-ve} -GFP ⁺ + anti-TIM3 mAb vs TIM3-GFP ⁺ + anti-TIM3 mAb	ns	ns	ns	ns	ns	na
TIM3-GFP ⁺ vs TIM3-GFP ⁺ + anti-TIM3 mAb	0.02 *	ns	ns	ns	ns	ns

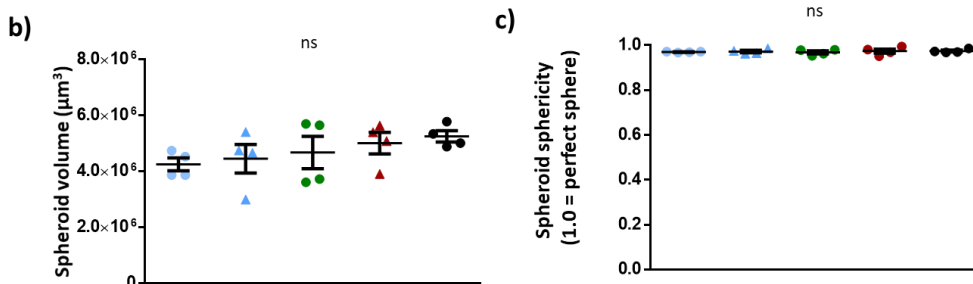
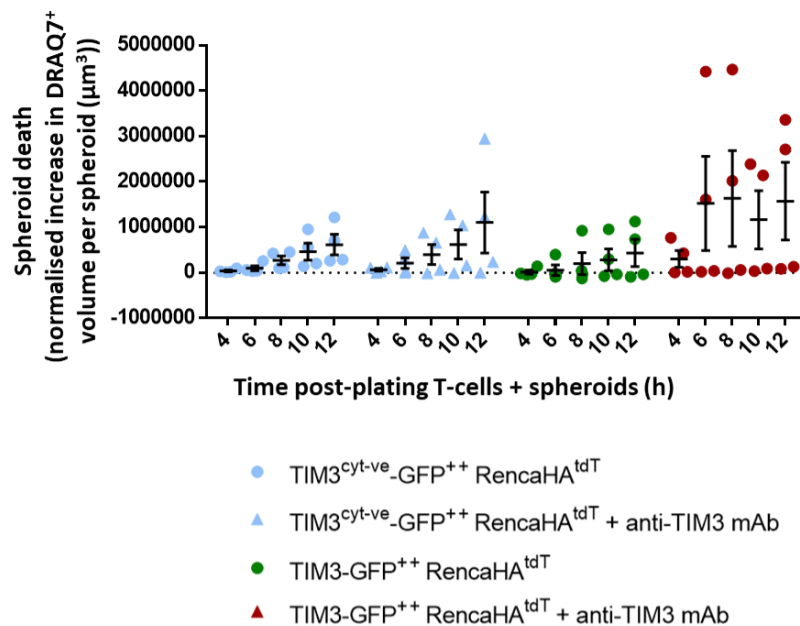


Figure 4.4 Differences in spheroid dimensions did not account for differences in cytotoxicity resulting from TIM3 overexpression, but SIL density was higher in the TIM3^{cyt-ve}-GFP groups. **a)** SIL density over the course of a 3D microscopic cytotoxicity assay is shown for TIM3^{cyt-ve}-GFP and TIM3-GFP ± anti-TIM3 groups. Means were compared by Two-Way ANOVA, matched by repeat and timepoint. **b)** Spheroid volume across Spheroid only, TIM3^{cyt-ve}-GFP and TIM3-GFP ± anti-TIM3 groups at 2h post-plating for the 3D microscopic cytotoxicity assay. **c)** Spheroid sphericity (how well spheroid shapes fit a perfect sphere) across groups at 2h post-plating; a value of 1.0 indicates a perfect sphere. In **b)** and **c)** means were compared by One-Way ANOVA, matched by repeat. For all graphs, individual points represent the mean of four independent repeats. n=2-6 spheroids per group, per repeat. Error bars show mean ± SEM and ns= non-significant p-values across all comparisons.



<i>Spheroid death, comparisons between groups</i>	4	6	8	10	12
TIM3 ^{cyt-ve} -GFP ⁺ vs TIM3 ^{cyt-ve} -GFP ⁺ + anti-TIM3 mAb	ns	ns	ns	ns	ns
TIM3 ^{cyt-ve} -GFP ⁺ vs TIM3-GFP ⁺	ns	ns	0.0008 ***	0.01 *	0.004 **
TIM3 ^{cyt-ve} -GFP ⁺ vs TIM3-GFP ⁺ + anti-TIM3 mAb	ns	ns	ns	ns	ns
TIM3 ^{cyt-ve} -GFP ⁺ + anti-TIM3 mAb vs TIM3-GFP ⁺	ns	0.003 **	0.0006 ***	0.01 *	0.003 **
TIM3 ^{cyt-ve} -GFP ⁺ + anti-TIM3 mAb vs TIM3-GFP ⁺ + anti-TIM3 mAb	ns	0.004 **	ns	ns	ns
TIM3-GFP ⁺ vs TIM3-GFP ⁺ + anti-TIM3 mAb	0.004	<0.0001 ****	<0.0001 ****	0.0003 ***	0.0001 ***

<i>Spheroid death over time, comparisons within each group</i>	6	8	10	12
TIM3 ^{cyt-ve} -GFP ⁺	ns	0.009 **	0.0002 ***	<0.0001 ****
TIM3 ^{cyt-ve} -GFP ⁺ + anti-TIM3 mAb	ns	0.02 *	0.001 **	<0.0001 ****
TIM3-GFP ⁺	ns	ns	ns	0.02 *
TIM3-GFP ⁺ + anti-TIM3 mAb	0.01 *	0.007 **	0.009 **	0.0006 ***

Figure 4.5 Spheroid death volumes normalised to SIL density levels indicated that the TIM3 cytoplasmic tail mediated the suppressive effect of TIM3-GFP overexpression in 3D by inhibition of spheroid death.

Spheroid death over the duration of a 3D microscopic cytotoxicity assay when spheroids were plated with 200,000 CL4 T-cells per well, which overexpressed TIM3^{cyt-ve}-GFP (the extracellular domain of TIM3) or full-length TIM3-GFP ± anti-TIM3 mAb. Spheroid dead volume at each

timepoint was normalised to the initial dead volume at 2h, to the average dead volume of the Spheroid only group and then to the extent of SIL infiltration (infiltration factor). (Infiltration factor= density at the spheroid surface/400. **Top panel**) indicates significant differences between groups at each time point, means were compared by Two-Way ANOVA, matched by repeat and timepoint. Means are of log-transformed data, due to positive skew. **Bottom panel**) indicates whether there was significant death over time within each group, means were compared to the mean at 4h within each group, using Two-Way ANOVA and Dunnett's test, matched by repeat and timepoint. Each individual point represents a mean of four independent repeats. Error bars show mean \pm SEM.

4.2.3. TIM3 overexpression did not significantly affect T-cell cytotoxicity in the 2D system, but enhanced IFN γ secretion.

Next, we determined whether the inhibitory effect of TIM3 overexpression by CL4 T-cells in the 3D system would translate to the 2D system. Ftractin-GFP⁺⁺ and TIM3-GFP⁺⁺ T-cells were plated onto 2D RencaHA^{tdT} target cells in the 2D microscopic cytotoxicity assay (Figure 4.6a). There were no significant differences in the rate of killing by Ftractin-GFP⁺⁺ and TIM3-GFP⁺⁺ T-cells with a minor stimulatory effect of TIM3 overexpression; acute blockade using anti-TIM3 mAb had no effect on the cytotoxicity of TIM3-GFP⁺⁺ T-cells (Figure 4.6b). Throughout this project, IFN γ secretion during 2D cytotoxicity assays was measured by collecting the supernatant from the assay plate wells at the end of the assay (18h after the cells were first cocultured). Interestingly, a significantly higher mean level of IFN γ was secreted by TIM3⁺⁺ T-cells *versus* Ftractin⁺⁺ T-cells, while there was no effect of acute-TIM3 blockade on IFN γ secretion by TIM3-GFP⁺⁺ T-cells (Figure 4.6c). Moreover, using pulsed RencaWT targets, data acquired by another lab member revealed a significantly enhanced rate of killing by TIM3-GFP⁺⁺ *versus* Ftractin-GFP⁺⁺ T-cells, further supporting a stimulatory role of TIM3 overexpression (data not shown).

4.2.4. TIM3 overexpression does not affect T-cell calcium signalling upon coupling to targets but does alter the ability of T-cells to couple to targets.

As TIM3-GFP overexpression was associated with enhanced IFN γ secretion, indicating a stimulatory role of TIM3 on CL4 T-cells, we hypothesised that TIM3-GFP overexpression also enhanced intracellular calcium levels upon T-cell coupling to targets. Fura-2-loaded TIM3⁺⁺ and Ftractin⁺⁺ T-cells were plated with RencaHA^{tdT} 2D target cells and intracellular calcium levels were measured during cell couple formation (Figure 4.7a). Moreover, we hypothesised that the frequency of T-cells that formed conjugates with Renca target cells would be enhanced by TIM3 overexpression as a result of elevated T-cell activation. Targets with both high peptide concentration at their surface (2 μ g/ml K^dHA peptide) or lower peptide concentration at their surface (target cells left unpulsed) were used. This is because the higher peptide stimulus would provide such a strong stimulatory signal that any subtle differences between TIM3-GFP⁺⁺ *versus* control T-cells would be hard to detect; the lower peptide stimulus enabled detection of smaller effects of TIM3 overexpression. Although no significant differences in the calcium flux between TIM3⁺⁺ and Ftractin⁺⁺ CL4 T-cells were observed regardless of the peptide stimulus strength (Figure 4.7b), the percentage of T-cells that contacted a Renca target cell and committed to a cell couple with that target, was significantly higher amongst TIM3⁺⁺ *versus* Ftractin⁺⁺ control cells (Figure 4.7d).

Overall, this data suggested that while TIM3 overexpression had a minor stimulatory effect on CD8 T-cell cytotoxicity in 2D, TIM3 could enhance IFN γ secretion and the ability of T-cells to form cell couples with tumour targets.

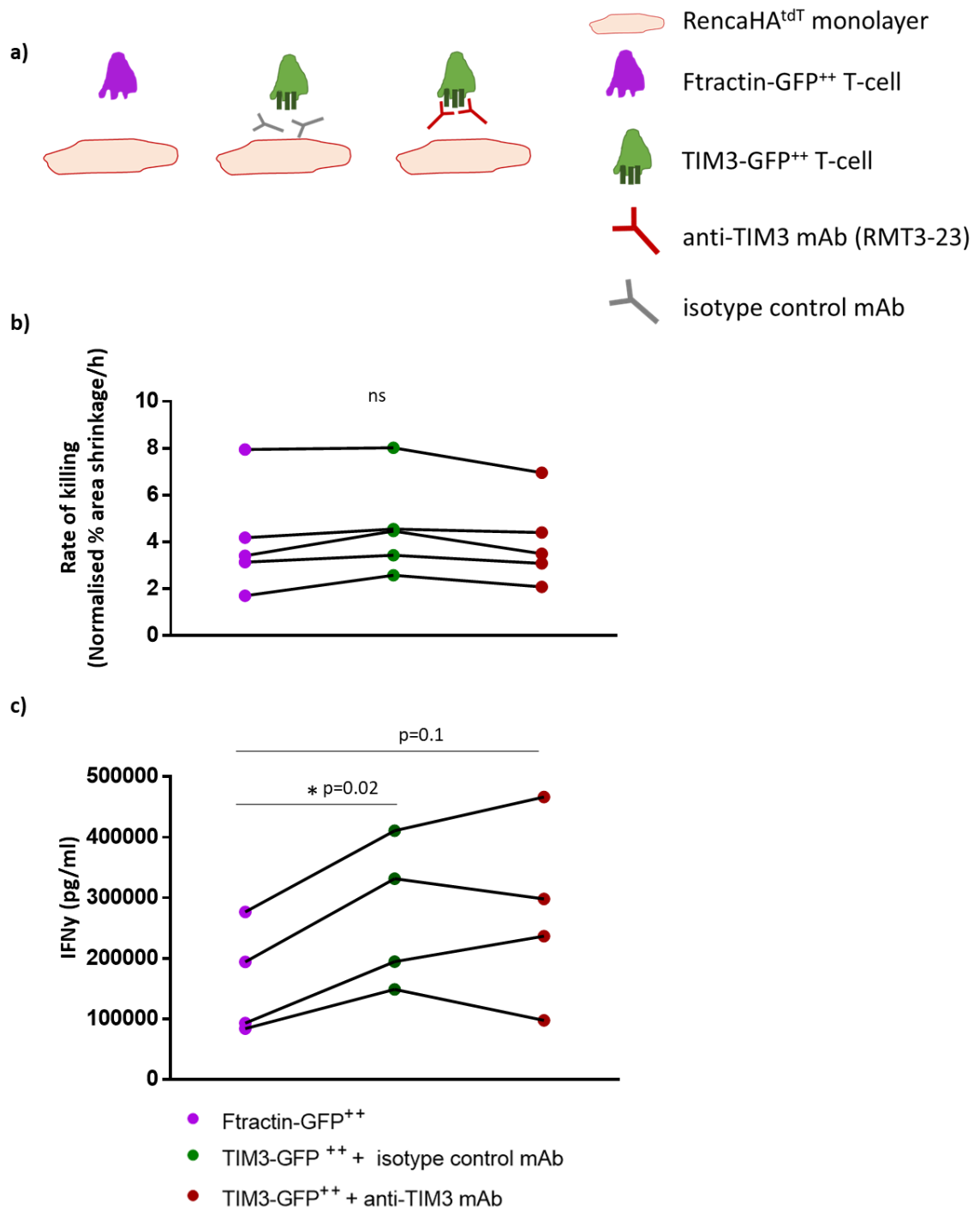


Figure 4.6 TIM3-GFP overexpression did not significantly affect CL4 T-cell cytotoxicity during co-incubation with K^dHA-pulsed 2D RencaHA^{tdT} target cells in the 2D microscopic cytotoxicity assay, but enhanced IFN γ secretion by CL4 T-cells.

a) CL4 T-cells that overexpressed Ftractin-GFP or TIM3-GFP plus anti-TIM3 mAb or isotype control mAb, were coincubated with 2 μ g/ml K^dHA pulsed RencaHA^{tdT} monolayer target cells in the 2D microscopic cytotoxicity assay. **b)** Each point shows the mean rate of killing by CL4 T-cells that overexpressed Ftractin-GFP or TIM3-GFP \pm anti-TIM3 mAb from one of five independent repeats. Individual points represent the mean from an independent repeat from three-four replicate wells and means were compared using a one-tailed, paired t-test. **c)** IFN γ concentration of supernatant from wells of the 2D microscopic cytotoxicity assay, each point represents the mean from three replicate wells, from a total of four independent repeats. For all graphs, lines connect data from the same independent repeat. ns = non-significant p-values across all comparisons.

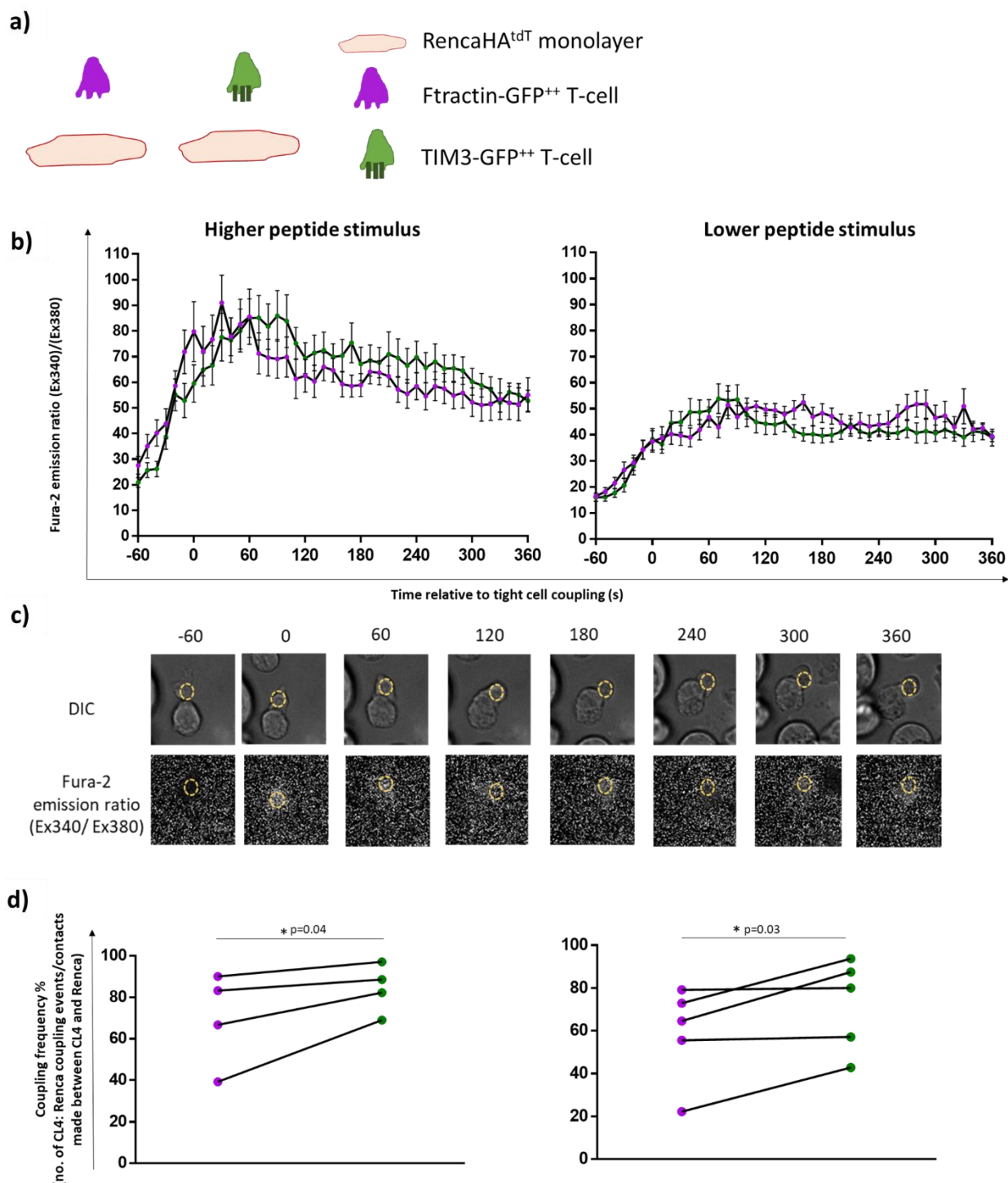


Figure 4.7 TIM3-GFP overexpression did not affect calcium flux within CL4 T-cells upon tight cell coupling to 2 μ g/ml or 2ng/ml K^dHA-pulsed 2D Renca target cells but enhanced the frequency of T-cells that formed tight couples.

a) Fura-2-loaded CL4 T-cells that overexpressed Ftractin-GFP or TIM3-GFP were plated onto a RencaHA^{tdT} target monolayer, which had either been pulsed with 2 μ g/ml K^dHA (higher peptide stimulus) or left unpulsed (lower peptide stimulus). Means at each timepoint were compared using multiple t-tests with the Holm-Sidak correction. **b)** Ratio of Fura-2 emission upon excitation at 340 nm over 380 nm is shown. Means \pm SEM are shown from 19 and 15 T-cells that overexpressed TIM3-GFP and Ftractin-GFP, respectively, from 4 independent repeats. **c)** Representative images demonstrating how a circular region within the coupling T-cell (top) is drawn manually using the DIC image and the corresponding region in the ratio image is measured for mean fluorescent intensity in order to gain the values plotted in **b)**, which indicate the T-cell

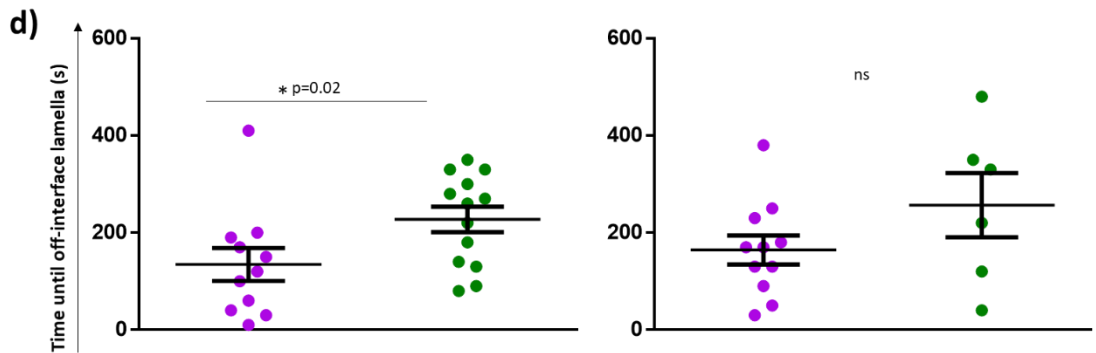
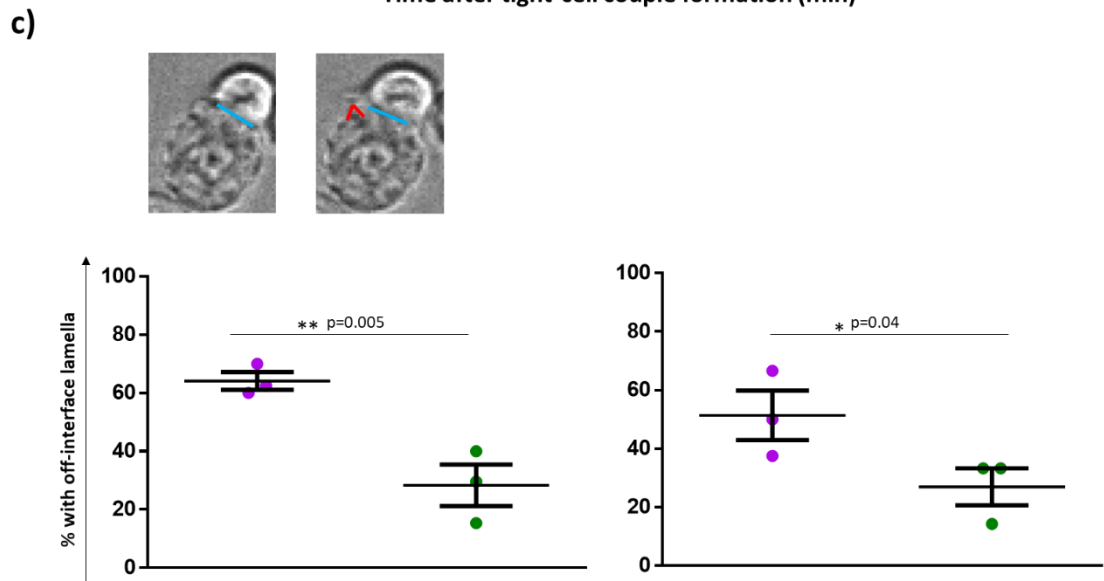
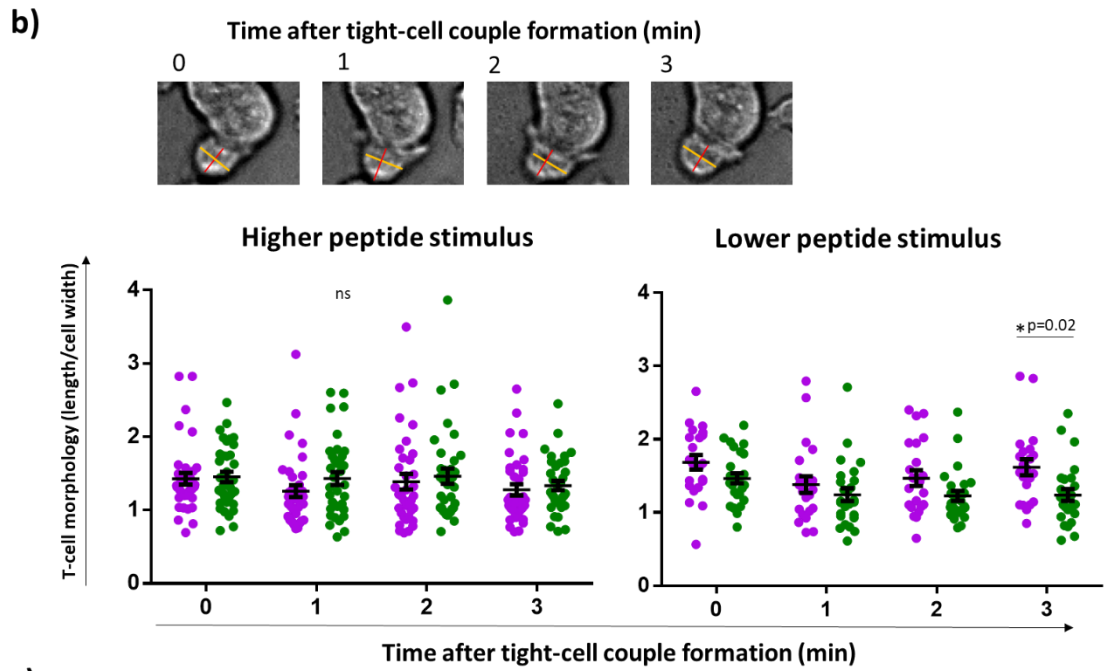
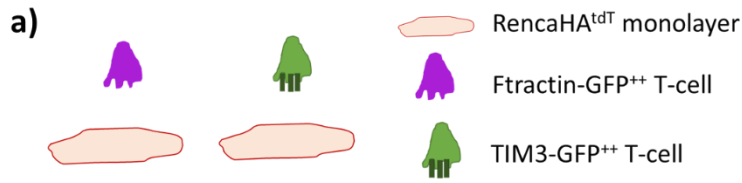
calcium flux during coupling from -60 to 360 seconds relative to cell couple formation. **d)** Cell coupling frequencies are shown with individual points representing one mean from four independent repeats. Lines connect data from the same independent repeat.

4.2.5. TIM3 overexpression improves T-cell polarisation and the stability of the interface when T-cells couple to targets.

As TIM3 overexpression enhanced the ability of T-cells to bind to their targets, the effect of TIM3 overexpression on parameters of T-cell polarisation and interface stability were investigated (Figure 4.8a). These parameters are relevant to effective T-cell coupling to tumour targets and delivery of the lytic hit (previously discussed). RencaHA^{tdT} targets were either pulsed with 2µg/ml K^dHA peptide or left unpulsed in order to produce targets with higher or lower peptide surface expression levels. The length to width ratio of a CD8 cytotoxic T-cell during coupling is a measure of how well a T-cell polarises itself to kill its target; a more elongated morphology is thought to be associated with less effective polarisation for delivery of the lytic hit. We found that the morphology of TIM3-GFP⁺⁺ and Ftractin-GFP⁺⁺ T-cells did not differ between conditions in the higher peptide stimulus settings, however, TIM3-GFP⁺⁺ T-cells had a significantly reduced length to width ratio *versus* Ftractin-GFP⁺⁺ control T-cells in the context of a lower peptide stimulus, three minutes after cell couple formation (Figure 4.8b).

Lamellipodia are membrane protrusions that enable a T-cell to stably adhere to its target and form an effective interface. Our lab has previously identified a phenotype of dysfunctional T-cells in which they display a higher frequency of off-interface lamellipodia (OIL). These OIL are likely to destabilise the T-cell: APC interface because rather than moving towards the target cell to support the interface, they momentarily pull the T-cell away from the interface. This has no productive outcome for T-cell delivery of the lytic hit. Ftractin-GFP⁺⁺ T-cells were found to display a higher mean percentage of OIL *versus* TIM3-GFP⁺⁺ T-cells in both higher and lower peptide stimulus conditions (Figure 4.8c). Moreover, the mean time after cell couple formation at which the OIL formed was significantly and non-significantly longer amongst TIM3⁺⁺ T-cells *versus* Ftractin⁺⁺ control cells in the context of higher and lower peptide stimulus, respectively (Figure 4.8d).

Overall, this data suggests that TIM3 overexpression may enhance the polarisation of T-cells and also the ability of these T-cells to stabilise their interface with Renca target cells in the 2D model.



● Ftractin-GFP⁺ RencaHA^{tdT}
 ● TIM3-GFP⁺ RencaHA^{tdT}

Figure 4.8 Overexpression of TIM3-GFP by CL4 T-cells, under higher and lower peptide stimulus conditions, did not and did affect T-cell elongation, respectively. Overexpression of TIM3-GFP by CL4 T-cells decreased the percentage of T-cells with off-interface lamellipodia and delayed the onset of off-interface lamellipodia in the context of both higher and lower peptide stimulus.

a) Fura-2-loaded CL4 T-cells that overexpressed F-actin-GFP or TIM3-GFP were plated onto a RencaHA^{tdT} target monolayer, which had either been pulsed with 2µg/ml K^dHA (higher peptide stimulus) or left unpulsed (lower peptide stimulus). **b)** The length (red line) and width (yellow line) of T-cells were measured upon tight coupling to targets as seen in the representative images, top panel; the graph below shows the ratio of length/width at 0-3mins after tight-cell coupling. Individual points represent a single T-cell. Data are from ≥22 cell couples per group, from at least three independent repeats per group. **c)** Representative images show a T-cell (top) coupling to a tumour cell (below) with the interface indicated by a blue line; the left image shows a cell couple where the T-cell does not display off-interface lamellipodia (OIL), while the right image shows the subsequent timepoint in which an OIL is observed, indicated by the red arrow. The percentage of T-cells with off-interface lamellipodia (OIL) is shown in the graph below, from three independent repeats per group. Individual points show the mean for an independent repeat. **d)** Time of the first appearance of off-synapse lamellipodia, from three independent repeats per group. Individual points represent a single T-cell. For all graphs, error bars show mean ± SEM and ns = non-significant p-values across all comparisons.

4.2.6. The TIM3 cytoplasmic tail mediated the enhanced IFN γ secretion, coupling frequency and improved interface stability of TIM3 overexpressing CL4 T-cells in 2D

It was of interest to determine if the TIM3 cytoplasmic tail was also responsible for the small stimulatory effects of TIM3 expression in 2D, as well as the suppressive effect in 3D. TIM3^{cyt-ve}-GFP⁺⁺ and TIM3-GFP⁺⁺ T-cells were plated onto 2D RencaHA^{tdT} target cells in the 2D microscopic cytotoxicity assay. As before, RencaHA^{tdT} targets were either pulsed with 2 μ g/ml K^dHA peptide or left unpulsed in order to produce targets with higher or lower peptide concentration at their surface. With a lower, but not higher, peptide stimulus TIM3-GFP⁺⁺ T-cells had a significantly higher ability to kill *versus* the truncated TIM3^{cyt-ve}-GFP T-cells (Figure 4.9a). Interestingly, a significantly higher level of IFN γ was secreted by TIM3-GFP⁺⁺ *versus* TIM3^{cyt-ve}-GFP⁺⁺ T-cells under lower peptide stimulus conditions. A non-significant similar trend in two out of three independent repeats was seen under higher peptide stimulus conditions. Together, these findings support the notion that a stimulatory role of TIM3 overexpression is mediated by the TIM3 cytoplasmic tail in the 2D system (Figure 4.9b).

As we previously found that TIM3-GFP overexpression conferred cells with an enhanced ability to form cell couples with target cells, we investigated if this was mediated by the TIM3 cytoplasmic tail. In previous data, the effects of TIM3-GFP overexpression *versus* control cells on coupling frequency or polarisation (Figure 4.7b, Figure 4.8a, b, c) did not vary depending on the level of peptide stimulus. Therefore, we only used unpulsed RencaHA^{tdT} target cells for these experiments; moreover, in this dataset the differences in rate of killing and IFN γ secretion levels were only significant in the context of a lower peptide stimulus (Figure 4.9a, b). In two independent experiments we found that there was a small non-significant increase in coupling frequencies amongst TIM3-GFP⁺⁺ *versus* TIM3^{cyt-ve}-GFP⁺⁺ T-cells, consistent with the effect of TIM3-GFP⁺⁺ overexpression *versus* Ftractin-GFP⁺⁺ control T-cells (Figure 4.9c).

As before (Figure 4.8a, b, c), we investigated whether TIM3⁺⁺ T-cells had enhanced polarisation and interface stability *versus* the TIM3^{cyt-ve}-GFP⁺⁺ cells. T-cell morphology (length/width ratio) between TIM3-GFP⁺⁺ and TIM3^{cyt-ve}-GFP⁺⁺ T-cells did not significantly differ between conditions (Figure 4.9d). The percentage of T-cells that displayed interface-destabilising OIL was significantly lower among TIM3-GFP⁺⁺ T-cells *versus* TIM3^{cyt-ve}-GFP⁺⁺ T-cells (Figure 4.9e). Moreover, the mean time after cell couple formation at which the OIL formed was significantly longer among TIM3-GFP⁺⁺ T-cells *versus* TIM3^{cyt-ve}-GFP⁺⁺ cells (Figure 4.9f).

Overall, this data supports the idea that the TIM3 cytoplasmic tail mediates the increased capacity of TIM3-overexpressing CL4 T-cells to couple and maintain stable interfaces with their targets in the 2D Renca model.

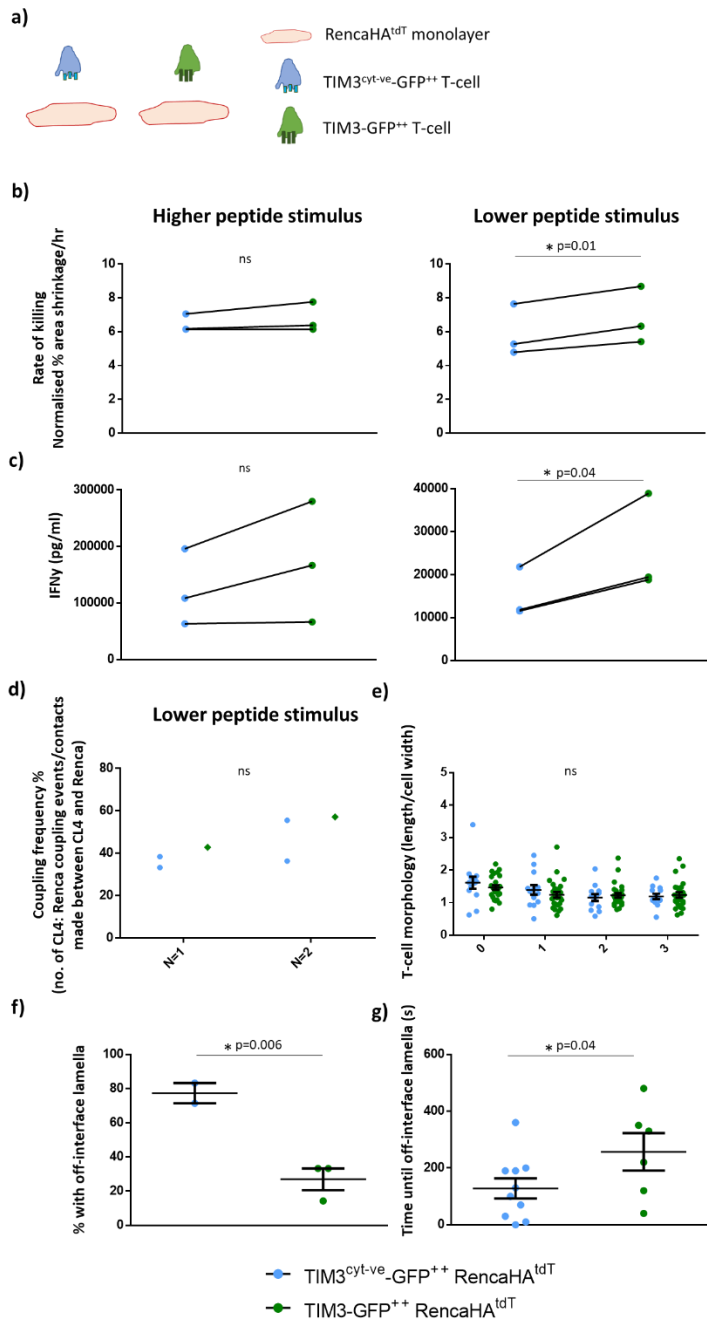


Figure 4.9 Data indicated that the TIM3 cytoplasmic tail enhanced the rate of killing and IFN γ secretion levels of TIM3-overexpressing CL4 under both higher and lower peptide stimulus conditions, with differences more evident in the context of a lower peptide stimulus. Under lower peptide stimulus, the TIM3 cytoplasmic tail also seemed to stabilise the interface between CL4 T-cells and target cells.

a) Fura-2-loaded CL4 T-cells that overexpressed TIM3^{cyt-ve}-GFP or TIM3-GFP were plated onto a RencaHA^{tdT} target monolayer, which had either been pulsed with 2 μ g/ml K^dHA (higher peptide stimulus) or left unpulsed (lower peptide stimulus). **b)** Each point shows the mean rate of killing by CL4 T-cells that overexpressed TIM3^{cyt-ve}-GFP or TIM3-GFP, from one of three independent repeats, with four replicate wells per group. Individual points represent the mean from an independent repeat and lines connect data from the same independent repeat. Means were compared using a one-tailed, paired t-test. **c)** IFN γ concentration of the supernatant from wells of the 2D microscopic cytotoxicity assay, individual points represent the mean from three replicate wells. Means were compared using a one-tailed paired t-test. **d)** Cell coupling frequencies are shown with each dot representing the proportion of cell couples observed in an individual

imaging run (imaging of one well for 15 minutes). Two imaging runs were conducted on TIM3^{cyt-ve}-GFP⁺⁺ T-cells in each of two independent repeats, while one imaging run was conducted for TIM3-GFP⁺⁺ T-cells in each independent repeat. **e)** The length and width of T-cells were measured upon tight coupling to targets; the ratio of length/width is shown at 0-3mins after tight-cell coupling. 26 and 13 cell couples were analysed for TIM3-GFP and TIM3^{cyt-ve}-GFP, respectively. Means were compared from two independent repeats by One-Way ANOVA. **f)** The percentage of T-cells with off-synapse lamellipodia, analysed across all coupling T-cells. **g)** time of the first appearance of off-synapse lamellipodia from two independent repeats. 6 and 10 T-cells were analysed for TIM3-GFP and TIM3^{cyt-ve}-GFP, respectively. Means in **f)** and **g)** were compared using a one-tailed unpaired t-test. Error bars show mean \pm SEM. ns = non-significant p-values across all comparisons.

4.2.7. Cell surface expression of MHC-I, CEACAM1 and Galectin-9 did not differ between RencaHA^{tdT} cells cultured in 2D and 3D.

Previous data demonstrated that TIM3 overexpression had a suppressive effect on CL4 T-cells cytotoxicity in the 3D but not the 2D microscopic assay. Therefore, we hypothesised that TIM3 ligand expression or K^dHA peptide presentation by Renca cells may differ between the 2D and 3D models. To assess whether there were differences in the cell surface expression of CEACAM1, Galectin-9 or MHC-I between RencaHA^{tdT} cells grown in 2D or 3D, single cell suspensions of Renca cells from 2D culture or spheroids were generated and stained to assess expression levels by flow cytometry. Live, single RencaHA^{tdT} cells were gated using the gating strategy shown in Supplementary Figure 8.1 for subsequent staining. No significant differences between the expression of these molecules were found between 2D and 3D cultured RencaHA^{tdT} cells, although there was a trend towards enhanced Galectin-9 expression in the 3D *versus* 2D system (Figure 4.10a, b). Notably, Galectin-9 is a highly secreted molecule and HMGB1 (a damage-associated molecular pattern protein which enables DCs to sense tumour-derived nucleic acids) can be secreted by tumour cells, thus it is of interest to establish the concentrations of these soluble TIM3 ligands in each system (439, 440). Regarding Galectin-9, the small increases in both the staining MFI and percentage of Galectin-9-positive cells in the 3D *versus* 2D culture makes it conceivable that there are larger differences in the soluble Galectin-9 concentrations between these systems. This is because soluble Galectin-9 could accumulate over time during the microscopic cytotoxicity assays, whereas the cell surface Galectin-9 expression levels represent a snapshot in time. Thus, we cannot rule out that differences in soluble Galectin-9 concentrations account for the different effects of TIM3 overexpression in the 2D and 3D systems. Moreover, the expression level of the TIM3 ligand phosphatidylserine was not assessed and could account for the differences observed. Furthermore, an unknown TIM3 ligand or factor may have caused the different effects of TIM3 overexpression between 2D and 3D systems.

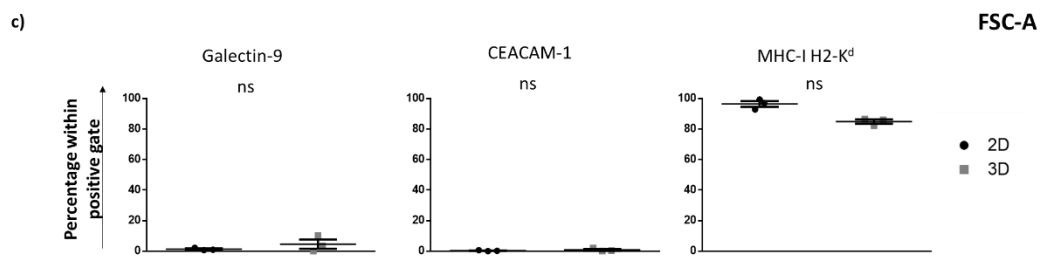
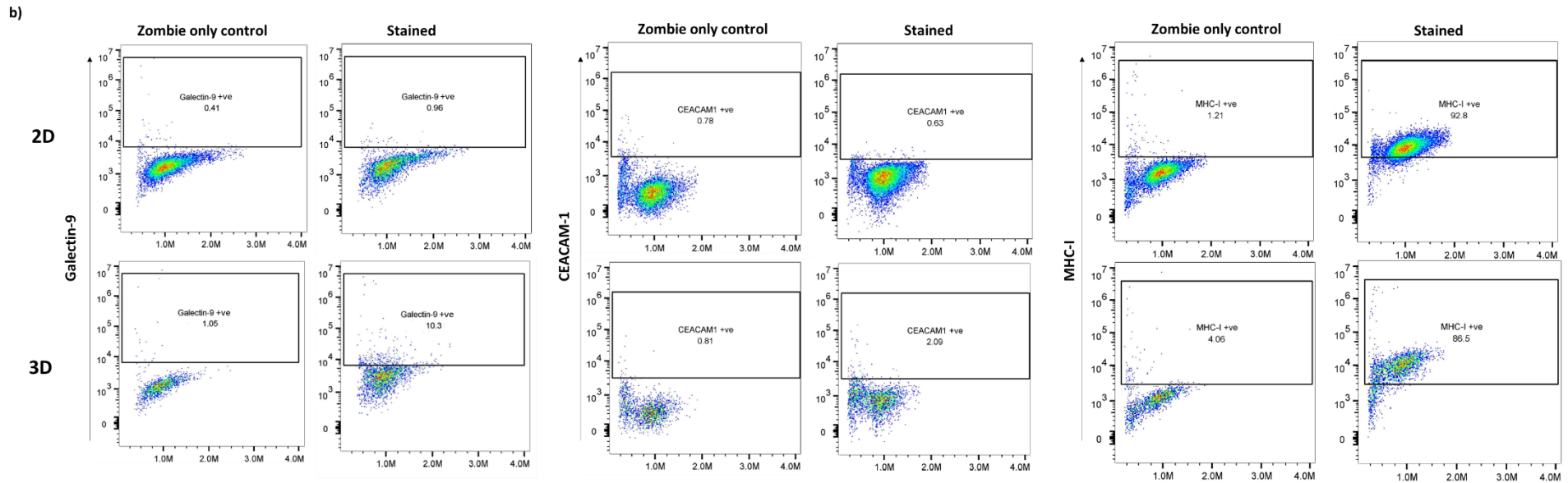
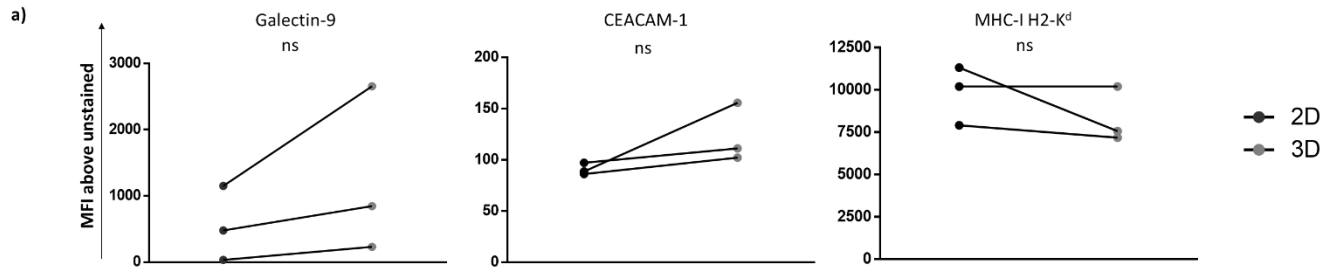


Figure 4.10 Cell surface expression levels of CEACAM1, Galectin-9 and MHC I did not significantly differ between Renca cells grown in 3D and 2D.

a) Renca cells from 2D and 3D culture were stained for Galectin-9, CEACAM1 and MHC-I. Median fluorescent intensity (MFI) above the control unstained (zombie dyed only) sample is shown. Each point represents the mean MFI from one of three independent repeats, and lines join means from the same independent repeat. Means were compared using one-tailed t-tests. **b)** Representative flow cytometry dot plots of Galectin-9, CEACAM1 and MHC-I cell surface expression by Renca cells grown in 2D and 3D, unstained (zombie dyed only) samples are shown alongside stained samples. **c)** Percentage of the Renca populations from 2D and 3D culture that fell within the positive gate for each of the three markers, with each data point representing one of three independent repeats.

4.3 Discussion

TIM3 is now widely regarded as a T-cell inhibitory receptor (246), based on an accumulation of *in vivo* and several *in vitro* 2D studies, yet there is evidence that it can amplify TCR signalling in 2D *in vitro* systems (215, 216). It is likely that TIM3 may signal differentially in a context-dependent manner, according to the availability of its ligands, other T-cell regulatory molecules and other unknown factors. Therefore, it is important to understand under what conditions TIM3 may enhance or inhibit CD8 T-cell effector function in order to better target TIM3 function for treatment of cancer, autoimmunity, or chronic infection. Since a 2D *versus* 3D tumour environment is likely to influence how TIM3 regulates the CD8 T-cell anti-tumour response, we investigated TIM3 function in both 2D and 3D RencaHA^{tdT} models. Moreover, it is unclear whether TIM3 blockade can directly modulate tumour-specific CD8 T-cell cytotoxicity in the absence of other cell types. This is important to determine in order to improve our understanding of which cell types mediate the therapeutic effects of TIM3 blockade, that are commonly observed in *in vivo* preclinical models. The findings in this chapter provide new insight into factors that influence TIM3 signalling in tumour-specific CD8 T-cells within the TME.

4.3.1. TIM3 overexpression by CL4 T-cells suppresses T-cell cytotoxicity in the RencaHA^{tdT} 3D model, in a manner reversible by acute anti-TIM3 blockade and dependent upon the TIM3 cytoplasmic tail.

We found that CL4 SILs transduced to overexpress TIM3-GFP exhibited suppressed cytotoxicity against RencaHA^{tdT} spheroids *versus* Ftractin-GFP-overexpressing SILs and this suppression was reversed using acute anti-TIM3 blockade. Furthermore, our data suggest the suppressive function of TIM3 is mediated by its cytoplasmic tail, as SILs overexpressing full-length TIM3 had reduced cytotoxicity compared to SILs that overexpressed truncated TIM3, without the cytoplasmic tail. This data corroborated studies which have demonstrated that TIM3 blockade synergises with PD-1 blockade to restrict tumour growth (325, 441) and improve *ex vivo* effector function of patient-derived CD8 T-cells (430, 442, 443). Further in support of an inhibitory role for TIM3, PD-1⁺TIM3⁺ TILs have been identified to be the most exhausted and abundant TILs in murine models of acute myelogenous leukaemia, CT26 colorectal cancer, B16 melanoma, and 4T1 mammary adenocarcinoma models; producing low levels of IL-2, IFN γ and failing to proliferate (325, 327). Additionally, TIM3 upregulation on exhausted T-cells is IL-27 dependent and causes T-cells to have low IL-2 and IFN γ -producing ability (181, 182). Importantly, our data support reports that TIM3 expression is associated with lower survival amongst patients with solid cancers (444) and that the number of TIM3⁺ TILs can act as a negative prognostic factor (445).

While *in vivo* models have identified inhibitory roles for TIM3 on CD8 T-cells by staining for TIM3 expression and applying TIM3 blockade, these studies cannot rule out the impact of other cell types on the therapeutic effect of TIM3 blockade. TIM3 has been shown to suppress anti-tumour NK cell cytotoxicity *in vitro* (252) and support NK-cell-dependent maternal-foetal tolerance (205). TIM3 can reduce CD8⁺ T-cell cytotoxicity indirectly by limiting CXCL9 secretion by tumour-associated DCs (206) and inhibit the activation of nucleic acid-sensing TLRs on intratumoural DCs in a HMGB1-dependent manner (242). Furthermore, in macrophages, TIM3 has been found to inhibit the release of proinflammatory cytokines (251), and reduce the engulfment of pathogenic bacteria (209). Some *in vitro* systems which have assessed TIM3 function include other immune cell types, for example, TIM3 blockade was shown to enhance the percentage of melanoma patient-derived IFN γ -producing CD8 T-cells during acute stimulation with NY-ESO-1 peptide-loaded PBMCs *in vitro* (430). In contrast, our study provides evidence for a direct inhibitory effect of TIM3 on tumour-infiltrating CD8 T-cells in a tumour spheroid model, in the absence of other immune cells. In corroboration of the idea that TIM3 can directly suppress T-cell function, an *in vitro* study stimulated Jurkat T-cells with anti-CD3/CD28 beads and found that TIM3 overexpression suppressed NFAT and NF κ B activity, and IL-2 secretion (425). Moreover, an *in vitro* system containing Galectin-9 expressing peptide-loaded B-cell lines and primary CD8 T-cells from healthy donors showed that TIM3 overexpression could cause Lck inactivation in primary CD8 T-cells, via induced TIM3 colocalisation with phosphatases in TCR clusters (426). Together with our data, these studies support the idea that TIM3 can directly suppress tumour-specific CD8 T-cells in the absence of other immune cells, in addition to regulation of other immune cell subsets. While it will be important to determine the relative influence of TIM3 on the anti-tumour function of various cell types within the TME, these findings demonstrate that functionally relevant TIM3 signalling pathways can be studied within reductionist CD8 T-cell: tumour models.

4.3.2. In the RencaHA^{tdT} 2D model, TIM3 overexpression had no significant effect on T-cell cytotoxicity or calcium flux but in a cytoplasmic tail-dependent manner: enhanced IFN γ secretion, and T-cell coupling frequencies.

In contrast to our findings using the 3D model, we found overexpression of TIM3-GFP by CL4 T-cells had a minimally positive effect on cytotoxicity against RencaHA^{tdT} monolayer targets *versus* Ftractin-GFP-overexpressing T-cells and this was indicated to rely on the cytoplasmic tail. It is worth noting that findings acquired by another member of the lab using HA^{pep}-pulsed RencaWT target cells found that TIM3 overexpression significantly enhanced T-cell cytotoxicity, supporting the notion that TIM3 can enhance T-cell cytotoxicity (data not shown). Furthermore, acute anti-TIM3 blockade had no effect, suggesting that TIM3 ligands known to cause inhibitory signalling through TIM3 were absent or at insufficient levels in this system. Interestingly, expression levels of the putative TIM3 ligands CEACAM1 and Galectin-9, did not significantly differ between the 3D

and 2D systems, although there was a consistent trend wherein Galectin-9 levels were elevated in the 3D system. As Galectin-9 is highly secreted, it is conceivable that the levels of soluble Galectin-9 may differ substantially more than the cell surface levels. This is because over the duration of the cytotoxicity assays, soluble Galectin-9 would likely accumulate in the wells. Furthermore, in the 3D model, the ECM of Matrigel provides a carbohydrate-rich scaffold in which soluble Galectin-9 can bind to glycosylated molecules and concentrate locally around the spheroids (446, 447). In contrast, in the 2D model, secreted galectin-9 would be free to diffuse throughout the entire medium thus leading to reduced interactions between galectin-9 and the T-cells *versus* the 3D system. Therefore, it is possible that enhanced galectin-9 expression by Renca cells in the 3D *versus* 2D model contributed to the different effects of TIM3 overexpression on T-cell cytotoxicity; it would be of interest to investigate this in future. Although the TIM3 blocking antibody used in these experiments is described to block the CEACAM1 and PtdSer binding sites on TIM3 (but not Galectin-9) (244), Galectin-9 may still have an accessory role in determining the effect of TIM3 blockade. This is because it has a distinct binding site on TIM3 and comprises two carbohydrate recognition domains joined by a flexible linker, which could enable it to bring together TIM3 and another TIM3 ligand, potentially enhancing T-cell suppression downstream of TIM3 ligation by that ligand (244). Additionally, the expression of MHC-I H2-K^d, which restricts the K^dHA peptide also did not differ suggesting that the availability of cognate pMHC was similar between the two systems. Levels of phosphatidylserine, which is blocked (in addition to CEACAM1) from interacting with TIM3 by the antibody used in this study, was not assessed in the 2D and 3D systems, but could also account for the differences (244). Alternatively, an unknown ligand or factor could be responsible, as some reports argue that Galectin-9 and CEACAM1 are not functional ligands of TIM3 (233, 255). Moreover, in the 2D system, TIM3 overexpression endowed T-cells with an enhanced ability to secrete IFN γ during cytotoxicity assays; again, this seemed to rely upon an intact TIM3 cytoplasmic tail. This finding corroborates data from the first study to describe a stimulatory role for unligated TIM3, which found that TIM3 overexpression enhanced IFN γ secretion (216). Interestingly, agonistic antibody abolished the stimulatory effect of TIM3 in that study, however we did not employ an agonistic antibody in this study (216). Another study provided evidence that TIM3 overexpression could cause stimulatory effects. Bat-3 binding to the cytoplasmic tail of unligated TIM3 was shown to recruit the active form of Lck to the IS to enhance IFN γ and IL-2 secretion, while reducing IL-10 secretion (215). In that study, ligation of TIM3 caused the release of Bat-3 from the cytoplasmic tail and the absence of Bat-3 in adoptively transferred CD4 T-cells increased the proportion of TIM3^{hi}IFN γ ^{lo} T-cells within an EAE model, suggesting that unligated TIM3 could stimulate IFN γ production in a Bat-3-dependent manner (215). On the other hand, this data contrasts with studies using hTIM3 where hTIM3 was found to suppress IL-2 production, NF κ B and NFAT activity in Jurkat cell lines (424, 425). In corroboration with a previous

study, there was no effect of TIM3 overexpression on intracellular calcium levels during T-cell activation (425). Interestingly, however, TIM3 overexpression enhanced the proportion of T-cells that formed cell couples with tumour cells, suggesting that in some contexts TIM3 could have a supportive role for tumour killing by CD8 T-cells. Together, the 2D and 3D data suggest that TIM3 can have both stimulatory and suppressive effects on CD8 tumour-specific T-cells, respectively, but the factors responsible for these differences are unknown. Identification of these factors could reveal new important modulators of TIM3 signalling.

4.3.2.1 In the RencaHA^{tdT} 2D model, during T-cell: tumour cell coupling, TIM3 overexpression slightly enhanced T-cell morphological polarisation that is conducive to delivery of the lytic hit, and enhanced T-cell: tumour cell interface stability.

As previous data indicated that TIM3 overexpression enhanced the ability of T-cells to commit to cell couples with 2D targets, we further investigated the morphological polarisation of T-cells upon cell coupling to tumour targets and the stability of the interfaces formed. In CD4 T-cells coupling to DCs, a more elongated morphology has been associated with a reduced F-actin accumulation at the IS and reduced calcium flux (434). Moreover, in CD4 T-cells coupling to B-cells, 3 stages have been defined: contact, partial engulfment (of the B-cell by the T-cell) and stabilisation of the interface (435). In that study, contact and partial engulfment occurred prior to the rise in calcium and during the stabilisation phase a more rounded morphology was associated with higher calcium signalling and a more stable interface (435). Although we saw no effect of TIM3 overexpression on intracellular calcium flux, we investigated whether TIM3 might regulate CD8 T-cell morphology upon coupling to targets, to enhance T-cell activation and potentially contribute to enhanced IFN γ secretion. TIM3 overexpression enabled T-cells to form a slightly more rounded morphology at later timepoints upon cell coupling to target cells under lower (unpulsed) but not higher peptide stimulus (2 μ g/ml K^dHA-pulsed) conditions, compared to F-actin control cells. However, compared to T-cells that overexpressed truncated TIM3 without the cytoplasmic tail (TIM3^{cyt-ve}), TIM3 overexpressing cells had a slightly more rounded morphology at earlier but not later timepoints (under lower peptide conditions). Overall, though there were different temporal patterns when using F-actin or TIM3^{cyt-ve} control cells, the data indicated that the cytoplasmic tail of TIM3 can support the adoption of a more rounded morphology by CD8 T-cells during the first three minutes of T-cell: tumour cell coupling. However, this effect was small and only evident under lower but not higher peptide stimulus conditions.

Next, we investigated how TIM3 might regulate the stability of the interface between CL4 T-cells and tumour targets. Our lab has previously observed that suppressed CL4 TILs display a higher frequency of off-interface lamellipodia (OIL) compared to *in vitro* cultured CL4 T-cells (187). These OIL are thought to destabilise the interface as they do not support T-cell attachment to the APC,

but instead pull the T-cell away from its target with no productive outcome for IS formation. Thus, it was of interest to determine if TIM3 might regulate the development of OIL. T-cells that overexpressed TIM3 displayed a lower frequency of OIL, later after cell couple formation, *versus* control Ftractin T-cells under both lower and higher peptide stimulus. The same effect was observed when T-cells overexpressing TIM3 were compared to TIM3^{noct} T-cells under lower peptide stimulus conditions. Overall, this data suggested that TIM3 signals through its cytoplasmic tail to reduce the frequency of OIL and support interface stability; along with the enhanced IFN γ secretion associated with TIM3 overexpression, this suggests that TIM3 can elevate T-cell activation and support delivery of the lytic hit through a more stable synapse in certain contexts. These findings are in corroboration with other evidence that TIM3 regulates synapse stability, as TIM3 blockade treatment was shown to increase the stability of interfaces between TIM3-expressing CD8 T-cells and galectin-9-expressing B-cells, as measured by CD3 enrichment at the IS (426). In our 2D system, the Renca targets expressed little if any of the TIM3 ligands galectin-9 and CEACAM1 on the cell surface, while TIM3 blockade has no effect, suggesting that the enhancement of synapse stability observed herein may occur downstream of unligated TIM3.

4.3.3. Conclusion

In conclusion, the RencaHA^{tdT} 2D and 3D models revealed context-dependent TIM3 signalling, dependent upon the TIM3 cytoplasmic tail, that modulated the functional efficacy of the tumour-specific CD8 T-cell response. Notably, we provide evidence that TIM3 had a small costimulatory effect on CD8 T-cells coincubated with 2D RencaHA^{tdT} targets via: a minor increase in cytotoxicity, elevation of IFN γ secretion, enhancement of the ability of CD8 T-cells to form couples with targets and stabilisation of the interface formed upon cell coupling between T-cells and tumour cells. Costimulatory effects of TIM3 in the 2D model were unaffected by TIM3 blockade treatment. Furthermore, we show that TIM3 had an inhibitory effect on CD8 T-cell cytotoxicity in the 3D RencaHA^{tdT} model and that the TIM3-mediated suppression could be reversed using acute TIM3 blockade (via the RMT3-23 monoclonal antibody). This provides evidence that TIM3 blockade can directly reverse the suppression of CD8 T-cell cytotoxicity, in the absence of other cell types.

In the following chapter, the 2D and 3D RencaHA^{tdT} models will be used to investigate whether a 2D *versus* 3D environment modulates if and how CEACAM1 and TIM3, *in cis* and *in trans*, coregulate the function of tumour-specific CD8 T-cells. CEACAM1 is the most recently proposed TIM3 ligand, but there is limited data on if and how CEACAM1 and TIM3 directly coregulate the function of tumour-specific CD8 T-cells, in the absence of other cell types, while *in vitro* data using 2D models have been conflicting. Thus, investigation of whether and how CEACAM1 modulates TIM3 signalling using our 2D and 3D models could help to shed light on these areas.

Chapter 5 Regulation of tumour-specific CD8 T-cell function by CEACAM1 and TIM3

5.1 Introduction

CEACAM1 was first described as a ligand for TIM3 *in cis* and *in trans* in 2015, where it was found to enhance TIM3 coexpression and induce inhibitory TIM3 signalling on the surface of T-cells, however, this has been disputed (221, 255). In humans, there are nine transmembrane-anchored and three secreted CEACAM1 isoforms which have one variable Ig domain and up to three extracellular constant Ig domains (254). Moreover, there are two types of CEACAM1 cytoplasmic domain: long (L) and short (S) which do and do not contain two ITIM motifs, respectively (254). CEACAM1-L isoforms are more commonly expressed in activated T-cells, except for in intestinal tissue, where CEACAM1-S isoforms dominate (254, 448). In mice, there are four isoforms including two long and two short isoforms. CEACAM1-4L, with four Ig domains, is the most abundantly expressed by human and murine T-cells (254). It is unclear whether transmembrane isoforms of CEACAM1-L have differential signalling, though all isoforms have the N-terminal Ig domain which is purported to bind to the FGCC' cleft of TIM3 (221, 246, 449).

Both TIM3 and CEACAM1-L have been separately associated with suppressing T-cells: TIM3 upregulation has been shown to reduce stimulatory IL-2, NFAT and NFκB activity and promote TIL exhaustion; although the mechanism for TIM3 inhibitory signalling is unknown, current evidence suggests that TIM3 suppresses TCR proximal signalling. TIM3 ligation leads to dissociation of BAT3 from the cytoplasmic tail and subsequent recruitment of the Src kinase FYN (215, 216); FYN is known to phosphorylate PAG, enabling recruitment of the tyrosine kinase Csk to lipid rafts containing active Lck (222). Csk facilitates inhibitory phosphorylation of Y505 on Lck, suggesting recruitment of FYN to the IS is one way in which ligated TIM3 suppresses TCR proximal signalling (222, 429). TIM3 has also been found in lipid rafts at the immune synapse (IS) of primary human CD8 T-cells bound to galectin-9 expressing B cells, where it was found to reduce synapse stability as measured by enrichment of CD3 at the cell couple interface (426). Moreover, during cell coupling between TIM3-expressing CD8 T-cells and galectin-9-expressing B cells, TIM3 colocalised with the phosphatase CD45 at the IS, suggesting that ligated TIM3 could recruit CD45 upon engagement with galectin-9 to inactivate Lck and suppress TCR proximal signalling (426). The intracellular tail of CEACAM1-L can recruit SHP-1 to dephosphorylate the TCR CD3-ζ chain and ZAP-70 to inhibit proximal T-cell signalling (450). Importantly, TIM3 and CEACAM1 coexpression has been described as a marker of highly exhausted TILs (248). In the *in vivo* RencaHA tumour model of adoptive T-cell transfer therapy used by our lab, CEACAM1 was found to be coexpressed with TIM3 and PD1 on 41% of CL4 TILs but less than 0.5% of CL4 T-cells from *in vitro* culture (382).

CL4 TILs displayed reduced cytotoxicity, intracellular calcium signalling and cell coupling abilities compared to *in vitro* cultured CL4 T-cells, thus associating CEACAM1 and TIM3 coexpression with T-cell suppression (187, 382). Supporting a role of CEACAM1 *in trans* to limit the T-cell response and enable immune tolerance, naïve CD4 T-cells from transgenic OT-II Rag2^{-/-} mice were shown to exhibit higher proliferation when adoptively transferred into OVA-immunised CEACAM1^{-/-} versus WT mice (221). CEACAM1 is a promising target to both suppress tumour growth directly and enhance the anti-tumour T-cell response: CEACAM1 has been found to promote tumour invasiveness and metastasis in addition to its immunomodulatory role, while increased intratumoural CEACAM1 expression has been associated with increased tumour progression in a range of cancers including melanoma, colorectal, lung, pancreatic and bladder cancer (254).

CEACAM1 as a regulator of TIM3 expression *in cis*:

A recent study proposed that CEACAM1 promoted TIM3 surface expression *in cis* in Jurkat cells (247). Furthermore, in primary human CD8 T-cells, the patterns of CEACAM1 and TIM3 cell surface expression were similar following *in vitro* activation; surface expression of both receptors was high during the early post-activation expansion phase and lower in late-stage effectors (247). In systems which co-transfected HEK293T cells with CEACAM1 and TIM3 to investigate coregulation of expression, conflicting evidence has been found. In support of CEACAM1 regulation of TIM3 expression, flag-tagged CEACAM1 enhanced HA-tagged hTIM3 expression at the surface of HEK293T cells and nearly all hTIM3-positive cells were CEACAM1 positive (221). Furthermore, hCEACAM1 and hTIM3 could be coimmunoprecipitated from HEK293T and activated primary CD4 T-cells, while mutations of the residues in the CEACAM1 or TIM3 IgV domains predicted to enable binding disrupted the coimmunoprecipitation (221). Moreover, spatial colocalization of hTIM3 and hCEACAM1 was found at the immune synapse of both HEK293T and activated CD4 and CD8 T-cells (221). In contrast, another study found that cotransfection of HEK293T with CEACAM1 had no effect on hTIM3 expression (255). On the other hand, CD4 T-cells from CEACAM1-deficient but not WT mice lacked TIM3 expression when the mice were administered the superantigen *Staphylococcus aureus* enterotoxin B (SEB) for tolerance induction, suggesting CEACAM1 was required for TIM3 expression (221). However, *in vitro* stimulation of healthy donor blood with superantigen staphylococcal enterotoxin E (SEE) induced upregulation of TIM3 on all proliferating CD4 and CD8 T-cells, while CEACAM1 upregulation was more delayed and restricted to a subset of that population, suggesting CEACAM1 expression *in cis* is not necessary for TIM3 surface expression (255). Overall, further investigation is needed to determine if CEACAM1 *in cis* promotes TIM3 cell surface expression as the evidence so far is limited.

CEACAM1 as a TIM3 ligand or indirect coregulator of T-cell function *in cis*

Regardless of coregulation of expression between these receptors, there is evidence that coexpression coregulates T-cell function and this may differ between CD4 and CD8 T-cells. It was shown that blood samples from HIV-infected individuals had an increased proportion of CD4 CEACAM1⁺TIM3⁺ T-cells compared to non-infected controls, but the equivalent CD8 subset did not change (221). In both CD4 and CD8 T-cells the proportion of IFN- γ -producing cells was lowest in the double *versus* single positive subsets, indicating that suppressive signalling resulting from CEACAM1 and TIM3 coexpression is shared across these subsets (221). Interestingly, coexpression of CEACAM1 and TIM3 had a larger suppressive effect in CD8 T-cells, whereas in CD4 T-cells CEACAM1 alone seemed to play a bigger suppressive role (221). It is of interest to determine if CEACAM1 coregulates CD8 T-cell function with TIM3 *in cis*, either through direct binding or indirectly. In further support of the idea that coexpression of CEACAM1 and TIM3 can enhance inhibitory signalling *in cis*, following the transfer of naïve WT T-cells into CEACAM1^{-/-} Rag^{-/-} mice in a colitis model, colon-infiltrating CEACAM1⁺TIM3⁺ cells expressed decreased levels of IFN- γ , IL-2 and IL-17 relative to lamina propria T-cells that expressed neither or either receptor alone (221). In addition, *in vivo* data from colorectal cancer patients has shown that the percentage of CEACAM1⁺TIM3⁺ CD8 T-cells in patient blood samples is positively correlated with more advanced stages of cancer (248). CEACAM1⁺TIM3⁺ cells from patients were also the most suppressed TIL subset compared to T-cells that were single-positive or double-negative for these receptors, with the lowest percentage of IFN- γ producing cells (248). Thus, based on its availability to TIM3 on activated T-cells and the additive suppressive effect of TIM3 and CEACAM1 coexpression *in cis*, CEACAM1 *in cis* is a strong candidate TIM3 ligand, while it is also well-positioned to modulate TIM3 signalling indirectly independent of direct binding. In the theoretical case of direct binding, the binding sites between CEACAM1 and TIM3 *in cis* are unknown, although it is conceivable that binding of CEACAM1 *in cis* may occur at the same sites as CEACAM1 binding to TIM3 *in trans*. Through its IgV domain, CEACAM1 *in trans* has been shown to bind to TIM3 at the FGCC' cleft of the TIM3 IgV domain; similarly, coimmunoprecipitation with mutant forms of CEACAM1 and TIM3 indicated that they bind *in cis* via their IgV domains, although this has yet to be replicated (221, 449). As murine and human TIM3 blockade antibodies with therapeutic effect bind to the TIM3 FGCC' cleft to block CEACAM1 binding to TIM3 *in trans*, it is of interest to determine if TIM3 blockade antibodies with therapeutic efficacy also block interactions between CEACAM1 and TIM3 *in cis* to regulate CD8 T-cell function- accordingly, this would indicate whether CEACAM1 *in cis* can bind to the FGCC' cleft of TIM3 (244).

CEACAM1 as a TIM3 ligand or indirect coregulator of T-cell function *in trans*

Upon TIM3 ligation, BAT3 dissociation from the TIM3 cytoplasmic tail is a proximal step in TIM-3 inhibitory signalling; this was first described in the context of galectin-9 binding to TIM3 (215). In support of CEACAM1 *in trans* regulation of TIM3 function, only CD4 T-cells from SEB-tolerised

Tim3^{Tg}, but not tolerization-resistant *Tim3^{Tg} Ceacam1^{-/-}* mice, showed BAT3 dissociation from mTIM3 when the N-terminal domain-Fc fusion protein from mCEACAM1 (N-CEACAM1-Fc) was bound to TIM3 *in trans* (221). This suggested that CEACAM1 expression *in cis* with TIM3 on T-cells was required for BAT3-mediated TIM3 inhibitory signalling induced by CEACAM1 *in trans*. Importantly, the study showed that N-CEACAM1-Fc, containing the CEACAM1 IgV domain fused to the Fc domain of IgG, bound similarly to *TIM3^{Tg}* and *TIM3^{Tg} Ceacam1^{-/-}* T-cells and very little to *Ceacam1^{-/-}* cells that lacked TIM3 expression (221). This supported the idea of a direct inhibitory heterophilic interaction between TIM3 and CEACAM1 *in trans* and *in cis*, that could mediate BAT3 release. In support of CEACAM1 as a TIM3 ligand *in cis* or *in trans*, CEACAM1 ligation of TIM3 appeared to support T-cell resistance to restimulation-induced cell death (RICD) in primary human CD8 T cells, by attenuating TIM3 costimulatory signalling (247). TIM3 costimulatory signalling was demonstrated by an increased phosphorylation of TCR signalling proteins and upregulation of the pro-apoptotic proteins BIM and FasL (247). TIM3 surface expression and intracellular localisation decreased and increased, respectively, as T-cells transitioned from the early post-activation expansion stage to late-stage effectors; similarly, CEACAM1 was expressed at lower levels on the surface of late-stage effector T-cells, compared to early post-expansion stage T-cells. The level of RICD in early post-activation stage T-cells could be decreased using recombinant CEACAM1 to disrupt putative endogenous TIM3-CEACAM1 interactions and siRNA knockdown of either CEACAM1 or TIM3, suggesting CEACAM1 induced inhibitory signals via binding to TIM3 (247). Additionally, RICD resistance could be abrogated by TIM3 blockade in T-cells using an antibody known to disrupt the CEACAM1 and TIM3 *in trans* interaction; this abrogation of RICD resistance occurred during the early expansion phase but not the late-effector stage following *in vitro* CD3/CD28/CD2-mediated activation, suggesting that different factors determine when CEACAM1 *in trans* and possibly *in cis*, induces inhibitory signalling via TIM3 (247). In contrast, a study using fluorescence resonance energy transfer (FRET) and binding assays with a triple parameter reporter (TPR) system, which enabled measurement of NFκB, AP-1 and NFAT nuclear activity in T-cell reporter cells, demonstrated no specific binding between CEACAM1 and TIM3 *in cis* or *in trans*. There was no effect of CEACAM1 *in cis* or *in trans* on AP1, NFAT or NFκB activity in TIM3-expressing T-cells (255). Moreover, T-cell reporter cells were transfected with chimeric receptors each comprised of: the TIM3 or CEACAM1 cytoplasmic domain, the CD28 transmembrane domain and the extracellular domain of the murine T-cell costimulatory receptor inducible costimulator (mICOS) (255). Ligation of chimeric TIM3 and CEACAM1 receptors with ICOS ligand (ICOS-L) expressed on T-cell stimulator cells induced inhibitory signalling via the cytoplasmic domain of both chimeric receptors, demonstrating inhibitory signalling could be mediated by both the TIM3 and CEACAM1 cytoplasmic tails (255). Overall, there is limited evidence on whether CEACAM1 *in*

trans acts as a TIM3 ligand, although there is more data to support the *in trans* versus *in cis* interaction.

CEACAM1 signalling and therapeutic synergy of TIM3 and CEACAM1 co-blockade

Recent evidence suggests how CEACAM1-L isoforms may mediate inhibitory signals; CEACAM1-4L ITIM phosphorylation by Lck required CEACAM1-4L homophilic binding and occurred prior to the association of CEACAM1-4L with SHP-1 and the TCR/CD3 complex (450). ITIM phosphorylation enabled CEACAM1-4L-mediated inhibitory signalling as CEACAM1-4L-associated SHP-1 reduced phosphorylation of ZAP-70, LAT, SLP76, ERK and PLC γ during TCR/CD3 ligation (450). Furthermore, CEACAM1-4L agonism using antibody that bound to the homophilic binding site (CC' loop within the IgV-domain) decreased T-cell degranulation (450). Thus, CEACAM1-4L inhibited proximal T-cell signalling to reduce T-cell cytotoxicity in the context of homophilic binding. Amongst CRC patients, the expression levels of TIM3 and CEACAM1 by CD8 TILs were shown to act as independent risk factors for CRC development, suggesting inhibitory signalling via CEACAM1 (248). On the other hand, stimulatory roles for CEACAM1-L have also been described including promotion of T-cell proliferation, NF κ B and AP-1 expression and stabilisation of the IS via Lck (451-453). Thus, CEACAM1, similar to TIM3, exhibits differential signalling in different experimental systems and the factors regulating this requires further investigation.

Additive effects of TIM3 and CEACAM1 co-blockade have been reported, suggesting that they both regulate T-cell cytotoxicity independently without clarifying whether they directly interact. In a murine model of glioblastoma anti-TIM3 or anti-CEACAM1 single blockade could induce around a third longer mean survival time, while co-blockade had an additive effect (249). The frequency of CD8 T-cells and proportion of Tregs was also increased and decreased, respectively, by both treatments alone with an additive effect upon co-blockade (249). Meanwhile, levels of IFN γ were highest, and levels of TGF β were lowest, in the combination treatment group compared to the single treatment groups (249). Long-term survivors also displayed immunological anti-tumour memory responses that prolonged their tumour-free status *versus* naïve mice upon tumour challenge (249). In a subcutaneous model of CT26 colorectal cancer, CEACAM1 and TIM3 co-blockade delayed tumour growth when administered on the same day as tumour cell inoculation, although TIM3 expression was associated with reduced TNF α and IL-2 production by PD1⁺ CD8 TILs following anti-CD3 activation, the study did not directly show the effect of CEACAM1 expression on T-cell function (221). Nevertheless, co-blockade enhanced TIL numbers in both CD4 and CD8 populations and expanded the tumour antigen-specific CD8 T-cell population (221). Co-blockade also elevated IFN- γ production by CD8 TILs and decreased IL-10 production by CD4 TILs (221). Lastly, tumour growth was decreased in CEACAM^{-/-} *versus* CEACAM^{+/+} mice, while CEACAM1 deficiency enhanced the number of tumour specific CD8⁺ cells in TDLN and decreased TIM3 expression by TILs (221). Thus, it is important to further elucidate the mechanisms by which CEACAM1 and TIM3 blockade therapies improve anti-tumour immunity and how they might interact with each other. Overall, these *in vivo* studies provide associative evidence, but do not

clarify whether CEACAM1 and TIM3 directly modulate CD8 T-cell responses or if these interactions affect other cell types to indirectly regulate CD8 T-cell responses; CEACAM1 is also expressed by CD4 T-cells, NK cells, B cells, neutrophils and macrophages (254), while TIM3 is expressed by CD4 T-cells, NK cells, DCs and macrophages. Previous studies also do not provide insight into how the coregulation of T-cells by TIM3 and CEACAM1 may differ in a 2D *versus* 3D tumour environment.

Rationale: investigating how CEACAM1 and TIM3 coregulate the function of tumour-specific CD8 T-cells *in cis* and *in trans* using the 2D and 3D Renca models

Overall, additive suppression of TILs by coexpression of TIM3 and CEACAM1 *in cis*, and the tumour-promoting effect of CEACAM1 upregulation on cancer cells, means these receptors are well-placed to act as binding partners or indirect coregulators that dampen T-cell cytotoxicity in the TME. Recent mechanistic studies provide evidence that CEACAM1 can promote TIM3 surface expression *in cis* and cause BAT3 release from the TIM3 cytoplasmic tail *in trans* -in the presence of CEACAM1 *in cis*- to dampen proximal signalling. However, opposing evidence argues that there are no functional interactions between TIM3 and CEACAM1 *in cis* or *in trans*. Data on CEACAM1 and TIM3 interactions are very limited and further investigation is necessary. CEACAM1 is a self-ligand *in cis* and *in trans* and it is unclear under what circumstances CEACAM1-CEACAM1 or putative CEACAM1-TIM3 interactions play a larger role in regulating the anti-tumour CD8 T-cell response. Regardless, the relevant ligands and coregulators of TIM3 signalling must be determined in order to understand the context-dependent nature of TIM3 signalling. Such knowledge will aid the optimisation of TIM3-targeting cancer therapies.

To our knowledge, previous studies that have investigated CEACAM1-mediated regulation of TIM3 signalling in T-cells have not measured how these receptors may directly coregulate the killing of tumour cells by CD8 T-cells, a parameter that is of primary importance for the targeting of TIM3 to improve anti-tumour immunity. Instead, previous studies have measured: cytokine secretion and transcription factor activity following stimulation of T-cells with anti-CD3 antibodies; the expression of CEACAM1 and TIM3 on TILs from mice or human patients, in parallel to tumour growth or progression of disease. Similarly, in non-tumour contexts, such as antigen-induced tolerance and viral infection, expression levels of CEACAM1 and TIM3 on T-cells has been measured in parallel with effector cytokine production by T-cells. Notably, *in vivo* models, although highly physiologically relevant, contain multiple cell types which can express CEACAM1 and TIM3. This confounds our understanding of the direct effect of these receptors on CD8 T-cell function. Furthermore, to our knowledge, there are no existing reports on: how CEACAM1 expression by tumour targets may modulate the polarisation of tumour-specific CD8 T-cells towards tumour targets, how CEACAM1 expression by tumour targets may modulate interface stability within these T-cell: tumour cell couples, and whether CEACAM1 and TIM3 *in trans* interactions can affect these processes. Additionally, the conflicting evidence in distinct experimental systems on whether CEACAM1 and TIM3 transduce inhibitory or costimulatory signals indicates that their signalling is context-dependent. It has not been previously investigated how CEACAM1 and TIM3 coregulate T-cell signalling in a 2D *versus* 3D tumour model, the latter of

which is described to comprise more physiologically relevant transcriptomes, metabolite gradients and mechanotransductive stimuli (346, 349, 353, 355, 357-359, 361, 365).

Here, we investigate whether CEACAM1-4L (the predominant CEACAM1 isoform expressed by activated T-cells) coregulates anti-tumour CD8 T-cell cytotoxicity- as measured by tumour death- when it is expressed *in cis* and *in trans* with TIM3 (Figure 5.1). We also explore whether coregulation of CD8 T-cell cytotoxicity by these receptors differs between the 2D *versus* 3D Renca models, as differences between these systems previously modulated TIM3 signalling (Figure 5.1). Furthermore, we investigate if and how CEACAM1-4L *in trans* and TIM3 might coregulate cell couple formation and interface stability between T-cells and Renca cells using the 2D Renca model, both of which are critical for an effective anti-tumour CD8 T-cell response but have not been previously described in this context (Figure 5.1). As previously discussed (Chapter 4), lamellipodia are membrane protrusions that enable T-cells to adhere to their targets, as they stretch towards the target cell to stabilise the cell couple interface. Off-interface-lamellipodia (OIL), however, have no productive effect on T-cell killing of tumour cells, because they move away from the target cell and destabilise the interface. Ultimately, further understanding of how these receptors context-dependently regulate CD8 T-cell functions will help to optimise both CEACAM1 and TIM3-targeting cancer therapies, both of which have demonstrated separate and additive therapeutic efficacy in preclinical trials.

In this chapter, the following aims are addressed:

- 1) To determine how CEACAM1 (the CEACAM1-4L isoform is used in this study but will be denoted as CEACAM1 from hereon) and TIM3 coexpression *in cis* on tumour-specific CD8 T-cells modulates T-cell function and whether this differs between 2D and 3D Renca tumour models using: microscopic cytotoxicity assays and IFN- γ ELISA.
- 2) To determine how CEACAM1 *in trans* interacts with TIM3 expressed on tumour-specific CD8 T-cells to modulate T-cell function and whether this differs between 2D and 3D Renca tumour models using: microscopic cytotoxicity assays, IFN- γ ELISA, imaging of calcium signalling.
- 3) To determine how CEACAM1 *in trans* might cooperate with TIM3 to modulate T-cell polarisation and cell coupling to tumour cells using microscopic assessment of: T-cell: tumour cell coupling abilities, T-cell morphology during cell coupling and interface stability as measured by presentation of off-interface lamellipodia.

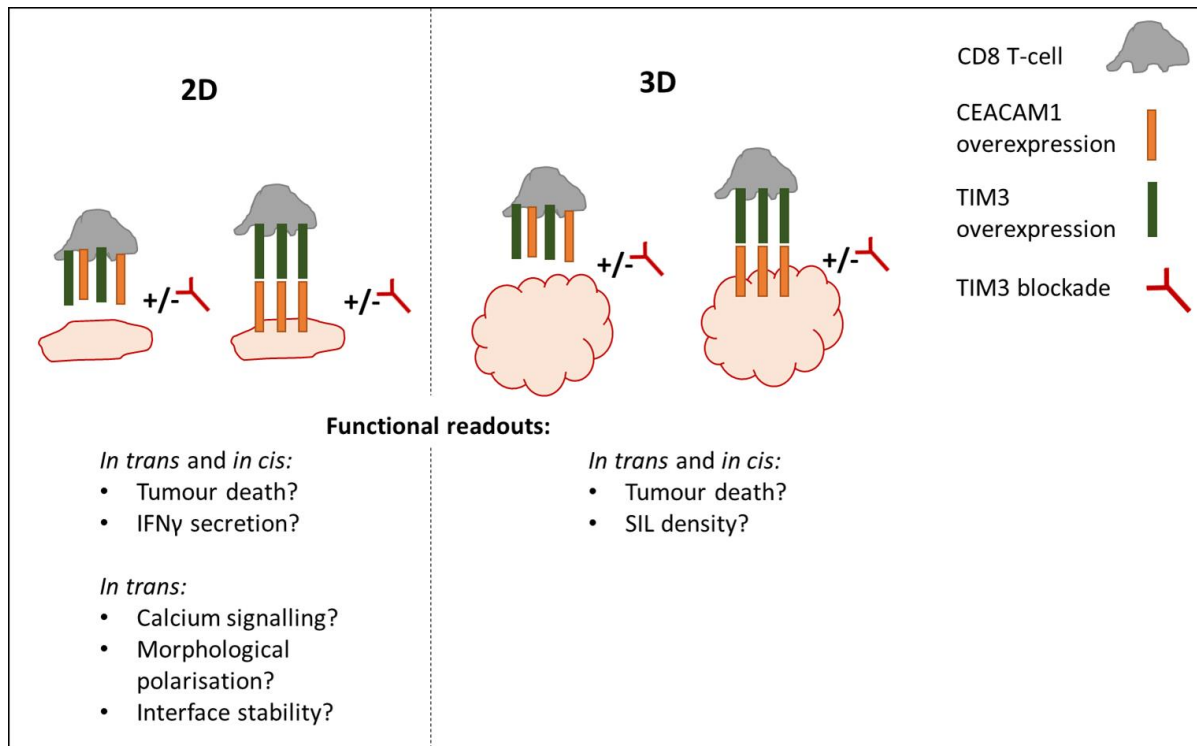


Figure 5.1 Graphical chapter overview: investigating how CEACAM1 *in cis* (on CL4 T-cells) and *in trans* (on Renca cells) coregulates tumour-specific CD8 T-cell function with TIM3, using the 2D and 3D Renca models and TIM3 blockade (using the RMT3-23 anti-TIM3 monoclonal antibody (mAb)).

5.2 Results

5.2.1. Transduction of CL4 T-cells with DNA constructs encoding CEACAM1 was associated with decreased transduction efficiency, but coexpression of CEACAM1 and TIM3 *in cis* was achieved.

Firstly, CL4 CD8 T-cells were retrovirally transduced to overexpress GFP-tagged TIM3, CEACAM1 or both (TIM3-GFP⁺⁺, CEACAM1-GFP⁺⁺ or CEACAM1-TIM3-GFP⁺⁺ CL4) which was confirmed by antibody staining and flow cytometric analysis for CEACAM1 and TIM3 (Figure 5.2a). GFP-positive CL4 T-cells were sorted 3 days post-transduction by FACS (Figure 5.2b). Notably, T-cells transduced with DNA constructs encoding CEACAM1 and CEACAM1-TIM3 had a much lower transduction efficiency (~1%) than T-cells transduced with the TIM3 construct (~60%). Nevertheless, the gating strategy enabled sufficient numbers of GFP-positive cells from all transduced populations to be obtained for subsequent microscopic cytotoxicity assays (Figure 5.2b). Despite consistent gating for GFP-positive T-cells and as a result of the different transduction efficiencies, TIM3-GFP⁺⁺ and CEACAM1-TIM3-GFP⁺⁺ T-cells had a ~50 and ~20-fold higher mean GFP (and therefore TIM3) expression level *versus* non-transduced T-cells, respectively (Figure 5.2c, left). Consistent with this, antibody staining for TIM3 confirmed a ~3-fold higher TIM3 expression level on TIM3-GFP⁺⁺ *versus* CEACAM1-TIM3-GFP⁺⁺ T-cells (Supplementary Figure 8.3b, left panel). It is worth noting that control Ftractin-GFP⁺⁺ cells were previously shown to lack both TIM3 and CEACAM1 expression (Chapter 4, Figure 1.1b), therefore, transduction was necessary to enable expression of these receptors on CL4 T-cells. Furthermore, non-transduced SILs upregulated TIM3-GFP by ~2-fold on average compared to T-cells that did not encounter spheroids (Figure 5.2c, left). Accordingly, TIM3-GFP⁺⁺ T-cells expressed significantly higher levels of TIM3 *versus* CEACAM1-TIM3-GFP⁺⁺ T-cells and non-transduced SILs, while CEACAM1-TIM3-GFP⁺⁺ T-cells expressed significantly higher (~20-fold higher) TIM3 levels *versus* non-transduced SILs (Figure 5.2c, left). According to GFP expression, the level of CEACAM1 expressed by CEACAM1⁺⁺ and CEACAM1-TIM3-GFP⁺⁺ T-cells did not significantly differ (Figure 5.2c, right). Accordingly, antibody staining for CEACAM1 confirmed a comparable CEACAM1 expression level on CEACAM1-GFP⁺⁺ *versus* CEACAM1-TIM3-GFP⁺⁺ cells, although the number of CEACAM1-TIM3-GFP⁺⁺ cells available for antibody staining was limited (Supplementary Figure 8.3b, right panel).

As a result of the retroviral transduction method used herein and the different efficiencies of transducing the above retroviral constructs into CL4 T-cells, there are technical caveats to consider when interpreting 2D and 3D cytotoxicity assays that used CEACAM1-TIM3-GFP⁺⁺ T-cells. Firstly, independent of protein functions, the overexpression of two different proteins *versus* one protein may have put an extra translational stress on CEACAM1-TIM3-GFP⁺⁺ cells by reducing the

number of free ribosomes, which could reduce the cytotoxic potential of these cells compared to T-cells that express only one protein (Ftractin-GFP⁺⁺, CEACAM1⁺⁺ and TIM3-GFP⁺⁺ T-cells) (454, 455). In future, the non-specific effect of double *versus* single protein overexpression on T-cell cytotoxicity should be further established by coexpressing TIM3 with a protein that is not a putative ligand and lacks functional effects, for example, by assessing the cytotoxicity of T-cells that overexpress both TIM3 and the olfactory receptor 2 (OLFR2) which is not endogenously expressed in T-cells. Nevertheless, the level of protein overexpression used herein has been previously shown to have no impact on T-cell activation as measured by the ability of T-cells to form cell couples with APCs, suggesting T-cell suppression from translational stress in this system is unlikely (456). Secondly, since GFP-sorted CEACAM1-TIM3-GFP⁺⁺ and CEACAM1-GFP⁺⁺ T-cells were a much smaller proportion of the presort population compared to the TIM3-GFP⁺⁺ population (Figure 5.2b), they each comprised a more selective population of the most activated cells. This is because successful retroviral transduction requires dissolution of the nuclear membrane during T-cell proliferation, and the most activated T-cells proliferate the most. Thus, independent of protein functions, it is conceivable that the CEACAM1-GFP and CEACAM1-TIM3-GFP populations used in the cytotoxicity assays are more activated than the TIM3-GFP⁺⁺ population, which comprised a larger proportion of the presort population. Overall, the caveat is that it is unclear how translational stress and the transduction efficiencies affected the functionality of the T-cell populations used in the cytotoxicity assays. Nevertheless, whichever effect is greater, (inhibition of CEACAM1-TIM3-GFP⁺⁺ T-cells due to translational stress, or enhanced activation of CEACAM1-GFP⁺⁺ and CEACAM1-TIM3-GFP⁺⁺ cells because they are from a smaller fraction of the most activated cells), any differences in how CEACAM1 and TIM3 coregulate T-cell functions in the 2D *versus* 3D models can still indicate whether there is context-dependent regulation between these receptors. Moreover, using TIM3 blockade treatment can be used to investigate if CEACAM1 and TIM3 directly bind via the FGCC' cleft of TIM3 to mediate effects. Lastly, the different TIM3-GFP⁺⁺ expression levels between CEACAM1-TIM3-GFP⁺⁺ and TIM3-GFP⁺⁺ will need to be taken into consideration when interpreting results (discussed later).

5.2.2. CEACAM1 overexpression alone had no effect on T-cell cytotoxicity *versus* control T-cells in the 2D and 3D Renca models.

Before we investigated the effect of CEACAM1 coexpression *in cis* with TIM3 on CL4 T-cells, we determined the effect of CEACAM1 overexpression alone on SIL cytotoxicity. Thus, CL4 CD8 T-cells were retrovirally transduced to overexpress GFP-tagged CEACAM1 or Ftractin (CEACAM1-GFP⁺⁺, Ftractin-GFP⁺⁺ CL4) and then plated in a 3D microscopic cytotoxicity assay with RencaHA^{tdT} spheroids (Figure 5.3a). The mean normalised increase in DRAQ7⁺ volume per spheroid did not differ between the CEACAM1-GFP⁺⁺ group *versus* the Ftractin-GFP⁺⁺ CL4 group at any timepoints (Figure 5.3b, left table). Although Ftractin-GFP⁺⁺ but not CEACAM1-GFP⁺⁺ T-cells caused a

significant increase in DRAQ7⁺ spheroid volume at 12h (compared to DRAQ7⁺ volume at 4h), there was no consistent effect across independent repeats (Figure 5.3b). SIL density (Figure 5.3b), spheroid volumes (Figure 5.3c) and spheroid shapes (Figure 5.3d) did not differ between groups.

To determine the effect of CEACAM1 overexpression on CL4 T-cell cytotoxicity in the 2D model, Ftractin-GFP⁺⁺ and CEACAM1-GFP⁺⁺ T-cells were plated in a 2D microscopic cytotoxicity assay. There were no significant differences in the rate of killing of Renca cells (Figure 5.3f) or IFN- γ secretion (Figure 5.3g) by Ftractin-GFP⁺⁺ and CEACAM1-GFP⁺⁺ T-cells.

Overall, these data indicated that CEACAM1 overexpression alone had no stimulatory or inhibitory effect on tumour specific CD8 T-cells in the 2D and 3D Renca models (Figure 5.4a).

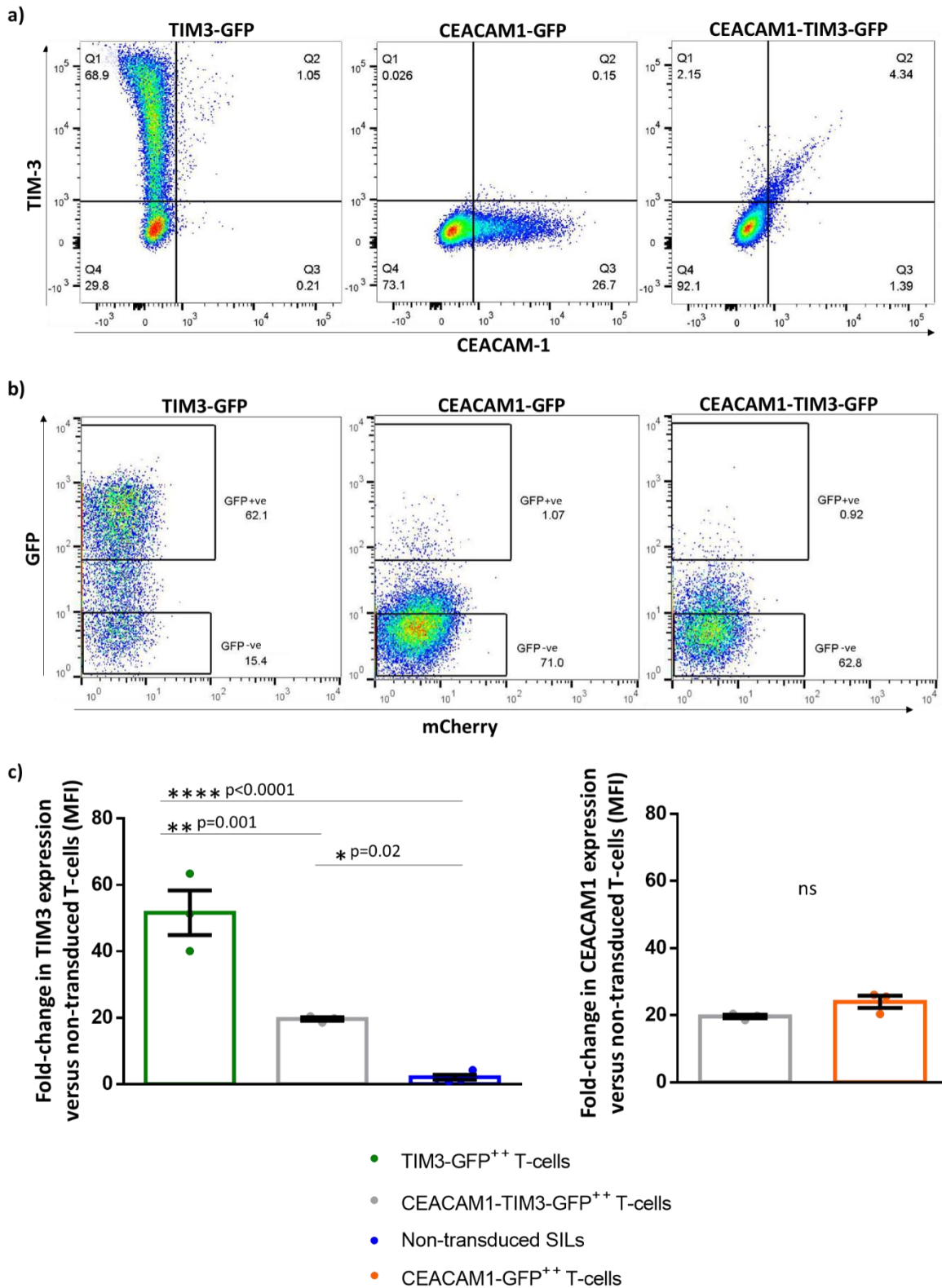
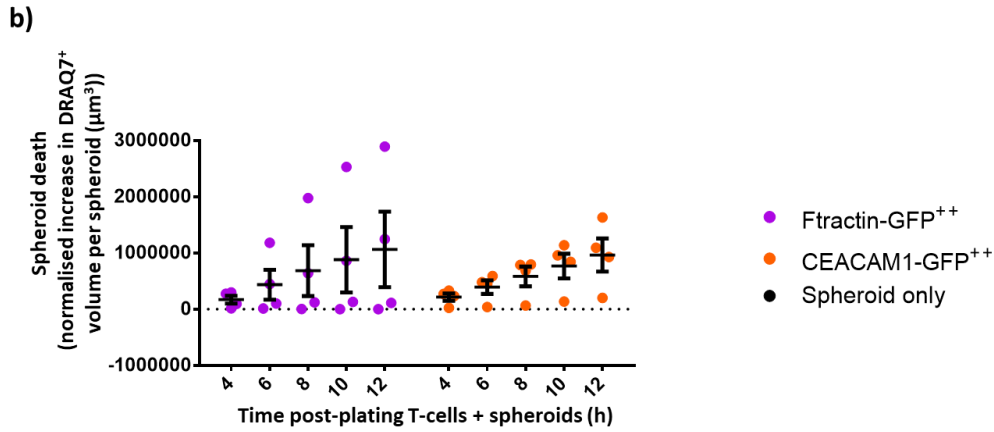
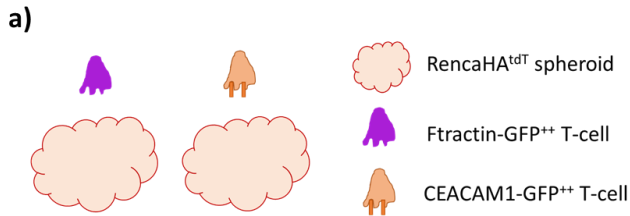


Figure 5.2 Transduction of CL4 T-cells with DNA constructs encoding CEACAM1 was associated with a decreased transduction efficiency, but coexpression of CEACAM1 and TIM3 *in cis* was achieved.

a) Representative flow cytometry dot plots of TIM3 and CEACAM1 expression by CD8 CL4 T-cells retrovirally transduced to overexpress TIM3-GFP, CEACAM1-GFP and CEACAM1-TIM3-GFP. For the CEACAM1-TIM3-GFP DNA transduction construct, cleavage of CEACAM1 from TIM3-GFP during translation at a P2A peptide linker enables separate coexpression of CEACAM1 and TIM3 *in cis*. **b)** Representative flow cytometry dot plots show the GFP-based sorting gate for transduced T-cells used in subsequent 2D and 3D cytotoxicity assays. A gate denoted 'GFP+ve' was used to

isolate T-cells that overexpressed proteins above a consistent threshold. Using this restricted gate helped to reduce variation in the protein overexpression levels between conditions; cells found between the lower boundary of the GFP+ve gate and upper boundary of the GFP-ve gate express low levels of the GFP-tagged protein. **c, left panel**) The fold-change in GFP median fluorescent intensity (MFI) in GFP-positive T-cells, *versus* non-transduced GFP-negative T-cells, is shown for T-cells transduced to overexpress TIM3-GFP (green) and CEACAM1-TIM3-GFP (blue). Non-transduced SILs were isolated from spheroids after overnight incubation in the 3D cytotoxicity assay and antibody-stained for TIM3 cell surface expression using flow cytometry; the fold-change in MFI of SILs *versus* T-cells cultured *in vitro* in the absence of spheroids is shown (blue). **c, right panel**) The fold-change in GFP MFI in GFP-positive T-cells, *versus* non-transduced GFP-negative T-cells is shown for T-cells transduced to overexpress CEACAM1-TIM3-GFP and CEACAM1-GFP. Each point in **c**) represents one of three and four independent repeats of data on transduced T-cells and SILs, respectively. Error bars show mean \pm SEM, and means were compared using One-Way ANOVA. *Representative dot plots of GFP *Data in a) was acquired by Hanin Alamir of the Wülfing laboratory.*



Time (h)						Time (h)					
Spheroid death, comparisons between groups						Spheroid death over time, comparisons within each group					
4	6	8	10	12		2	4	6	8	10	12
ns	ns	ns	ns	ns		ns	ns	ns	ns	ns	ns
CEACAM1-GFP ⁺ vs Ftractin-GFP ⁺						Ftractin-GFP ⁺					
						ns					
						0.03 *					

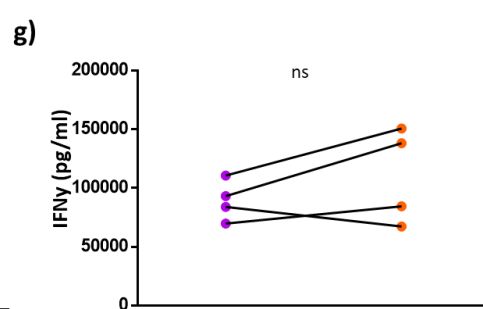
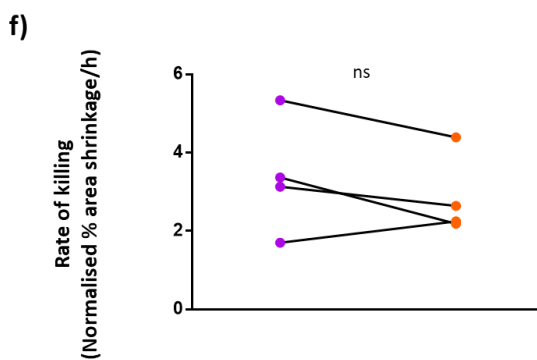
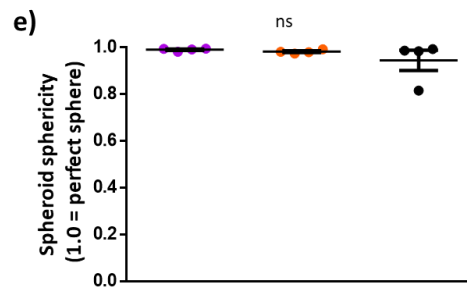
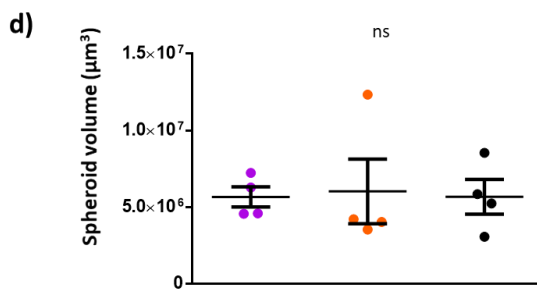
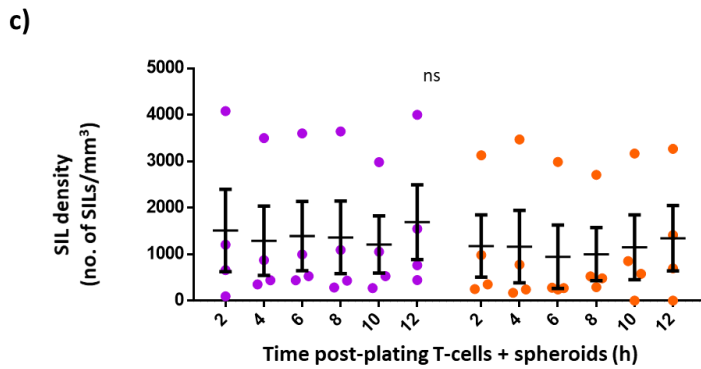


Figure 5.3 CEACAM1 overexpression did not affect CL4 T-cell cytotoxicity in the 3D or 2D RencaHA^{tdT} models.

a) Spheroids were plated with 200,000 CL4 T-cells per well, which overexpressed CEACAM1-GFP or Ftractin-GFP in the 3D microscopy cytotoxicity assay. **b)** Spheroid dead volume at each timepoint was normalised to the initial dead volume at 2h and then to the average dead volume of the Spheroid only group. **b, left table)** shows no significant differences between groups at each time point, means were compared by Two-Way ANOVA, matched by repeat and timepoint. **b, right table)** shows significant death over time within each group, means were compared to the mean at 4h within each group, using Two-Way ANOVA and Dunnett's test, matched by repeat and timepoint. **c)** SIL density over the course of a 3D microscopic cytotoxicity assay is shown for both groups plated with T-cells, means were compared by Two-Way ANOVA, matched by repeat and timepoint. **d)** Spheroid volume across all groups at 2h post-plating for the 3D microscopic cytotoxicity assay. In **c)** and **d)** means were compared using a One-Way ANOVA, matched by repeat. **e)** Spheroid sphericity (how well spheroid shapes fit a perfect sphere) across both groups at 2h post-plating; a value of 1.0 indicates a perfect sphere. **f)** 2 µg/ml K^dHA pulsed RencaHA^{tdT} cells were plated as target cells with CL4 T-cells for 2D microscopic cytotoxicity assays. Individual points show the mean rate of killing by CL4 T-cells that overexpressed CEACAM1-GFP or Ftractin-GFP from one of four independent repeats. Lines connect data from the same independent repeat. Means are representative of four replicate wells. **g)** IFN-γ concentration of supernatant from wells of the 2D microscopic cytotoxicity assay, each point represents the mean from three replicate wells, from four total independent repeats. In **f)** and **g)** means were compared using one-tailed paired t-tests. For all graphs, individual points represent a mean of four independent repeats. n=3-5 spheroids per group, per repeat. For all graphs, error bars show mean ± SEM and ns= non-significant p-values across all comparisons.

5.2.3. In the 3D Renca model, coexpression of CEACAM1 with TIM3 *in cis* on CD8 T-cells abrogated TIM3-dependent inhibitory signalling, in a manner not reversible by acute TIM3 blockade.

In order to determine the effect of CEACAM1 coexpression *in cis* with TIM3 on CL4 T-cells, TIM3-GFP⁺⁺, CEACAM1-GFP⁺⁺ or CEACAM1-TIM3-GFP⁺⁺ CL4 T-cells were plated in a 3D microscopic cytotoxicity assay with RencaHA^{tdT} spheroids (Figure 5.4a). The mean normalised increase in DRAQ7⁺ volume per spheroid was significantly higher in the CEACAM1-GFP⁺⁺ group *versus* the TIM3-GFP⁺⁺ CL4 group at 10 and 12h (Figure 5.4b, left table). Moreover, the mean normalised increase in DRAQ7⁺ volume per spheroid was significantly higher in the CEACAM1-TIM3-GFP⁺⁺ group *versus* the TIM3-GFP⁺⁺ group at 12h, while there were no significant differences in the DRAQ7⁺ spheroid volumes between the CEACAM1-GFP⁺⁺ and CEACAM1-TIM3-GFP⁺⁺ groups at any timepoint (Figure 5.4b). CEACAM1-GFP⁺⁺ and CEACAM1-TIM3-GFP⁺⁺ T-cells caused a significant increase in DRAQ7⁺ volume per spheroid (compared to the DRAQ7⁺ spheroid volume at 4h) by 10 and 12h post-plating of T-cells with spheroids, respectively, whereas TIM3-GFP⁺⁺ T-cells did not cause a significant increase in DRAQ7⁺ spheroid volume at any timepoint (Figure 5.4b, right table).

To establish if the results regarding spheroid death were due to different levels of T-cell cytotoxicity, possible confounding factors were assessed for differences between groups. No significant differences in SIL density were found although a non-significant trend was observed wherein the mean CEACAM1-TIM3-GFP⁺⁺ SIL density was lower than in the CEACAM1-GFP⁺⁺ or TIM3-GFP⁺⁺ groups over all timepoints, suggesting an altered ability of the T-cells to adhere to spheroids (Figure 5.4c). This further confirmed that the cytotoxic potential of CEACAM1-TIM3-GFP SILs was higher *versus* TIM3⁺⁺ SILs on a per cell basis as, in general, less SILs caused higher spheroid death, when CEACAM-TIM3-GFP⁺⁺ and TIM3⁺⁺ SILs were compared. Spheroid volumes (Figure 5.4d) or spheroid shapes (Figure 5.4e) did not differ between treatment groups.

Notably, a caveat to these experiments is that T-cells transduced to overexpress both TIM3-GFP and CEACAM1 *in cis* had a lower TIM3-GFP expression level *versus* T-cells that overexpressed TIM3-GFP alone (~2.5 times less), according to the GFP-positivity of transduced cells and antibody staining (Figure 5.2c, Supplementary Figure 8.3b). Therefore, the differences between the CEACAM1-TIM3-GFP⁺⁺ and TIM3-GFP⁺⁺ groups could be due to the reduced expression level of TIM3 and therefore reduced suppression of the double positive T-cells in the 3D microscopic cytotoxicity assay. However, CEACAM1-TIM3-GFP⁺⁺ T-cells still expressed ~20-fold higher levels of TIM3 *versus* non-transduced T-cells which expressed almost no TIM3, therefore, it would be surprising if this level of TIM3 overexpression was insufficient to transmit inhibitory signals to suppress T-cell cytotoxicity in the 3D model. It is of interest in future to confirm that the levels of TIM3 expressed by CEACAM1-TIM3-GFP⁺⁺ T-cells could still suppress CL4 T-cell cytotoxicity in the 3D model, in the absence of CEACAM1 coexpression- unfortunately, this was not completed

during this project, although preliminary data from the lab has suggested that levels of TIM3 on CEACAM1-TIM3-GFP⁺⁺ *versus* TIM3-GFP⁺⁺ cells could suppress T-cell cytotoxicity to a similar degree in the 3D model. As we expect that the level of TIM3 expressed by CEACAM1-TIM3-GFP⁺⁺ cells was sufficient to significantly suppress T-cell cytotoxicity, the finding that there was no significant difference in cytotoxicity between CEACAM1-TIM3-GFP⁺⁺ and CEACAM1-GFP⁺⁺ cells, (the latter of which lacked TIM3 expression) suggested that coexpression of CEACAM1 counteracted TIM3-mediated suppression of CEACAM1-TIM3-GFP⁺⁺ T-cells.

In this case, CEACAM1 either directly bound to TIM3 to abrogate TIM3-mediated suppression, or indirectly counteracted TIM3 inhibitory signalling. We tested whether there was a direct interaction between CEACAM1 and the FGCC' cleft of TIM3 *in cis*, by plating CEACAM1-TIM3-GFP⁺⁺ T-cells ± anti-TIM3 mAb into a 3D microscopic cytotoxicity assay (Figure 5.5a). (TIM3 blockade treatment in all experiments in this project involved 1h pre-incubation of T-cells with the anti-TIM3 mAb, in addition to TIM3 blockade treatment throughout the assay.) An anti-CEACAM1 blocking antibody was not included in these experiments due to a lack of an available antibody clone with confirmed CEACAM1 blocking activity. No significant differences in spheroid death were found in the presence of anti-TIM3 blockade at each timepoint (Figure 5.5b, left panel). Although there was a significant increase in DRAQ7⁺ volume per spheroid (compared to DRAQ7⁺ spheroid volume at 4h) in the presence but not absence of acute TIM3 blockade, it was not a consistent difference across independent repeats (Figure 5.5b, right table). Although non-significant, acute TIM3 blockade treatment consistently enhanced the SIL density of these double positive T-cells over time (Figure 5.5c). This is interesting in the context of previous data which indicated that CEACAM1-TIM3-GFP⁺⁺ SILs infiltrated at lower density *versus* either CEACAM1-GFP⁺⁺ or TIM3-GFP⁺⁺ SILs (Figure 5.4c). Spheroid volumes (Figure 5.5d) or spheroid shapes (Figure 5.5e) did not differ between treatment groups.

Overall, one caveat of these experiments is that the lower TIM3 expression level on double positive T-cells could account for the reduced suppression of CEACAM1-TIM3-GFP⁺⁺ *versus* TIM3-GFP⁺⁺ cells, if TIM3 caused dose-dependent T-cell suppression. However, given that CEACAM1-TIM3-GFP⁺⁺ T-cells express ~20-fold higher levels of TIM3 *versus* non-transduced cells (which similar to CEACAM1-GFP⁺⁺ T-cells, express no/almost no TIM3), we expect that this TIM3 expression level could still transmit suppressive signalling to reduce T-cell cytotoxicity. As the cytotoxicity of CEACAM1-TIM3-GFP⁺⁺ and CEACAM1-GFP⁺⁺ T-cells (the latter of which lacked TIM3 expression) did not significantly differ, the expression of CEACAM1 *in cis* with TIM3 on T-cells seemed to counteract TIM3-mediated suppression of CEACAM1-TIM3-GFP⁺⁺ T-cells. TIM3 blockade treatment did not affect the cytotoxicity of CEACAM1-TIM3-GFP⁺⁺ T-cells, suggesting that CEACAM1 coexpression abrogated TIM3-mediated suppression without a requirement for

binding the FGCC' cleft of TIM3. On the other hand, although not significant, TIM3 blockade treatment enhanced the density of CEACAM1-TIM3-GFP⁺⁺ SILs, suggesting that CEACAM1 reduced T-cell adherence to spheroids as a result of direct binding to the TIM3 FGCC' cleft.

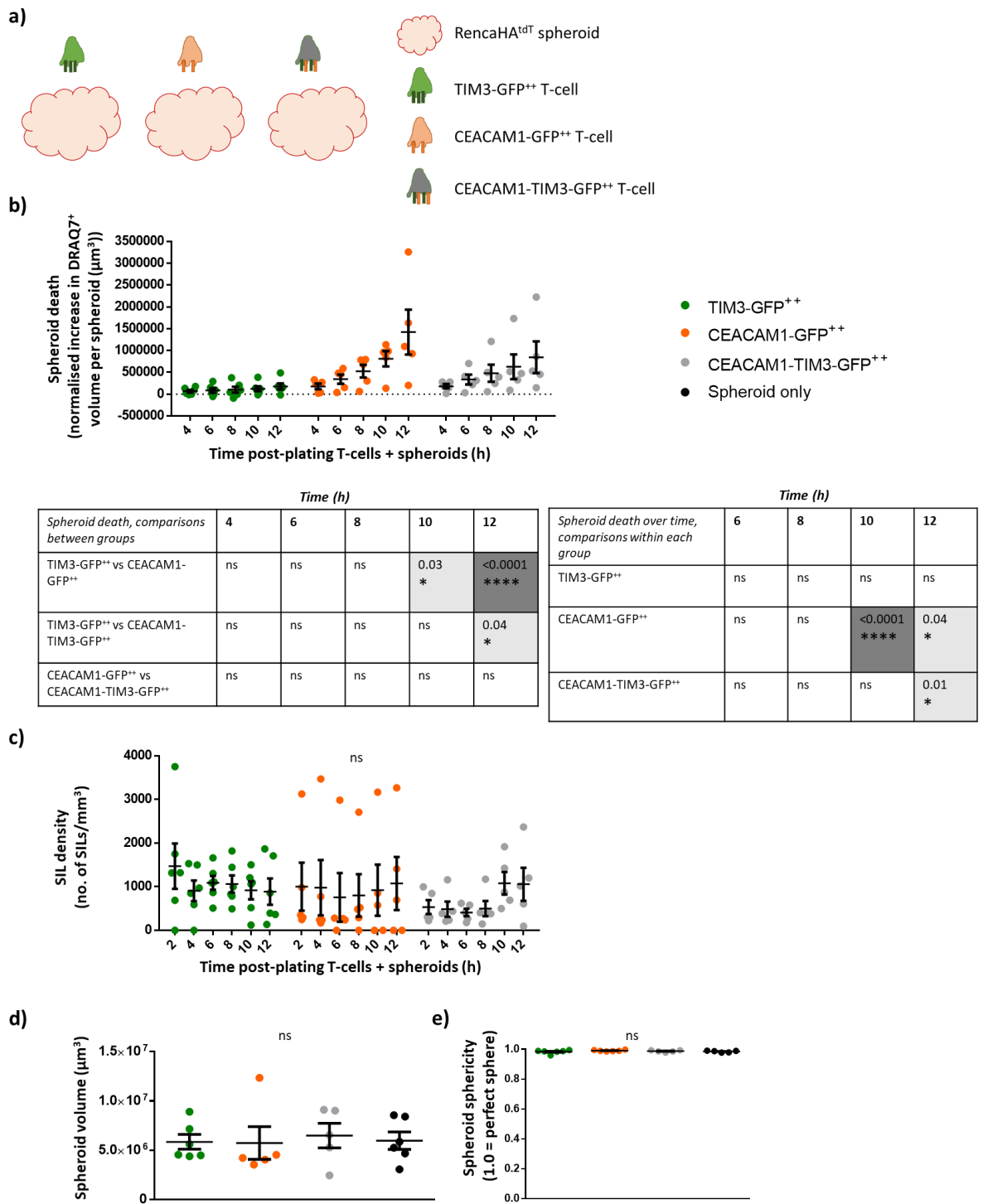


Figure 5.4 In the 3D microscopic cytotoxicity assay, CEACAM1 co-expression with TIM3 *in cis* enhanced and inhibited CL4 cytotoxicity compared to CL4 T-cells which overexpressed solely TIM3 or CEACAM1, respectively. Differences in SIL density and spheroid dimensions did not account for differences in cytotoxicity resulting from TIM3 and/or CEACAM1 overexpression. **a)** Spheroids were plated with 200,000 CL4 T-cells which overexpressed CEACAM1-GFP, TIM3-GFP or both *in cis* (CEACAM1-TIM3-GFP), per well, in the 3D microscopic cytotoxicity assay. **b)** Spheroid dead volume at each timepoint was normalised to the initial dead volume at 2h and then to the average dead volume of the Spheroid only group. **b, left table)** shows significant differences between groups at each time point, means were compared at each time point using a Two-Way ANOVA, matched by timepoint, but not repeat, as two repeats lacked either the CEACAM1-GFP or CEACAM1-TIM-GFP condition. **b, right table)** shows significant death over time within each group, means were compared to the mean at 4h within each group, using Two-Way

ANOVA and Dunnett's test, matched by timepoint. **c)** SIL density over the course of a 3D microscopic cytotoxicity assay is shown for all groups plated with T-cells. **d)** Spheroid volume across all groups at 2h post-plating for the 3D microscopic cytotoxicity assay. **e)** Spheroid sphericity (how well spheroid shapes fit a perfect sphere) across groups at 2h post-plating; a value of 1.0 indicates a perfect sphere. Means were compared using a One-Way ANOVA. For all graphs, each individual point represents a mean of five independent repeats, n=2-4 spheroids per group, per repeat. Error bars show Mean \pm SEM and ns= non-significant p-values across all comparisons.

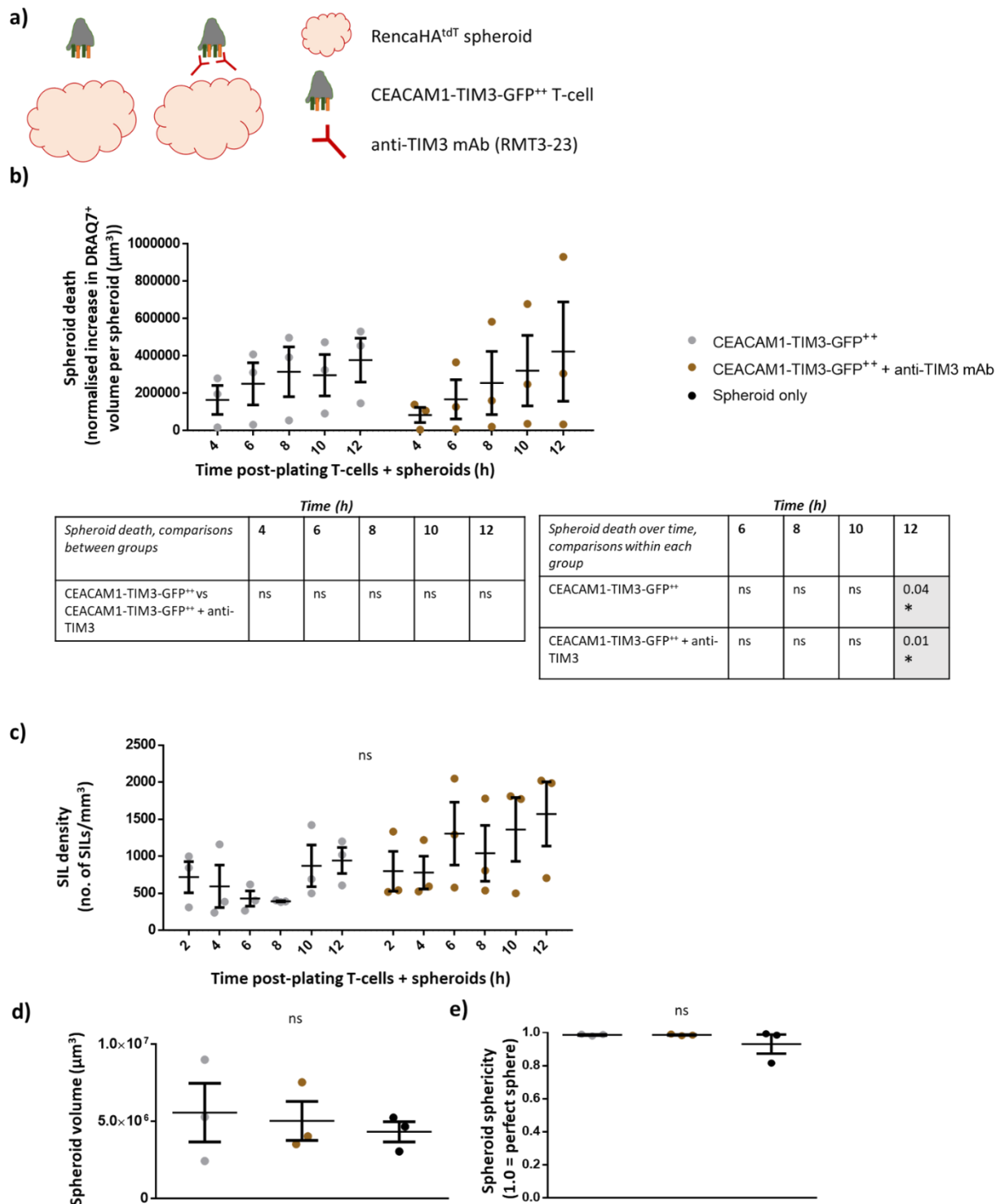


Figure 5.5 Acute TIM3 blockade using incubation with anti-TIM3 mAb did not affect the cytotoxicity of CL4 T-cells which co-expressed CEACAM1 and TIM3 *in cis* during the 3D microscopic cytotoxicity assay. Differences in spheroid dimensions did not contribute to the lack of effect of acute TIM3 blockade of CL4 T-cells which co-expressed CEACAM1 and TIM3 *in cis*. SIL densities were indicated to differ between groups.

a) Spheroids were plated with 200,000 CL4 T-cells per well, which overexpressed both CEACAM1 and TIM3 (CEACAM1-TIM3-GFP) *in cis* ± anti-TIM3 mAb in the 3D microscopy cytotoxicity assay. TIM3 blockade treatment in this project involved 1h preincubation of T-cells with anti-TIM3 mAb, and the presence of TIM3 blockade throughout the entire assay. Spheroid dead volume at each timepoint was normalised to the initial dead volume at 2h and then to the average dead volume of the Spheroid only group. **b, left table)** shows no significant differences between groups at each time point, means were compared at each time point using a Two-Way ANOVA, matched by

repeat and timepoint. **b, right table)** shows significant death over time within each group, means were compared to the mean at 4h within each group, using Two-Way ANOVA and Dunnett's test, matched by repeat and timepoint. **c)** SIL density over the course of a 3D microscopic cytotoxicity assay is shown for all groups plated with T-cells. **d)** Spheroid volume across all groups at 2h post-plating for the 3D microscopic cytotoxicity assay. **e)** Spheroid sphericity (how well spheroid shapes fit a perfect sphere) across groups at 2h post-plating; a value of 1.0 indicates a perfect sphere. Each individual point represents a mean of three independent repeats. n=3-4 spheroids per group, per repeat. Means were compared using a One-Way ANOVA, matched by repeat. For all graphs, error bars show Mean \pm SEM and ns= non-significant p-values across all comparisons.

5.2.4. In the 2D Renca model, coexpression of CEACAM1 with TIM3 *in cis* abrogated TIM3-dependent stimulatory signalling, in a manner not reversible by acute TIM3 blockade.

To establish the effect of CEACAM1 and TIM3 coexpression *in cis* on CL4 T-cell cytotoxicity in the 2D Renca model, Ftractin-GFP⁺⁺, TIM3-GFP⁺⁺, CEACAM1-GFP⁺⁺ and CEACAM1-TIM3-GFP⁺⁺ CL4 T-cells were plated onto RencaHA^{tdT} target cells in the 2D microscopic cytotoxicity assay (Figure 5.6a). CEACAM1-TIM3-GFP⁺⁺ T-cells displayed a significantly reduced rate of killing *versus* TIM3-GFP⁺⁺ T-cells (Figure 5.6b). CEACAM1-TIM3-GFP⁺⁺ T-cells also displayed a marginally reduced rate of killing *versus* CEACAM1-GFP⁺⁺ and Ftractin-GFP⁺⁺ T-cells (Figure 5.6b). There were no significant differences in the rate of killing between Ftractin-GFP⁺⁺, CEACAM1-GFP⁺⁺ and TIM3-GFP⁺⁺ T-cells, in line with the lack of effect of CEACAM1 expression alone *versus* Ftractin⁺⁺ cells in the 3D assay (Figure 5.3b) although, as previously discussed (Chapter 4 Figure 1.6b), TIM3-GFP⁺⁺ cells showed a small stimulatory effect *versus* Ftractin-GFP⁺⁺ T-cells.

Notably, a significantly lower level of IFN- γ was secreted by Ftractin-GFP, CEACAM1-GFP⁺⁺ and CEACAM1-TIM3-GFP⁺⁺ compared to TIM3-GFP⁺⁺ cells. There were no significant differences in IFN- γ secretion between Ftractin-GFP, CEACAM1-GFP⁺⁺ and CEACAM-TIM3-GFP⁺⁺ T-cells during the assay, in corroboration with the comparable cytotoxicity data across these groups (Figure 5.6c).

In total, the data suggested that CEACAM1 coexpression *in cis* abrogated the stimulatory effect of TIM3 overexpression. This is similar to the effect of CEACAM1 coexpression with TIM3 *in cis* in the 3D model, where CEACAM1 coexpression with TIM3 counteracted TIM3-mediated suppression. As TIM3 has a small stimulatory effect in the 2D model, it is possible that the reduced expression level of TIM3 on CEACAM1-TIM3-GFP⁺⁺ *versus* TIM3-GFP⁺⁺ T-cells accounted for the reduced activation of the double positive cells, however, as discussed previously, it is unlikely that a 50-fold *versus* 20-fold upregulation of TIM3 would cause large differences in stimulatory signalling.

To determine if CEACAM1 bound to the FGCC' cleft on TIM3 to suppress T-cell effector functions, CEACAM1-TIM3-GFP⁺⁺ T-cells \pm anti-TIM3 mAb were plated onto RencaHA^{tdT} target cells in the 2D microscopic cytotoxicity assay (Figure 5.7a). Acute blockade using anti-TIM3 mAb had no effect on the rate of killing or IFN- γ secretion by CEACAM1-TIM3-GFP⁺⁺ T-cells (Figure 5.7b, c). Thus, as in the 3D model, we concluded that CEACAM1 abrogated the stimulatory effect of TIM3 without a requirement for binding the FGCC' cleft on TIM3.

Overall, as previously mentioned, overexpression of two *versus* one protein could potentially explain the relatively suppressed state of CEACAM1-TIM3-GFP⁺⁺ cells in the 2D system, however, this cannot be clarified without further experiments and we believe this to be unlikely (previously discussed). Caveats aside, it is likely that CEACAM1 abrogated the stimulatory effect of TIM3 overexpression in the 2D model; previously, CEACAM1 abrogated the inhibitory effect of TIM3 overexpression in the 3D model. Together, the data from both models suggest a consistent role of

CEACAM1 *in cis* to abrogate stimulatory or inhibitory TIM3 signalling without a requirement for binding the TIM3 FGCC' cleft.

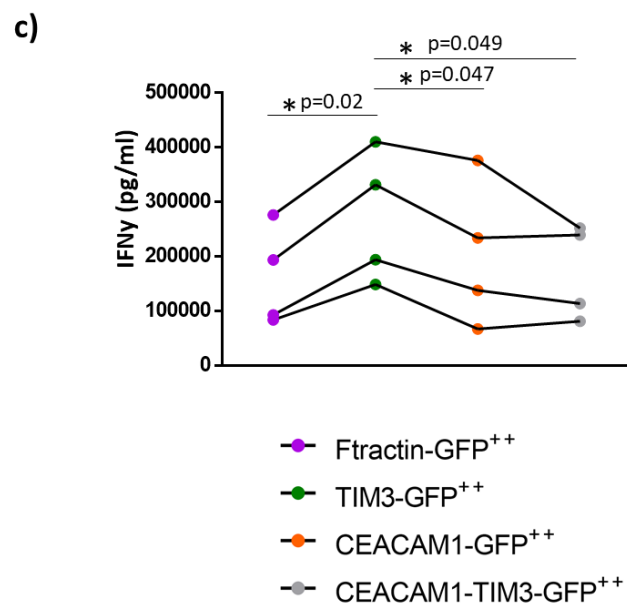
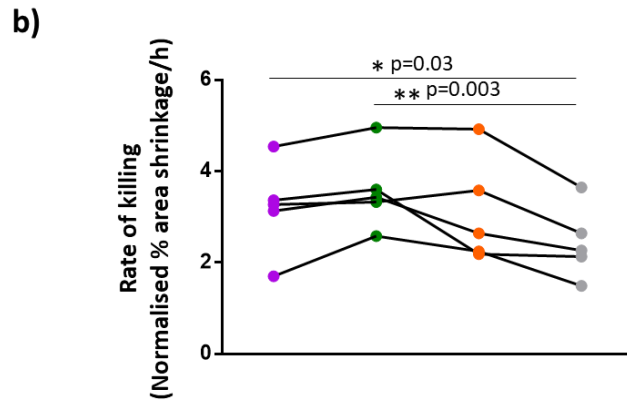
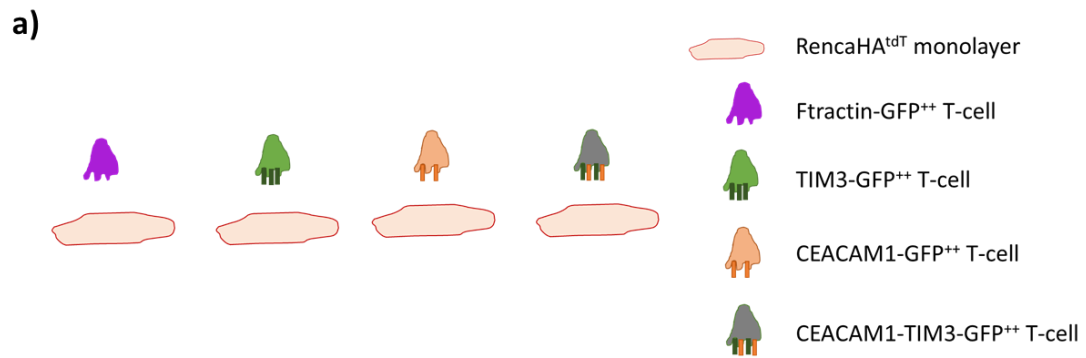
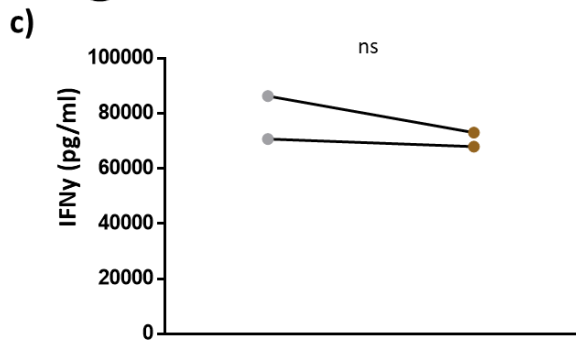
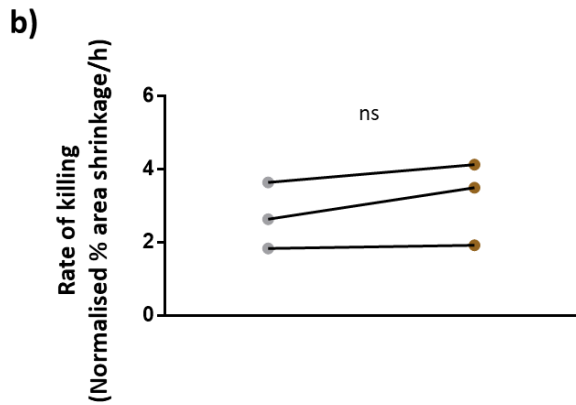
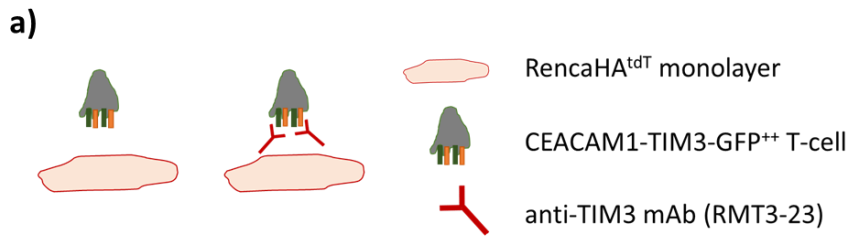


Figure 5.6 CEACAM1 co-expression with TIM3 *in cis* suppressed CL4 T-cell cytotoxicity and IFN γ secretion during co-incubation with K^dHA-pulsed 2D RencaHA^{tdT} target cells in the 2D microscopic cytotoxicity assay, compared to either TIM3 or CEACAM1 overexpressing CL4 T-cells, while TIM3 overexpressing T-cells secreted a higher level of IFN γ compared to CEACAM1 overexpressing T-cells.

a) 2 μ g/ml K^dHA pulsed RencaHA^{tdT} cells were plated as target cells with CL4 T-cells for 2D microscopic cytotoxicity assays. Individual points shows the mean rate of killing by CL4 T-cells that overexpressed CEACAM1-GFP, TIM3-GFP or both *in cis* (CEACAM1-TIM3-GFP) from one of four independent repeats. Lines connect data from the same independent repeat. Means are representative of four replicate wells. **b)** IFN γ concentration of supernatant from wells of the 2D microscopic cytotoxicity assay at the end of the assay (18h after co-incubation of T-cells and RencaHA^{tdT} cells); each point represents the mean from three replicate wells, from four total independent repeats. For both graphs, means were compared using a One-Way ANOVA, matched by repeat.



- CEACAM1-TIM3-GFP⁺⁺
- CEACAM1-TIM3-GFP⁺⁺ + anti-TIM3 mAb

Figure 5.7 Acute TIM3 blockade using incubation with anti-TIM3 mAb did not affect cytotoxicity or IFN γ secretion by CL4 T-cells which co-expressed CEACAM1 and TIM3 *in cis*, during the 2D microscopic cytotoxicity assay.

a) 2 $\mu\text{g/ml}$ K^dHA pulsed RencaHA^{tdT} cells were plated as target cells with CL4 T-cells for 2D microscopic cytotoxicity assays. **b)** Each point shows the mean rate of killing by CL4 T-cells that overexpressed both CEACAM1 and TIM3 *in cis* (CEACAM1-TIM3-GFP) \pm anti-TIM3 mAb from one of three independent repeats. Individual points represent the mean of an independent repeat and lines connect data from the same independent repeat, from a total of three independent repeats. Means from three-four replicate wells were compared using a one-tailed, paired t-test. **c)** IFN- γ concentration of supernatant from wells of the 2D microscopic cytotoxicity assay, each point represents the mean from three replicate wells, for a total of two independent repeats. For all graphs means were compared using a one-tailed paired t-test and ns= non-significant p-value.

5.2.5. CEACAM1 *in trans* inhibits tumour-specific CD8 killing but enhanced IFN- γ secretion irrespective of TIM3 expression by T-cells.

Next, we investigated the possibility that CEACAM1 functions as a TIM3 ligand *in trans*, expressed by opposing tumour cells. Accordingly, the RencaHA cell line was transfected to overexpress CEACAM1-tdTomato relative to the control RencaHA line (Figure 5.8a, left), to form the RencaHA^{CEAC1} cell line (Figure 5.8a, right). TIM3-GFP⁺⁺, Ftractin-GFP⁺⁺ and CEACAM1⁺⁺ CL4 T-cells were plated, in parallel, onto either RencaHA^{tdT} or RencaHA^{CEAC1} target cells in the 2D microscopic cytotoxicity assay (Figure 5.8b). The rate of killing by TIM3-GFP⁺⁺ and Ftractin-GFP⁺⁺ T-cells was significantly suppressed by the presence of CEACAM1 *in trans* irrespective of acute anti-TIM3 blockade (Figure 5.8c, left and middle). Although non-significant, in the majority of independent repeats, the level of IFN- γ secreted by Ftractin-GFP⁺⁺ and TIM3-GFP⁺⁺ T-cells was enhanced when CEACAM1 was expressed *in trans* (Figure 5.8d, left and middle). CEACAM1-GFP⁺⁺ cells showed the same pattern of reduced killing rate and enhanced IFN- γ secretion in response to CEACAM1 overexpression *in trans*, albeit without reaching statistical significance (Figure 5.8c, d, right). Overall, CEACAM1 *in trans* inhibited T-cell cytotoxicity, but slightly elevated IFN- γ secretion irrespective of TIM3 or CEACAM1 expression by the T-cells, both of which are reported to be CEACAM1 ligands. The intact IFN γ secretion by T-cells suggested that CEACAM1 *in trans* did not broadly attenuate proximal TCR signalling processes- which are reported to be regulated by these receptors. Instead, CEACAM1 *in trans* may have regulated more specific pathways, such as cytoskeletal rearrangements necessary for the execution of cytolytic killing.

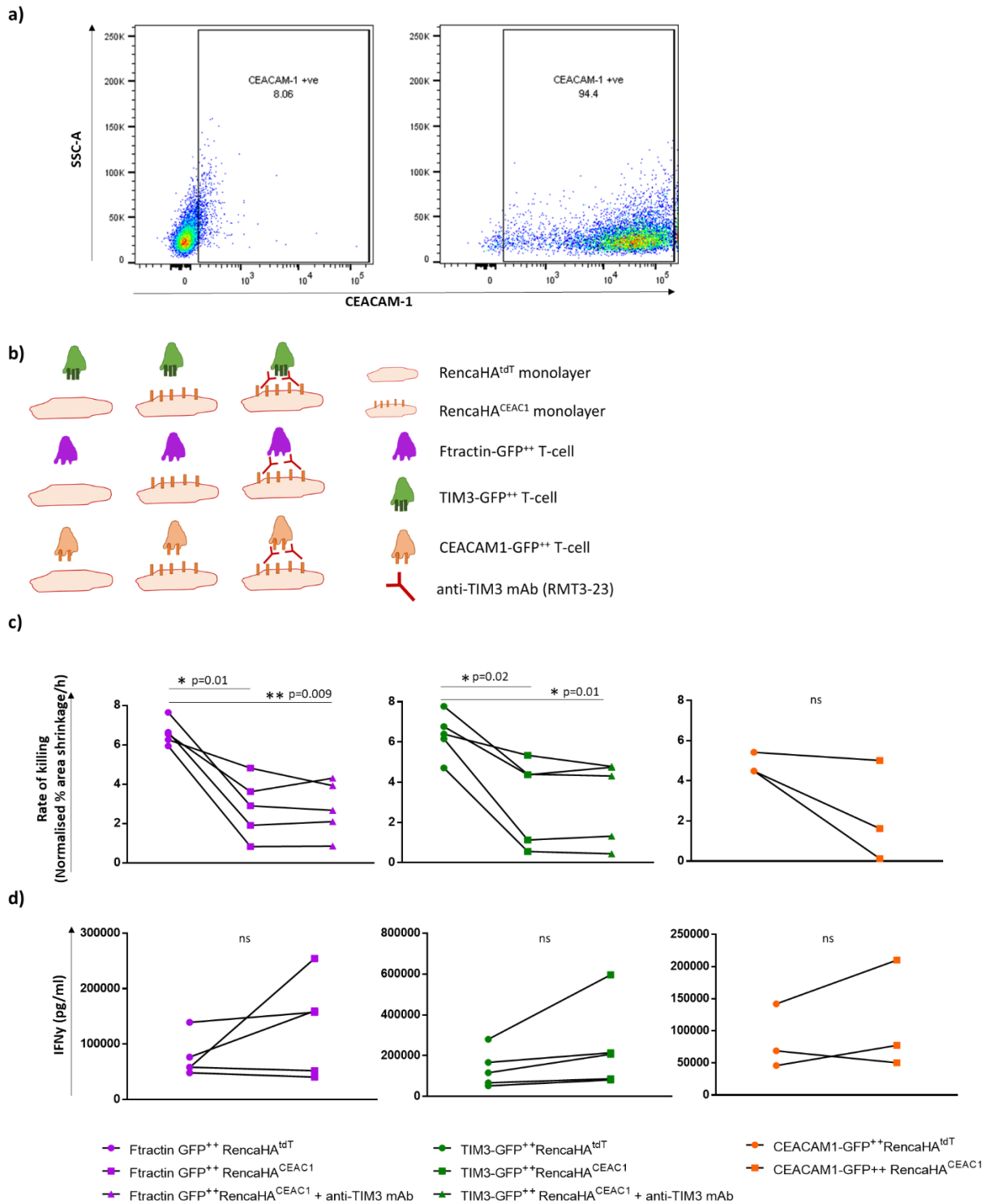


Figure 5.8 RencaHA cells were transduced to overexpress CEACAM1-tdTomato. CEACAM1 *in trans* had no affect on calcium flux or coupling frequency of Ftractin CL4 T-cells. CEACAM1 *in trans* inhibits CL4 T-cell killing irrespective of TIM3 expression level or acute anti-TIM3 blockade.

a) RencaHA^{tdT} and RencaHA^{CEAC1} lines were stained to detect CEACAM1 expression level, a dot plot of side scatter area, *versus* CEACAM1-APC fluorescent intensity is plotted. **b)** 2 µg/ml K^dHA pulsed RencaHA^{tdT} and RencaHA^{CEAC1} cells were plated as target cells with CL4 T-cells for 2D microscopic cytotoxicity assays. **c)** Each point shows the mean rate of killing by CL4 T-cells that overexpressed Ftractin-GFP, CEACAM1-GFP or TIM3-GFP, ± anti-TIM3 mAb. Means from four replicate wells were compared using a One-Way ANOVA for each T-cell type. Individual points represent the mean from an independent repeat. **d)** IFN-γ concentration of supernatant from wells of the 2D microscopic cytotoxicity assay, each point represents the mean from three replicate wells, for a total of four, five and three independent repeats for Ftractin-GFP, TIM3-GFP and CEACAM1-GFP

groups, respectively. Means were compared using a one-tailed paired t-test. Lines connect data from the same independent repeat. ns= non-significant p-value.

5.2.6. CEACAM1 *in trans* does not suppress tumour-specific CD8 T-cell calcium flux during cell coupling to targets or the ability of the T-cells to couple to targets but causes defective T-cell polarisation and reduced stability of the T-cell: target cell interface in 2D.

To confirm that a general attenuation of proximal TCR signalling was not responsible for the inhibition of CL4 T-cell cytotoxicity (irrespective of TIM3 and CEACAM1 overexpression on T-cells), we investigated whether CEACAM1 *in trans* impacted on calcium signalling during cell coupling between T-cells and Renca targets. Fura-2 is a calcium sensor fluorescent dye which can be used to quantify calcium flux in T-cells, although it does not enable absolute measurements of intracellular calcium concentration (457). Fura-2-loaded Ftractin⁺⁺ T-cells were plated with RencaHA^{tdT} or RencaHA^{CEAC1} 2D target cells, and intracellular calcium flux was measured during couple formation (Figure 5.9a). As expected, no significant differences in the calcium flux of Ftractin⁺⁺ CL4 T-cells was observed in response to CEACAM1 overexpression *in trans* (Figure 5.9b). We then hypothesised that CL4 T-cell: Renca cell coupling frequencies may be reduced in the presence of CEACAM1 *in trans*, as the formation of cell couples is the first step required for the execution of cytolytic killing. However, the percentage of Ftractin-GFP⁺⁺ T-cells that committed to cell couple formation upon contacting Renca target cells was unaffected by CEACAM1 overexpression by target cells (Figure 5.9c).

Next, we hypothesised that the presence of CEACAM1 *in trans* may induce a polarisation defect in CL4 T-cells upon coupling to Renca target cells, causing defective delivery of cytotoxic granules and reduced T-cell cytotoxicity. As previously discussed, measurement of the length: width ratio of T-cells upon cell coupling to Renca targets quantifies how elongated the cell is; a more elongated morphology is associated with less effective T-cell polarisation for delivery of the lytic hit (434, 435). We also hypothesised that CEACAM1 *in trans* may destabilise the interface between T-cells and Renca cells, suppressing T-cell cytotoxicity. As before, we measured the frequency and time of onset of off-interface lamellipodia (OIL) displayed by T-cells. Lamellipodia are membrane protrusions that enable T-cells to adhere to their targets when they stretch towards the target cell to stabilise the interface; OIL, however, disrupt T-cell killing of tumour cells, because they move away from the target cell and destabilise the interface (187, 437, 438). To investigate how CEACAM1 *in trans* might regulate CL4 T-cell polarisation and interface stability, TIM3-GFP⁺⁺ and Ftractin-GFP⁺⁺ cells were plated with RencaHA^{tdT} or RencaHA^{CEAC1} 2D target cells (Figure 5.10a).

Upon coincubation with RencaHA^{CEAC1} *versus* RencaHA^{tdT} cells, Ftractin-GFP⁺⁺ T-cells had a significantly more elongated morphology at 1min and 3mins post-couple formation (Figure 5.10b, top). Furthermore, the percentage of Ftractin-GFP⁺⁺ T-cells displaying OIL was significantly higher upon cell coupling to RencaHA^{CEAC1} compared to RencaHA^{tdT} cells (Figure 5.10c top). However, the

time of onset of OIL did not differ when Ftractin-GFP⁺⁺ cells coupled to either RencaHA^{tdT} or RencaHA^{CEAC1} targets (Figure 5.10d top).

Upon coincubation with RencaHA^{CEAC1} *versus* RencaHA^{tdT} cells, TIM3-GFP⁺⁺ T-cells had a significantly more elongated morphology at the initiation of couple formation (0mins) and at 1 and 3mins (Figure 5.10b, middle). As with Ftractin-GFP⁺⁺ T-cells, the percentage of TIM3-GFP⁺⁺ cells displaying OIL was significantly higher upon cell coupling to RencaHA^{CEAC1} compared to RencaHA^{tdT} cells (Figure 5.10c middle). Unlike Ftractin-GFP⁺⁺ cells, there was a significantly shorter mean time before TIM3-GFP⁺⁺ T-cells displayed OIL when they coupled to RencaHA^{CEAC1} targets *versus* RencaHA^{tdT} control (Figure 5.10d, middle).

As previously discussed, when Ftractin-GFP⁺⁺ and TIM3-GFP⁺⁺ T-cells coupled to RencaHA^{tdT} targets there was no significant TIM3-specific effect on T-cell morphology, although TIM3-GFP⁺⁺ T-cells were slightly rounder under lower peptide stimulus conditions. Meanwhile, TIM3-GFP⁺⁺ T-cells, *versus* Ftractin-GFP⁺⁺ T-cells, displayed: a higher coupling frequency, less OIL, and the onset of OIL in TIM3-GFP⁺⁺ T-cells was later (Chapter 4, Figure 1.5b). Upon coupling to Renca^{CEAC1} targets, TIM3-GFP⁺⁺ cells showed a significantly more elongated morphology *versus* Ftractin-GFP⁺⁺ cells at earlier timepoints of 0 and 1mins after cell couple formation indicating a small TIM3-specific effect of CEACAM1 *in trans* (Figure 5.10c bottom). Notably, TIM3 overexpression (compared to Ftractin-GFP⁺⁺ T-cells) reduced the percentage of T-cells displaying OIL by ~12% with RencaHA^{CEAC1} targets (Figure 5.10c bottom) and ~50% with and RencaHA^{tdT} targets (Chapter 4 Figure 1.5c). Furthermore, unlike with RencaHA^{tdT} targets, there was no significant difference between the mean time until OIL were displayed when comparing TIM3-GFP⁺⁺ and Ftractin-GFP⁺⁺ T-cells coupling to RencaHA^{CEAC1} targets (Figure 5.10d, bottom). Together, the data suggests that CEACAM1 *in trans* inhibited TIM3-dependent interface stabilisation, by causing faster and more frequent onset of interface-destabilising OIL.

Overall, CEACAM1 overexpression by RencaHA cells *in trans* had an inhibitory effect on polarisation of both Ftractin-GFP⁺⁺ and TIM3-GFP⁺⁺ cells, as measured by T-cell morphology, and interface stability, as measured by the frequency of cells that displayed OIL. This effect of CEACAM1 *in trans* to inhibit effective polarisation and destabilise the interface, regardless of TIM3 expression level, suggests that these mechanisms accounted for the decreased cytotoxicity of CL4 T-cells against Renca targets that overexpress CEACAM1. Although it had no discernible effect on cytotoxicity, TIM3-GFP⁺⁺ but not Ftractin-GFP⁺⁺ cells exhibited a faster onset of OIL when CEACAM1 was overexpressed *in trans*, suggesting that CEACAM1 *in trans* counteracted the previously observed costimulatory effect of TIM3 to delay the onset of OIL. In support of this idea, whereas TIM3 overexpression (compared to Ftractin-GFP⁺⁺ T-cells) was previously found to delay the onset of OIL in the context of RencaHA^{tdT} targets, TIM3 overexpression had no impact on the

temporal onset of OIL with RencaHA^{CEAC1} targets. TIM3-GFP⁺⁺ T-cells *versus* Ftractin-GFP⁺⁺ cells were more elongated at early timepoints upon cell coupling suggesting that CEACAM1 *in trans* had a TIM3-specific effect. In further support of CEACAM1-mediated abrogation of the interface-stabilising effect of TIM3 overexpression, TIM3 overexpression (compared to Ftractin-GFP⁺⁺ T-cells) was associated with a ~4-fold smaller reduction in the proportion of T-cells displaying OIL when Renca targets overexpressed CEACAM1 (compared to RencaHA^{tdT} targets).

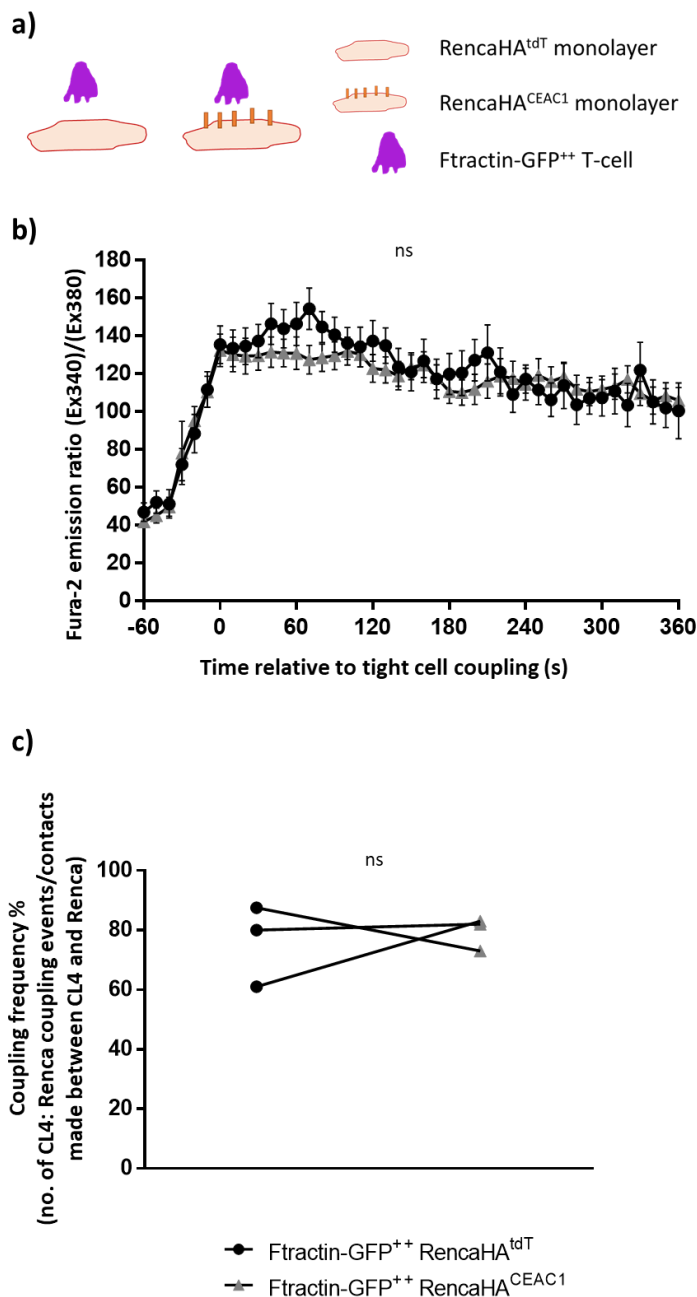


Figure 5.9 CEACAM1 *in trans* overexpressed by Renca had no effect on calcium flux or coupling frequency of Ftractin CL4 T-cells to 2D targets.

a) Fura-2-loaded CL4 T-cells that overexpressed Ftractin-GFP were plated onto a RencaHA^{tdT} target monolayer, which had been pulsed with 2 $\mu\text{g}/\text{ml}$ K^dHA. Means at each timepoint were compared using multiple t-tests with the Holm Sidak correction. **b)** Ratio of Fura-2 emission upon excitation at 340nm over 380nm is shown. Individual points represent the mean and error bars represent means \pm SEM shown for 27 and 15 T-cells that coupled to RencaHA^{CEAC1} and RencaHA^{tdT} targets, respectively, from 3 independent repeats. **c)** Cell coupling frequencies are shown with individual points representing the mean from three independent repeats.

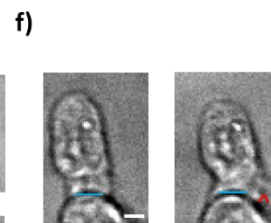
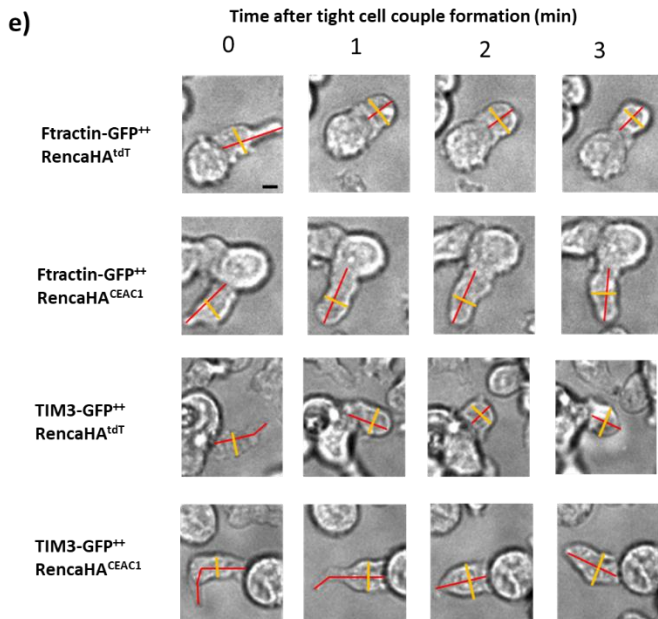
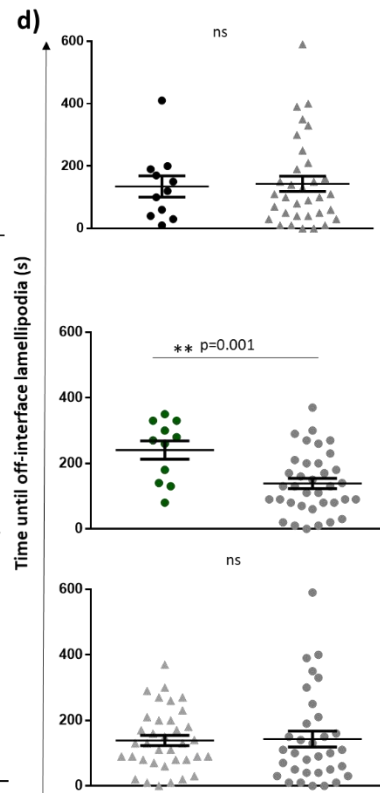
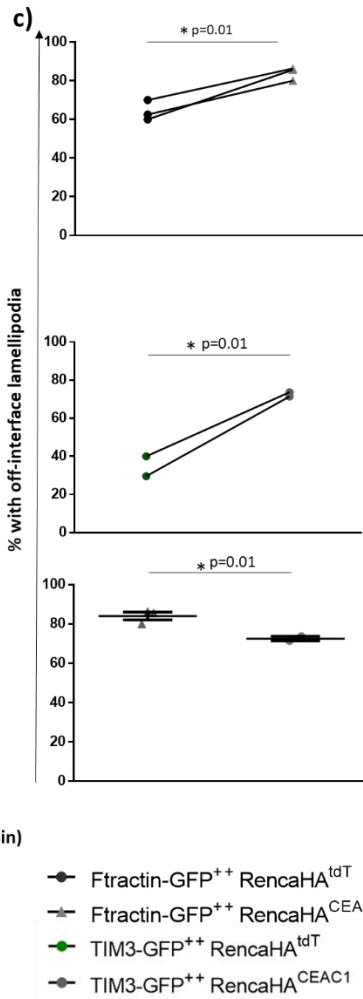
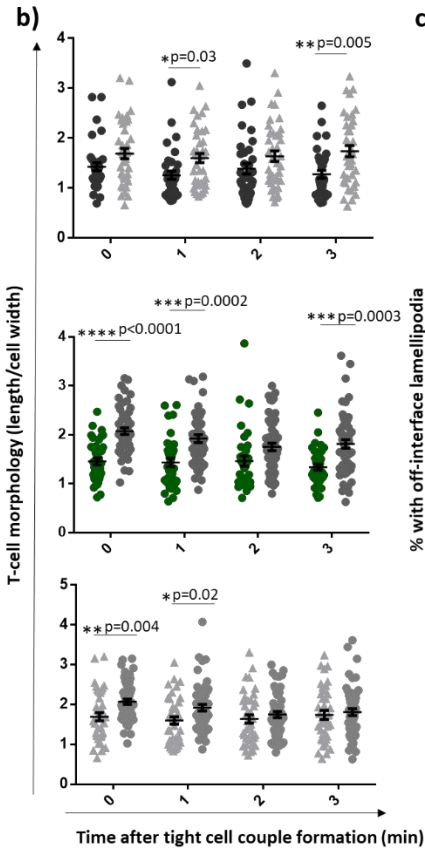
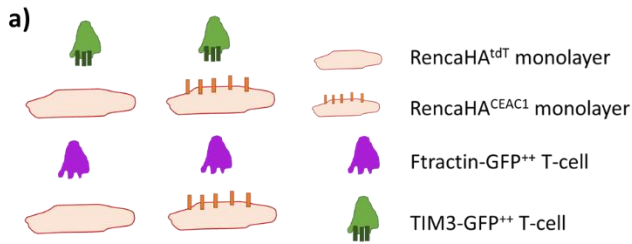


Figure 5.10 CL4 T-cells that coupled to Renca targets that overexpressed CEACAM1 *in trans* displayed a longer morphology and a higher frequency of off-interface lamellipodia irrespective of TIM3 expression level by CL4 T-cells. T-cells which overexpressed TIM3-GFP, but not Ftractin-GFP, showed a faster onset of off-interface lamellipodia when coupling to targets that overexpressed CEACAM1 *in trans*. With Renca^{CEAC1} targets, at early timepoints, CL4 that overexpressed TIM3-GFP *versus* Ftractin-GFP showed a longer morphology, and a lower percentage of cells that displayed off-interface lamellipodia was higher, while time of off-interface lamellipodia did not differ.

a) Fura-2-loaded CL4 T-cells that overexpressed Ftractin-GFP or TIM3-GFP were plated onto a RencaHA^{tdT} or RencaHA^{CEAC1} target monolayer, which had been pulsed with 2 µg/ml K^dHA. **b)** The length and width of T-cells were measured upon tight coupling to targets; the ratio of length/width is shown at 0-3mins after tight-cell coupling. Elongation data was calculated for ≥36 cell couples for each group, from 2-4 independent repeats per group. Individual data points represent a single T-cell. **c)** The percentage of T-cells with off-interface lamellipodia, calculated for ≥20 couples per group, individual data points represent means and lines connect means from the same independent repeat. **d)** Time of the first appearance of off-interface lamellipodia, individual data points represent a single T-cell. In **c)** and **d)** groups using T-cells that overexpressed TIM3-GFP and Ftractin-GFP, used data from two and three independent repeats, respectively. Error bars represent mean ± SEM and ns= non-significant p-values across all comparisons. **e)** Representative images of the length (red line) and width (yellow line) of T-cells at 0-3 minutes upon coupling to tumour targets. **f)** Representative image, left, shows a T-cell coupling to a RencaHA^{CEAC1} target cell without off-interface lamellipodia (OIL), and the formation of an OIL in the subsequent timepoint in the right image. Scale bars represent 5 µm.

5.2.7. Renca cells that overexpress CEACAM1 form spheroids with altered morphology.

It was of interest to see whether CEACAM1 *in trans* also altered the tumour-specific CD8 T-cell response in the 3D Renca spheroid model. Interestingly, RencaHA^{CEAC1} cells grew into spheroids that exhibited a more elongated and irregular morphology *versus* the highly spherical RencaHA^{tdT} spheroids (Figure 5.11b). Quantification of spheroid morphology revealed that the longitudinal/perpendicular ratio of RencaHA^{CEAC1} spheroids was significantly higher than of RencaHA^{tdT} spheroids (Figure 5.11a).

Since higher CEACAM1 expression by tumour cells is positively correlated with increased invasiveness and metastasis of tumour cells *in vivo*, the altered morphology of RencaHA^{CEAC1} spheroids could result from an increased ability of these cells to invade the surrounding ECM.

Importantly, as a more elongated and irregular spheroid morphology would correspond to a larger surface area: volume ratio in RencaHA^{CEAC1} *versus* RencaHA^{tdT} control spheroids and CL4 T-cells kill spheroids from the outside-in (previously described in Chapter 3, 1.11a, b), future 3D microscopic assays will calculate SIL densities using the surface areas rather than volumes of spheroids, to minimise the confounding effect of different spheroid shapes between RencaHA^{CEAC1} and RencaHA^{tdT} spheroids.

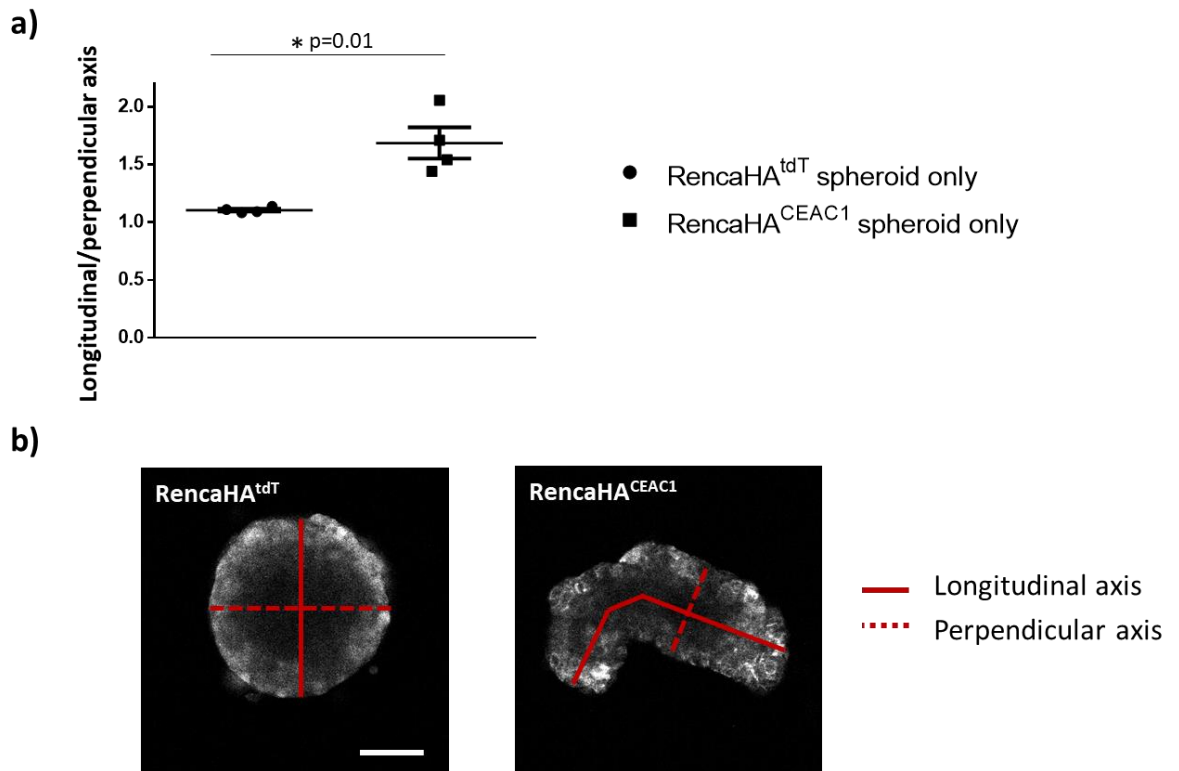


Figure 5.11 RencaHA^{CEAC1} spheroids displayed a more irregular and elongated morphology compared to RencaHA^{tdT} spheroids.

10-day-old RencaHA^{tdT} and RencaHA^{CEAC1} spheroids were imaged using a confocal microscope and the longitudinal and perpendicular axes were measured. **a)** Ratio of longitudinal/perpendicular spheroid axes. Individual points represent the mean from an independent repeat, with a total of four independent repeats. Error bars show mean \pm SEM. **b)** Annotated representative grayscale images of a RencaHA^{tdT} (left) and RencaHA^{CEAC1} (right) spheroid; red lines illustrate the measurement of the spheroid axes, scale bar represents 100 μ m.

5.2.8. CEACAM1 overexpression by RencaHA^{tdT} spheroids *in trans* inhibits tumour-specific CD8 T-cell killing in the 3D Renca model.

Ftractin-GFP⁺⁺ T-cells were plated in a 3D microscopic cytotoxicity assay with RencaHA^{tdT} or RencaHA^{CEAC1} spheroids (Figure 5.12a). The mean normalised increase in DRAQ7⁺ volume per spheroid did not differ significantly between RencaHA^{tdT} versus RencaHA^{CEAC1} spheroids (Figure 5.12b, left table). However, there was a significant increase in DRAQ7⁺ volume per spheroid (compared to the spheroid DRAQ7⁺ volume at 4h) in the RencaHA^{tdT} group at 12h but not in the RencaHA^{CEAC1} group, suggesting that there may be a small inhibitory effect of CEACAM1 *in trans* (Figure 5.12b, right table). Overall, while CEACAM1 *in trans* strongly inhibited the cytotoxicity of Ftractin-GFP⁺⁺ T-cells in the 2D model, there was a very small, if any, inhibitory effect in the 3D model. The inhibition of T-cell cytotoxicity (by CEACAM1 *in trans*) in the 2D model was associated with defective T-cell polarisation and reduced interface stability; in this system T-cells formed interfaces with single Renca cells, therefore CEACAM1 *in trans* would have bound to a localised area of the T-cell. In contrast, at the undulated surface of a spheroid, T-cells are likely to make contact with multiple surrounding Renca cells, in addition to the primary target cell. It is conceivable that CEACAM1 *in trans* interactions with broader areas of the T-cell surface could therefore mitigate any localised, inhibitory effects on T-cell polarisation towards the primary target cell- repolarisation towards the primary target cell would then still occur. This is one possible explanation for how CEACAM1 *in trans* might inhibit T-cell polarisation and cytotoxicity in the 2D but not 3D model, accounting for the above observations.

TIM3-GFP⁺⁺ T-cells were plated in a 3D microscopic cytotoxicity assay with RencaHA^{tdT} or RencaHA^{CEAC1} spheroids (Figure 5.13a). The mean normalised increase in DRAQ7⁺ volume per spheroid was significantly higher in RencaHA^{tdT} versus RencaHA^{CEAC1} spheroids at 12h (Figure 5.13b, left table). Moreover, there was a significant increase in DRAQ7⁺ volume per spheroid (compared to the DRAQ7⁺ spheroid volume at 4h) in the RencaHA^{tdT} group at 12h but not in the RencaHA^{CEAC1} group (Figure 5.13b, right table). Overall, CEACAM1 *in trans* inhibited the cytotoxicity of TIM3-GFP⁺⁺ T-cells in both the 2D and 3D models. Although the inhibition of cytotoxicity in the 2D model did not appear to be TIM3-specific, in the 2D system, CEACAM1 *in trans* counteracted TIM3-dependent stabilisation of the interface between T-cells and Renca targets. In the 3D model, CEACAM1 *in trans* inhibited the cytotoxicity of TIM3-GFP⁺⁺ SILs, suggesting that it transduced an inhibitory signal through TIM3, rather than counteract TIM3 signalling as was the case with CEACAM1 *in cis*.

Spheroid volumes did not differ between groups in all experiments (Figure 5.12d, Figure 5.13d). Ftractin-GFP⁺⁺ SIL densities at the surface of spheroids also did not differ between groups (Figure 5.12c). Interestingly, at all timepoints except 4h, TIM3-GFP⁺⁺ SIL densities at the surface of

spheroids were higher in the RencaHA^{CEAC1} *versus* RencaHA^{tdT} group (Figure 5.13c). To account for differences in SIL densities, spheroid death values normalised to SIL densities are shown later in datasets that include TIM3 blockade treatment (Figure 5.14d, Figure 5.15d).

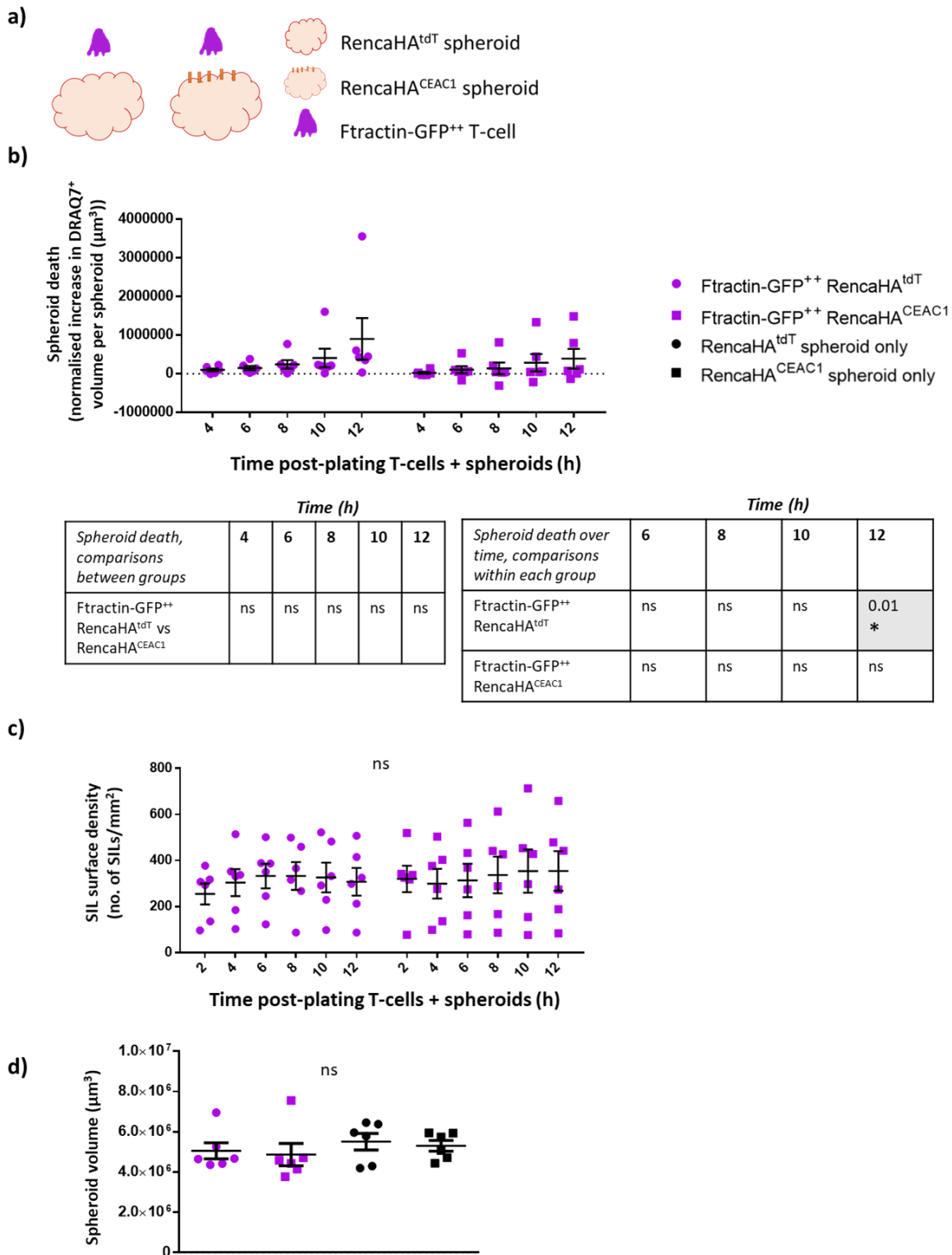


Figure 5.12 CEACAM1 *in trans* overexpression by RencaHA spheroids was indicated to inhibit the cytotoxicity of CL4 that overexpressed Ftractin-GFP. SIL densities and volumes at the surface of spheroids did not differ between groups.

a) RencaHA^{tdT} and RencaCEAC1^{tdT} spheroids were plated with 200,000 CL4 T-cells per well, which overexpressed Ftractin-GFP for the 3D microscopic cytotoxicity assay. Spheroid dead volume at each timepoint was normalised to the initial dead volume at 2h and then to the average dead volume of the Spheroid only group. **b, left table)** shows significant differences between groups at each time point, means were compared at each time point using a Two-Way ANOVA, matched by repeat and timepoint. Means are of log-transformed data, due to positive skew. **b, right table)**

shows significant death over time within each group, means were compared to the mean at 4h within each group, using Two-Way ANOVA and Dunnett's test, matched by repeat and timepoint. **c)** SIL density over the course of a 3D microscopic cytotoxicity assay is shown for groups plated with T-cells. Means were compared at each time point using a Two-Way ANOVA, matched by repeat and timepoint. **d)** Spheroid volume across all groups at 2h post-plating for the 3D microscopic cytotoxicity assay. Each individual point represents a mean of six independent repeats; n=3-4 spheroids per group, per repeat. Means were compared using a One-Way ANOVA, matched by repeat. For all graphs, individual points represent the mean from an independent experiment and error bars show mean \pm SEM. ns= non-significant p-values across all comparisons.

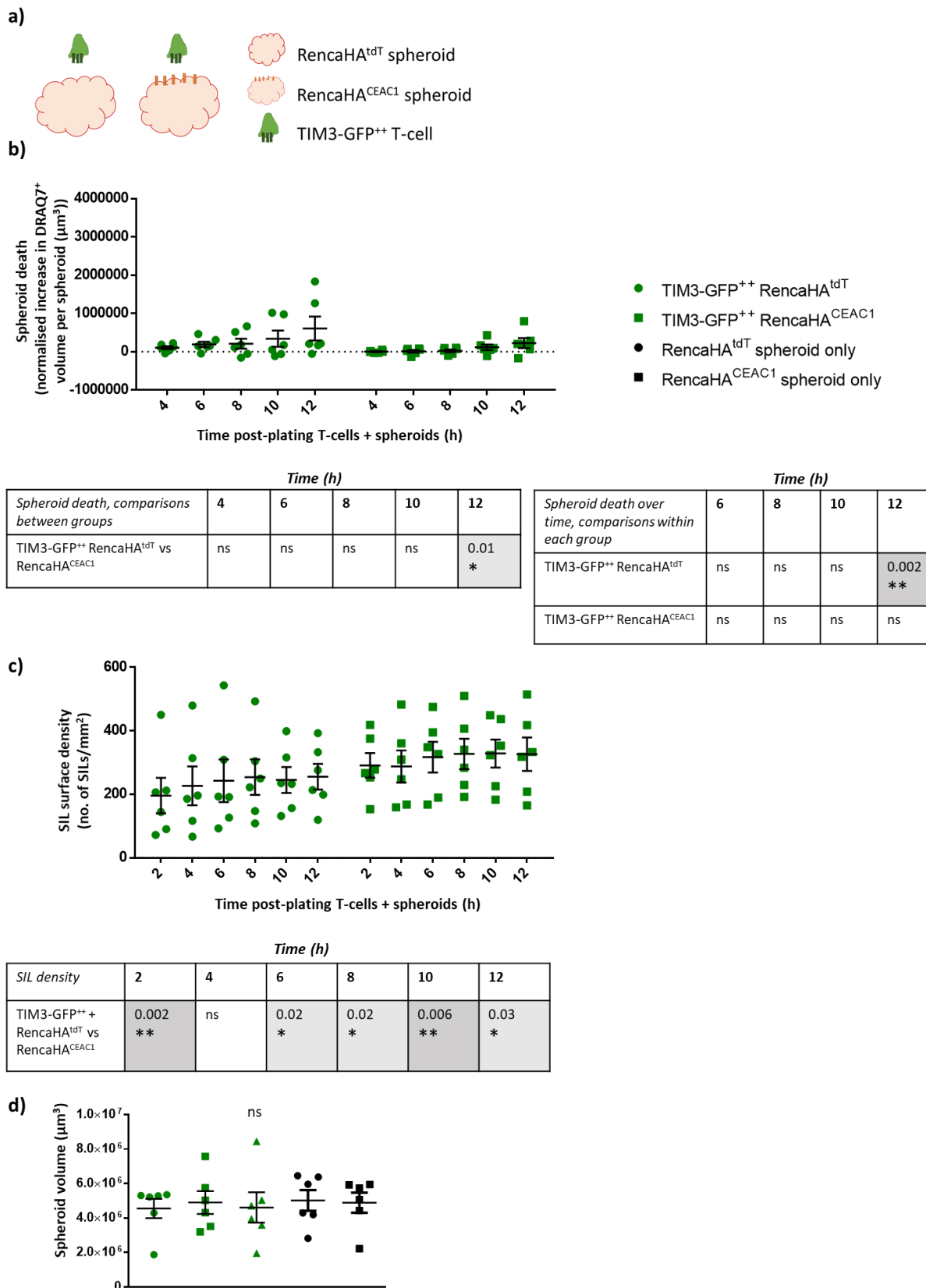


Figure 5.13 CEACAM1 *in trans* overexpression by RencaHA spheroids inhibited cytotoxicity of CL4 that overexpressed TIM3-GFP. SIL densities at the surface of spheroids differed between groups, but spheroid volumes did not differ.

a) RencaHA^{tdT} and RencaHA^{CEAC1} spheroids were plated with 200,000 CL4 T-cells per well, which overexpressed TIM3-GFP for the 3D microscopy cytotoxicity assay. Spheroid dead volume at each timepoint was normalised to the initial dead volume at 2h and then to the average dead volume

of the Spheroid only group. **b, left table)** shows significant differences between groups at each time point, means were compared at each time point using a Two-Way ANOVA, matched by repeat and timepoint. **b, right table)** shows significant death over time within each group, means were compared to the mean at 4h within each group, using Two-Way ANOVA and Dunnett's test, matched by repeat and timepoint. **c)** SIL density over the course of a 3D microscopic cytotoxicity assay is shown for groups plated with T-cells. Means were compared at each time point using a Two-Way ANOVA, matched by repeat and timepoint. **d)** Spheroid volume across all groups at 2h post-plating for the 3D microscopic cytotoxicity assay. n=3-4 spheroids per group, per repeat. Means were compared using a One-Way ANOVA, matched by repeat. For all graphs, individual points represent a mean of six independent repeats and error bars show mean \pm SEM. ns= non-significant p-values across all comparisons.

5.2.9. CEACAM1 acts *in trans* to suppress tumour-specific CD8 T-cell killing and the suppression is reversible by acute TIM3 blockade, suggesting CEACAM1 *in trans* can act as a functional ligand for TIM3

It was possible that the small suppressive effect of CEACAM1 *in trans* on Ftractin-GFP⁺⁺ cells- according to the delayed onset of a significant increase in spheroid death- was due to upregulation of TIM-3 by Ftractin-GFP⁺⁺ SILs *in situ* during the assay; SILs have been previously shown to upregulate TIM3 2-fold *versus* CL4 T-cells that have not encountered spheroids (Figure 5.2c). In order to determine if the possible small suppressive effect of CEACAM1 *in trans* was due to low expression levels of TIM3 on SILs, Ftractin-GFP⁺⁺ T-cells were plated in a 3D microscopic cytotoxicity assay with RencaHA^{tdT} spheroids or RencaHA^{CEAC1} spheroids ± acute TIM3 blockade (Figure 5.14a). There were no effects of CEACAM1 *in trans* on Ftractin-GFP SIL cytotoxicity, and no effect of TIM3 blockade treatment (Figure 5.14b).

In this dataset, Ftractin-GFP⁺⁺ SIL densities were significantly higher at the surface of RencaHA^{CEAC1} *versus* RencaHA^{tdT} spheroids while acute-TIM3 blockade reversed the CEACAM1-mediated enhancement of SIL densities (Figure 5.14c). To account for differences in SIL surface densities between conditions, spheroid dead volumes were normalised to the SIL surface densities at the relevant timepoints. The mean density-normalised DRAQ7⁺ spheroid volume did not significantly differ when Renca expressed CEACAM1, irrespective of acute TIM3 blockade (Figure 5.14d). In support of no inhibitory effect of CEACAM1 *in trans* on Ftractin-GFP⁺⁺ SILs, in one of three independent repeats, there was higher spheroid death in the RencaHA^{CEAC1} spheroid groups *versus* the RencaHA^{tdT} group. Spheroid volumes (Figure 5.12e) did not differ between groups.

Next, we investigated whether acute TIM3 blockade could reverse the TIM-3-dependent suppressive effect of CEACAM1 *in trans* in the 3D system. For this purpose, TIM3-GFP⁺⁺ T-cells were plated in a 3D microscopic cytotoxicity assay with RencaHA^{tdT} or RencaHA^{CEAC1} spheroids ± acute TIM3 blockade (Figure 5.15a). The mean normalised increase in DRAQ7⁺ volume per spheroid was significantly lower in RencaHA^{CEAC1} spheroids compared to RencaHA^{tdT} spheroids or RencaHA^{CEAC1} spheroids treated with acute anti-TIM3 blockade (Figure 5.15b, left table).

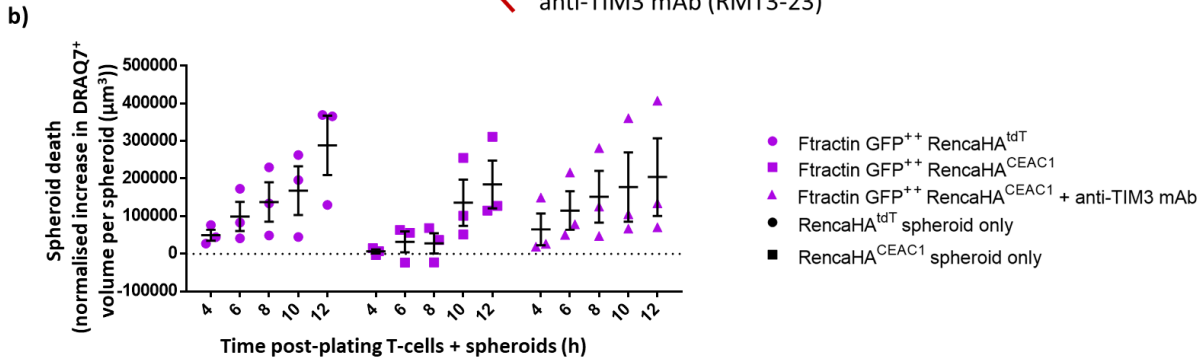
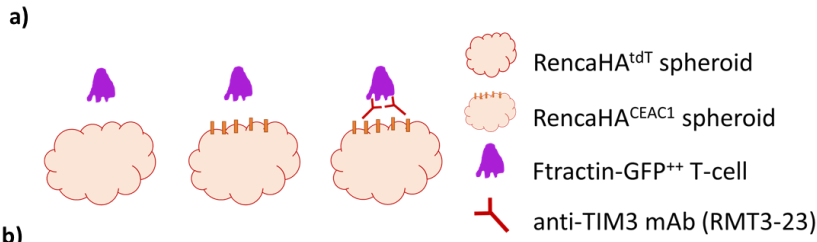
Moreover, there was a significant increase in DRAQ7⁺ spheroid volume (compared to the DRAQ7⁺ volume at 4h) in the RencaHA^{tdT} group and RencaHA^{CEAC1} + anti-TIM3 mAb at 10h but not in the RencaHA^{CEAC1} group without TIM3 blockade (Figure 5.15b, right table).

As discussed previously, TIM3⁺⁺ SIL densities at the surface of spheroids were significantly higher in RencaHA^{CEAC1} spheroids without acute TIM3 blockade *versus* the RencaHA^{tdT} group at 2, 8 and 10, 12 hours (Figure 5.15c). Moreover, TIM3-GFP⁺⁺ SIL surface densities were significantly higher in the RencaHA^{CEAC1} + anti-TIM3 group compared to the RencaHA^{tdT} group at all timepoints (Figure 5.15c). Interestingly, SIL surface densities were significantly higher in RencaHA^{CEAC1} spheroids in

the presence *versus* absence of acute TIM3 blockade at 4-8h (Figure 5.15c). This suggested that the enhanced SIL densities in RencaHA^{CEAC1} versus RencaHA^{tdT} spheroids likely resulted from CEACAM1 ligating to a non-TIM3 binding partner, while TIM3 ligation by CEACAM1 *in trans* reduced SIL densities. As before, spheroid dead volumes were normalised to the SIL surface densities at the relevant timepoints. The mean density-normalised spheroid death was significantly reduced at 12h when Renca overexpressed CEACAM1 *in trans versus* RencaHA^{tdT} spheroids, and the suppressive effect of CEACAM1 *in trans* was reversed by acute TIM3 blockade (Figure 5.15d). There were no significant differences in the mean density-normalised spheroid death between RencaHA^{tdT} spheroids and RencaHA^{CEAC1} spheroids treated with acute TIM3 blockade. Spheroid volumes did not differ between groups (Figure 5.15e).

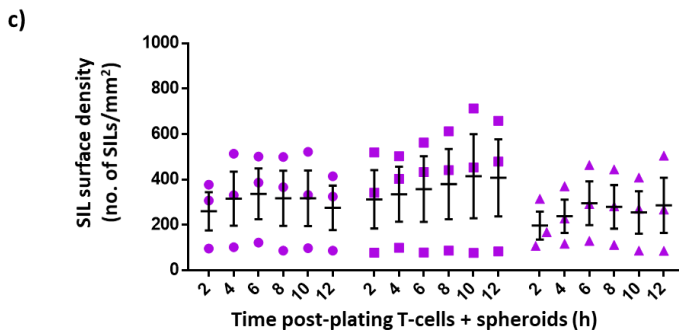
Overall, these data suggested that the TIM3-dependent suppressive effect of CEACAM1 *in trans* can be reversed by acute TIM3 blockade in the 3D Renca model. Previously, a non-significant enhancement of SIL density upon acute TIM3 blockade of CEACAM1-TIM3-GFP⁺⁺ T-cells was observed, suggesting that CEACAM *in cis* interactions with TIM3 suppressed the adherence of T-cells to spheroids (Figure 5.5c). Together with the data herein that demonstrated increased SIL densities upon TIM3 blockade in the context of CEACAM1 overexpression on Renca cells, our findings suggest that in the 3D model, CEACAM1 and TIM3 negatively coregulated SIL adherence to spheroids. Finally, we have no evidence for why acute TIM3 blockade reduced Ftractin-GFP⁺⁺ SIL densities in RencaHA^{CEAC1} spheroids, but it is possible that a small upregulation of TIM3 in Ftractin-GFP⁺⁺ SILs may have a different effect compared to high overexpression of TIM3 (it was previously shown that SILs have a 2-fold increase in TIM3 expression *versus* control T-cells that have not encountered spheroids, while TIM3-GFP⁺⁺ T-cells have a ~50-fold increase *versus* control non-transduced T-cells).

A summary of all the data from Chapters 4 and 5 is shown in Figure 1.15 to aid the following discussion section.



	Time (h)				
<i>Spheroid death, comparisons between groups</i>	4	6	8	10	12
Ftractin-GFP ⁺ RencaHA ^{tdT} vs Ftractin-GFP ⁺ RencaHA ^{CEAC1}	ns	ns	ns	ns	ns
Ftractin-GFP ⁺ RencaHA ^{tdT} vs Ftractin-GFP ⁺ RencaHA ^{CEAC1} + anti-TIM3 mAb	ns	ns	ns	ns	ns
Ftractin-GFP ⁺ RencaHA ^{CEAC1} vs Ftractin-GFP ⁺ RencaHA ^{CEAC1} + anti-TIM3 mAb	ns	ns	ns	ns	ns

	Time (h)			
<i>Spheroid death over time, comparisons within each group</i>	6	8	10	12
Ftractin-GFP ⁺ RencaHA ^{tdT}	ns	ns	ns	0.002 **
Ftractin-GFP ⁺ RencaHA ^{CEAC1}	ns	ns	ns	0.02 *
Ftractin-GFP ⁺ RencaHA ^{CEAC1} + anti-TIM3	ns	ns	ns	ns



	Time (h)						
<i>SIL density</i>	2	4	6	8	10	12	
Ftractin-GFP ⁺ RencaHA ^{tdT} vs Ftractin-GFP ⁺ RencaHA ^{CEAC1}	ns	ns	ns	0.001 **	0.002 **	<0.0001 ****	
Ftractin-GFP ⁺ RencaHA ^{tdT} vs Ftractin-GFP ⁺ RencaHA ^{CEAC1} + anti-TIM3 mAb	0.04 *	0.01 *	ns	ns	0.05 *	ns	
Ftractin-GFP ⁺ RencaHA ^{CEAC1} vs Ftractin-GFP ⁺ RencaHA ^{CEAC1} + anti-TIM3 mAb	0.0003	0.002	0.04 *	0.04 *	<0.0001 ***	0.0002 ***	

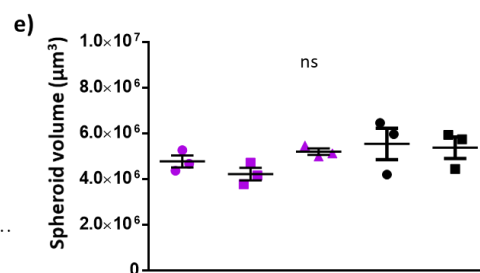
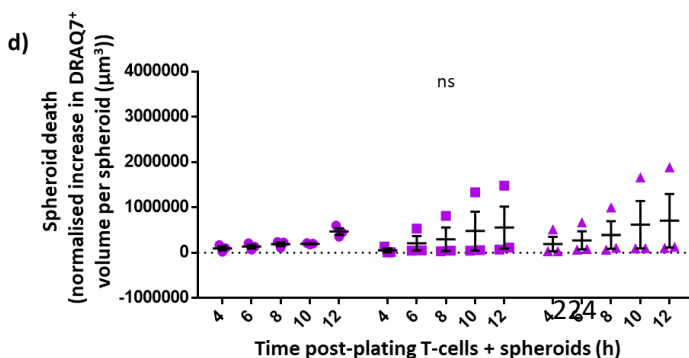
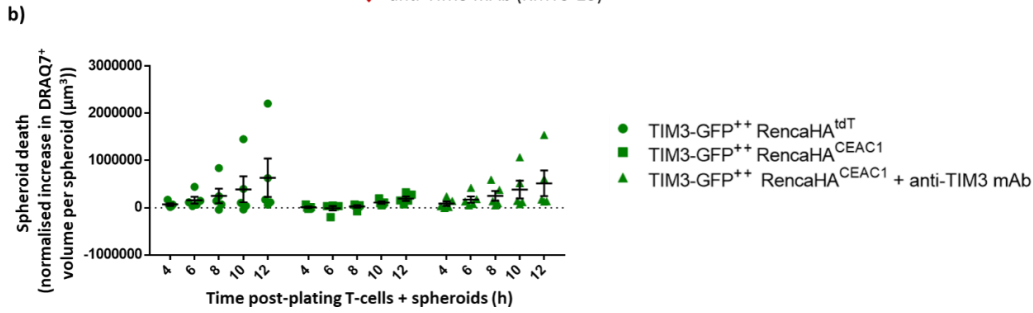
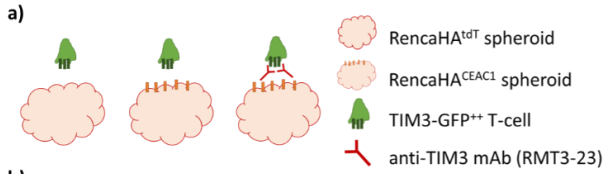


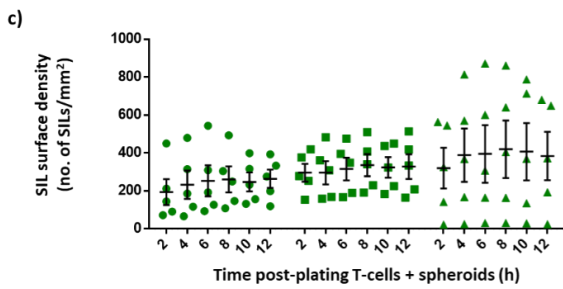
Figure 5.14 Acute TIM3 blockade had no effect on CEACAM1-mediated suppression of CL4 T-cells that overexpressed Ftractin-GFP. SIL densities differed between conditions, spheroid volumes did not. Normalisation of spheroid death to SIL densities showed suppression of T-cell cytotoxicity by CEACAM1 but this was not reversed by acute anti-TIM3 blockade.

a) RencaHA^{tdT} and RencaCEAC1^{tdT} spheroids were plated with 200,000 CL4 T-cells per well, which overexpressed Ftractin-GFP \pm anti-TIM3 mAb for the 3D microscopic cytotoxicity assay. Spheroid dead volume at each timepoint was normalised to the initial dead volume at 2h and then to the average dead volume of the Spheroid only group. **b, left panel)** shows significant differences between groups at each time point, means were compared at each time point using a Two-Way ANOVA, matched by repeat and timepoint. **b, right panel)** shows significant death over time within each group, means were compared to the mean at 4h within each group, using Two-Way ANOVA and Dunnett's test, matched by repeat and timepoint. **c)** SIL density over the course of a 3D microscopic cytotoxicity assay is shown for groups plated with T-cells. Means were compared at each time point using a Two-Way ANOVA, matched by repeat and timepoint. **d)** Mean spheroid death at 12h across groups, normalised to the infiltration factor, a measure of the SIL density at the spheroid surface. **e)** Spheroid volume across all groups at 2h post-plating for the 3D microscopic cytotoxicity assay. n=3-4 spheroids per group, per repeat. Means were compared using a One-Way ANOVA, matched by repeat. For all graphs, error bars show mean \pm SEM and ns= non-significant p-values across all comparisons. Each individual point represents a mean of three independent repeats.

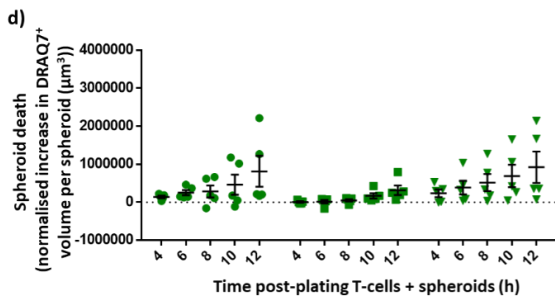


Spheroid death, comparisons between groups	Time (h)				
	4	6	8	10	12
TIM3-GFP ⁺⁺ RencaHA ^{tdT} vs TIM3-GFP ⁺⁺ RencaHA ^{CEAC1}	ns	ns	ns	0.02 *	0.0004 ***
TIM3-GFP ⁺⁺ RencaHA ^{tdT} vs TIM3-GFP ⁺⁺ RencaHA ^{CEAC1} + anti-TIM3 mAb	ns	ns	ns	ns	ns
TIM3-GFP ⁺⁺ RencaHA ^{CEAC1} vs TIM3-GFP ⁺⁺ RencaHA ^{CEAC1} + anti-TIM3 mAb	ns	ns	0.03 *	ns	0.009 **

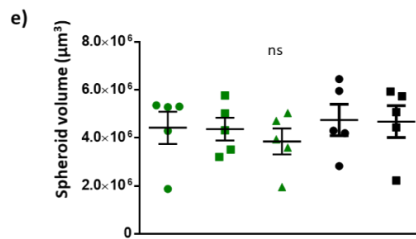
Spheroid death over time, comparisons within each group	Time (h)			
	6	8	10	12
TIM3-GFP ⁺⁺ RencaHA ^{tdT}	ns	ns	0.01 *	<0.0001 ****
TIM3-GFP ⁺⁺ RencaHA ^{CEAC1}	ns	ns	ns	ns
TIM3-GFP ⁺⁺ RencaHA ^{CEAC1} + anti-TIM3	ns	ns	0.02 *	0.0007 ***



SIL density	Time (h)					
	2	4	6	8	10	12
TIM3-GFP ⁺⁺ RencaHA ^{tdT} vs TIM3-GFP ⁺⁺ RencaHA ^{CEAC1}	0.01 *	ns	ns	0.001 **	0.002 **	<0.0001 ****
TIM3-GFP ⁺⁺ RencaHA ^{tdT} vs TIM3-GFP ⁺⁺ RencaHA ^{CEAC1} + anti-TIM3 mAb	0.002 **	0.0002 ***	0.0005 ***	0.0001 ***	0.0001 ***	0.004 **
TIM3-GFP ⁺⁺ RencaHA ^{CEAC1} vs TIM3-GFP ⁺⁺ RencaHA ^{CEAC1} + anti-TIM3 mAb	ns	0.02 *	0.05 *	0.04 *	ns	ns



Spheroid death normalised to SIL density, comparisons between groups	Time (h)				
	4	6	8	10	12
TIM3-GFP ⁺⁺ RencaHA ^{tdT} vs TIM3-GFP ⁺⁺ RencaHA ^{CEAC1}	ns	ns	ns	ns	0.009 **
TIM3-GFP ⁺⁺ RencaHA ^{tdT} vs TIM3-GFP ⁺⁺ RencaHA ^{CEAC1} + anti-TIM3 mAb	ns	ns	ns	ns	ns
TIM3-GFP ⁺⁺ RencaHA ^{CEAC1} vs TIM3-GFP ⁺⁺ RencaHA ^{CEAC1} + anti-TIM3 mAb	ns	ns	0.01 *	0.006 **	0.001 **



Spheroid death over time, comparisons within each group	Time (h)			
	6	8	10	12
TIM3-GFP ⁺⁺ RencaHA ^{tdT}	ns	ns	0.01 *	<0.0001 ****
TIM3-GFP ⁺⁺ RencaHA ^{CEAC1}	ns	ns	ns	ns
TIM3-GFP ⁺⁺ RencaHA ^{CEAC1} + anti-TIM3	ns	ns	0.02 *	0.0007 ***

Figure 5.15 Acute TIM3 blockade reversed CEACAM1-mediated suppression of CL4 T-cells that overexpressed TIM3-GFP. SIL densities differed between conditions, spheroid volumes did not. Normalisation of spheroid death to SIL densities showed suppression of T-cell cytotoxicity by CEACAM1 that was partially reversed by acute anti-TIM3 blockade.

a) RencaHA^{tdT} and RencaCEAC1^{tdT} spheroids were plated with 200,000 CL4 T-cells per well, which overexpressed TIM3-GFP \pm anti-TIM3 mAb. Spheroid dead volume at each timepoint was normalised to the initial dead volume at 2h and then to the average dead volume of the Spheroid only group. **b, left table)** shows significant differences between groups at each time point, means were compared at each time point using a Two-Way ANOVA, matched by repeat and timepoint. **b, right table)** shows significant death over time within each group, means were compared to the mean at 4h within each group, using Two-Way ANOVA and Dunnett's test, matched by repeat and timepoint. **c)** SIL density over the course of a 3D microscopic cytotoxicity assay is shown for groups plated with T-cells. Means were compared at each time point using a Two-Way ANOVA, matched by repeat and timepoint. **d)** Mean spheroid death at 12h across groups, normalised to the infiltration factor, a measure of the SIL density at the spheroid surface. Means were compared using One-Way ANOVA. **e)** Spheroid volume across all groups at 2h post-plating for the 3D microscopic cytotoxicity assay. n=3-4 spheroids per group, per repeat. Means were compared using a One-Way ANOVA, matched by repeat. For all graphs, error bars show mean \pm SEM and ns= non-significant p-values across all comparisons. Each individual point represents a mean of 5 independent repeats.

3D	CL4 T-cell (TIM3 expression level before added to spheroids)	Cytotoxicity (versus control Ftractin-GFP ⁺ T-cells)	SIL density (versus control Ftractin-GFP ⁺ T-cells)	Effect of acute TIM3 blockade on cytotoxicity/SIL density 		
RencaHA^{tdT} 	Ftractin⁺ (none) 	Equivalent	Equivalent	No effect		
	TIM3⁺ (~50-fold higher vs non-transduced) 	Lower	Equivalent	Complete reversion of suppression		
	CEACAM1⁺ (no TIM3 expression) 	Equivalent	Equivalent	-----		
	CEACAM1TIM3⁺ (~20-fold higher vs non-transduced T-cells) 	Equivalent	Non-sig. lower	No effect on cytotoxicity, non-sig. higher SIL densities		
3D	CL4 T-cell (TIM3 expression level before added to spheroids)	Cytotoxicity (versus control RencaHA targets)	SIL density	Effect of acute TIM3 blockade on cytotoxicity/SIL density 		
RencaHA^{CEAC1} 	Ftractin⁺ (no TIM3 expression) 	Equivalent	Higher	No effect		
	TIM3⁺ (~50-fold higher than non-transduced) 	Lower	Higher	Complete reversion of suppression of cytotoxicity, higher SIL densities		
2D	CL4 T-cell (TIM3 expression level before added to Renca)	Cytotoxicity (versus control Ftractin-GFP ⁺ T-cells)	IFN-γ secretion (versus Ftractin-GFP ⁺ T-cells)	Effect of acute TIM3 blockade on cytotoxicity/ IFNγ 	Morphology (versus Ftractin-GFP ⁺ T-cells)	Off-interface lamellipodia (versus control Ftractin-GFP ⁺ T-cells)
RencaHA^{tdT} 	Ftractin⁺ (none) 	Equivalent	Equivalent	No effect	Equivalent	Equivalent
	TIM3⁺ (~50-fold higher vs non-transduced) 	Non-significantly higher	Higher	No effect	Rounder (under lower peptide stimulus conditions)	Lower frequency, later onset
	CEACAM1⁺ (no TIM3 expression) 	Equivalent	Equivalent	-----	-----	-----
	CEACAM1TIM3⁺ (~20-fold higher vs non-transduced T-cells) 	Slightly lower	Equivalent	No effect	-----	-----
2D	CL4 T-cell (TIM3 expression level before added to Renca)	Cytotoxicity (versus control RencaHA targets)	IFN-γ secretion (versus control RencaHA targets)	Effect of acute TIM3 blockade on cytotoxicity/ IFNγ 	Morphology (versus control RencaHA targets)	Off-interface lamellipodia (versus control RencaHA targets)
RencaHA^{CEAC1} 	Ftractin⁺ (none) 	Lower	Non-significantly higher	No effect	More elongated	Higher frequency, equivalent onset
	TIM3⁺ (~50-fold higher vs non-transduced) 	Lower	Non-significantly higher	No effect	More elongated (more elongated versus Ftractin-GFP ⁺ cells at early timepoints)	Higher frequency, earlier onset (lower frequency, same onset versus Ftractin-GFP ⁺ T-cells)

Figure 5.16 Summary: how TIM3 regulates tumour-specific CL4 CD8 T-cell function in the 2D and 3D Renca tumour models and the role of CEACAM1 *in trans* and *in cis*.

5.3 Discussion

TIM3 has been shown to require ligation to transmit inhibitory signalling. To date, several putative ligands have been described: Galectin-9, CEACAM1, HMGB1 and PtdSer (221, 224, 236, 439). However, there are conflicting data on whether Galectin-9, CEACAM1 and HMGB1 are true TIM3 ligands, suggesting there may be context-dependent regulation of TIM3 ligands (221, 233, 242, 244, 255). Using *in vitro* T-cell models, CEACAM1 was shown to promote TIM3 surface expression and bind to TIM3 directly, while other experiments provided no evidence for the receptors binding (221, 244, 255). One study has shown that therapeutic murine and human antibodies interfere with TIM3 binding to CEACAM1 and PtdSer, but not with Galectin-9, though modulation of TIM3 function by Galectin-9 and HMGB1 could not be ruled out (HMGB1 binding to TIM3 could not be recapitulated in that study) (244). In the same study, the antibody clone RMT3-23 (used in our study) was found to be the most effective at blocking TIM3 binding to PtdSer and CEACAM1, compared to other TIM3 blocking antibodies (244).

While *in vivo* models have indicated that CEACAM1 supports TIM3-dependent inhibitory signalling in T-cells to regulate T-cell exhaustion and tolerance, it is unknown whether CEACAM1 and TIM3 directly coregulate the anti-tumour CD8 T-cell response *in vivo*, or if these receptors act through other cell types such as DCs, macrophages, and CD4 T-cells to indirectly regulate CD8 T-cell function. *In vitro* models thus far have not measured how CEACAM1 and TIM3 coregulate the cytotoxicity of CD8 T-cells by direct measurement of tumour cell death, instead they have measured T-cell cytokine production, degranulation, and transcription factor activity. We previously found that TIM3 signalling in tumour-specific CL4 CD8 T-cells differed between the 2D and 3D Renca tumour models (Chapter 4). It is unknown whether putative CEACAM1-mediated regulation of TIM3 signalling may differ in 2D *versus* 3D environments. An understanding of the environmental factors that affect how these receptors coregulate CD8 T-cell function is needed to understand conflicting data. Lastly, we previously found that TIM3 enhanced T-cell coupling abilities, T-cell polarisation and interface stability during T-cell coupling to Renca targets; until now, it is unknown whether CEACAM1 and TIM3 coregulate aspects of T-cell polarisation and interface stability during T-cell coupling to tumour cells. It is also unknown whether CEACAM1 and TIM3 coregulate the ability of T-cells to form cell couples with tumour targets, or T-cell calcium signalling during cell couple formation.

In this chapter, we used the 2D and 3D Renca models in parallel to investigate how TIM3 and CEACAM1-4L (*in cis* and *in trans*) coregulate tumour-specific CD8 T-cell cytotoxicity in 2D *versus* 3D environments, using direct measurements of tumour cell death. Furthermore, using the 2D Renca model, we investigated whether CEACAM1-4L on Renca cells regulates T-cell coupling abilities, calcium signalling, polarisation and interface stability within T-cell: tumour cell couples;

we also investigated how the expression of TIM3 on T-cells affected this. Such knowledge can aid the development of improved TIM3 and CEACAM1-targeting therapies for cancer patients.

5.3.1. Technical caveats to consider: investigating the role of CEACAM1 *in cis* in modulating TIM3-dependent T-cell signalling.

Importantly, there are several caveats in the 2D and 3D microscopic cytotoxicity assays which involved T-cells that coexpressed CEACAM1 and TIM3 *in cis* (CEACAM1-TIM3-GFP⁺⁺ T-cells). CEACAM1 and TIM3 coexpression was achieved by transducing CL4 T-cells with a retroviral vector that encoded CEACAM1 and TIM3-GFP, joined by a ribosome-skipping 2A peptide linker, to enable translation of both CEACAM1 and TIM3-GFP at a 1:1 ratio. However, T-cell transduction efficiencies of the CEACAM1-GFP and CEACAM1-TIM3-GFP constructs were lower than the transduction efficiency of the TIM3-GFP construct, which may be due to lower viral titres (not measured) arising from the higher relative length of the CEACAM1-GFP and CEACAM1-TIM3-GFP sequences (458). Ultimately, the level of TIM3 expressed by CEACAM1-TIM3⁺⁺ SILs was lower (20-fold upregulation *versus* non-transduced T-cells) than that expressed by TIM3-GFP⁺⁺ T-cells which were transduced to overexpress TIM3 alone (50-fold upregulation *versus* non-transduced T-cells). Since previous data showed a suppressive and stimulatory effect of TIM3 in 3D and 2D, respectively, it is expected that a lower level of TIM3 on the double positive *versus* TIM3-GFP⁺⁺ cells would cause less suppression in the 3D and less stimulation in the 2D models- if CEACAM1 overexpression had no functional effect. Evidence for such dose-dependent TIM3 signalling has been previously reported: higher expression levels of TIM3 on Jurkat cells, in a doxycycline-inducible system, dose-dependently enhanced IL-2 and IFN- γ levels (216). This suggested that in certain environments increasing TIM3 expression causes a corresponding increase in T-cell stimulation, although this was using anti-TCR/CD28 stimulation, rather than APCs (216). In other contexts, higher TIM3 expression has been associated with increased T-cell suppression; it was shown that PD1⁺ TIL populations expressing high, *versus* both low and high levels of TIM3, secreted lower levels of TNF- α and IL-2. However, in this study higher TIM3 expression was also associated with higher CEACAM1 expression and the effect of CEACAM1 expression alone in the TILs was not assessed (221). Given that TIM3-GFP⁺⁺ T-cells expressed ~2.5-fold higher levels of TIM3 *versus* CEACAM1-TIM3-GFP⁺⁺ T-cells, while CEACAM1-TIM3-GFP⁺⁺ T-cells still expressed ~20-fold higher levels of TIM3 *versus* non-transduced T-cells, we believe it is unlikely that the suppressive and stimulatory effects of TIM3 would be largely lost in the double-positive T-cell populations. Nevertheless, to address the caveat in our system, it would be of interest to confirm that the levels of TIM3 expressed by CEACAM1-TIM3-GFP⁺⁺ T-cells could still suppress CL4 T-cell cytotoxicity in the 3D model. Unfortunately, in this project, time constraints on cell sorting did not enable this to be addressed.

Another caveat is that independent of protein functions, the overexpression of two different proteins *versus* one protein may have increased the translational stress on CEACAM1-TIM3-GFP⁺⁺ cells *versus* T-cells that overexpressed one protein (Ftractin-GFP⁺⁺, CEACAM1⁺⁺ and TIM3-GFP⁺⁺ T-cells). Translational stress could negatively impact on T-cell effector functions (454, 455). In future, the non-specific effect of double *versus* single protein overexpression on T-cell cytotoxicity should be further established by coexpressing TIM3 with a protein that is not a putative ligand and has no functional effects, for example, by assessing the cytotoxicity of T-cells that overexpress both TIM3 and the olfactory receptor 2 (ORF2) – which is not normally expressed by T-cells- *versus* either alone. Based on previous data from our lab, however, we believe that any increase in translational burden associated with the levels of overexpression in our experiments is unlikely to have any functional effects (456).

Furthermore, as GFP-sorted CEACAM1-TIM3-GFP⁺⁺ and CEACAM1-GFP⁺⁺ T-cells were each a much smaller proportion of the presort populations compared to the TIM3-GFP⁺⁺ population (Figure 5.2b), they each comprised a more selective population of the most activated cells. This is because successful retroviral transduction requires dissolution of the nuclear membrane during T-cell proliferation and the most activated T-cells proliferate the most (459, 460). Thus, independent of protein functions, it is conceivable that the CEACAM1-GFP⁺⁺ and CEACAM1-TIM3-GFP⁺⁺ populations used in the cytotoxicity assays are more activated than the TIM3-GFP⁺⁺ population, which comprises a larger proportion of the presort population. To address this latter caveat, future experiments could transduce T-cells with a GFP-encoding construct (without a functional protein), then compare the cytotoxicity and effector functions of T-cells that comprise the top 2 per cent of the GFP-positive population (similar to the CEACAM1-TIM3-GFP⁺⁺ T-cells used in this project) *versus* the top 40% of the population (similar to the TIM3-GFP⁺⁺ T-cells). This could help to understand the impact of sorting a more selective population of the most activated (most efficiently transduced) cells.

Overall, it will be important to bear the above caveats in mind when interpreting data from experiments that investigated a possible coregulation of T-cell functions by CEACAM1 and TIM3 *in cis*. Nevertheless, any consistent effects of CEACAM1 coexpression *in cis* with TIM3 can help to direct future investigation into how these receptors interact. Moreover, TIM3 blockade treatment using the antibody clone RMT3-23 was used to provide evidence of whether CEACAM1 directly binds to the FGCC' cleft of TIM3 to mediate functional effects, which is currently unclear.

5.3.2. CEACAM1 coexpression with TIM3 *in cis* abrogated the suppressive effect of TIM3 overexpression on T-cell cytotoxicity.

In contrast to previous reports that CEACAM1 promoted cell surface expression of TIM3, we did not find enhancement in expression of either receptor upon coexpression of the other (221, 247).

To determine if CEACAM1 overexpression alone by CL4 T-cells had functional effects on T-cell killing, we compared the cytotoxicity of SILs that overexpressed CEACAM1 (CEACAM1⁺⁺) or Ftractin (Ftractin⁺⁺). There were no significant differences in cytotoxicity or infiltration between these groups, suggesting that CEACAM1 overexpression alone by CL4 T-cells had no functional effects on the tumour-specific CL4 T-cell response in the 3D model. Additionally, in the 2D model, CEACAM1⁺⁺ T-cells showed comparable cytotoxicity and IFN- γ secretion *versus* Ftractin-GFP⁺⁺ control cells, further supporting the idea that CEACAM1 had no functional effect on CL4 T-cells in this model. This finding was at odds with evidence that CEACAM1-L isoforms inhibit T-cell activation via cytoplasmic ITIM motifs and recruitment of SHP1 (221, 450). However, our results could be explained if there were insufficient levels of CEACAM1 ligands on Renca cells; CEACAM1, a primary ligand of itself, was only expressed by ~8% of RencaHA^{tdT} cells, while CEACAM5 expression levels- which is the only CEA family member that binds to CEACAM1 with high affinity- was not assessed. Additionally, it has been reported that the functional effects of CEACAM1 signalling may be context-dependent, as in some studies CEACAM1 induced stimulatory signalling (451-453).

Next, we found that CEACAM1 coexpression with TIM3 *in cis* by CL4 T-cells abrogated TIM3-dependent suppression of T-cell cytotoxicity in the RencaHA^{tdT} 3D model. CL4 SILs transduced to overexpress TIM3-GFP exhibited the most suppressed cytotoxicity against RencaHA^{tdT} spheroids, *versus* SILs that overexpressed CEACAM1-TIM3-GFP or CEACAM1-GFP. Meanwhile, CEACAM1-TIM3-GFP⁺⁺ and CEACAM1-GFP⁺⁺ SILs displayed comparable cytotoxicity. Previous findings (Chapter 4) revealed that TIM3 blockade reversed TIM3-mediated suppression of T-cell cytotoxicity in the 3D microscopic cytotoxicity assay, demonstrating that the assay timescale was sufficient to see functional effects of TIM3 blockade treatment. While CEACAM1 has been shown to bind to the FGCC' cleft on TIM3 *in trans*, whether CEACAM1 can also interact with TIM3 via this binding site to modulate T-cell function is unknown (221, 244, 449). Therefore, to investigate whether the suppressive effect of TIM3 on T-cell cytotoxicity was abrogated by direct binding of CEACAM1 to the FGCC' cleft of TIM3 *in cis*, CEACAM1-TIM3⁺⁺ SILs were treated with acute TIM3 blockade. There was no effect of acute TIM3 blockade on the cytotoxicity of CEACAM1-TIM3 SILs, demonstrating that coregulation of T-cell cytotoxicity by these receptors did not require binding of CEACAM1 to the FGCC' cleft of TIM3 *in cis*.

In summary, we propose that CEACAM1 *in cis* abrogated TIM3-mediated suppression in this system, in a manner that did not require direct binding to the FGCC' cleft of TIM3.

5.3.3. CEACAM1 coexpression with TIM3 *in cis* abrogated the stimulatory effect of TIM3

overexpression on T-cell cytotoxicity and IFN- γ secretion in the RencaHA^{tdT} 2D model.

As CEACAM1 interfered with TIM3-mediated suppression in the 3D model, it was of interest to see whether this result was shared in the 2D model. In contrast to the data from the 3D model, CEACAM1-TIM3⁺⁺ CL4 T-cells displayed suppressed cytotoxicity compared to TIM3-GFP⁺⁺ T-cells. Meanwhile, CEACAM1-TIM3⁺⁺ T-cells had similar cytotoxicity to Ftractin-GFP⁺⁺ and CEACAM1-GFP⁺⁺ T-cells. In corroboration with the cytotoxicity data, CEACAM1-TIM3⁺⁺ T-cells secreted significantly reduced levels of IFN- γ compared to TIM3⁺⁺ cells but secreted similar levels of IFN- γ compared to CEACAM1⁺⁺ or Ftractin-GFP⁺⁺ T-cells. This suggested that CEACAM1 counteracted stimulatory signalling downstream of TIM3 *in cis* and corroborated the finding that CEACAM1⁺TIM3⁺ CD4 T-cells from mice produced less IFN- γ compared to TIM3⁺ T-cells (221). Moreover, as in the 3D model, acute blockade of CEACAM1-TIM3⁺⁺ T-cells had no effect on T-cell cytotoxicity, suggesting that CEACAM1 and TIM3 did not directly bind via the FGCC' cleft on TIM3 to modulate cytotoxicity in the 2D or 3D models; TIM3 blockade also had no effect on IFN- γ secretion.

Overall, we propose that in the 2D and 3D Renca models, CEACAM1 consistently plays a 'TIM3-abrogator' role to reverse TIM3-mediated stimulation or inhibition of T-cell cytotoxicity, dependent on the context. This mechanism either involves direct binding of CEACAM1 and TIM3 *in cis* at a site distinct from the FGCC' cleft, or indirect coregulation by these receptors.

5.3.4. CEACAM1 overexpression *in trans* by RencaHA targets suppressed CL4 T-cell cytotoxicity in both the 2D and 3D models, but the suppressive effect was only reversible via acute TIM3 blockade in the 3D model.

CEACAM1 overexpression by RencaHA cells (RencaHA^{CEAC1}) was associated with a more elongated and irregular spheroid morphology, which supports findings that CEACAM1 can promote cell migration and invasion in cancer cells (461, 462). CL4 T-cells transduced to overexpress TIM3-GFP, Ftractin-GFP and CEACAM1-GFP exhibited comparably suppressed cytotoxicity in the 2D microscopic cytotoxicity assay when plated with RencaHA^{CEAC1} targets compared to control RencaHA^{tdT} targets. Acute TIM3 blockade could not reverse the suppressive effect of CEACAM1 *in trans* in the 2D assay, confirming that CEACAM1 expressed on Renca induced inhibitory signalling in the T-cells independent of acute TIM3 blockade- this antibody has previously been shown to block the CEACAM1 and TIM3 *in trans* binding site (244). This corroborates evidence that CEACAM1 can mediate inhibitory T-cell signalling *in trans*, although the responsible binding partner on T-cells in the 2D Renca model is unclear (221, 247, 463). Despite the suppression of T-cell cytotoxicity by CEACAM1 *in trans*, TIM3-GFP⁺⁺, Ftractin-GFP⁺⁺ and CEACAM1-GFP⁺⁺ T-cells all secreted slightly higher levels of IFN γ when plated with RencaHA^{CEAC1} *versus* RencaHA^{tdT} targets in

the 2D microscopic cytotoxicity assay. As IFN γ is produced downstream of the major TCR proximal signalling pathways, including NFAT and NF κ B activity, this finding suggested that CEACAM1 *in trans* did not broadly suppress TCR proximal signalling (discussed in Section 1.3.5), although it adds to evidence that IFN γ production may not always correlate with T-cell cytotoxicity (103, 464). Rather than affecting T-cell cytotoxicity, it is conceivable that overexpression of CEACAM1 simply endowed Renca cells with a general resistance to T-cell mediated killing (not investigated within this project), nevertheless, it was important to further establish if CEACAM1 *in trans* had any effects on T-cell function (discussed later, Section 1.3.5).

CL4 SILs that overexpressed TIM3 in the 3D microscopic cytotoxicity assay displayed suppressed cytotoxicity when plated with RencaHA^{CEAC1} spheroids compared to control RencaHA^{tdT} spheroids. On the other hand, CL4 SILs that overexpressed Ftractin showed comparable cytotoxicity when plated with RencaHA^{CEAC1} spheroids and RencaHA^{tdT} spheroids. In support of a direct interaction between TIM3 and CEACAM1 *in trans*, acute TIM3 blockade reversed the suppressive effect of CEACAM1 *in trans* on TIM3⁺⁺ SILs. This corroborates the idea that CEACAM1 *in trans* can mediate inhibitory signalling via TIM-3, but since TIM3⁺⁺ CL4 T-cells lack CEACAM1 expression *in cis*, our data suggest that CEACAM1 expression *in cis* is not required for *in trans* inhibition, in contrast to previous findings- it was previously reported that CEACAM1 *in cis* was required for BAT3 dissociation from the TIM3 cytoplasmic tail upon *in trans* binding by CEACAM1-Ig (221). As previously discussed, BAT3 dissociation downstream of TIM3 ligation by galectin-9 and CEACAM1 is associated with inhibitory signalling by reducing the local pool of Lck at the IS (215, 221). TIM3-GFP⁺⁺ and often Ftractin-GFP⁺⁺ SIL surface densities were elevated in RencaHA^{CEAC1} *versus* control spheroids. Surprisingly, acute blockade further enhanced TIM3-GFP⁺⁺ SIL densities but slightly decreased Ftractin⁺⁺ SIL densities in RencaHA^{CEAC1} spheroids. Firstly, the enhanced SIL densities on RencaHA^{CEAC1} spheroids could be due to CEACAM1 facilitating the adhesion of T-cells to spheroids via heterophilic interactions with other CEA family members on the T-cells, such as CEACAM5, although this was not determined in this project. Secondly, the elevated TIM3-GFP⁺⁺ SIL densities upon blockade of the *in trans* interaction of CEACAM1 and TIM3 could result from blockade of TIM3 and CEACAM1 signalling that suppressed T-cell attachment to spheroids. Although there is evidence for CEACAM1 but not TIM3-mediated regulation of the T-cell actin cytoskeleton, the latter cannot be ruled out (462). We have no evidence to explain the disparate effects of blockade on TIM3-GFP⁺⁺ and Ftractin-GFP⁺⁺ SILs, but given that SILs have been shown to upregulate TIM3 by ~2-fold *versus* T-cells that have not encountered spheroids and TIM3-GFP⁺⁺ T-cells express ~50-fold higher levels of TIM3 *versus* non-transduced T-cells, the data indicates that different levels of TIM3 expression could differentially modulate the effect of CEACAM1 *in trans* on T-cell adherence to spheroids.

Overall, acute TIM3 blockade treatment reversed the TIM3-dependent suppression of CD8 T-cells that was mediated by CEACAM1 *in trans*, suggesting that CEACAM1 directly bound to TIM3 *in trans* via the TIM3 FGCC' cleft to induce inhibitory signalling and suppress the cytotoxicity of tumour-specific CD8 T-cells.

5.3.5. CEACAM1 overexpression *in trans* by RencaHA targets caused defective T-cell polarisation and interface stability, with no effect on coupling frequencies or calcium signalling, during T-cell coupling with Renca targets in the 2D model.

As previously discussed, TIM3-GFP⁺⁺, Ftractin-GFP⁺⁺ and CEACAM1-GFP⁺⁺ T-cells all secreted slightly higher levels of IFN γ but exhibited lower cytotoxicity when plated with RencaHA^{CEAC1} *versus* RencaHA^{tdT} targets in the 2D microscopic cytotoxicity assay. As the effects of CEACAM1 *in trans* on CL4 T-cell cytotoxicity or IFN- γ secretion in the 2D model were not modulated by overexpression of CEACAM1 or TIM3 on T-cells, we hypothesised that CEACAM1 *in trans* may negatively regulate the cytoskeleton-controlled execution of cytolytic killing rather than broader TCR proximal signalling pathways- which are thought to be regulated by TIM3 and CEACAM1. To investigate this hypothesis, we studied the effects of CEACAM1 *in trans* on intracellular calcium signalling in T-cells during cell coupling to Renca targets, as this is one primary readout for the level of TCR proximal signalling; CEACAM1 expression *in trans* had no effect on T-cell calcium signalling. Combined with the lack of an inhibitory effect on IFN γ secretion, which occurs downstream of TCR proximal signalling, this calcium data suggested that CEACAM1 *in trans* did not modulate T-cell cytotoxicity by broad suppression of TCR proximal signalling. We then studied the effect of CEACAM1 *in trans* on the cell coupling frequencies of T-cells and tumour targets, as this is the first step in cytoskeleton-regulated execution of the cytolytic killing but found no effect on cell coupling frequencies. We then hypothesised that CEACAM1 might ligate to a binding partner on T-cells *in trans* to dysregulate cytoskeletal rearrangements important for effective morphological polarisation and interface stability upon cell coupling. This could provide an explanation for the reduced killing of RencaHA^{CEAC1} *versus* control RencaHA targets, despite T-cells exhibiting enhanced IFN- γ secretion and equivalent calcium signalling and cell coupling abilities across these targets. Interestingly, we found that CEACAM1 *in trans* caused T-cells to display a more elongated morphology during cell coupling and a higher frequency of OIL; a more elongated morphology has been associated with reduced T-cell activation and lower synapse stability, while OIL destabilise the cell couple interface (434, 435). Interestingly, TIM3-GFP⁺⁺ T-cells were more elongated than Ftractin-GFP⁺⁺ T-cells at early timepoints after cell coupling to RencaHA^{CEAC1} targets, while TIM3⁺⁺ but not Ftractin⁺⁺ cells displayed OIL sooner after cell coupling in the presence of CEACAM1 *in trans*. Furthermore, TIM3 overexpression was previously found to reduce the percentage of T-cells that displayed OIL by ~50% in the context of RencaHA^{tdT} targets (Chapter 4 Figure 1.8), but in the context of RencaHA^{CEAC1} targets, TIM3 overexpression reduced

the frequency of OIL by a much lower ~12%, suggesting that CEACAM1 *in trans* partially abrogated the interface-stabilising effect of TIM3.

As TIM3-GFP⁺⁺, CEACAM1-GFP⁺⁺ and Ftractin-GFP⁺⁺ T-cells (which lack TIM3 expression) were comparably suppressed by CEACAM1 overexpression on Renca cells in the 2D model, it is likely CEACAM1 ligation of an undetermined binding partner (not TIM3 or CEACAM1) on T-cells had a predominant role in deregulating T-cell polarisation and interface stability to inhibit T-cell cytotoxicity. Further investigation is required to link these aspects of T-cell polarisation and interface stability directly to the reduced cytotoxicity of T-cells plated with RencaHA^{CEAC1} versus RencaHA^{tdT} monolayer targets. It would be of interest to determine if the observed defects are associated with decreased F-actin clearance from the centre to the periphery of the IS, as has been previously described in CD8 CL4 TILs from RencaHA tumours that failed to polarise and formed unstable immune synapses compared to control T-cells (187). Our findings also suggested that CEACAM1 *in trans* partially abrogated TIM3 signalling that, in the absence of CEACAM1 overexpression *in trans*, enhanced T-cell polarisation and interface stability in the 2D model. Although the effects in the 2D model did not measurably impact on T-cell cytotoxicity, it is of interest to determine how TIM3 ligation by CEACAM1 *in trans* may impact T-cell polarisation and interface stability in the 3D environment. Lastly, we cannot rule out that CEACAM1 overexpression by Renca cells intrinsically endowed these cells with enhanced resistance to apoptosis, however the observed defects in T-cell polarisation and interface stability upon cell coupling suggest that disruption of T-cell cytolytic killing is at least partially responsible for the decreased death of RencaHA^{CEAC1} versus RencaHA^{tdT} targets.

5.3.6. Conclusion

In summary, in the 3D model, CEACAM1 *in cis* reversed TIM3-mediated inhibition of T-cell cytotoxicity. Similarly, in the 2D model, CEACAM1 *in cis* reversed TIM3-dependent T-cell stimulation. In both the 3D and 2D models, CEACAM1 did not bind to the FGCC' cleft of the TIM3 IgV domain *in cis* to alter T-cell function, as acute TIM3 blockade using the antibody clone RMT3-23 did not reverse the altered cytotoxicity displayed by CEACAM-TIM3-GFP⁺⁺ T-cells. Thus, it is of interest to determine if CEACAM1 *in cis* indirectly or directly, via another binding site on TIM3, regulates T-cell function by acting as a 'TIM3-abrogator', reversing both stimulatory and inhibitory TIM3 signalling in different contexts.

CEACAM1 *in trans* appeared to cooperate with TIM3 to inhibit tumour-specific CL4 CD8 T-cell cytotoxicity in the 3D but not the 2D RencaHA model. In the 3D model, acute TIM3 blockade reversed *in trans* CEACAM1-mediated suppression of TIM3-overexpressing SILs via both enhancement of SIL density and restoration of cytotoxicity. This supports the notion that CEACAM1 *in trans* can act as a TIM3 ligand, via binding to the FGCC' cleft on TIM3, to suppress the

anti-tumour T-cell response in certain contexts. Despite the lack of a TIM3-specific effect on T-cell cytotoxicity in the 2D model, CEACAM1 *in trans* inhibited T-cell morphological polarisation and partially abrogated the interface-stabilising effects of TIM3 upon cell coupling between T-cells and Renca cells.

Chapter 6 General Discussion

6.1 Overview of project rationale and aim

PD1/PDL1 and CTLA4 blockade agents are FDA-approved for clinical treatment of many tumour types and have synergistic efficacy when used in combination, however, combined treatment is associated with high rates of autoimmune side effects (>50% patients), called immune-related adverse events (irAEs) (315, 317). In particular, CTLA4 is upregulated by activated T-cells systemically and CTLA4 blockade commonly results in more than 30% of patients experiencing grade 3 or 4 irAEs (315, 316). On the other hand, compared to CTLA4, TIM3 is upregulated more specifically in the TME *versus* the periphery, making TIM3 blockade a less toxic and more promising treatment to use in combination with PD1 blockade (465). TIM3 and PD1 coexpression marks the most exhausted T-cells in tumour and chronic viral infection settings (325, 327, 430, 466). Moreover, TIM3 is commonly upregulated by T-cells in response to PD1/PDL1 blockade treatment, enabling tumours to gain therapeutic resistance and in preclinical studies co-blockade is more beneficial than single treatments (257, 329, 330, 430, 442). Understanding the regulators of TIM3 signalling in CD8 T-cells is important because while preclinical studies suggest that TIM3 is a promising target for immunotherapy, limited clinical data indicates a low toxicity of TIM3 blockade, but a low therapeutic efficacy of TIM3 blockade in combination with PD1 blockade (332, 333). This suggests a need to identify the contextual factors that regulate the efficacy of TIM3 blockade therapies, including an understanding of which TIM3 ligands induce TIM3 signalling and which cell types are targeted by TIM3 blockade to enhance the anti-tumour immune response. Further understanding of the context-dependent nature of TIM3 signalling could pave the way for improved administration of TIM3 blockade, including the identification of biomarkers for patients that will benefit most from this treatment or additional targeting of factors that modulate TIM3 signalling. Notably, it is currently unclear whether TIM3 blockade treatments can directly reverse the suppression of tumour-specific CD8 T-cell cytotoxicity, or if the therapeutic effects of TIM3 blockade are mediated by other cell types which indirectly promote CD8 T-cell responses.

Tumour cells grown *in vitro* in 3D *versus* 2D have been shown to undergo both transcriptomic and proteomic changes which increase their similarity to *in vivo* tumours and can enhance their capacity to suppress tumour-specific T-cells (359-367, 369, 372, 374, 375). However, TIM3 signalling in T-cells has been primarily studied using less physiologically relevant *in vitro* 2D models, or *in vivo*, where it is difficult to ascertain the direct effects of TIM3 on CD8 T-cells. Therefore, the overall aim of this project was to develop and characterise a 3D RencaHA spheroid model, which could be used in parallel with the 2D RencaHA monolayer model to investigate how TIM3 regulates the tumour-specific CD8 T-cell response, including the ability of T-cells to kill

tumour targets. It was of interest to identify if a 3D *versus* 2D environment could modulate the nature of TIM3 signalling, which can shed light on the contextual regulators of TIM3 signalling. Additionally, CEACAM1 *in cis* and *in trans* is the most recently proposed TIM3 ligand, however, data on how CEACAM1 regulates TIM3 signalling in CD8 T-cells is limited, and in contrast to the original study, a subsequent study found no evidence for coregulation of T-cell function by CEACAM1 and TIM3 (221, 255, 449). More data are needed to establish if CEACAM1 regulates TIM3 signalling, either through direct binding or indirectly, and if coregulation of T-cell function by these receptors may be context-dependent. Therefore, it was of interest to investigate how CEACAM1 may coregulate T-cell function with TIM3 both *in cis* and *in trans* and if this differs between a 2D and 3D environment, the latter of which has not been previously studied.

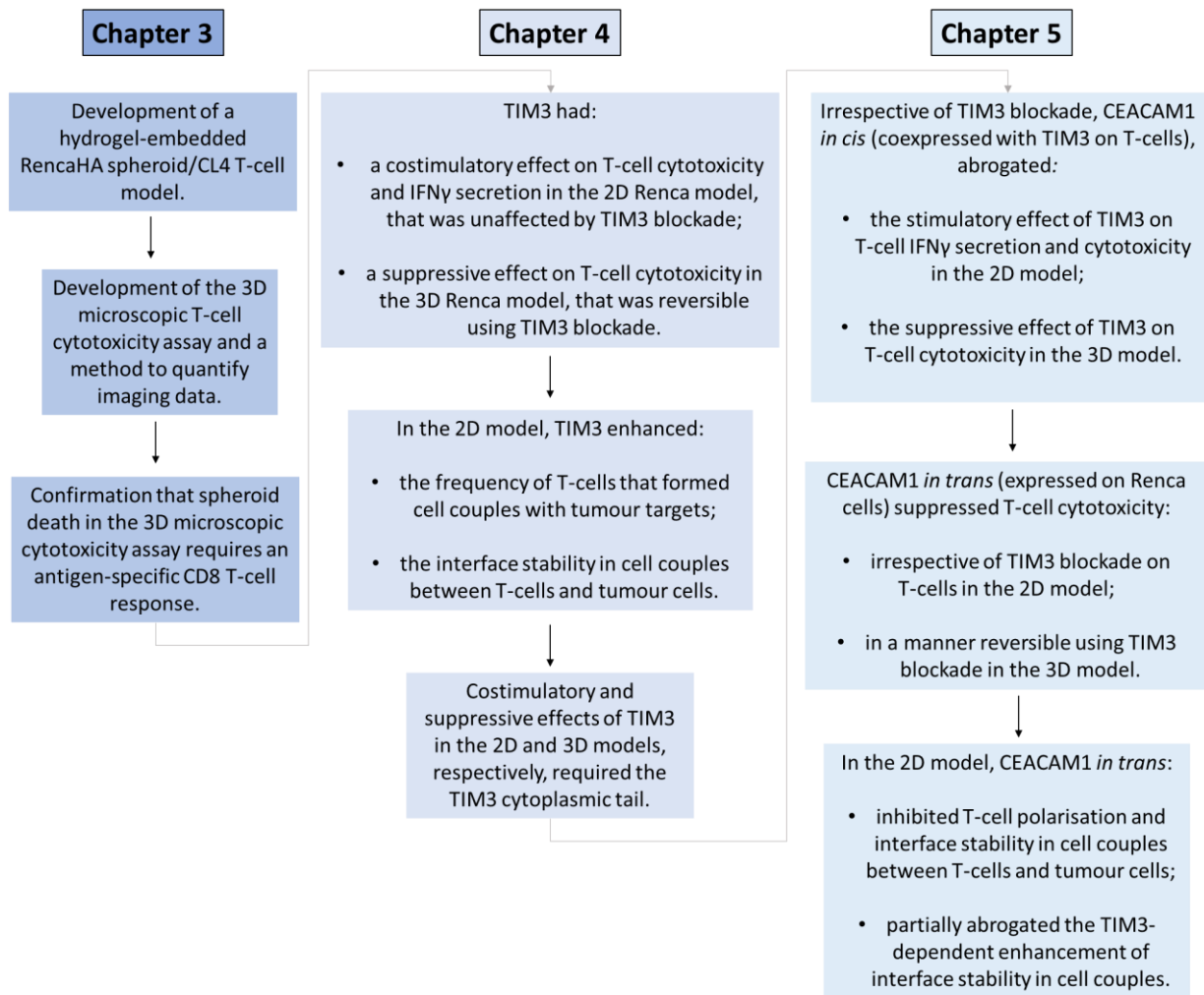


Figure 6.1 Schematic overview of key thesis findings.

6.2 Development and characterisation of a 3D RencaHA model to study the tumour-specific CL4 CD8 T-cell response

A 3D RencaHA model was developed which could be used to investigate tumour-induced immunosuppression of tumour-specific CD8 T-cells. RencaHA cells were grown into well-rounded compact spheroids in the hydrogel Matrigel which is derived from Engelbreth-Holm-Swarm murine sarcomas and comprises the basement membrane proteins including laminin, type IV collagen and entactin (467). 10-day old RencaHA spheroids, which were used in functional assays throughout this project, did not display hypoxia, which was in corroboration with findings that hypoxia develops in spheroids with a diameter $\geq 500\mu\text{m}$ (390). RencaHA spheroids also had a dead core, therefore the 3D RencaHA model likely recapitulated necrotic regions which are commonly found in *in vivo* tumours- the central dead region of spheroids is typically necrotic in other spheroid models and can result from reduced access to oxygen, glucose, and/or low pH caused by increased glycolysis (390, 468). Tumour necrosis has been found to positively correlate with tumour progression and the suppression of tumour-specific CD8 T-cells (353, 354, 356). Therefore, in future, it is of interest to determine whether the dead core was due to central necrosis or another cell death pathway such as apoptosis, in order to further confirm the physiological relevance of the model. A 3D microscopic cytotoxicity assay was developed that enabled the imaging of T-cell interactions with tumour spheroids and measurement of T-cell-dependent tumour cell death, over 12 hours from the initial plating of T-cells with tumour spheroids. T-cell-mediated spheroid death was shown to require antigen-specificity, demonstrating that this model could be used to study the antigen-specific T-cell response, and the immunosuppressive mechanisms which inhibit this response.

A key limitation of the 3D RencaHA model was that CL4 T-cells had highly limited motility in Matrigel. T-cells which adhered to spheroids were usually within $50\mu\text{m}$ of the spheroid surface at the start of the assay, in contrast, activated TILs *in vivo* have been described to migrate at an average speed of nearly $10\mu\text{m}$ per minute (422). The migration of T-cells through Matrigel *in vitro* has been shown to rely on the secretion of matrix metalloproteinase 9 (MMP9) by T-cells, which cleaves ECM components, therefore, it is likely that CL4 T-cells secrete low levels of this protease (469-471). Induction of MMP9 upregulation in CL4 T-cells could enhance their motility to more physiological levels in the RencaHA spheroid model. Vascular endothelial growth factor (VEGF) has been found to induce MMP9 upregulation in normal splenic cells and is highly expressed in *in vivo* tumours, therefore, it could be used to enhance MMP9 secretion by CL4 T-cells during the 3D microscopic cytotoxicity assay (472). To establish if VEGF could be used for this purpose, the expression of the VEGF receptors VEGFR-1 and VEGFR-2, which have been found to be expressed on primary murine T-cells, could be assessed in activated CL4 T-cells (472). Additionally, although

previous attempts to grow RencaHA spheroids using alginate or non-adherent wells failed to generate compact, well-rounded spheroids, it would be of interest to pursue alternative spheroid growth techniques, as the ability to grow one spheroid per well, instead of four-hundred spheroids per well, would likely decrease the variability of data from the 3D microscopic cytotoxicity assay. This is because a lack of precise control regarding the distribution of spheroids throughout each Matrigel dome may impact on the local concentration of growth factors and chemokines surrounding a given spheroid. For example, in non-adherent wells, cancer-associated fibroblasts (CAFs) could be co-cultured with RencaHA cells to provide a source of ECM, instead of Matrigel, which may promote the formation of compact spheroids in a format of one spheroid per well (473). Another source of variability in the 3D cytotoxicity assay is the previously reported batch-to-batch variability in the proteomic composition and stiffness of Matrigel (474), which could be addressed in future by using synthetic hydrogels or as previously mentioned, CAFs as a source of ECM in coculture. Relevant to both the 2D and 3D cytotoxicity assays, week-to-week variability in the cytotoxicity of CL4 T-cells also contributes to assay variability because cells are harvested from a different animal each week and T-cells are typically passaged by a different combination of lab members each week, on days 6 and 7 of the Phoenix transfection/T-cell transduction timeline (Figure 2.1 Retroviral transduction of CL4 T-cells using the ecotropic Phoenix packaging cell line). To address these points in future, a CL4 T-cell line has been recently produced by the lab and could reduce this source of variation, as culture of the CL4 T-cell line involves restimulation of the T-cells each week by the same user, without passaging by other lab members on days 6 and 7. Nevertheless, although it will be important to further reduce the sources of variation in the 3D imaging assay results, the spheroid growth method used herein provides initial evidence that RencaHA spheroids can be grown in 3D to better recapitulate aspects of the *in vivo* RencaHA TME *versus* the monolayer model.

In the 3D microscopic cytotoxicity assay, the viability dye DRAQ7 was used to label dead cells as a measure of T-cell cytotoxicity. In future, the RencaHA^{GzmB} and RencaHA^{Casp8} lines generated during this project could be used to assess whether tumour cells are killed by the granzyme B or Fas/FasL pathways, respectively, thus providing a more precise measure of T-cell-dependent killing in addition to DRAQ7 labelling. RencaHA^{GzmB} and RencaHA^{Casp8} cells express fluorescent reporters which can be enzymatically cleaved upon granzyme B delivery into the target cell or intracellular caspase 8 activation, respectively. Enzymatic cleavage of a nuclear export signal from the fluorophore (tdTomato) causes the fluorescent signal to translocate from an exclusively cytoplasmic to a nuclear and cytoplasmic distribution- we can call such translocation events 'fill-in death events'. Thus, it is of interest to continue the development of an image analysis pipeline that can automatically detect and quantify these fill-in death events, to improve the readout of T-cell cytotoxicity in the 3D microscopic assay.

We also found that CL4 T-cells failed to kill tumour spheroids in the presence of polyclonal CD8 T-cells in the same wells, therefore, it is of interest to establish what factor(s) were released by polyclonal CD8 T-cells to suppress CL4 T-cell cytotoxicity, as it may reveal a yet undescribed mechanism of immunosuppression of adoptively transferred CL4 T-cells by endogenous CD8 T-cells within *in vivo* RencaHA tumours. For example, polyclonal CD8 T-cells could be isolated from the 3D microscopic cytotoxicity assay and stained for the expression of CD39 and CD73, which are ectoenzymes that generate adenosine from ATP. Adenosine, produced by CD4 Tregs, has been identified as a key soluble suppressor of CD8 T-cells in RencaHA tumours, in a manner dependent on adenosine 2a receptor (A2aR) signalling, but it is unknown whether CD8 Tregs may also contribute to immunosuppressive adenosine production in this model (328).

6.3 Divergent TIM3 signalling in the 3D versus 2D RencaHA model

Using the 3D and 2D microscopic cytotoxicity assays in parallel, we investigated how murine TIM3 (mTIM3) overexpression regulated the function of tumour-specific CD8 CL4 T-cells. Firstly, TIM3 overexpression on T-cells had a small stimulatory effect in 2D, as measured by slightly enhanced cytotoxicity and increased IFN γ secretion. This finding corroborated a study in which mTIM3 enhanced NFAT, AP1 and NF κ B activity in TCR/CD28 stimulated Jurkat cells which had been transiently transfected to overexpress TIM3 (216). Moreover, our findings are consistent with a study in which the frequency of IFN γ -producing cells was higher in CD3/CD28 activated, primary CD4 murine T-cells which had been stably transfected with mTIM3 *versus* GFP-transfected control T-cells. Our finding also supports the recent report that human TIM3 (hTIM3) enhanced MEK-ERK and Akt-mTOR signalling following TCR stimulation, which together promoted the phosphorylation of the ribosomal component S6 in Jurkat cells (258). Furthermore, another study found that CD8 T-cells from TIM3 KO *versus* WT mice displayed decreased Akt/mTOR signalling, degranulation, and IFN γ production, while CD3/CD28 activated murine T-cells which overexpressed TIM3 displayed enhanced levels of phosphorylated S6 which is produced downstream of Akt/mTOR signalling (257). TIM3 has also been described to enhance TCR proximal signalling as measured by increased tyrosine phosphorylation of proteins in whole WT murine T-cells compared to TIM3 knockdown T-cells (247). Together, these data and our findings using the 2D RencaHA model support the notion that TIM3 can have costimulatory effects under certain contexts. However, studies highlighting a costimulatory role for TIM3 are in the minority compared to the vast body of *in vitro* and *in vivo* studies which provide evidence for coinhibitory signalling via TIM3 (246, 331).

In contrast to the 2D tumour model, TIM3 overexpression on T-cells suppressed T-cell cytotoxicity in the 3D model. This corroborates *in vitro* studies which have demonstrated coinhibitory signalling downstream of TIM3 (424, 425). Stable overexpression of hTIM3 in Jurkat T-cell lines

was shown to inhibit IL-2 secretion in addition to NF κ B and NFAT activation following CD3/CD28 stimulation (425). Corroborating that finding, another study showed that hTIM3 overexpression reduced nuclear translocation of NFAT and IL-2 expression in stably transfected Jurkat T-cells stimulated with phorbol myristate acetate (PMA) and the calcium ionophore calcimycin (424). Moreover, primary human CD4 T-cells from healthy donors which expressed high *versus* low levels of TIM3 following CD3/CD28 activation *in vitro* exhibited decreased IL2 transcription and reduced NFAT and AP1 nuclear translocation upon PMA/calcimycin restimulation (424). A limitation to the latter finding is that the differentiation state of T-cells which expressed low *versus* high levels of TIM3 following *in vitro* stimulation may have been distinct prior to TIM3 upregulation; this could account for the observed differences in NFAT, AP1 activation and IL-2 secretion. In another study, TIM3⁺ MART-1-specific primary human CD8 T-cells expanded using peptide-loaded artificial APCs exhibited reduced NFAT and NF κ B activity and decreased IL-2 secretion compared to naïve TIM3⁻ CD8 T-cells (425). However, prolonged stimulation of MART-1-specific primary CD8 T-cells likely induced broad changes in the expression of T-cell signalling proteins that were not induced in the naïve control cells, making it hard to determine whether the effects were solely due to TIM3 expression. Unlike in the 2D model, IFN γ secretion during the 3D microscopic cytotoxicity assay was not quantified as it could not be proven that the same total number of T-cells were in contact with the hundreds of spheroids within each well. In future, a setup using one spheroid per well would enable the quantification of cytokine secretion by T-cells during the 3D microscopic cytotoxicity assay using enzyme-linked immunosorbent assay (ELISA).

Overall, *in vitro* TIM3 signalling studies have primarily utilised Jurkat T-cell lines and both costimulatory and coinhibitory effects have been observed within this system. While coinhibitory signalling has been observed in the context of both PMA/calcium ionophore and CD3/CD28 stimulation, costimulatory signalling has been observed using CD3/CD28 or TCR/CD28 stimulation; it remains an open question whether the method of T-cell activation may affect the nature of TIM3 signalling. Namely, PMA and calcium ionophore bypass the need for TCR stimulation and directly activate protein kinase C (PKC) and induce calcium signalling, respectively (475). On the other hand, CD3/CD28 and TCR/CD28 activation induce phosphorylation of the CD3 chains in the TCR complex. Additionally, divergent TIM3 signalling could also be explained by different expression levels of TIM3 ligands in the cell cultures utilised by different laboratories, for example, the expression levels of galectin-9 and CEACAM1 were not assessed in the aforementioned studies. As our studies utilised 2D and 3D models in parallel, which both involved the activation of effector CL4 CD8 T-cells by RencaHA tumour cells bearing cognate antigen, the divergent signalling in the two models cannot be accounted for by different activation methods or cell batches/types. Instead, it is possible that known or unknown TIM3 binding partners, which regulate TIM3 signalling, were differentially expressed in the 2D *versus* 3D RencaHA models. Mass

spectrometry could be used to identify proteins that are differentially expressed in 2D- versus 3D-cultured RencaHA cells. This could help to identify unknown TIM3 ligands or signalling intermediates that are important for costimulatory or coinhibitory TIM3 signalling. Furthermore, different mechanotransductive stimuli and soluble factors between the two models may influence which TIM3 signalling pathways are activated. Additionally, our data support the notion that 3D tumour models better recapitulate the *in vivo* TME versus monolayer models, as the majority of *in vivo* data demonstrate an inhibitory role for TIM3 (246, 331). TIM3 is a marker of exhausted T-cells which have a reduced capacity to proliferate and secrete cytokines such as IL-2 and IFN γ (325, 327). Meanwhile, several studies have demonstrated that TIM3 blockade in combination with PD1 blockade can inhibit tumour growth and prolong survival in murine tumour models, thus supporting TIM3 inhibitory signalling (325, 327, 329, 330).

As TIM3 had a costimulatory effect on T-cells in the 2D model, we hypothesised that TIM3 may support effective coupling of T-cells to target cells and the stability of the interface in cell couples, both of which are critical steps for effective cytotoxic killing and sustained TCR signalling that supports IFN γ secretion. We found that TIM3 overexpression increased the frequency of T-cells that formed cell couples with Renca targets. TIM3 overexpression also enhanced the stability of the interface within cell couples, as measured by a reduced and delayed formation of interface-destabilising off-interface lamellipodia (OIL) following cell couple formation. Such a role for TIM3 has not been previously described. The immunosuppressed state of CL4 TILs, isolated from RencaHA tumours and characterised *in vitro*, was previously associated with the enhanced recruitment of cofilin, a protein which depolymerises F-actin, to the IS of TILs versus control T-cells cultured *in vitro*. This was proposed to decrease the clearance of F-actin from the centre of the IS and reduce F-actin accumulation at the periphery of the IS which suppressed T-cell cytotoxicity (187). In that study, F-actin accumulation at the IS in T-cells during cell coupling was observed using confocal imaging of F-actin-GFP-transduced TILs and control T-cells as they coupled to tumour targets; the application of a computational analysis enabled quantification of F-actin enrichment at the IS (187). As TIM3 enhanced the cell coupling ability of T-cells to tumour targets and the interface stability within cell couples, it is of interest to determine whether TIM3 overexpression enhances F-actin clearance from the centre to the periphery of the IS, thus promoting the formation and stability of the interface in cell couples. If TIM3 supports these processes, it would be interesting to identify the intermediates which couple TIM3 ligation to downstream cytoskeletal reorganisation. Additionally, it would be of interest to determine if TIM3 can enhance cell couple formation and interface stability in the context of 3D tumour targets or if this capacity is lost in the 3D environment. Given the suppressive effect of TIM3 overexpression in the 3D RencaHA model, it is also possible that TIM3 inhibits these processes in the 3D environment.

Costimulatory and coinhibitory TIM3 signalling has been found to be mediated by the TIM3 cytoplasmic tail (216, 217, 258, 424, 425). Having established that TIM3 regulates the tumour-specific CD8 T-cell response in the 2D and 3D models, we investigated whether the functional effects of TIM3 overexpression were mediated by the cytoplasmic tail of TIM3. To do this we used a truncated form of TIM3, which lacked the cytoplasmic tail. In corroboration with previous findings, we found that the cytoplasmic tail of TIM3 was required for both costimulatory and coinhibitory TIM3 signalling. While the suppressive effects of TIM3 could be reversed using TIM3 blockade treatment using the antibody clone RMT3-23, the stimulatory effects of TIM3 signalling were unaffected by TIM3 blockade. This is in line with evidence that TIM3 blockade can reverse suppression of T-cells *in vivo*, and that stimulatory signalling occurs when TIM3 is unligated (215, 216, 325, 328-330). In future, it is of interest to generate mutant forms of TIM3 which substitute the tyrosine residues thought to be critical for TIM3 signalling in the TIM3 tail (Y256 and Y263 in mTIM3) (216, 258, 424). These mutant forms of TIM3 could be used alongside WT TIM3 in order to determine the sites on the cytoplasmic tail that are required for the altered cytotoxicity in both the 2D and 3D models. If mutating Y256 and/or Y263 abrogates the stimulatory effects of TIM3 in the 2D model, it would be of interest to determine if costimulatory signalling is BAT3-dependent and coinhibitory signalling is FYN-dependent, as has been proposed (215-217, 221, 246).

6.4 CEACAM1 *in cis* abrogates TIM3 signalling in the 3D and 2D RencaHA models

Two major studies have investigated whether CEACAM1 can act as a ligand for TIM3. One study provided coimmunoprecipitation data and associative *in vivo* evidence that CEACAM1 can act as a TIM3 ligand both *in cis* and *in trans*, while the other used binding studies and fluorescence resonance energy transfer (FRET) to find no evidence for a direct interaction between TIM3 and CEACAM1 *in trans* and *in cis*, respectively (221, 255). In the former study, CEACAM1 overexpression was found to support the cell surface expression of TIM3, as HEK293T cells co-transfected with CEACAM1 and TIM3 expressed higher levels of TIM3 *versus* control cells transfected with TIM3 alone (221). This effect was described to be a result of putative *in cis* interactions: firstly TIM3 and CEACAM1 could be coimmunoprecipitated from co-transfected HEK293T cells, primary mouse T-cells and primary human T-cells; secondly, mutation of amino acids in the TIM3 FGCC' cleft partially abrogated CEACAM1 and TIM3 co-immunoprecipitation (221). This finding was corroborated by another study where co-transfection of Jurkat cells with CEACAM1 and TIM3 enhanced TIM3 expression *versus* TIM3 transfection alone (247). In contrast, using our retroviral transduction system, we found that CEACAM1 overexpression had no effect on the cell surface expression of endogenous TIM3, while CL4 T-cells transduced to overexpress both CEACAM1 and TIM3 *in cis* expressed a lower level of TIM3 *versus* CL4 T-cells transduced to

overexpress TIM3 alone. However, it is more likely that the reduced level of TIM3 expressed by T-cells transduced to overexpress both CEACAM1 and TIM3, *versus* TIM3 alone, was simply due to a reduced retroviral titre in the supernatant used to transduce the double-positive *versus* single positive T-cells, although this was not measured. Nevertheless, we found no evidence for upregulation of endogenous TIM3 following CEACAM1 overexpression, suggesting that CEACAM1 does not promote TIM3 surface expression. This was in corroboration with evidence that CEACAM1 is not required for TIM3 surface expression: upon *in vitro* stimulation with staphylococcal enterotoxin E (SEE) or CD3/CD28 antibodies, human T-cells homogeneously upregulated TIM3 whereas only a small subset of these cells expressed CEACAM1 (255).

Next, we found that, upon overexpression *in cis* with TIM3 on T-cells, CEACAM1 abrogated both the costimulatory effect of TIM3 on IFN γ secretion and T-cell cytotoxicity in the 2D RencaHA model, and the suppressive effect of TIM3 on T-cell cytotoxicity in the 3D model. Our data from the 2D model support findings that T-cells which coexpress CEACAM1 and TIM3 *in cis* secrete reduced levels of IFN γ *versus* T-cells that express TIM3 alone (221, 248). Abrogation of TIM3 costimulatory signalling by CEACAM1 *in cis* has not previously been described, although TIM3 costimulatory signalling and CEACAM1-mediated inhibitory signalling have been separately proposed (216, 221, 247, 257, 258). Although ligation of TIM3 is thought to induce inhibitory signalling, our findings using the 2D RencaHA model did not provide evidence for a direct interaction between TIM3 and CEACAM1, as acute TIM3 blockade did not alter the effects of CEACAM1 and TIM3 coexpression (215, 217, 221). This does not rule out the possibility that CEACAM1 and TIM3 can bind *in cis* at an alternative binding site distinct from the FGCC' cleft of TIM3, which is the site blocked by the blocking antibody used (clone RMT3-23) and the proposed binding site of CEACAM1 *in trans* (244). Alternatively, CEACAM1 may have indirectly abrogated TIM3 costimulatory signalling without direct binding.

Our findings that CEACAM1 *in cis* abrogated suppressive TIM3 signalling in the 3D RencaHA model fall in line with data demonstrating an elevated activation state, as measured by CD25 expression, of SEE-activated human T-cells which expressed both CEACAM1 and TIM3 *versus* TIM3 alone (255). However, in that study, the same effect did not occur in CD3/CD28 activated T-cells (255). Our data directly measure tumour cell death as a readout for T-cell cytotoxicity and it is likely that different parameters of T-cell activation may lead to different conclusions regarding the effect of CEACAM1 coexpression with TIM3. More data on the coregulation of other T-cell activation parameters by TIM3 and CEACAM1 *in cis* is therefore required to establish which aspects of T-cell signalling they may control. Finally, as in the 2D model, the effects of CEACAM *in cis* were unaffected by TIM3 blockade treatment in the 3D model, suggesting that the functional effects did not result from CEACAM1 and TIM3 directly binding via the FGCC' cleft of TIM3 (244). This

suggested that CEACAM1 may have indirectly (without binding to TIM3) abrogated TIM3 signalling in the 2D and 3D models, or that CEACAM1 directly bound to TIM3 *in cis* at a different binding site to that described for the *in trans* interaction.

6.5 CEACAM1 *in trans* induces inhibitory signalling through TIM3

In the 2D RencaHA model, the overexpression of CEACAM1 *in trans* by Renca cells inhibited the cytotoxicity of CL4 T-cells, regardless of TIM3 expression levels on T-cells. This effect of CEACAM1 to inhibit T-cells *in trans* corroborates findings that CEACAM1 upregulation by melanoma cells can inhibit TIL cytotoxicity and IFN γ secretion (476, 477). This findings also falls in line with evidence that CEACAM1 expression positively correlates with tumour progression in a variety of tumour types including melanoma, colorectal, non-small cell lung cancer, and pancreatic cancer (254). However, whereas inhibition of TIL cytotoxicity has been associated with homophilic CEACAM1-CEACAM1 interactions, our staining data suggested a lack of CEACAM1 expression by CL4 T-cells on the day of the microscopic cytotoxicity assays. This suggests that another CEACAM1 binding partner, expressed on T-cells, transduced inhibitory signals upon binding to CEACAM1 *in trans*, or that T-cells expressed low, but functionally relevant, levels of CEACAM1 that were undetectable through antibody staining. Moreover, in our data from the 2D model, CEACAM1 *in trans* did not inhibit IFN γ secretion by T-cells, in contrast to previous accounts of TIL suppression via CEACAM1 homophilic interactions (476). This difference and the lack of CEACAM1 expression by T-cells as detected by antibody staining suggests that CEACAM1 *in trans* may have bound to another unknown binding partner on T-cells to suppress T-cell cytotoxicity- it would be of interest in future to establish if CEACAM5 is expressed by CL4 T-cells, as it is also a reported ligand for CEACAM1 (245). Moreover, the apparent reduced cytotoxic potential of T-cells against Renca targets that overexpress CEACAM1 may have resulted from tumour cell-intrinsic effects of CEACAM1 overexpression. Therefore, it would be of interest to use a blocking CEACAM1 antibody to establish if CEACAM1 requires *in trans* interactions in order to suppress T-cell killing. Nevertheless, CEACAM1 engagement of TIM3 *in trans* partially abrogated the interface-stabilising effects of TIM3 to delay and reduce the frequency of OIL, supporting the previous finding that CEACAM1 can counteract TIM3 signalling.

In the 3D model, CEACAM1 *in trans* suppressed T-cell cytotoxicity in a TIM3-dependent manner and this suppression was reversible using TIM3 blockade. Therefore, this suggested that CEACAM1 *in trans* could bind directly to the FGCC' cleft of TIM3 to suppress T-cell signalling. This supports the finding that CEACAM1 can act as a TIM3 ligand *in trans* (221). Moreover, it supports the finding that murine and human TIM3 blocking antibodies with therapeutic effect block CEACAM1 *in trans* binding to TIM3 (244). On the other hand, our data contrasts with evidence that TIM3 and CEACAM1 do not interact *in trans* (expressed by reporter T-cells and stimulator T-

cells) to regulate AP1, NFAT or NFκB signalling in T-cells (255). Our data also conflict with evidence from ELISA and flow cytometric binding assays using recombinant proteins comprised of the IgV portions of TIM3 and CEACAM1 fused to Fc domains which found no evidence for *in trans* interactions (255). As the suppressive effects of CEACAM1 *in trans* on T-cell cytotoxicity was dependent on the level of TIM3 expression on T-cells in the 3D model, but not in the 2D model, it is likely that altered expression of other proteins by RencaHA cells accounted for the differential effects across the two models. Similarly, it is likely that the conflicting data regarding the role of CEACAM1 *in trans* result from different expression of other CEACAM1 or TIM3 binding partners in the cells used. As discussed previously, mass spectrometry of 2D and 3D cultured RencaHA^{CEAC1} cells could provide an insight into which other proteins are required for CEACAM1 to induce inhibitory signalling downstream of TIM3. Overall, our data provide evidence that CEACAM1 and TIM3 can differentially coregulate T-cell signalling in a context-dependent manner, however, more data are required to establish the relevant signalling pathways.

Chapter 7 Bibliography

1. Duan, L., and E. Mukherjee. 2016. Janeway's Immunobiology, Ninth Edition. *The Yale Journal of Biology and Medicine* 89: 424-425.
2. Chaplin, D. D. 2010. Overview of the immune response. *The Journal of allergy and clinical immunology* 125: S3-S23.
3. Alexander, K. L., S. R. Targan, and C. O. Elson, 3rd. 2014. Microbiota activation and regulation of innate and adaptive immunity. *Immunological reviews* 260: 206-220.
4. Goldszmid, R. S., A. Dzutsev, and G. Trinchieri. 2014. Host immune response to infection and cancer: unexpected commonalities. *Cell host & microbe* 15: 295-305.
5. Gurtner, G. C., S. Werner, Y. Barrandon, and M. T. Longaker. 2008. Wound repair and regeneration. *Nature* 453: 314-321.
6. Farkona, S., E. P. Diamandis, and I. M. Blasutig. 2016. Cancer immunotherapy: the beginning of the end of cancer? *BMC Med* 14: 73.
7. Turvey, S. E., and D. H. Broide. 2010. Innate immunity. *The Journal of allergy and clinical immunology* 125: S24-S32.
8. Roh, J. S., and D. H. Sohn. 2018. Damage-Associated Molecular Patterns in Inflammatory Diseases. *Immune network* 18: e27-e27.
9. Wu, S.-Y., T. Fu, Y.-Z. Jiang, and Z.-M. Shao. 2020. Natural killer cells in cancer biology and therapy. *Molecular Cancer* 19: 120.
10. Abel, A. M., C. Yang, M. S. Thakar, and S. Malarkannan. 2018. Natural Killer Cells: Development, Maturation, and Clinical Utilization. *Frontiers in Immunology* 9.
11. Eberl, G., M. Colonna, J. P. Di Santo, and A. N. J. McKenzie. 2015. Innate lymphoid cells: A new paradigm in immunology. *Science* 348: aaa6566.
12. Fu, C., and A. Jiang. 2018. Dendritic Cells and CD8 T Cell Immunity in Tumor Microenvironment. *Front Immunol* 9: 3059.
13. LeBien, T. W., and T. F. Tedder. 2008. B lymphocytes: how they develop and function. *Blood* 112: 1570-1580.
14. Boyd, S. D., and S. A. Joshi. 2014. High-Throughput DNA Sequencing Analysis of Antibody Repertoires. *Microbiol Spectr* 2.
15. Krangel, M. S. 2009. Mechanics of T cell receptor gene rearrangement. *Current opinion in immunology* 21: 133-139.
16. Neefjes, J., M. L. M. Jongsma, P. Paul, and O. Bakke. 2011. Towards a systems understanding of MHC class I and MHC class II antigen presentation. *Nature Reviews Immunology* 11: 823-836.
17. Schubert, U., L. C. Antón, J. Gibbs, C. C. Norbury, J. W. Yewdell, and J. R. Bennink. 2000. Rapid degradation of a large fraction of newly synthesized proteins by proteasomes. *Nature* 404: 770-774.
18. Reits, E. A. J., J. C. Vos, M. Grommé, and J. Neefjes. 2000. The major substrates for TAP in vivo are derived from newly synthesized proteins. *Nature* 404: 774-778.
19. Heath, W. R., and F. R. Carbone. 2001. Cross-presentation in viral immunity and self-tolerance. *Nat Rev Immunol* 1: 126-134.
20. Segura, E., and S. Amigorena. 2015. Chapter One - Cross-Presentation in Mouse and Human Dendritic Cells. In *Advances in Immunology*. F. W. Alt, ed. Academic Press. 1-31.
21. Guermonprez, P., L. Saveanu, M. Kleijmeer, J. Davoust, P. Van Endert, and S. Amigorena. 2003. ER-phagosome fusion defines an MHC class I cross-presentation compartment in dendritic cells. *Nature* 425: 397-402.
22. Bertholet, S., R. Goldszmid, A. Morrot, A. Debrabant, F. Afrin, C. Collazo-Custodio, M. Houde, M. Desjardins, A. Sher, and D. Sacks. 2006. Leishmania Antigens Are Presented to CD8 T Cells by a Transporter Associated with Antigen Processing-Independent Pathway In Vitro and In Vivo. *The Journal of Immunology* 177: 3525-3533.

23. Schumacher, T. N., M. T. Heemels, J. J. Neefjes, W. M. Kast, C. J. Melief, and H. L. Ploegh. 1990. Direct binding of peptide to empty MHC class I molecules on intact cells and in vitro. *Cell* 62: 563-567.
24. Eisen, H. N., X. H. Hou, C. Shen, K. Wang, V. K. Tanguturi, C. Smith, K. Kozyrsky, L. Nambiar, C. A. McKinley, J. Chen, and R. J. Cohen. 2012. Promiscuous binding of extracellular peptides to cell surface class I MHC protein. *Proc Natl Acad Sci U S A* 109: 4580-4585.
25. Vitiello, A., T. A. Potter, and L. A. Sherman. 1990. The role of beta 2-microglobulin in peptide binding by class I molecules. *Science* 250: 1423-1426.
26. Takahama, Y. 2006. Journey through the thymus: stromal guides for T-cell development and selection. *Nat Rev Immunol* 6: 127-135.
27. Masopust, D., and J. M. Schenkel. 2013. The integration of T cell migration, differentiation and function. *Nature Reviews Immunology* 13: 309-320.
28. Smith-Garvin, J. E., G. A. Koretzky, and M. S. Jordan. 2009. T cell activation. *Annual review of immunology* 27: 591-619.
29. Sawamura, Y. 1991. [Isolation and expansion of glioma-infiltrating lymphocytes in vitro: an analysis of their surface phenotypes and antitumor activities]. *Hokkaido Igaku Zasshi* 66: 868-878.
30. Shahinian, A., K. Pfeffer, K. P. Lee, T. M. Kündig, K. Kishihara, A. Wakeham, K. Kawai, P. S. Ohashi, C. B. Thompson, and T. W. Mak. 1993. Differential T cell costimulatory requirements in CD28-deficient mice. *Science* 261: 609-612.
31. King, C. L., J. Xianli, C. H. June, R. Abe, and K. P. Lee. 1996. CD28-deficient mice generate an impaired Th2 response to *Schistosoma mansoni* infection. *Eur J Immunol* 26: 2448-2455.
32. Zhu, J., H. Yamane, and W. E. Paul. 2010. Differentiation of effector CD4 T cell populations. *Annual review of immunology* 28: 445-489.
33. Kapsenberg, M. L. 2003. Dendritic-cell control of pathogen-driven T-cell polarization. *Nat Rev Immunol* 3: 984-993.
34. Schweitzer, A. N., and A. H. Sharpe. 1998. Studies using antigen-presenting cells lacking expression of both B7-1 (CD80) and B7-2 (CD86) show distinct requirements for B7 molecules during priming versus restimulation of Th2 but not Th1 cytokine production. *J Immunol* 161: 2762-2771.
35. Brownlie, R. J., and R. Zamoyska. 2013. T cell receptor signalling networks: branched, diversified and bounded. *Nature Reviews Immunology* 13: 257-269.
36. Love, P. E., and S. M. Hayes. 2010. ITAM-mediated signaling by the T-cell antigen receptor. *Cold Spring Harbor perspectives in biology* 2: a002485-a002485.
37. Billadeau, D. D., J. C. Nolz, and T. S. Gomez. 2007. Regulation of T-cell activation by the cytoskeleton. *Nature Reviews Immunology* 7: 131-143.
38. Trebak, M., and J.-P. Kinet. 2019. Calcium signalling in T cells. *Nature reviews. Immunology* 19: 154-169.
39. Hwang, J.-R., Y. Byeon, D. Kim, and S.-G. Park. 2020. Recent insights of T cell receptor-mediated signaling pathways for T cell activation and development. *Experimental & Molecular Medicine* 52: 750-761.
40. Hogan, P. G., R. S. Lewis, and A. Rao. 2010. Molecular basis of calcium signaling in lymphocytes: STIM and ORAI. *Annu Rev Immunol* 28: 491-533.
41. Hogan, P. G., L. Chen, J. Nardone, and A. Rao. 2003. Transcriptional regulation by calcium, calcineurin, and NFAT. *Genes Dev* 17: 2205-2232.
42. Wülfing, C., J. D. Rabinowitz, C. Beeson, M. D. Sjaastad, H. M. McConnell, and M. M. Davis. 1997. Kinetics and extent of T cell activation as measured with the calcium signal. *The Journal of experimental medicine* 185: 1815-1825.
43. Grynkiewicz, G., M. Poenie, and R. Y. Tsien. 1985. A new generation of Ca²⁺ indicators with greatly improved fluorescence properties. *J Biol Chem* 260: 3440-3450.
44. Acuto, O., and F. Michel. 2003. CD28-mediated co-stimulation: a quantitative support for TCR signalling. *Nat Rev Immunol* 3: 939-951.

45. Luckheeram, R. V., R. Zhou, A. D. Verma, and B. Xia. 2012. CD4(+)T cells: differentiation and functions. *Clin Dev Immunol* 2012: 925135.
46. O'Shea, J. J., and W. E. Paul. 2010. Mechanisms underlying lineage commitment and plasticity of helper CD4+ T cells. *Science* 327: 1098-1102.
47. Lighvani, A. A., D. M. Frucht, D. Jankovic, H. Yamane, J. Aliberti, B. D. Hisson, B. V. Nguyen, M. Gadina, A. Sher, W. E. Paul, and J. J. O'Shea. 2001. T-bet is rapidly induced by interferon-gamma in lymphoid and myeloid cells. *Proc Natl Acad Sci U S A* 98: 15137-15142.
48. Anderson, A. C., G. M. Lord, V. Dardalhon, D. H. Lee, C. A. Sabatos-Peyton, L. H. Glimcher, and V. K. Kuchroo. 2010. T-bet, a Th1 transcription factor regulates the expression of Tim-3. *Eur J Immunol* 40: 859-866.
49. Heinzl, F. P., M. D. Sadick, B. J. Holaday, R. L. Coffman, and R. M. Locksley. 1989. Reciprocal expression of interferon gamma or interleukin 4 during the resolution or progression of murine leishmaniasis. Evidence for expansion of distinct helper T cell subsets. *J Exp Med* 169: 59-72.
50. Peng, S. L., S. J. Szabo, and L. H. Glimcher. 2002. T-bet regulates IgG class switching and pathogenic autoantibody production. *Proceedings of the National Academy of Sciences* 99: 5545-5550.
51. Cox, M. A., L. E. Harrington, and A. J. Zajac. 2011. Cytokines and the inception of CD8 T cell responses. *Trends in immunology* 32: 180-186.
52. Harrington, L. E., R. D. Hatton, P. R. Mangan, H. Turner, T. L. Murphy, K. M. Murphy, and C. T. Weaver. 2005. Interleukin 17-producing CD4+ effector T cells develop via a lineage distinct from the T helper type 1 and 2 lineages. *Nat Immunol* 6: 1123-1132.
53. Liang, S. C., X. Y. Tan, D. P. Luxenberg, R. Karim, K. Dunussi-Joannopoulos, M. Collins, and L. A. Fouser. 2006. Interleukin (IL)-22 and IL-17 are coexpressed by Th17 cells and cooperatively enhance expression of antimicrobial peptides. *J Exp Med* 203: 2271-2279.
54. Tesmer, L. A., S. K. Lundy, S. Sarkar, and D. A. Fox. 2008. Th17 cells in human disease. *Immunological reviews* 223: 87-113.
55. Lee, H.-M., J. L. Bautista, and C.-S. Hsieh. 2011. Chapter 2 - Thymic and Peripheral Differentiation of Regulatory T Cells. In *Advances in Immunology*. R. Alexander, and S. Shimon, eds. Academic Press. 25-71.
56. Curotto de Lafaille, M. A., A. C. Lino, N. Kutchukhidze, and J. J. Lafaille. 2004. CD25⁻ T Cells Generate CD25⁺ Foxp3⁺ Regulatory T Cells by Peripheral Expansion. *The Journal of Immunology* 173: 7259-7268.
57. Dhamne, C., Y. Chung, A. Alousi, L. Cooper, and D. Tran. 2013. Peripheral and Thymic Foxp3+ Regulatory T Cells in Search of Origin, Distinction, and Function. *Frontiers in Immunology* 4.
58. Shevryev, D., and V. Tereshchenko. 2020. Treg Heterogeneity, Function, and Homeostasis. *Frontiers in Immunology* 10.
59. van der Merwe, P. A., D. L. Bodian, S. Daenke, P. Linsley, and S. J. Davis. 1997. CD80 (B7-1) binds both CD28 and CTLA-4 with a low affinity and very fast kinetics. *J Exp Med* 185: 393-403.
60. Qureshi, O. S., Y. Zheng, K. Nakamura, K. Attridge, C. Manzotti, E. M. Schmidt, J. Baker, L. E. Jeffery, S. Kaur, Z. Briggs, T. Z. Hou, C. E. Fetter, G. Anderson, L. S. Walker, and D. M. Sansom. 2011. Trans-endocytosis of CD80 and CD86: a molecular basis for the cell-extrinsic function of CTLA-4. *Science* 332: 600-603.
61. Gu, P., J. Fang Gao, C. A. D'Souza, A. Kowalczyk, K.-Y. Chou, and L. Zhang. 2012. Trogocytosis of CD80 and CD86 by induced regulatory T cells. *Cellular & Molecular Immunology* 9: 136-146.
62. Schmidt, A., N. Oberle, and P. Krammer. 2012. Molecular Mechanisms of Treg-Mediated T Cell Suppression. *Frontiers in Immunology* 3.
63. Zarek, P. E., C. T. Huang, E. R. Lutz, J. Kowalski, M. R. Horton, J. Linden, C. G. Drake, and J. D. Powell. 2008. A2A receptor signaling promotes peripheral tolerance by inducing T-cell anergy and the generation of adaptive regulatory T cells. *Blood* 111: 251-259.

64. Cekic, C., and J. Linden. 2014. Adenosine A2A receptors intrinsically regulate CD8+ T cells in the tumor microenvironment. *Cancer Res* 74: 7239-7249.
65. Deaglio, S., K. M. Dwyer, W. Gao, D. Friedman, A. Usheva, A. Erat, J. F. Chen, K. Enjoji, J. Linden, M. Oukka, V. K. Kuchroo, T. B. Strom, and S. C. Robson. 2007. Adenosine generation catalyzed by CD39 and CD73 expressed on regulatory T cells mediates immune suppression. *J Exp Med* 204: 1257-1265.
66. Fallarino, F., U. Grohmann, K. W. Hwang, C. Orabona, C. Vacca, R. Bianchi, M. L. Belladonna, M. C. Fioretti, M. L. Alegre, and P. Puccetti. 2003. Modulation of tryptophan catabolism by regulatory T cells. *Nat Immunol* 4: 1206-1212.
67. Fallarino, F., U. Grohmann, S. You, B. C. McGrath, D. R. Cavener, C. Vacca, C. Orabona, R. Bianchi, M. L. Belladonna, C. Volpi, P. Santamaria, M. C. Fioretti, and P. Puccetti. 2006. The combined effects of tryptophan starvation and tryptophan catabolites down-regulate T cell receptor zeta-chain and induce a regulatory phenotype in naive T cells. *J Immunol* 176: 6752-6761.
68. Mezrich, J. D., J. H. Fechner, X. Zhang, B. P. Johnson, W. J. Burlingham, and C. A. Bradfield. 2010. An interaction between kynurenine and the aryl hydrocarbon receptor can generate regulatory T cells. *J Immunol* 185: 3190-3198.
69. McMurchy, A. N., and M. K. Levings. 2012. Suppression assays with human T regulatory cells: a technical guide. *Eur J Immunol* 42: 27-34.
70. Davidson, T. S., R. J. DiPaolo, J. Andersson, and E. M. Shevach. 2007. Cutting Edge: IL-2 is essential for TGF-beta-mediated induction of Foxp3+ T regulatory cells. *J Immunol* 178: 4022-4026.
71. Chen, W., W. Jin, N. Hardegen, K. J. Lei, L. Li, N. Marinos, G. McGrady, and S. M. Wahl. 2003. Conversion of peripheral CD4+CD25- naive T cells to CD4+CD25+ regulatory T cells by TGF-beta induction of transcription factor Foxp3. *J Exp Med* 198: 1875-1886.
72. Zeng, H., R. Zhang, B. Jin, and L. Chen. 2015. Type 1 regulatory T cells: a new mechanism of peripheral immune tolerance. *Cellular & molecular immunology* 12: 566-571.
73. Weiner, H. L. 2001. Induction and mechanism of action of transforming growth factor-beta-secreting Th3 regulatory cells. *Immunol Rev* 182: 207-214.
74. Yasukawa, M., H. Ohminami, J. Arai, Y. Kasahara, Y. Ishida, and S. Fujita. 2000. Granule exocytosis, and not the fas/fas ligand system, is the main pathway of cytotoxicity mediated by alloantigen-specific CD4(+) as well as CD8(+) cytotoxic T lymphocytes in humans. *Blood* 95: 2352-2355.
75. Yamada, A., R. Arakaki, M. Saito, Y. Kudo, and N. Ishimaru. 2017. Dual Role of Fas/FasL-Mediated Signal in Peripheral Immune Tolerance. *Frontiers in Immunology* 8.
76. Russell, J. H., and T. J. Ley. 2002. Lymphocyte-mediated cytotoxicity. *Annu Rev Immunol* 20: 323-370.
77. Kaech, S. M., and R. Ahmed. 2001. Memory CD8+ T cell differentiation: initial antigen encounter triggers a developmental program in naïve cells. *Nat Immunol* 2: 415-422.
78. Lieberman, J. 2003. The ABCs of granule-mediated cytotoxicity: new weapons in the arsenal. *Nat Rev Immunol* 3: 361-370.
79. Voskoboinik, I., J. C. Whisstock, and J. A. Trapani. 2015. Perforin and granzymes: function, dysfunction and human pathology. *Nature Reviews Immunology* 15: 388-400.
80. Law, R. H., N. Lukoyanova, I. Voskoboinik, T. T. Caradoc-Davies, K. Baran, M. A. Dunstone, M. E. D'Angelo, E. V. Orlova, F. Coulibaly, S. Verschoor, K. A. Browne, A. Ciccone, M. J. Kuiper, P. I. Bird, J. A. Trapani, H. R. Saibil, and J. C. Whisstock. 2010. The structural basis for membrane binding and pore formation by lymphocyte perforin. *Nature* 468: 447-451.
81. Nakajima, H., H. L. Park, and P. A. Henkart. 1995. Synergistic roles of granzymes A and B in mediating target cell death by rat basophilic leukemia mast cell tumors also expressing cytolysin/perforin. *J Exp Med* 181: 1037-1046.
82. Cullen, S. P., M. Brunet, and S. J. Martin. 2010. Granzymes in cancer and immunity. *Cell Death Differ* 17: 616-623.
83. Barry, M., J. A. Heibein, M. J. Pinkoski, S. F. Lee, R. W. Moyer, D. R. Green, and R. C. Bleackley. 2000. Granzyme B short-circuits the need for caspase 8 activity during granule-

- mediated cytotoxic T-lymphocyte killing by directly cleaving Bid. *Mol Cell Biol* 20: 3781-3794.
84. Alimonti, J. B., L. Shi, P. K. Baijal, and A. H. Greenberg. 2001. Granzyme B induces BID-mediated cytochrome c release and mitochondrial permeability transition. *J Biol Chem* 276: 6974-6982.
 85. Masson, D., P. J. Peters, H. J. Geuze, J. Borst, and J. Tschopp. 1990. Interaction of chondroitin sulfate with perforin and granzymes of cytolytic T-cells is dependent on pH. *Biochemistry* 29: 11229-11235.
 86. Blumenthal, R., P. J. Millard, M. P. Henkart, C. W. Reynolds, and P. A. Henkart. 1984. Liposomes as targets for granule cytolysin from cytotoxic large granular lymphocyte tumors. *Proc Natl Acad Sci U S A* 81: 5551-5555.
 87. Dupuis, M., E. Schaerer, K. H. Krause, and J. Tschopp. 1993. The calcium-binding protein calreticulin is a major constituent of lytic granules in cytolytic T lymphocytes. *J Exp Med* 177: 1-7.
 88. Bird, C. H., V. R. Sutton, J. Sun, C. E. Hirst, A. Novak, S. Kumar, J. A. Trapani, and P. I. Bird. 1998. Selective regulation of apoptosis: the cytotoxic lymphocyte serpin proteinase inhibitor 9 protects against granzyme B-mediated apoptosis without perturbing the Fas cell death pathway. *Mol Cell Biol* 18: 6387-6398.
 89. Metkar, S. S., B. Wang, M. Aguilar-Santelises, S. M. Raja, L. Uhlin-Hansen, E. Podack, J. A. Trapani, and C. J. Froelich. 2002. Cytotoxic cell granule-mediated apoptosis: perforin delivers granzyme B-serglycin complexes into target cells without plasma membrane pore formation. *Immunity* 16: 417-428.
 90. Balaji, K. N., N. Schaschke, W. Machleidt, M. Catalfamo, and P. A. Henkart. 2002. Surface cathepsin B protects cytotoxic lymphocytes from self-destruction after degranulation. *The Journal of experimental medicine* 196: 493-503.
 91. Siegel, R. M., J. K. Frederiksen, D. A. Zacharias, F. K. Chan, M. Johnson, D. Lynch, R. Y. Tsien, and M. J. Lenardo. 2000. Fas preassociation required for apoptosis signaling and dominant inhibition by pathogenic mutations. *Science* 288: 2354-2357.
 92. Kaufmann, T., A. Strasser, and P. J. Jost. 2012. Fas death receptor signalling: roles of Bid and XIAP. *Cell Death Differ* 19: 42-50.
 93. Kischkel, F. C., S. Hellbardt, I. Behrmann, M. Germer, M. Pawlita, P. H. Krammer, and M. E. Peter. 1995. Cytotoxicity-dependent APO-1 (Fas/CD95)-associated proteins form a death-inducing signaling complex (DISC) with the receptor. *Embo j* 14: 5579-5588.
 94. Boldin, M. P., E. E. Varfolomeev, Z. Pancer, I. L. Mett, J. H. Camonis, and D. Wallach. 1995. A novel protein that interacts with the death domain of Fas/APO1 contains a sequence motif related to the death domain. *J Biol Chem* 270: 7795-7798.
 95. Muzio, M., A. M. Chinnaiyan, F. C. Kischkel, K. O'Rourke, A. Shevchenko, J. Ni, C. Scaffidi, J. D. Bretz, M. Zhang, R. Gentz, M. Mann, P. H. Krammer, M. E. Peter, and V. M. Dixit. 1996. FLICE, a novel FADD-homologous ICE/CED-3-like protease, is recruited to the CD95 (Fas/APO-1) death-inducing signaling complex. *Cell* 85: 817-827.
 96. Boatright, K. M., M. Renatus, F. L. Scott, S. Sperandio, H. Shin, I. M. Pedersen, J. E. Ricci, W. A. Edris, D. P. Sutherlin, D. R. Green, and G. S. Salvesen. 2003. A unified model for apical caspase activation. *Mol Cell* 11: 529-541.
 97. Beaudouin, J., C. Liesche, S. Aschenbrenner, M. Hörner, and R. Eils. 2013. Caspase-8 cleaves its substrates from the plasma membrane upon CD95-induced apoptosis. *Cell Death Differ* 20: 599-610.
 98. Green, D. R., and F. Llambi. 2015. Cell Death Signaling. *Cold Spring Harbor perspectives in biology* 7: a006080.
 99. Intlekofer, A. M., N. Takemoto, E. J. Wherry, S. A. Longworth, J. T. Northrup, V. R. Palanivel, A. C. Mullen, C. R. Gasink, S. M. Kaech, J. D. Miller, L. Gapin, K. Ryan, A. P. Russ, T. Lindsten, J. S. Orange, A. W. Goldrath, R. Ahmed, and S. L. Reiner. 2005. Effector and memory CD8+ T cell fate coupled by T-bet and eomesodermin. *Nat Immunol* 6: 1236-1244.

100. Teixeira, L. K., B. P. Fonseca, A. Vieira-de-Abreu, B. A. Barboza, B. K. Robbs, P. T. Bozza, and J. P. Viola. 2005. IFN-gamma production by CD8+ T cells depends on NFAT1 transcription factor and regulates Th differentiation. *J Immunol* 175: 5931-5939.
101. Schoenborn, J. R., and C. B. Wilson. 2007. Regulation of Interferon- γ During Innate and Adaptive Immune Responses. In *Advances in Immunology*. Academic Press. 41-101.
102. Bhat, P., G. Leggatt, N. Waterhouse, and I. H. Frazer. 2017. Interferon- γ derived from cytotoxic lymphocytes directly enhances their motility and cytotoxicity. *Cell death & disease* 8: e2836-e2836.
103. Horton, H., N. Russell, E. Moore, I. Frank, R. Baydo, C. H. Daughton, D. Lee, M. Deers, M. Hudgens, K. Weinhold, and M. J. McElrath. 2004. Correlation between Interferon- γ Secretion and Cytotoxicity, in Virus-Specific Memory T Cells. *The Journal of Infectious Diseases* 190: 1692-1696.
104. Zhou, F. 2009. Molecular mechanisms of IFN-gamma to up-regulate MHC class I antigen processing and presentation. *Int Rev Immunol* 28: 239-260.
105. Ligocki, A. J., J. R. Brown, and J. Y. Niederkorn. 2016. Role of interferon- γ and cytotoxic T lymphocytes in intraocular tumor rejection. *J Leukoc Biol* 99: 735-747.
106. Whitmire, J. K., J. T. Tan, and J. L. Whitton. 2005. Interferon-gamma acts directly on CD8+ T cells to increase their abundance during virus infection. *The Journal of experimental medicine* 201: 1053-1059.
107. Refaeli, Y., L. Van Parijs, S. I. Alexander, and A. K. Abbas. 2002. Interferon gamma is required for activation-induced death of T lymphocytes. *J Exp Med* 196: 999-1005.
108. Driver, J. P., J. J. Racine, C. Ye, D. J. Lamont, B. N. Newby, C. M. Leeth, H. D. Chapman, T. M. Brusko, Y. G. Chen, C. E. Mathews, and D. V. Serreze. 2017. Interferon- γ Limits Diabetogenic CD8(+) T-Cell Effector Responses in Type 1 Diabetes. *Diabetes* 66: 710-721.
109. Ratner, A., and W. R. Clark. 1993. Role of TNF-alpha in CD8+ cytotoxic T lymphocyte-mediated lysis. *J Immunol* 150: 4303-4314.
110. Zheng, L., G. Fisher, R. E. Miller, J. Peschon, D. H. Lynch, and M. J. Lenardo. 1995. Induction of apoptosis in mature T cells by tumour necrosis factor. *Nature* 377: 348-351.
111. Bertrand, F., J. Rochotte, C. Colacios, A. Montfort, A.-F. Tilkin-Mariamé, C. Touriol, P. Rochaix, I. Lajoie-Mazenc, N. Andrieu-Abadie, T. Levade, H. Benoist, and B. Ségui. 2015. Blocking Tumor Necrosis Factor α Enhances CD8 T-cell-Dependent Immunity in Experimental Melanoma. *Cancer Research* 75: 2619-2628.
112. Calzascia, T., M. Pellegrini, H. Hall, L. Sabbagh, N. Ono, A. R. Elford, T. W. Mak, and P. S. Ohashi. 2007. TNF-alpha is critical for antitumor but not antiviral T cell immunity in mice. *J Clin Invest* 117: 3833-3845.
113. Vuddamalay, Y., M. Attia, R. Vicente, C. Pomié, G. Enault, B. Leobon, O. Joffre, P. Romagnoli, and J. P. M. van Meerwijk. 2016. Mouse and human CD8(+) CD28(low) regulatory T lymphocytes differentiate in the thymus. *Immunology* 148: 187-196.
114. Vuddamalay, Y., and J. P. M. van Meerwijk. 2017. CD28(-) and CD28(low)CD8(+) Regulatory T Cells: Of Mice and Men. *Frontiers in immunology* 8: 31-31.
115. Liu, J., D. Chen, G. D. Nie, and Z. Dai. 2015. CD8(+)CD122(+) T-Cells: A Newly Emerging Regulator with Central Memory Cell Phenotypes. *Front Immunol* 6: 494.
116. Flippe, L., S. Bézie, I. Anegon, and C. Guillonneau. 2019. Future prospects for CD8(+) regulatory T cells in immune tolerance. *Immunol Rev* 292: 209-224.
117. Wei, S., I. Kryczek, L. Zou, B. Daniel, P. Cheng, P. Mottram, T. Curiel, A. Lange, and W. Zou. 2005. Plasmacytoid dendritic cells induce CD8+ regulatory T cells in human ovarian carcinoma. *Cancer Res* 65: 5020-5026.
118. Rifa'i, M., Z. Shi, S. Y. Zhang, Y. H. Lee, H. Shiku, K. Isobe, and H. Suzuki. 2008. CD8+CD122+ regulatory T cells recognize activated T cells via conventional MHC class I- α alphabetaTCR interaction and become IL-10-producing active regulatory cells. *Int Immunol* 20: 937-947.
119. Zhang, L., A. M. Bertucci, R. Ramsey-Goldman, R. K. Burt, and S. K. Datta. 2009. Regulatory T cell (Treg) subsets return in patients with refractory lupus following stem cell transplantation, and TGF-beta-producing CD8+ Treg cells are associated with

- immunological remission of lupus. *Journal of immunology (Baltimore, Md. : 1950)* 183: 6346-6358.
120. Najafian, N., T. Chitnis, A. D. Salama, B. Zhu, C. Benou, X. Yuan, M. R. Clarkson, M. H. Sayegh, and S. J. Khoury. 2003. Regulatory functions of CD8+CD28- T cells in an autoimmune disease model. *The Journal of clinical investigation* 112: 1037-1048.
 121. Krummel, M. F., and I. Macara. 2006. Maintenance and modulation of T cell polarity. *Nature Immunology* 7: 1143-1149.
 122. Friedl, P., and E. B. Bröcker. 2000. T cell migration in three-dimensional extracellular matrix: guidance by polarity and sensations. *Dev Immunol* 7: 249-266.
 123. Gupton, S. L., K. L. Anderson, T. P. Kole, R. S. Fischer, A. Ponti, S. E. Hitchcock-DeGregori, G. Danuser, V. M. Fowler, D. Wirtz, D. Hanein, and C. M. Waterman-Storer. 2005. Cell migration without a lamellipodium: translation of actin dynamics into cell movement mediated by tropomyosin. *J Cell Biol* 168: 619-631.
 124. Jacobelli, J., S. A. Chmura, D. B. Buxton, M. M. Davis, and M. F. Krummel. 2004. A single class II myosin modulates T cell motility and stopping, but not synapse formation. *Nat Immunol* 5: 531-538.
 125. Wülfing, C., and M. M. Davis. 1998. A Receptor/Cytoskeletal Movement Triggered by Costimulation During T Cell Activation. *Science* 282: 2266-2269.
 126. Dupré, L., R. Houmadi, C. Tang, and J. Rey-Barroso. 2015. T Lymphocyte Migration: An Action Movie Starring the Actin and Associated Actors. *Frontiers in immunology* 6: 586-586.
 127. Dustin, M. L. 2008. Hunter to gatherer and back: immunological synapses and kinapses as variations on the theme of amoeboid locomotion. *Annu Rev Cell Dev Biol* 24: 577-596.
 128. Pinner, S. E., and E. Sahai. 2009. Integrin-independent movement of immune cells. *F1000 biology reports* 1: 67-67.
 129. Huse, M. 2012. Microtubule-organizing center polarity and the immunological synapse: protein kinase C and beyond. *Frontiers in Immunology* 3.
 130. Radoja, S., M. Saio, D. Schaer, M. Koneru, S. Vukmanovic, and A. B. Frey. 2001. CD8⁺ Tumor-Infiltrating T Cells Are Deficient in Perforin-Mediated Cytolytic Activity Due to Defective Microtubule-Organizing Center Mobilization and Lytic Granule Exocytosis. *The Journal of Immunology* 167: 5042-5051.
 131. Serrador, J. M., M. Nieto, J. L. Alonso-Lebrero, M. A. del Pozo, J. Calvo, H. Furthmayr, R. Schwartz-Albiez, F. Lozano, R. González-Amaro, P. Sánchez-Mateos, and F. Sánchez-Madrid. 1998. CD43 interacts with moesin and ezrin and regulates its redistribution to the uropods of T lymphocytes at the cell-cell contacts. *Blood* 91: 4632-4644.
 132. del Pozo, M. A., C. Cabañas, M. C. Montoya, A. Ager, P. Sánchez-Mateos, and F. Sánchez-Madrid. 1997. ICAMs redistributed by chemokines to cellular uropods as a mechanism for recruitment of T lymphocytes. *J Cell Biol* 137: 493-508.
 133. Krummel, M. F., M. D. Sjaastad, C. Wülfing, and M. M. Davis. 2000. Differential clustering of CD4 and CD3zeta during T cell recognition. *Science* 289: 1349-1352.
 134. Tibaldi, E. V., R. Salgia, and E. L. Reinherz. 2002. CD2 molecules redistribute to the uropod during T cell scanning: implications for cellular activation and immune surveillance. *Proc Natl Acad Sci U S A* 99: 7582-7587.
 135. Serrador, J. M., J. L. Alonso-Lebrero, M. A. del Pozo, H. Furthmayr, R. Schwartz-Albiez, J. Calvo, F. Lozano, and F. Sánchez-Madrid. 1997. Moesin interacts with the cytoplasmic region of intercellular adhesion molecule-3 and is redistributed to the uropod of T lymphocytes during cell polarization. *The Journal of cell biology* 138: 1409-1423.
 136. Tsukita, S., and S. Yonemura. 1997. ERM (ezrin/radixin/moesin) family: from cytoskeleton to signal transduction. *Curr Opin Cell Biol* 9: 70-75.
 137. Ludford-Menting, M. J., J. Oliaro, F. Sacirbegovic, E. T. Cheah, N. Pedersen, S. J. Thomas, A. Pasam, R. Iazzolino, L. E. Dow, N. J. Waterhouse, A. Murphy, S. Ellis, M. J. Smyth, M. H. Kershaw, P. K. Darcy, P. O. Humbert, and S. M. Russell. 2005. A network of PDZ-containing proteins regulates T cell polarity and morphology during migration and immunological synapse formation. *Immunity* 22: 737-748.

138. Kuhné, M. R., J. Lin, D. Yablonski, M. N. Mollenauer, L. I. Ehrlich, J. Huppa, M. M. Davis, and A. Weiss. 2003. Linker for activation of T cells, zeta-associated protein-70, and Src homology 2 domain-containing leukocyte protein-76 are required for TCR-induced microtubule-organizing center polarization. *J Immunol* 171: 860-866.
139. Stowers, L., D. Yelon, L. J. Berg, and J. Chant. 1995. Regulation of the polarization of T cells toward antigen-presenting cells by Ras-related GTPase CDC42. *Proc Natl Acad Sci U S A* 92: 5027-5031.
140. Combs, J., S. J. Kim, S. Tan, L. A. Ligon, E. L. Holzbaur, J. Kuhn, and M. Poenie. 2006. Recruitment of dynein to the Jurkat immunological synapse. *Proc Natl Acad Sci U S A* 103: 14883-14888.
141. Krause, M., A. S. Sechi, M. Konradt, D. Monner, F. B. Gertler, and J. Wehland. 2000. Fyn-binding protein (Fyb)/SLP-76-associated protein (SLAP), Ena/vasodilator-stimulated phosphoprotein (VASP) proteins and the Arp2/3 complex link T cell receptor (TCR) signaling to the actin cytoskeleton. *J Cell Biol* 149: 181-194.
142. Stinchcombe, J. C., E. Majorovits, G. Bossi, S. Fuller, and G. M. Griffiths. 2006. Centrosome polarization delivers secretory granules to the immunological synapse. *Nature* 443: 462-465.
143. Stinchcombe, J. C., and G. M. Griffiths. 2007. Secretory mechanisms in cell-mediated cytotoxicity. *Annu Rev Cell Dev Biol* 23: 495-517.
144. Holsinger, L. J., I. A. Graef, W. Swat, T. Chi, D. M. Bautista, L. Davidson, R. S. Lewis, F. W. Alt, and G. R. Crabtree. 1998. Defects in actin-cap formation in Vav-deficient mice implicate an actin requirement for lymphocyte signal transduction. *Curr Biol* 8: 563-572.
145. Henney, C. S., and J. E. Bubbers. 1973. Antigen-T Lymphocyte Interactions: Inhibition by Cytochalasin B. *The Journal of Immunology* 111: 85.
146. Labno, C. M., C. M. Lewis, D. You, D. W. Leung, A. Takesono, N. Kamberos, A. Seth, L. D. Finkelstein, M. K. Rosen, P. L. Schwartzberg, and J. K. Burkhardt. 2003. Itk functions to control actin polymerization at the immune synapse through localized activation of Cdc42 and WASP. *Curr Biol* 13: 1619-1624.
147. Wülfing, C., A. Bauch, G. R. Crabtree, and M. M. Davis. 2000. The vav exchange factor is an essential regulator in actin-dependent receptor translocation to the lymphocyte-antigen-presenting cell interface. *Proc Natl Acad Sci U S A* 97: 10150-10155.
148. Tybulewicz, V. L. J., and R. B. Henderson. 2009. Rho family GTPases and their regulators in lymphocytes. *Nature reviews. Immunology* 9: 630-644.
149. Monks, C. R., B. A. Freiberg, H. Kupfer, N. Sciaky, and A. Kupfer. 1998. Three-dimensional segregation of supramolecular activation clusters in T cells. *Nature* 395: 82-86.
150. DeMond, A. L., K. D. Mossman, T. Starr, M. L. Dustin, and J. T. Groves. 2008. T cell receptor microcluster transport through molecular mazes reveals mechanism of translocation. *Biophysical journal* 94: 3286-3292.
151. Kaizuka, Y., A. D. Douglass, R. Varma, M. L. Dustin, and R. D. Vale. 2007. Mechanisms for segregating T cell receptor and adhesion molecules during immunological synapse formation in Jurkat T cells. *Proceedings of the National Academy of Sciences of the United States of America* 104: 20296-20301.
152. Sims, T. N., T. J. Soos, H. S. Xenias, B. Dubin-Thaler, J. M. Hofman, J. C. Waite, T. O. Cameron, V. K. Thomas, R. Varma, C. H. Wiggins, M. P. Sheetz, D. R. Littman, and M. L. Dustin. 2007. Opposing effects of PKCtheta and WASp on symmetry breaking and relocation of the immunological synapse. *Cell* 129: 773-785.
153. Varma, R., G. Campi, T. Yokosuka, T. Saito, and M. L. Dustin. 2006. T cell receptor-proximal signals are sustained in peripheral microclusters and terminated in the central supramolecular activation cluster. *Immunity* 25: 117-127.
154. Barda-Saad, M., A. Braiman, R. Titerence, S. C. Bunnell, V. A. Barr, and L. E. Samelson. 2005. Dynamic molecular interactions linking the T cell antigen receptor to the actin cytoskeleton. *Nat Immunol* 6: 80-89.

155. Smith, A., Y. R. Carrasco, P. Stanley, N. Kieffer, F. D. Batista, and N. Hogg. 2005. A talin-dependent LFA-1 focal zone is formed by rapidly migrating T lymphocytes. *J Cell Biol* 170: 141-151.
156. Kumari, S., S. Curado, V. Mayya, and M. L. Dustin. 2014. T cell antigen receptor activation and actin cytoskeleton remodeling. *Biochimica et Biophysica Acta (BBA) - Biomembranes* 1838: 546-556.
157. Schietinger, A., and P. D. Greenberg. 2014. Tolerance and exhaustion: defining mechanisms of T cell dysfunction. *Trends Immunol* 35: 51-60.
158. Schietinger, A., J. J. Delrow, R. S. Basom, J. N. Blattman, and P. D. Greenberg. 2012. Rescued tolerant CD8 T cells are preprogrammed to reestablish the tolerant state. *Science* 335: 723-727.
159. Martin, M. D., and V. P. Badovinac. 2018. Defining Memory CD8 T Cell. *Front Immunol* 9: 2692.
160. Pennock, N. D., J. T. White, E. W. Cross, E. E. Cheney, B. A. Tamburini, and R. M. Kedl. 2013. T cell responses: naive to memory and everything in between. *Advances in physiology education* 37: 273-283.
161. Macallan, D. C., J. A. M. Borghans, and B. Asquith. 2017. Human T Cell Memory: A Dynamic View. *Vaccines* 5: 5.
162. Angelosanto, J. M., S. D. Blackburn, A. Crawford, and E. J. Wherry. 2012. Progressive loss of memory T cell potential and commitment to exhaustion during chronic viral infection. *J Virol* 86: 8161-8170.
163. Wherry, E. J., and M. Kurachi. 2015. Molecular and cellular insights into T cell exhaustion. *Nature reviews. Immunology* 15: 486-499.
164. Zajac, A. J., J. N. Blattman, K. Murali-Krishna, D. J. Sourdive, M. Suresh, J. D. Altman, and R. Ahmed. 1998. Viral immune evasion due to persistence of activated T cells without effector function. *J Exp Med* 188: 2205-2213.
165. Wherry, E. J., J. N. Blattman, K. Murali-Krishna, R. van der Most, and R. Ahmed. 2003. Viral persistence alters CD8 T-cell immunodominance and tissue distribution and results in distinct stages of functional impairment. *J Virol* 77: 4911-4927.
166. Fuller, M. J., and A. J. Zajac. 2003. Ablation of CD8 and CD4 T cell responses by high viral loads. *J Immunol* 170: 477-486.
167. Wherry, E. J. 2011. T cell exhaustion. *Nat Immunol* 12: 492-499.
168. Im, S. J., M. Hashimoto, M. Y. Gerner, J. Lee, H. T. Kissick, M. C. Burger, Q. Shan, J. S. Hale, J. Lee, T. H. Nast, A. H. Sharpe, G. J. Freeman, R. N. Germain, H. I. Nakaya, H. H. Xue, and R. Ahmed. 2016. Defining CD8+ T cells that provide the proliferative burst after PD-1 therapy. *Nature* 537: 417-421.
169. Jadhav, R. R., S. J. Im, B. Hu, M. Hashimoto, P. Li, J. X. Lin, W. J. Leonard, W. J. Greenleaf, R. Ahmed, and J. J. Goronzy. 2019. Epigenetic signature of PD-1+ TCF1+ CD8 T cells that act as resource cells during chronic viral infection and respond to PD-1 blockade. *Proc Natl Acad Sci U S A* 116: 14113-14118.
170. Speiser, D. E., D. T. Utzschneider, S. G. Oberle, C. Münz, P. Romero, and D. Zehn. 2014. T cell differentiation in chronic infection and cancer: functional adaptation or exhaustion? *Nat Rev Immunol* 14: 768-774.
171. Blank, C. U., W. N. Haining, W. Held, P. G. Hogan, A. Kallies, E. Lugli, R. C. Lynn, M. Philip, A. Rao, N. P. Restifo, A. Schietinger, T. N. Schumacher, P. L. Schwartzberg, A. H. Sharpe, D. E. Speiser, E. J. Wherry, B. A. Youngblood, and D. Zehn. 2019. Defining 'T cell exhaustion'. *Nat Rev Immunol* 19: 665-674.
172. Siddiqui, I., K. Schaeuble, V. Chennupati, S. A. Fuertes Marraco, S. Calderon-Copete, D. Pais Ferreira, S. J. Carmona, L. Scarpellino, D. Gfeller, S. Pradervand, S. A. Luther, D. E. Speiser, and W. Held. 2019. Intratumoral Tcf1(+)/PD-1(+)/CD8(+) T Cells with Stem-like Properties Promote Tumor Control in Response to Vaccination and Checkpoint Blockade Immunotherapy. *Immunity* 50: 195-211.e110.
173. Utzschneider, D. T., M. Charmoy, V. Chennupati, L. Pousse, D. P. Ferreira, S. Calderon-Copete, M. Danilo, F. Alfei, M. Hofmann, D. Wieland, S. Pradervand, R. Thimme, D. Zehn,

- and W. Held. 2016. T Cell Factor 1-Expressing Memory-like CD8(+) T Cells Sustain the Immune Response to Chronic Viral Infections. *Immunity* 45: 415-427.
174. Wu, T., Y. Ji, E. A. Moseman, H. C. Xu, M. Manghani, M. Kirby, S. M. Anderson, R. Handon, E. Kenyon, A. Elkahlon, W. Wu, P. A. Lang, L. Gattinoni, D. B. McGavern, and P. L. Schwartzberg. 2016. The TCF1-Bcl6 axis counteracts type I interferon to repress exhaustion and maintain T cell stemness. *Science immunology* 1: eaai8593.
 175. Zhou, X., S. Yu, D. M. Zhao, J. T. Harty, V. P. Badovinac, and H. H. Xue. 2010. Differentiation and persistence of memory CD8(+) T cells depend on T cell factor 1. *Immunity* 33: 229-240.
 176. Jeannot, G., C. Boudousquié, N. Gardiol, J. Kang, J. Huelsken, and W. Held. 2010. Essential role of the Wnt pathway effector Tcf-1 for the establishment of functional CD8 T cell memory. *Proc Natl Acad Sci U S A* 107: 9777-9782.
 177. Paley, M. A., D. C. Kroy, P. M. Odorizzi, J. B. Johnnidis, D. V. Dolfi, B. E. Barnett, E. K. Bikoff, E. J. Robertson, G. M. Lauer, S. L. Reiner, and E. J. Wherry. 2012. Progenitor and terminal subsets of CD8+ T cells cooperate to contain chronic viral infection. *Science* 338: 1220-1225.
 178. Scott, A. C., F. DüNDAR, P. Zumbo, S. S. Chandran, C. A. Klebanoff, M. Shakiba, P. Trivedi, L. Menocal, H. Appleby, S. Camara, D. Zamarin, T. Walther, A. Snyder, M. R. Femia, E. A. Comen, H. Y. Wen, M. D. Hellmann, N. Anandasabapathy, Y. Liu, N. K. Altorki, P. Lauer, O. Levy, M. S. Glickman, J. Kaye, D. Betel, M. Philip, and A. Schietinger. 2019. TOX is a critical regulator of tumour-specific T cell differentiation. *Nature* 571: 270-274.
 179. Wherry, E. J., S. J. Ha, S. M. Kaeck, W. N. Haining, S. Sarkar, V. Kalia, S. Subramaniam, J. N. Blattman, D. L. Barber, and R. Ahmed. 2007. Molecular signature of CD8+ T cell exhaustion during chronic viral infection. *Immunity* 27: 670-684.
 180. Driessens, G., J. Kline, and T. F. Gajewski. 2009. Costimulatory and coinhibitory receptors in anti-tumor immunity. *Immunological reviews* 229: 126-144.
 181. Chihara, N., A. Madi, T. Kondo, H. Zhang, N. Acharya, M. Singer, J. Nyman, N. D. Marjanovic, M. S. Kowalczyk, C. Wang, S. Kurtulus, T. Law, Y. Etminan, J. Nevin, C. D. Buckley, P. R. Burkett, J. D. Buenrostro, O. Rozenblatt-Rosen, A. C. Anderson, A. Regev, and V. K. Kuchroo. 2018. Induction and transcriptional regulation of the co-inhibitory gene module in T cells. *Nature* 558: 454-459.
 182. Zhu, C., K. Sakuishi, S. Xiao, Z. Sun, S. Zaghouni, G. Gu, C. Wang, D. J. Tan, C. Wu, M. Rangachari, T. Pertel, H. T. Jin, R. Ahmed, A. C. Anderson, and V. K. Kuchroo. 2015. An IL-27/NFIL3 signalling axis drives Tim-3 and IL-10 expression and T-cell dysfunction. *Nat Commun* 6: 6072.
 183. Hui, E., J. Cheung, J. Zhu, X. Su, M. J. Taylor, H. A. Wallweber, D. K. Sasmal, J. Huang, J. M. Kim, I. Mellman, and R. D. Vale. 2017. T cell costimulatory receptor CD28 is a primary target for PD-1-mediated inhibition. *Science* 355: 1428-1433.
 184. Sheppard, K. A., L. J. Fitz, J. M. Lee, C. Benander, J. A. George, J. Wooters, Y. Qiu, J. M. Jussif, L. L. Carter, C. R. Wood, and D. Chaudhary. 2004. PD-1 inhibits T-cell receptor induced phosphorylation of the ZAP70/CD3zeta signalosome and downstream signaling to PKCtheta. *FEBS Lett* 574: 37-41.
 185. Hamanishi, J., M. Mandai, M. Iwasaki, T. Okazaki, Y. Tanaka, K. Yamaguchi, T. Higuchi, H. Yagi, K. Takakura, N. Minato, T. Honjo, and S. Fujii. 2007. Programmed cell death 1 ligand 1 and tumor-infiltrating CD8 T lymphocytes are prognostic factors of human ovarian cancer. *Proceedings of the National Academy of Sciences* 104: 3360-3365.
 186. Thompson, R. H., M. D. Gillett, J. C. Cheville, C. M. Lohse, H. Dong, W. S. Webster, K. G. Krejci, J. R. Lobo, S. Sengupta, L. Chen, H. Zincke, M. L. Blute, S. E. Strome, B. C. Leibovich, and E. D. Kwon. 2004. Costimulatory B7-H1 in renal cell carcinoma patients: Indicator of tumor aggressiveness and potential therapeutic target. *Proceedings of the National Academy of Sciences of the United States of America* 101: 17174-17179.
 187. Ambler, R., G. L. Edmunds, S. L. Tan, S. Cirillo, J. I. Pernes, X. Ruan, J. Huete-Carrasco, C. C. W. Wong, J. Lu, J. Ward, G. Toti, A. J. Hedges, S. J. Dovedi, R. F. Murphy, D. J. Morgan, and

- C. Wülfing. 2020. PD-1 suppresses the maintenance of cell couples between cytotoxic T cells and target tumor cells within the tumor. *Sci Signal* 13.
188. Oyewole-Said, D., V. Konduri, J. Vazquez-Perez, S. A. Weldon, J. M. Levitt, and W. K. Decker. 2020. Beyond T-Cells: Functional Characterization of CTLA-4 Expression in Immune and Non-Immune Cell Types. *Frontiers in Immunology* 11.
189. Schneider, H., J. Downey, A. Smith, B. H. Zinselmeyer, C. Rush, J. M. Brewer, B. Wei, N. Hogg, P. Garside, and C. E. Rudd. 2006. Reversal of the TCR stop signal by CTLA-4. *Science* 313: 1972-1975.
190. Grohmann, U., C. Orabona, F. Fallarino, C. Vacca, F. Calcinaro, A. Falorni, P. Candeloro, M. L. Belladonna, R. Bianchi, M. C. Fioretti, and P. Puccetti. 2002. CTLA-4-Ig regulates tryptophan catabolism in vivo. *Nat Immunol* 3: 1097-1101.
191. Maruhashi, T., I. M. Okazaki, D. Sugiura, S. Takahashi, T. K. Maeda, K. Shimizu, and T. Okazaki. 2018. LAG-3 inhibits the activation of CD4(+) T cells that recognize stable pMHCII through its conformation-dependent recognition of pMHCII. *Nat Immunol* 19: 1415-1426.
192. Huard, B., P. Prigent, M. Tournier, D. Bruniquel, and F. Triebel. 1995. CD4/major histocompatibility complex class II interaction analyzed with CD4- and lymphocyte activation gene-3 (LAG-3)-Ig fusion proteins. *Eur J Immunol* 25: 2718-2721.
193. Workman, C. J., K. J. Dugger, and D. A. Vignali. 2002. Cutting edge: molecular analysis of the negative regulatory function of lymphocyte activation gene-3. *J Immunol* 169: 5392-5395.
194. Huang, C. T., C. J. Workman, D. Flies, X. Pan, A. L. Marson, G. Zhou, E. L. Hipkiss, S. Ravi, J. Kowalski, H. I. Levitsky, J. D. Powell, D. M. Pardoll, C. G. Drake, and D. A. Vignali. 2004. Role of LAG-3 in regulatory T cells. *Immunity* 21: 503-513.
195. Triebel, F., S. Jitsukawa, E. Baixeras, S. Roman-Roman, C. Genevee, E. Viegas-Pequignot, and T. Hercend. 1990. LAG-3, a novel lymphocyte activation gene closely related to CD4. *J Exp Med* 171: 1393-1405.
196. Graydon, C. G., S. Mohideen, and K. R. Fowke. 2021. LAG3's Enigmatic Mechanism of Action. *Frontiers in immunology* 11: 615317-615317.
197. Wang, J., M. F. Sanmamed, I. Datar, T. T. Su, L. Ji, J. Sun, L. Chen, Y. Chen, G. Zhu, W. Yin, L. Zheng, T. Zhou, T. Badri, S. Yao, S. Zhu, A. Boto, M. Sznol, I. Melero, D. A. A. Vignali, K. Schalper, and L. Chen. 2019. Fibrinogen-like Protein 1 Is a Major Immune Inhibitory Ligand of LAG-3. *Cell* 176: 334-347.e312.
198. Maeda, T. K., D. Sugiura, I. M. Okazaki, T. Maruhashi, and T. Okazaki. 2019. Atypical motifs in the cytoplasmic region of the inhibitory immune co-receptor LAG-3 inhibit T cell activation. *J Biol Chem* 294: 6017-6026.
199. Boles, K. S., W. Vermi, F. Facchetti, A. Fuchs, T. J. Wilson, T. G. Diacovo, M. Cella, and M. Colonna. 2009. A novel molecular interaction for the adhesion of follicular CD4 T cells to follicular DC. *Eur J Immunol* 39: 695-703.
200. Levin, S. D., D. W. Taft, C. S. Brandt, C. Bucher, E. D. Howard, E. M. Chadwick, J. Johnston, A. Hammond, K. Bontadelli, D. Ardourel, L. Hebb, A. Wolf, T. R. Bukowski, M. W. Rixon, J. L. Kuijper, C. D. Ostrander, J. W. West, J. Bilsborough, B. Fox, Z. Gao, W. Xu, F. Ramsdell, B. R. Blazar, and K. E. Lewis. 2011. Vstm3 is a member of the CD28 family and an important modulator of T-cell function. *Eur J Immunol* 41: 902-915.
201. Stanietsky, N., T. L. Rovis, A. Glasner, E. Seidel, P. Tsukerman, R. Yamin, J. Enk, S. Jonjic, and O. Mandelboim. 2013. Mouse TIGIT inhibits NK-cell cytotoxicity upon interaction with PVR. *Eur J Immunol* 43: 2138-2150.
202. Stanietsky, N., H. Simic, J. Arapovic, A. Toporik, O. Levy, A. Novik, Z. Levine, M. Beiman, L. Dassa, H. Achdout, N. Stern-Ginossar, P. Tsukerman, S. Jonjic, and O. Mandelboim. 2009. The interaction of TIGIT with PVR and PVRL2 inhibits human NK cell cytotoxicity. *Proc Natl Acad Sci U S A* 106: 17858-17863.
203. Joller, N., J. P. Hafler, B. Brynedal, N. Kassam, S. Spoerl, S. D. Levin, A. H. Sharpe, and V. K. Kuchroo. 2011. Cutting edge: TIGIT has T cell-intrinsic inhibitory functions. *J Immunol* 186: 1338-1342.

204. Monney, L., C. A. Sabatos, J. L. Gaglia, A. Ryu, H. Waldner, T. Chernova, S. Manning, E. A. Greenfield, A. J. Coyle, R. A. Sobel, G. J. Freeman, and V. K. Kuchroo. 2002. Th1-specific cell surface protein Tim-3 regulates macrophage activation and severity of an autoimmune disease. *Nature* 415: 536-541.
205. Li, Y., J. Zhang, D. Zhang, X. Hong, Y. Tao, S. Wang, Y. Xu, H. Piao, W. Yin, M. Yu, Y. Zhang, Q. Fu, D. Li, X. Chang, and M. Du. 2017. Tim-3 signaling in peripheral NK cells promotes maternal-fetal immune tolerance and alleviates pregnancy loss. *Sci Signal* 10.
206. de Mingo Pulido, Á., A. Gardner, S. Hiebler, H. Soliman, H. S. Rugo, M. F. Krummel, L. M. Coussens, and B. Ruffell. 2018. TIM-3 Regulates CD103(+) Dendritic Cell Function and Response to Chemotherapy in Breast Cancer. *Cancer cell* 33: 60-74.e66.
207. Jiang, X., T. Zhou, Y. Xiao, J. Yu, S. Dou, G. Chen, R. Wang, H. Xiao, C. Hou, W. Wang, Q. Shi, J. Feng, Y. Ma, B. Shen, Y. Li, and G. Han. 2016. Tim-3 promotes tumor-promoting M2 macrophage polarization by binding to STAT1 and suppressing the STAT1-miR-155 signaling axis. *Oncoimmunology* 5: e1211219.
208. Nakayama, M., H. Akiba, K. Takeda, Y. Kojima, M. Hashiguchi, M. Azuma, H. Yagita, and K. Okumura. 2009. Tim-3 mediates phagocytosis of apoptotic cells and cross-presentation. *Blood* 113: 3821-3830.
209. Wang, Z., D. Sun, G. Chen, G. Li, S. Dou, R. Wang, H. Xiao, C. Hou, Y. Li, J. Feng, B. Shen, and G. Han. 2017. Tim-3 inhibits macrophage control of *Listeria monocytogenes* by inhibiting Nrf2. *Sci Rep* 7: 42095.
210. Xu, L., Y. Huang, L. Tan, W. Yu, D. Chen, C. Lu, J. He, G. Wu, X. Liu, and Y. Zhang. 2015. Increased Tim-3 expression in peripheral NK cells predicts a poorer prognosis and Tim-3 blockade improves NK cell-mediated cytotoxicity in human lung adenocarcinoma. *Int Immunopharmacol* 29: 635-641.
211. Pang, N., X. Alimu, R. Chen, M. Muhashi, J. Ma, G. Chen, F. Zhao, L. Wang, J. Qu, and J. Ding. 2021. Activated Galectin-9/Tim3 promotes Treg and suppresses Th1 effector function in chronic lymphocytic leukemia. *Faseb j* 35: e21556.
212. Kuchroo, V. K., V. Dardalhon, S. Xiao, and A. C. Anderson. 2008. New roles for TIM family members in immune regulation. *Nature Reviews Immunology* 8: 577-580.
213. Freeman, G. J., J. M. Casasnovas, D. T. Umetsu, and R. H. DeKruyff. 2010. TIM genes: a family of cell surface phosphatidylserine receptors that regulate innate and adaptive immunity. *Immunological reviews* 235: 172-189.
214. Meyers, J. H., C. A. Sabatos, S. Chakravarti, and V. K. Kuchroo. 2005. The TIM gene family regulates autoimmune and allergic diseases. *Trends Mol Med* 11: 362-369.
215. Rangachari, M., C. Zhu, K. Sakuishi, S. Xiao, J. Karman, A. Chen, M. Angin, A. Wakeham, E. A. Greenfield, R. A. Sobel, H. Okada, P. J. McKinnon, T. W. Mak, M. M. Addo, A. C. Anderson, and V. K. Kuchroo. 2012. Bat3 promotes T cell responses and autoimmunity by repressing Tim-3-mediated cell death and exhaustion. *Nat Med* 18: 1394-1400.
216. Lee, J., E. W. Su, C. Zhu, S. Hainline, J. Phuah, J. A. Moroco, T. E. Smithgall, V. K. Kuchroo, and L. P. Kane. 2011. Phosphotyrosine-dependent coupling of Tim-3 to T-cell receptor signaling pathways. *Mol Cell Biol* 31: 3963-3974.
217. van de Weyer, P. S., M. Muehlfeit, C. Klose, J. V. Bonventre, G. Walz, and E. W. Kuehn. 2006. A highly conserved tyrosine of Tim-3 is phosphorylated upon stimulation by its ligand galectin-9. *Biochem Biophys Res Commun* 351: 571-576.
218. Sabatos, C. A., S. Chakravarti, E. Cha, A. Schubart, A. Sanchez-Fueyo, X. X. Zheng, A. J. Coyle, T. B. Strom, G. J. Freeman, and V. K. Kuchroo. 2003. Interaction of Tim-3 and Tim-3 ligand regulates T helper type 1 responses and induction of peripheral tolerance. *Nat Immunol* 4: 1102-1110.
219. Möller-Hackbarth, K., C. Dewitz, O. Schweigert, A. Trad, C. Garbers, S. Rose-John, and J. Scheller. 2013. A disintegrin and metalloprotease (ADAM) 10 and ADAM17 are major sheddases of T cell immunoglobulin and mucin domain 3 (Tim-3). *J Biol Chem* 288: 34529-34544.
220. Cao, E., X. Zang, U. A. Ramagopal, A. Mukhopadhyaya, A. Fedorov, E. Fedorov, W. D. Zencheck, J. W. Lary, J. L. Cole, H. Deng, H. Xiao, T. P. D'Irenzo, J. P. Allison, S. G.

- Nathenson, and S. C. Almo. 2007. T cell immunoglobulin mucin-3 crystal structure reveals a galectin-9-independent ligand-binding surface. *Immunity* 26: 311-321.
221. Huang, Y. H., C. Zhu, Y. Kondo, A. C. Anderson, A. Gandhi, A. Russell, S. K. Dougan, B. S. Petersen, E. Melum, T. Pertel, K. L. Clayton, M. Raab, Q. Chen, N. Beauchemin, P. J. Yazaki, M. Pyzik, M. A. Ostrowski, J. N. Glickman, C. E. Rudd, H. L. Ploegh, A. Franke, G. A. Petsko, V. K. Kuchroo, and R. S. Blumberg. 2015. CEACAM1 regulates TIM-3-mediated tolerance and exhaustion. *Nature* 517: 386-390.
222. Davidson, D., M. Bakinowski, M. L. Thomas, V. Horejsi, and A. Veillette. 2003. Phosphorylation-dependent regulation of T-cell activation by PAG/Cbp, a lipid raft-associated transmembrane adaptor. *Mol Cell Biol* 23: 2017-2028.
223. Heusschen, R., A. W. Griffioen, and V. L. Thijssen. 2013. Galectin-9 in tumor biology: a jack of multiple trades. *Biochim Biophys Acta* 1836: 177-185.
224. Zhu, C., A. C. Anderson, A. Schubart, H. Xiong, J. Imitola, S. J. Khoury, X. X. Zheng, T. B. Strom, and V. K. Kuchroo. 2005. The Tim-3 ligand galectin-9 negatively regulates T helper type 1 immunity. *Nat Immunol* 6: 1245-1252.
225. Wada, J., K. Ota, A. Kumar, E. I. Wallner, and Y. S. Kanwar. 1997. Developmental regulation, expression, and apoptotic potential of galectin-9, a beta-galactoside binding lectin. *J Clin Invest* 99: 2452-2461.
226. Lahm, H., S. André, A. Hoeflich, J. R. Fischer, B. Sordat, H. Kaltner, E. Wolf, and H. J. Gabius. 2001. Comprehensive galectin fingerprinting in a panel of 61 human tumor cell lines by RT-PCR and its implications for diagnostic and therapeutic procedures. *J Cancer Res Clin Oncol* 127: 375-386.
227. Kashio, Y., K. Nakamura, M. J. Abedin, M. Seki, N. Nishi, N. Yoshida, T. Nakamura, and M. Hirashima. 2003. Galectin-9 induces apoptosis through the calcium-calpain-caspase-1 pathway. *J Immunol* 170: 3631-3636.
228. Kageshita, T., Y. Kashio, A. Yamauchi, M. Seki, M. J. Abedin, N. Nishi, H. Shoji, T. Nakamura, T. Ono, and M. Hirashima. 2002. Possible role of galectin-9 in cell aggregation and apoptosis of human melanoma cell lines and its clinical significance. *Int J Cancer* 99: 809-816.
229. Irie, A., A. Yamauchi, K. Kontani, M. Kihara, D. Liu, Y. Shirato, M. Seki, N. Nishi, T. Nakamura, H. Yokomise, and M. Hirashima. 2005. Galectin-9 as a prognostic factor with antimetastatic potential in breast cancer. *Clin Cancer Res* 11: 2962-2968.
230. Kasamatsu, A., K. Uzawa, D. Nakashima, H. Koike, M. Shiiba, H. Bukawa, H. Yokoe, and H. Tanzawa. 2005. Galectin-9 as a regulator of cellular adhesion in human oral squamous cell carcinoma cell lines. *Int J Mol Med* 16: 269-273.
231. Kang, C. W., A. Dutta, L. Y. Chang, J. Mahalingam, Y. C. Lin, J. M. Chiang, C. Y. Hsu, C. T. Huang, W. T. Su, Y. Y. Chu, and C. Y. Lin. 2015. Apoptosis of tumor infiltrating effector TIM-3+CD8+ T cells in colon cancer. *Sci Rep* 5: 15659.
232. Dardalhon, V., A. C. Anderson, J. Karman, L. Apetoh, R. Chandwaskar, D. H. Lee, M. Cornejo, N. Nishi, A. Yamauchi, F. J. Quintana, R. A. Sobel, M. Hirashima, and V. K. Kuchroo. 2010. Tim-3/galectin-9 pathway: regulation of Th1 immunity through promotion of CD11b+Ly-6G+ myeloid cells. *J Immunol* 185: 1383-1392.
233. Leitner, J., A. Rieger, W. F. Pickl, G. Zlabinger, K. Grabmeier-Pfistershammer, and P. Steinberger. 2013. TIM-3 does not act as a receptor for galectin-9. *PLoS Pathog* 9: e1003253.
234. Fadok, V. A., D. R. Voelker, P. A. Campbell, J. J. Cohen, D. L. Bratton, and P. M. Henson. 1992. Exposure of phosphatidylserine on the surface of apoptotic lymphocytes triggers specific recognition and removal by macrophages. *J Immunol* 148: 2207-2216.
235. Zhou, Z. 2007. New phosphatidylserine receptors: clearance of apoptotic cells and more. *Dev Cell* 13: 759-760.
236. DeKruyff, R. H., X. Bu, A. Ballesteros, C. Santiago, Y. L. Chim, H. H. Lee, P. Karisola, M. Pichavant, G. G. Kaplan, D. T. Umetsu, G. J. Freeman, and J. M. Casasnovas. 2010. T cell/transmembrane, Ig, and mucin-3 allelic variants differentially recognize

- phosphatidylserine and mediate phagocytosis of apoptotic cells. *J Immunol* 184: 1918-1930.
237. Kobayashi, N., P. Karisola, V. Peña-Cruz, D. M. Dorfman, M. Jinushi, S. E. Umetsu, M. J. Butte, H. Nagumo, I. Chernova, B. Zhu, A. H. Sharpe, S. Ito, G. Dranoff, G. G. Kaplan, J. M. Casanovas, D. T. Umetsu, R. H. Dekruyff, and G. J. Freeman. 2007. TIM-1 and TIM-4 glycoproteins bind phosphatidylserine and mediate uptake of apoptotic cells. *Immunity* 27: 927-940.
 238. Poon, I. K. H., C. D. Lucas, A. G. Rossi, and K. S. Ravichandran. 2014. Apoptotic cell clearance: basic biology and therapeutic potential. *Nature reviews. Immunology* 14: 166-180.
 239. Lee, S.-A., M. S. Kwak, S. Kim, and J.-S. Shin. 2014. The role of high mobility group box 1 in innate immunity. *Yonsei medical journal* 55: 1165-1176.
 240. Yang, D., Q. Chen, H. Yang, K. J. Tracey, M. Bustin, and J. J. Oppenheim. 2007. High mobility group box-1 protein induces the migration and activation of human dendritic cells and acts as an alarmin. *J Leukoc Biol* 81: 59-66.
 241. Dumitriu, I. E., P. Baruah, B. Valentinis, R. E. Voll, M. Herrmann, P. P. Nawroth, B. Arnold, M. E. Bianchi, A. A. Manfredi, and P. Rovere-Querini. 2005. Release of high mobility group box 1 by dendritic cells controls T cell activation via the receptor for advanced glycation end products. *J Immunol* 174: 7506-7515.
 242. Chiba, S., M. Baghdadi, H. Akiba, H. Yoshiyama, I. Kinoshita, H. Dosaka-Akita, Y. Fujioka, Y. Ohba, J. V. Gorman, J. D. Colgan, M. Hirashima, T. Uede, A. Takaoka, H. Yagita, and M. Jinushi. 2012. Tumor-infiltrating DCs suppress nucleic acid-mediated innate immune responses through interactions between the receptor TIM-3 and the alarmin HMGB1. *Nat Immunol* 13: 832-842.
 243. Tesniere, A., F. Schlemmer, V. Boige, O. Kepp, I. Martins, F. Ghiringhelli, L. Aymeric, M. Michaud, L. Apetoh, L. Barault, J. Mendiboure, J. P. Pignon, V. Jooste, P. van Endert, M. Ducreux, L. Zitvogel, F. Piard, and G. Kroemer. 2010. Immunogenic death of colon cancer cells treated with oxaliplatin. *Oncogene* 29: 482-491.
 244. Sabatos-Peyton, C. A., J. Nevin, A. Brock, J. D. Venable, D. J. Tan, N. Kassam, F. Xu, J. Taraszka, L. Wesemann, T. Pertel, N. Acharya, M. Klapholz, Y. Etminan, X. Jiang, Y. H. Huang, R. S. Blumberg, V. K. Kuchroo, and A. C. Anderson. 2018. Blockade of Tim-3 binding to phosphatidylserine and CEACAM1 is a shared feature of anti-Tim-3 antibodies that have functional efficacy. *Oncoimmunology* 7: e1385690.
 245. Gray-Owen, S. D., and R. S. Blumberg. 2006. CEACAM1: contact-dependent control of immunity. *Nature Reviews Immunology* 6: 433-446.
 246. Wolf, Y., A. C. Anderson, and V. K. Kuchroo. 2020. TIM3 comes of age as an inhibitory receptor. *Nat Rev Immunol* 20: 173-185.
 247. Lake, C. M., K. Voss, B. M. Bauman, K. Pohida, T. Jiang, G. Dveksler, and A. L. Snow. 2021. TIM-3 drives temporal differences in restimulation-induced cell death sensitivity in effector CD8(+) T cells in conjunction with CEACAM1. *Cell Death Dis* 12: 400.
 248. Zhang, Y., P. Cai, L. Li, L. Shi, P. Chang, T. Liang, Q. Yang, Y. Liu, L. Wang, and L. Hu. 2017. Co-expression of TIM-3 and CEACAM1 promotes T cell exhaustion in colorectal cancer patients. *Int Immunopharmacol* 43: 210-218.
 249. Li, J., X. Liu, Y. Duan, Y. Liu, H. Wang, S. Lian, G. Zhuang, and Y. Fan. 2017. Combined Blockade of T Cell Immunoglobulin and Mucin Domain 3 and Carcinoembryonic Antigen-Related Cell Adhesion Molecule 1 Results in Durable Therapeutic Efficacy in Mice with Intracranial Gliomas. *Med Sci Monit* 23: 3593-3602.
 250. Yang, X., X. Jiang, G. Chen, Y. Xiao, S. Geng, C. Kang, T. Zhou, Y. Li, X. Guo, H. Xiao, C. Hou, R. Wang, Z. Lin, X. Li, J. Feng, Y. Ma, B. Shen, Y. Li, and G. Han. 2013. T cell Ig mucin-3 promotes homeostasis of sepsis by negatively regulating the TLR response. *J Immunol* 190: 2068-2079.
 251. Jiang, X., J. Yu, Q. Shi, Y. Xiao, W. Wang, G. Chen, Z. Zhao, R. Wang, H. Xiao, C. Hou, J. Feng, Y. Ma, B. Shen, L. Wang, Y. Li, and G. Han. 2015. Tim-3 promotes intestinal

- homeostasis in DSS colitis by inhibiting M1 polarization of macrophages. *Clin Immunol* 160: 328-335.
252. Ndhlovu, L. C., S. Lopez-Vergès, J. D. Barbour, R. B. Jones, A. R. Jha, B. R. Long, E. C. Schoeffler, T. Fujita, D. F. Nixon, and L. L. Lanier. 2012. Tim-3 marks human natural killer cell maturation and suppresses cell-mediated cytotoxicity. *Blood* 119: 3734-3743.
253. da Silva, I. P., A. Gallois, S. Jimenez-Baranda, S. Khan, A. C. Anderson, V. K. Kuchroo, I. Osman, and N. Bhardwaj. 2014. Reversal of NK-cell exhaustion in advanced melanoma by Tim-3 blockade. *Cancer Immunol Res* 2: 410-422.
254. Dankner, M., S. D. Gray-Owen, Y. H. Huang, R. S. Blumberg, and N. Beauchemin. 2017. CEACAM1 as a multi-purpose target for cancer immunotherapy. *Oncoimmunology* 6: e1328336.
255. De Sousa Linhares, A., F. Kellner, S. Jutz, G. J. Zlabinger, H. J. Gabius, J. B. Huppa, J. Leitner, and P. Steinberger. 2020. TIM-3 and CEACAM1 do not interact in cis and in trans. *Eur J Immunol* 50: 1126-1141.
256. Zhu, C., K. O. Dixon, K. Newcomer, G. Gu, S. Xiao, S. Zaghoulani, M. A. Schramm, C. Wang, H. Zhang, K. Goto, E. Christian, M. Rangachari, O. Rosenblatt-Rosen, H. Okada, T. Mak, M. Singer, A. Regev, and V. Kuchroo. 2021. Tim-3 adaptor protein Bat3 is a molecular checkpoint of T cell terminal differentiation and exhaustion. *Sci Adv* 7.
257. Avery, L., J. Filderman, A. L. Szymczak-Workman, and L. P. Kane. 2018. Tim-3 co-stimulation promotes short-lived effector T cells, restricts memory precursors, and is dispensable for T cell exhaustion. *Proc Natl Acad Sci U S A* 115: 2455-2460.
258. Kataoka, S., P. Manandhar, J. Lee, C. J. Workman, H. Banerjee, A. L. Szymczak-Workman, M. Kvorjak, J. Lohmueller, and L. P. Kane. 2021. The costimulatory activity of Tim-3 requires Akt and MAPK signaling and its recruitment to the immune synapse. *Sci Signal* 14.
259. Wherry, E. J., D. L. Barber, S. M. Kaech, J. N. Blattman, and R. Ahmed. 2004. Antigen-independent memory CD8 T cells do not develop during chronic viral infection. *Proc Natl Acad Sci U S A* 101: 16004-16009.
260. den Boer, A. T., G. J. D. van Mierlo, M. F. Fransen, C. J. M. Melief, R. Offringa, and R. E. M. Toes. 2004. The Tumoricidal Activity of Memory CD8⁺ T Cells Is Hampered by Persistent Systemic Antigen, but Full Functional Capacity Is Regained in an Antigen-Free Environment. *The Journal of Immunology* 172: 6074-6079.
261. Hanahan, D., and R. A. Weinberg. 2000. The hallmarks of cancer. *Cell* 100: 57-70.
262. Hanahan, D., and R. A. Weinberg. 2011. Hallmarks of cancer: the next generation. *Cell* 144: 646-674.
263. Brierley J. D., G. M. K., Wittekind C. 2017. *The TNM classification of malignant tumours*. Wiley Blackwell, Oxford.
264. Sennino, B., and D. M. McDonald. 2012. Controlling escape from angiogenesis inhibitors. *Nat Rev Cancer* 12: 699-709.
265. Chen, Y.-f., and L.-w. Fu. 2011. Mechanisms of acquired resistance to tyrosine kinase inhibitors. *Acta Pharmaceutica Sinica B* 1: 197-207.
266. Burnet, F. M. 1970. The concept of immunological surveillance. *Prog Exp Tumor Res* 13: 1-27.
267. Smyth, M. J., G. P. Dunn, and R. D. Schreiber. 2006. Cancer immunosurveillance and immunoediting: the roles of immunity in suppressing tumor development and shaping tumor immunogenicity. *Adv Immunol* 90: 1-50.
268. Mittal, D., M. M. Gubin, R. D. Schreiber, and M. J. Smyth. 2014. New insights into cancer immunoediting and its three component phases—elimination, equilibrium and escape. *Current Opinion in Immunology* 27: 16-25.
269. Dunn, G. P., L. J. Old, and R. D. Schreiber. 2004. The three Es of cancer immunoediting. *Annu Rev Immunol* 22: 329-360.
270. Chen, D. S., and I. Mellman. 2013. Oncology meets immunology: the cancer-immunity cycle. *Immunity* 39: 1-10.

271. Gardner, A., and B. Ruffell. 2016. Dendritic Cells and Cancer Immunity. *Trends in immunology* 37: 855-865.
272. Wculek, S. K., F. J. Cueto, A. M. Mujal, I. Melero, M. F. Krummel, and D. Sancho. 2020. Dendritic cells in cancer immunology and immunotherapy. *Nature Reviews Immunology* 20: 7-24.
273. Munn, D. H., and A. L. Mellor. 2006. The tumor-draining lymph node as an immune-privileged site. *Immunol Rev* 213: 146-158.
274. Munn, D. H., M. D. Sharma, J. R. Lee, K. G. Jhaver, T. S. Johnson, D. B. Keskin, B. Marshall, P. Chandler, S. J. Antonia, R. Burgess, C. L. Slingluff, Jr., and A. L. Mellor. 2002. Potential regulatory function of human dendritic cells expressing indoleamine 2,3-dioxygenase. *Science* 297: 1867-1870.
275. Norian, L. A., P. C. Rodriguez, L. A. O'Mara, J. Zabaleta, A. C. Ochoa, M. Cella, and P. M. Allen. 2009. Tumor-infiltrating regulatory dendritic cells inhibit CD8+ T cell function via L-arginine metabolism. *Cancer Res* 69: 3086-3094.
276. Mimura, K., K. Kono, A. Takahashi, Y. Kawaguchi, and H. Fujii. 2007. Vascular endothelial growth factor inhibits the function of human mature dendritic cells mediated by VEGF receptor-2. *Cancer Immunol Immunother* 56: 761-770.
277. Musha, H., H. Ohtani, T. Mizoi, M. Kinouchi, T. Nakayama, K. Shiiba, K. Miyagawa, H. Nagura, O. Yoshie, and I. Sasaki. 2005. Selective infiltration of CCR5(+)CXCR3(+) T lymphocytes in human colorectal carcinoma. *Int J Cancer* 116: 949-956.
278. Harlin, H., Y. Meng, A. C. Peterson, Y. Zha, M. Tretiakova, C. Slingluff, M. McKee, and T. F. Gajewski. 2009. Chemokine expression in melanoma metastases associated with CD8+ T-cell recruitment. *Cancer Res* 69: 3077-3085.
279. Mulligan, A. M., I. Raitman, L. Feeley, D. Pinnaduwage, L. T. Nguyen, F. P. O'Malley, P. S. Ohashi, and I. L. Andrusis. 2013. Tumoral lymphocytic infiltration and expression of the chemokine CXCL10 in breast cancers from the Ontario Familial Breast Cancer Registry. *Clin Cancer Res* 19: 336-346.
280. Hong, M., A. L. Puaux, C. Huang, L. Loumagne, C. Tow, C. Mackay, M. Kato, A. Prévost-Blondel, M. F. Avril, A. Nardin, and J. P. Abastado. 2011. Chemotherapy induces intratumoral expression of chemokines in cutaneous melanoma, favoring T-cell infiltration and tumor control. *Cancer Res* 71: 6997-7009.
281. Tannenbaum, C. S., R. Tubbs, D. Armstrong, J. H. Finke, R. M. Bukowski, and T. A. Hamilton. 1998. The CXC chemokines IP-10 and Mig are necessary for IL-12-mediated regression of the mouse RENCA tumor. *J Immunol* 161: 927-932.
282. Guirnalda, P., L. Wood, R. Goenka, J. Crespo, and Y. Paterson. 2013. Interferon γ -induced intratumoral expression of CXCL9 alters the local distribution of T cells following immunotherapy with *Listeria monocytogenes*. *Oncoimmunology* 2: e25752.
283. Griffioen, A. W., C. A. Damen, S. Martinotti, G. H. Blijham, and G. Groenewegen. 1996. Endothelial intercellular adhesion molecule-1 expression is suppressed in human malignancies: the role of angiogenic factors. *Cancer Res* 56: 1111-1117.
284. Piali, L., A. Fichtel, H. J. Terpe, B. A. Imhof, and R. H. Gisler. 1995. Endothelial vascular cell adhesion molecule 1 expression is suppressed by melanoma and carcinoma. *J Exp Med* 181: 811-816.
285. Hellwig, S. M., C. A. Damen, N. P. van Adrichem, G. H. Blijham, G. Groenewegen, and A. W. Griffioen. 1997. Endothelial CD34 is suppressed in human malignancies: role of angiogenic factors. *Cancer Lett* 120: 203-211.
286. Shrimali, R. K., Z. Yu, M. R. Theoret, D. Chinnasamy, N. P. Restifo, and S. A. Rosenberg. 2010. Antiangiogenic agents can increase lymphocyte infiltration into tumor and enhance the effectiveness of adoptive immunotherapy of cancer. *Cancer Res* 70: 6171-6180.
287. Johansson, A., J. Hamzah, C. J. Payne, and R. Ganss. 2012. Tumor-targeted TNF α stabilizes tumor vessels and enhances active immunotherapy. *Proc Natl Acad Sci U S A* 109: 7841-7846.

288. Radoja, S., and A. B. Frey. 2000. Cancer-induced defective cytotoxic T lymphocyte effector function: another mechanism how antigenic tumors escape immune-mediated killing. *Mol Med* 6: 465-479.
289. Frey, A. B., and N. Monu. 2008. Signaling defects in anti-tumor T cells. *Immunological reviews* 222: 192-205.
290. Koneru, M., D. Schaer, N. Monu, A. Ayala, and A. B. Frey. 2005. Defective Proximal TCR Signaling Inhibits CD8⁺ Tumor-Infiltrating Lymphocyte Lytic Function. *The Journal of Immunology* 174: 1830-1840.
291. Koneru, M., N. Monu, D. Schaer, J. Barletta, and A. B. Frey. 2006. Defective adhesion in tumor infiltrating CD8⁺ T cells. *J Immunol* 176: 6103-6111.
292. Ramsay, A. G., A. J. Clear, G. Kelly, R. Fatah, J. Matthews, F. MacDougall, T. A. Lister, A. M. Lee, M. Calaminici, and J. G. Gribben. 2009. Follicular lymphoma cells induce T-cell immunologic synapse dysfunction that can be repaired with lenalidomide: implications for the tumor microenvironment and immunotherapy. *Blood* 114: 4713-4720.
293. Ramsay, A. G., A. J. Johnson, A. M. Lee, G. Gorgün, R. Le Dieu, W. Blum, J. C. Byrd, and J. G. Gribben. 2008. Chronic lymphocytic leukemia T cells show impaired immunological synapse formation that can be reversed with an immunomodulating drug. *J Clin Invest* 118: 2427-2437.
294. Chanan-Khan, A. A., and B. D. Cheson. 2008. Lenalidomide for the treatment of B-cell malignancies. *J Clin Oncol* 26: 1544-1552.
295. Ramsay, A. G., A. J. Clear, R. Fatah, and J. G. Gribben. 2012. Multiple inhibitory ligands induce impaired T-cell immunologic synapse function in chronic lymphocytic leukemia that can be blocked with lenalidomide: establishing a reversible immune evasion mechanism in human cancer. *Blood* 120: 1412-1421.
296. Egeblad, M., E. S. Nakasone, and Z. Werb. 2010. Tumors as organs: complex tissues that interface with the entire organism. *Dev Cell* 18: 884-901.
297. Kalluri, R., and M. Zeisberg. 2006. Fibroblasts in cancer. *Nature Reviews Cancer* 6: 392-401.
298. Frantz, C., K. M. Stewart, and V. M. Weaver. 2010. The extracellular matrix at a glance. *Journal of cell science* 123: 4195-4200.
299. Salmon, H., K. Franciszkiewicz, D. Damotte, M. C. Dieu-Nosjean, P. Validire, A. Trautmann, F. Mami-Chouaib, and E. Donnadieu. 2012. Matrix architecture defines the preferential localization and migration of T cells into the stroma of human lung tumors. *J Clin Invest* 122: 899-910.
300. De Francesco, E. M., R. Lappano, M. F. Santolla, S. Marsico, A. Caruso, and M. Maggiolini. 2013. HIF-1 α /GPER signaling mediates the expression of VEGF induced by hypoxia in breast cancer associated fibroblasts (CAFs). *Breast Cancer Res* 15: R64.
301. Henke, E., R. Nandigama, and S. Ergün. 2020. Extracellular Matrix in the Tumor Microenvironment and Its Impact on Cancer Therapy. *Frontiers in Molecular Biosciences* 6.
302. Mariathasan, S., S. J. Turley, D. Nickles, A. Castiglioni, K. Yuen, Y. Wang, E. E. Kadel Iii, H. Koeppen, J. L. Astarita, R. Cubas, S. Jhunjhunwala, R. Banchereau, Y. Yang, Y. Guan, C. Chalouni, J. Ziai, Y. Şenbabaoğlu, S. Santoro, D. Sheinson, J. Hung, J. M. Giltane, A. A. Pierce, K. Mesh, S. Lianoglou, J. Riegler, R. A. D. Carano, P. Eriksson, M. Höglund, L. Somarriba, D. L. Halligan, M. S. van der Heijden, Y. Lorient, J. E. Rosenberg, L. Fong, I. Mellman, D. S. Chen, M. Green, C. Derleth, G. D. Fine, P. S. Hegde, R. Bourgon, and T. Powles. 2018. TGF β attenuates tumour response to PD-L1 blockade by contributing to exclusion of T cells. *Nature* 554: 544-548.
303. Tauriello, D. V. F., S. Palomo-Ponce, D. Stork, A. Berenguer-Llgero, J. Badia-Ramentol, M. Iglesias, M. Sevillano, S. Ibiza, A. Cañellas, X. Hernando-Momblona, D. Byrom, J. A. Matarin, A. Calon, E. I. Rivas, A. R. Nebreda, A. Riera, C. S.-O. Attolini, and E. Batlle. 2018. TGF β drives immune evasion in genetically reconstituted colon cancer metastasis. *Nature* 554: 538-543.

304. Currie, E., A. Schulze, R. Zechner, T. C. Walther, and R. V. Farese, Jr. 2013. Cellular fatty acid metabolism and cancer. *Cell Metab* 18: 153-161.
305. Iyengar, P., V. Espina, T. W. Williams, Y. Lin, D. Berry, L. A. Jelicks, H. Lee, K. Temple, R. Graves, J. Pollard, N. Chopra, R. G. Russell, R. Sasisekharan, B. J. Trock, M. Lippman, V. S. Calvert, E. F. Petricoin, 3rd, L. Liotta, E. Dadachova, R. G. Pestell, M. P. Lisanti, P. Bonaldo, and P. E. Scherer. 2005. Adipocyte-derived collagen VI affects early mammary tumor progression in vivo, demonstrating a critical interaction in the tumor/stroma microenvironment. *J Clin Invest* 115: 1163-1176.
306. Bergers, G., and L. E. Benjamin. 2003. Tumorigenesis and the angiogenic switch. *Nat Rev Cancer* 3: 401-410.
307. Lyden, D., K. Hattori, S. Dias, C. Costa, P. Blaikie, L. Butros, A. Chadburn, B. Heissig, W. Marks, L. Witte, Y. Wu, D. Hicklin, Z. Zhu, N. R. Hackett, R. G. Crystal, M. A. Moore, K. A. Hajjar, K. Manova, R. Benezra, and S. Rafii. 2001. Impaired recruitment of bone-marrow-derived endothelial and hematopoietic precursor cells blocks tumor angiogenesis and growth. *Nat Med* 7: 1194-1201.
308. Gabrilovich, D. I., and S. Nagaraj. 2009. Myeloid-derived suppressor cells as regulators of the immune system. *Nat Rev Immunol* 9: 162-174.
309. Lindau, D., P. Gielen, M. Kroesen, P. Wesseling, and G. J. Adema. 2013. The immunosuppressive tumour network: myeloid-derived suppressor cells, regulatory T cells and natural killer T cells. *Immunology* 138: 105-115.
310. Nagaraj, S., K. Gupta, V. Pisarev, L. Kinarsky, S. Sherman, L. Kang, D. L. Herber, J. Schneck, and D. I. Gabrilovich. 2007. Altered recognition of antigen is a mechanism of CD8+ T cell tolerance in cancer. *Nat Med* 13: 828-835.
311. Chen, Y., Y. Song, W. Du, L. Gong, H. Chang, and Z. Zou. 2019. Tumor-associated macrophages: an accomplice in solid tumor progression. *J Biomed Sci* 26: 78.
312. Zhou, J., Z. Tang, S. Gao, C. Li, Y. Feng, and X. Zhou. 2020. Tumor-Associated Macrophages: Recent Insights and Therapies. *Frontiers in Oncology* 10.
313. Noy, R., and J. W. Pollard. 2014. Tumor-associated macrophages: from mechanisms to therapy. *Immunity* 41: 49-61.
314. Hodi, F. S., S. J. O'Day, D. F. McDermott, R. W. Weber, J. A. Sosman, J. B. Haanen, R. Gonzalez, C. Robert, D. Schadendorf, J. C. Hassel, W. Akerley, A. J. van den Eertwegh, J. Lutzky, P. Lorigan, J. M. Vaubel, G. P. Linette, D. Hogg, C. H. Ottensmeier, C. Lebbé, C. Peschel, I. Quirt, J. I. Clark, J. D. Wolchok, J. S. Weber, J. Tian, M. J. Yellin, G. M. Nichol, A. Hoos, and W. J. Urba. 2010. Improved survival with ipilimumab in patients with metastatic melanoma. *N Engl J Med* 363: 711-723.
315. Seidel, J. A., A. Otsuka, and K. Kabashima. 2018. Anti-PD-1 and Anti-CTLA-4 Therapies in Cancer: Mechanisms of Action, Efficacy, and Limitations. *Front Oncol* 8: 86.
316. Topalian, S. L., C. G. Drake, and D. M. Pardoll. 2015. Immune checkpoint blockade: a common denominator approach to cancer therapy. *Cancer Cell* 27: 450-461.
317. Ribas, A., and J. D. Wolchok. 2018. Cancer immunotherapy using checkpoint blockade. *Science* 359: 1350-1355.
318. Chambers, C. A., M. S. Kuhns, J. G. Egen, and J. P. Allison. 2001. CTLA-4-mediated inhibition in regulation of T cell responses: mechanisms and manipulation in tumor immunotherapy. *Annu Rev Immunol* 19: 565-594.
319. Weber, J. S., S. P. D'Angelo, D. Minor, F. S. Hodi, R. Gutzmer, B. Neyns, C. Hoeller, N. I. Khushalani, W. H. Miller, Jr., C. D. Lao, G. P. Linette, L. Thomas, P. Lorigan, K. F. Grossmann, J. C. Hassel, M. Maio, M. Sznol, P. A. Ascierto, P. Mohr, B. Chmielowski, A. Bryce, I. M. Svane, J. J. Grob, A. M. Krackhardt, C. Horak, A. Lambert, A. S. Yang, and J. Larkin. 2015. Nivolumab versus chemotherapy in patients with advanced melanoma who progressed after anti-CTLA-4 treatment (CheckMate 037): a randomised, controlled, open-label, phase 3 trial. *Lancet Oncol* 16: 375-384.
320. Brummelman, J., E. M. C. Mazza, G. Alvisi, F. S. Colombo, A. Grilli, J. Mikulak, D. Mavilio, M. Alloisio, F. Ferrari, E. Lopci, P. Novellis, G. Veronesi, and E. Lugli. 2018. High-

dimensional single cell analysis identifies stem-like cytotoxic CD8(+) T cells infiltrating human tumors. *J Exp Med* 215: 2520-2535.

321. Yost, K. E., A. T. Satpathy, D. K. Wells, Y. Qi, C. Wang, R. Kageyama, K. L. McNamara, J. M. Granja, K. Y. Sarin, R. A. Brown, R. K. Gupta, C. Curtis, S. L. Bucktrout, M. M. Davis, A. L. S. Chang, and H. Y. Chang. 2019. Clonal replacement of tumor-specific T cells following PD-1 blockade. *Nat Med* 25: 1251-1259.
322. Kamphorst, A. O., A. Wieland, T. Nasti, S. Yang, R. Zhang, D. L. Barber, B. T. Konieczny, C. Z. Daugherty, L. Koenig, K. Yu, G. L. Sica, A. H. Sharpe, G. J. Freeman, B. R. Blazar, L. A. Turka, T. K. Owonikoko, R. N. Pillai, S. S. Ramalingam, K. Araki, and R. Ahmed. 2017. Rescue of exhausted CD8 T cells by PD-1-targeted therapies is CD28-dependent. *Science* 355: 1423-1427.
323. Larkin, J., V. Chiarion-Sileni, R. Gonzalez, J. J. Grob, C. L. Cowey, C. D. Lao, D. Schadendorf, R. Dummer, M. Smylie, P. Rutkowski, P. F. Ferrucci, A. Hill, J. Wagstaff, M. S. Carlino, J. B. Haanen, M. Maio, I. Marquez-Rodas, G. A. McArthur, P. A. Ascierto, G. V. Long, M. K. Callahan, M. A. Postow, K. Grossmann, M. Sznol, B. Dreno, L. Bastholt, A. Yang, L. M. Rollin, C. Horak, F. S. Hodi, and J. D. Wolchok. 2015. Combined Nivolumab and Ipilimumab or Monotherapy in Untreated Melanoma. *N Engl J Med* 373: 23-34.
324. Sánchez-Fueyo, A., J. Tian, D. Picarella, C. Domenig, X. X. Zheng, C. A. Sabatos, N. Manlongat, O. Bender, T. Kamradt, V. K. Kuchroo, J.-C. Gutiérrez-Ramos, A. J. Coyle, and T. B. Strom. 2003. Tim-3 inhibits T helper type 1-mediated auto- and alloimmune responses and promotes immunological tolerance. *Nature Immunology* 4: 1093-1101.
325. Sakuishi, K., L. Apetoh, J. M. Sullivan, B. R. Blazar, V. K. Kuchroo, and A. C. Anderson. 2010. Targeting Tim-3 and PD-1 pathways to reverse T cell exhaustion and restore anti-tumor immunity. *J Exp Med* 207: 2187-2194.
326. Ngiow, S. F., B. von Scheidt, H. Akiba, H. Yagita, M. W. L. Teng, and M. J. Smyth. 2011. Anti-TIM3 Antibody Promotes T Cell IFN- γ -Mediated Antitumor Immunity and Suppresses Established Tumors. *Cancer Research* 71: 3540-3551.
327. Zhou, Q., M. E. Munger, R. G. Veenstra, B. J. Weigel, M. Hirashima, D. H. Munn, W. J. Murphy, M. Azuma, A. C. Anderson, V. K. Kuchroo, and B. R. Blazar. 2011. Coexpression of Tim-3 and PD-1 identifies a CD8+ T-cell exhaustion phenotype in mice with disseminated acute myelogenous leukemia. *Blood* 117: 4501-4510.
328. Edmunds, G. L., C. C. W. Wong, R. Ambler, E. Milodowski, H. Alamir, S. J. Cross, G. Galea, C. Wülfing, and D. J. Morgan. 2021. The adenosine 2a receptor and TIM3 directly inhibit killing of tumor cells by cytotoxic T lymphocytes through interference with cytoskeletal polarization. *bioRxiv*: 2021.2005.2020.444944.
329. Koyama, S., E. A. Akbay, Y. Y. Li, G. S. Herter-Sprie, K. A. Buczkowski, W. G. Richards, L. Gandhi, A. J. Redig, S. J. Rodig, H. Asahina, R. E. Jones, M. M. Kulkarni, M. Kuraguchi, S. Palakurthi, P. E. Fecci, B. E. Johnson, P. A. Janne, J. A. Engelman, S. P. Gangadharan, D. B. Costa, G. J. Freeman, R. Bueno, F. S. Hodi, G. Dranoff, K. K. Wong, and P. S. Hammerman. 2016. Adaptive resistance to therapeutic PD-1 blockade is associated with upregulation of alternative immune checkpoints. *Nat Commun* 7: 10501.
330. Shayan, G., R. Srivastava, J. Li, N. Schmitt, L. P. Kane, and R. L. Ferris. 2017. Adaptive resistance to anti-PD1 therapy by Tim-3 upregulation is mediated by the PI3K-Akt pathway in head and neck cancer. *Oncoimmunology* 6: e1261779.
331. Acharya, N., C. Sabatos-Peyton, and A. C. Anderson. 2020. Tim-3 finds its place in the cancer immunotherapy landscape. *J Immunother Cancer* 8.
332. Harding, J. J., A. Patnaik, V. Moreno, M. Stein, A. M. Jankowska, N. V. d. Mendizabal, Z. T. Liu, M. Koneru, and E. Calvo. 2019. A phase Ia/Ib study of an anti-TIM-3 antibody (LY3321367) monotherapy or in combination with an anti-PD-L1 antibody (LY3300054): Interim safety, efficacy, and pharmacokinetic findings in advanced cancers. *Journal of Clinical Oncology* 37: 12-12.
333. Curigliano, G., H. Gelderblom, N. Mach, T. Doi, W. M. D. Tai, P. Forde, J. Sarantopoulos, P. L. Bedard, C.-C. Lin, S. Hodi, S. Wilgenhof, A. Santoro, C. Sabatos-Peyton, T. Longmire, K. Wan, P. Nikolopoulos, L. Manenti, and A. Naing. 2019. Abstract CT183: Phase (Ph) I/II

- study of MBG453± spartalizumab (PDR001) in patients (pts) with advanced malignancies. *Cancer Research* 79: CT183-CT183.
334. Rosenberg, S. A., and N. P. Restifo. 2015. Adoptive cell transfer as personalized immunotherapy for human cancer. *Science* 348: 62-68.
 335. Besser, M. J., R. Shapira-Frommer, A. J. Treves, D. Zippel, O. Itzhaki, L. Hershkovitz, D. Levy, A. Kubi, E. Hovav, N. Chermoshniuk, B. Shalmon, I. Hardan, R. Catane, G. Markel, S. Apter, A. Ben-Nun, I. Kuchuk, A. Shimoni, A. Nagler, and J. Schachter. 2010. Clinical responses in a phase II study using adoptive transfer of short-term cultured tumor infiltration lymphocytes in metastatic melanoma patients. *Clin Cancer Res* 16: 2646-2655.
 336. Dudley, M. E., J. R. Wunderlich, J. C. Yang, R. M. Sherry, S. L. Topalian, N. P. Restifo, R. E. Royal, U. Kammula, D. E. White, S. A. Mavroukakis, L. J. Rogers, G. J. Gracia, S. A. Jones, D. P. Mangiameli, M. M. Pelletier, J. Gea-Banacloche, M. R. Robinson, D. M. Berman, A. C. Filie, A. Abati, and S. A. Rosenberg. 2005. Adoptive cell transfer therapy following non-myeloablative but lymphodepleting chemotherapy for the treatment of patients with refractory metastatic melanoma. *J Clin Oncol* 23: 2346-2357.
 337. Dudley, M. E., J. C. Yang, R. Sherry, M. S. Hughes, R. Royal, U. Kammula, P. F. Robbins, J. Huang, D. E. Citrin, S. F. Leitman, J. Wunderlich, N. P. Restifo, A. Thomasian, S. G. Downey, F. O. Smith, J. Klapper, K. Morton, C. Laurencot, D. E. White, and S. A. Rosenberg. 2008. Adoptive cell therapy for patients with metastatic melanoma: evaluation of intensive myeloablative chemoradiation preparative regimens. *J Clin Oncol* 26: 5233-5239.
 338. Locke, F. L., A. Ghobadi, C. A. Jacobson, D. B. Miklos, L. J. Lekakis, O. O. Oluwole, Y. Lin, I. Braunschweig, B. T. Hill, J. M. Timmerman, A. Deol, P. M. Reagan, P. Stiff, I. W. Flinn, U. Farooq, A. Goy, P. A. McSweeney, J. Munoz, T. Siddiqi, J. C. Chavez, A. F. Herrera, N. L. Bartlett, J. S. Wiezorek, L. Navale, A. Xue, Y. Jiang, A. Bot, J. M. Rossi, J. J. Kim, W. Y. Go, and S. S. Neelapu. 2019. Long-term safety and activity of axicabtagene ciloleucel in refractory large B-cell lymphoma (ZUMA-1): a single-arm, multicentre, phase 1-2 trial. *Lancet Oncol* 20: 31-42.
 339. Schuster, S. J., M. R. Bishop, C. S. Tam, E. K. Waller, P. Borchmann, J. P. McGuirk, U. Jäger, S. Jaglowski, C. Andreadis, J. R. Westin, I. Fleury, V. Bachanova, S. R. Foley, P. J. Ho, S. Mielke, J. M. Magenau, H. Holte, S. Pantano, L. B. Pacaud, R. Awasthi, J. Chu, Ö. Anak, G. Salles, and R. T. Maziarz. 2019. Tisagenlecleucel in Adult Relapsed or Refractory Diffuse Large B-Cell Lymphoma. *N Engl J Med* 380: 45-56.
 340. Peng, W., G. Lizée, and P. Hwu. 2013. Blockade of the PD-1 pathway enhances the efficacy of adoptive cell therapy against cancer. *Oncoimmunology* 2: e22691-e22691.
 341. Chapuis, A. G., I. M. Roberts, J. A. Thompson, K. A. Margolin, S. Bhatia, S. M. Lee, H. L. Sloan, I. P. Lai, E. A. Farrar, F. Wagener, K. C. Shibuya, J. Cao, J. D. Wolchok, P. D. Greenberg, and C. Yee. 2016. T-Cell Therapy Using Interleukin-21-Primed Cytotoxic T-Cell Lymphocytes Combined With Cytotoxic T-Cell Lymphocyte Antigen-4 Blockade Results in Long-Term Cell Persistence and Durable Tumor Regression. *J Clin Oncol* 34: 3787-3795.
 342. Shi, L. Z., S. Goswami, T. Fu, B. Guan, J. Chen, L. Xiong, J. Zhang, D. Ng Tang, X. Zhang, L. Vence, J. Blando, J. P. Allison, R. Collazo, J. Gao, and P. Sharma. 2019. Blockade of CTLA-4 and PD-1 Enhances Adoptive T-cell Therapy Efficacy in an ICOS-Mediated Manner. *Cancer Immunology Research* 7: 1803-1812.
 343. Drasdo, D., and S. Hohme. 2005. A single-cell-based model of tumor growth in vitro: monolayers and spheroids. *Phys Biol* 2: 133-147.
 344. Freyer, J. P., and R. M. Sutherland. 1986. Regulation of growth saturation and development of necrosis in EMT6/Ro multicellular spheroids by the glucose and oxygen supply. *Cancer Res* 46: 3504-3512.
 345. Luk, C. K., and R. M. Sutherland. 1987. Nutrient modification of proliferation and radiation response in EMT6/Ro spheroids. *Int J Radiat Oncol Biol Phys* 13: 885-895.
 346. Sha, W., C. Olesch, H. Hanaka, O. Radmark, A. Weigert, and B. Brune. 2013. Necrosis in DU145 prostate cancer spheroids induces COX-2/mPGES-1-derived PGE2 to promote tumor growth and to inhibit T cell activation. *Int J Cancer* 133: 1578-1588.

347. Hlatky, L., R. K. Sachs, and E. L. Alpen. 1988. Joint oxygen-glucose deprivation as the cause of necrosis in a tumor analog. *J Cell Physiol* 134: 167-178.
348. Tannock, I. F., and I. Kopelyan. 1986. Influence of glucose concentration on growth and formation of necrosis in spheroids derived from a human bladder cancer cell line. *Cancer Res* 46: 3105-3110.
349. Bell, H. S., I. R. Whittle, M. Walker, H. A. Leaver, and S. B. Wharton. 2001. The development of necrosis and apoptosis in glioma: experimental findings using spheroid culture systems. *Neuropathol Appl Neurobiol* 27: 291-304.
350. Fischer, K., P. Hoffmann, S. Voelkl, N. Meidenbauer, J. Ammer, M. Edinger, E. Gottfried, S. Schwarz, G. Rothe, S. Hoves, K. Renner, B. Timischl, A. Mackensen, L. Kunz-Schughart, R. Andreesen, S. W. Krause, and M. Kreutz. 2007. Inhibitory effect of tumor cell-derived lactic acid on human T cells. *Blood* 109: 3812-3819.
351. Freyer, J. P. 1988. Role of necrosis in regulating the growth saturation of multicellular spheroids. *Cancer Res* 48: 2432-2439.
352. Daster, S., N. Amatruda, D. Calabrese, R. Ivanek, E. Turrini, R. A. Drosler, P. Zajac, C. Fimognari, G. C. Spagnoli, G. Iezzi, V. Mele, and M. G. Muraro. 2017. Induction of hypoxia and necrosis in multicellular tumor spheroids is associated with resistance to chemotherapy treatment. *Oncotarget* 8: 1725-1736.
353. Gamrekeshvili, J., C. Kruger, R. von Wasielewski, M. Hoffmann, K. M. Huster, D. H. Busch, M. P. Manns, F. Korangy, and T. F. Greten. 2007. Necrotic tumor cell death in vivo impairs tumor-specific immune responses. *J Immunol* 178: 1573-1580.
354. Bredholt, G., M. Mannelqvist, I. M. Stefansson, E. Birkeland, T. H. Bo, A. M. Oyan, J. Trovik, K. H. Kalland, I. Jonassen, H. B. Salvesen, E. Wik, and L. A. Akslen. 2015. Tumor necrosis is an important hallmark of aggressive endometrial cancer and associates with hypoxia, angiogenesis and inflammation responses. *Oncotarget* 6: 39676-39691.
355. Tomes, L., E. Emberley, Y. Niu, S. Troup, J. Pastorek, K. Strange, A. Harris, and P. H. Watson. 2003. Necrosis and hypoxia in invasive breast carcinoma. *Breast Cancer Res Treat* 81: 61-69.
356. Lam, J. S., O. Shvarts, J. W. Said, A. J. Pantuck, D. B. Seligson, M. E. Aldridge, M. H. Bui, X. Liu, S. Horvath, R. A. Figlin, and A. S. Belldegrun. 2005. Clinicopathologic and molecular correlations of necrosis in the primary tumor of patients with renal cell carcinoma. *Cancer* 103: 2517-2525.
357. Leek, R. D., R. J. Landers, A. L. Harris, and C. E. Lewis. 1999. Necrosis correlates with high vascular density and focal macrophage infiltration in invasive carcinoma of the breast. *Br J Cancer* 79: 991-995.
358. Feder-Mengus, C., S. Ghosh, A. Reschner, I. Martin, and G. C. Spagnoli. 2008. New dimensions in tumor immunology: what does 3D culture reveal? *Trends Mol Med* 14: 333-340.
359. Han, K., S. E. Pierce, A. Li, K. Spees, G. R. Anderson, J. A. Seoane, Y. H. Lo, M. Dubreuil, M. Olivas, R. A. Kamber, M. Wainberg, K. Kostyrko, M. R. Kelly, M. Yousefi, S. W. Simpkins, D. Yao, K. Lee, C. J. Kuo, P. K. Jackson, A. Sweet-Cordero, A. Kundaje, A. J. Gentles, C. Curtis, M. M. Winslow, and M. C. Bassik. 2020. CRISPR screens in cancer spheroids identify 3D growth-specific vulnerabilities. *Nature* 580: 136-141.
360. Na, J. C., J. H. Kim, S. Y. Kim, Y. R. Gu, D. Y. Jun, H. H. Lee, Y. E. Yoon, K. H. Choi, S. J. Hong, and W. K. Han. 2020. Establishment of patient-derived three-dimensional organoid culture in renal cell carcinoma. *Investig Clin Urol* 61: 216-223.
361. Pickl, M., and C. H. Ries. 2009. Comparison of 3D and 2D tumor models reveals enhanced HER2 activation in 3D associated with an increased response to trastuzumab. *Oncogene* 28: 461-468.
362. Barros, A. S., E. C. Costa, A. S. Nunes, D. de Melo-Diogo, and I. J. Correia. 2018. Comparative study of the therapeutic effect of Doxorubicin and Resveratrol combination on 2D and 3D (spheroids) cell culture models. *Int J Pharm* 551: 76-83.
363. Lee, G. Y., P. A. Kenny, E. H. Lee, and M. J. Bissell. 2007. Three-dimensional culture models of normal and malignant breast epithelial cells. *Nat Methods* 4: 359-365.

364. Lee, J. M., P. Mhawech-Fauceglia, N. Lee, L. C. Parsanian, Y. G. Lin, S. A. Gayther, and K. Lawrenson. 2013. A three-dimensional microenvironment alters protein expression and chemosensitivity of epithelial ovarian cancer cells in vitro. *Lab Invest* 93: 528-542.
365. Brady, L., R. M. Gil da Costa, I. M. Coleman, C. K. Matson, M. C. Risk, R. T. Coleman, and P. S. Nelson. 2020. A comparison of prostate cancer cell transcriptomes in 2D monoculture vs 3D xenografts identify consistent gene expression alterations associated with tumor microenvironments. *Prostate* 80: 491-499.
366. Kenny, P. A., G. Y. Lee, C. A. Myers, R. M. Neve, J. R. Semeiks, P. T. Spellman, K. Lorenz, E. H. Lee, M. H. Barcellos-Hoff, O. W. Petersen, J. W. Gray, and M. J. Bissell. 2007. The morphologies of breast cancer cell lines in three-dimensional assays correlate with their profiles of gene expression. *Mol Oncol* 1: 84-96.
367. Riedl, A., M. Schleder, K. Pudelko, M. Stadler, S. Walter, D. Unterleuthner, C. Unger, N. Kramer, M. Hengstschlager, L. Kenner, D. Pfeiffer, G. Krupitza, and H. Dolznig. 2017. Comparison of cancer cells in 2D vs 3D culture reveals differences in AKT-mTOR-S6K signaling and drug responses. *J Cell Sci* 130: 203-218.
368. Takagi, A., M. Watanabe, Y. Ishii, J. Morita, Y. Hirokawa, T. Matsuzaki, and T. Shiraishi. 2007. Three-dimensional cellular spheroid formation provides human prostate tumor cells with tissue-like features. *Anticancer Res* 27: 45-53.
369. Ekert, J. E., K. Johnson, B. Strake, J. Pardinas, S. Jarantow, R. Perkinson, and D. C. Colter. 2014. Three-dimensional lung tumor microenvironment modulates therapeutic compound responsiveness in vitro--implication for drug development. *PLoS One* 9: e92248.
370. Jager, E., J. Karbach, S. Gnjatic, A. Neumann, A. Bender, D. Valmori, M. Ayyoub, E. Ritter, G. Ritter, D. Jager, D. Panicali, E. Hoffman, L. Pan, H. Oettgen, L. J. Old, and A. Knuth. 2006. Recombinant vaccinia/fowlpox NY-ESO-1 vaccines induce both humoral and cellular NY-ESO-1-specific immune responses in cancer patients. *Proc Natl Acad Sci U S A* 103: 14453-14458.
371. Zajac, P., D. Oertli, W. Marti, M. Adamina, M. Bolli, U. Guller, C. Noppen, E. Padovan, E. Schultz-Thater, M. Heberer, and G. Spagnoli. 2003. Phase I/II clinical trial of a nonreplicative vaccinia virus expressing multiple HLA-A0201-restricted tumor-associated epitopes and costimulatory molecules in metastatic melanoma patients. *Hum Gene Ther* 14: 1497-1510.
372. Dangles-Marie, V., S. Richon, M. El-Behi, H. Echchakir, G. Dorothee, J. Thiery, P. Validire, I. Vergnon, J. Menez, M. Ladjimi, S. Chouaib, D. Bellet, and F. Mami-Chouaib. 2003. A three-dimensional tumor cell defect in activating autologous CTLs is associated with inefficient antigen presentation correlated with heat shock protein-70 down-regulation. *Cancer Res* 63: 3682-3687.
373. Binder, R. J., N. E. Blachere, and P. K. Srivastava. 2001. Heat shock protein-chaperoned peptides but not free peptides introduced into the cytosol are presented efficiently by major histocompatibility complex I molecules. *J Biol Chem* 276: 17163-17171.
374. Ghosh, S., R. Rosenthal, P. Zajac, W. P. Weber, D. Oertli, M. Heberer, I. Martin, G. C. Spagnoli, and A. Reschner. 2005. Culture of melanoma cells in 3-dimensional architectures results in impaired immunorecognition by cytotoxic T lymphocytes specific for Melan-A/MART-1 tumor-associated antigen. *Ann Surg* 242: 851-857, discussion 858.
375. Feder-Mengus, C., S. Ghosh, W. P. Weber, S. Wyler, P. Zajac, L. Terracciano, D. Oertli, M. Heberer, I. Martin, G. C. Spagnoli, and A. Reschner. 2007. Multiple mechanisms underlie defective recognition of melanoma cells cultured in three-dimensional architectures by antigen-specific cytotoxic T lymphocytes. *Br J Cancer* 96: 1072-1082.
376. Sugiura, A., and J. C. Rathmell. 2018. Metabolic Barriers to T Cell Function in Tumors. *J Immunol* 200: 400-407.
377. van der Windt, G. J., and E. L. Pearce. 2012. Metabolic switching and fuel choice during T-cell differentiation and memory development. *Immunol Rev* 249: 27-42.
378. Brand, A., K. Singer, G. E. Koehl, M. Kolitzus, G. Schoenhammer, A. Thiel, C. Matos, C. Bruss, S. Klobuch, K. Peter, M. Kastenberger, C. Bogdan, U. Schleicher, A. Mackensen, E.

- Ullrich, S. Fichtner-Feigl, R. Kesselring, M. Mack, U. Ritter, M. Schmid, C. Blank, K. Dettmer, P. J. Oefner, P. Hoffmann, S. Walenta, E. K. Geissler, J. Pouyssegur, A. Villunger, A. Steven, B. Seliger, S. Schreml, S. Haferkamp, E. Kohl, S. Karrer, M. Berneburg, W. Herr, W. Mueller-Klieser, K. Renner, and M. Kreutz. 2016. LDHA-Associated Lactic Acid Production Blunts Tumor Immunosurveillance by T and NK Cells. *Cell Metab* 24: 657-671.
379. Zboralski, D., K. Hoehlig, D. Eulberg, A. Fromming, and A. Vater. 2017. Increasing Tumor-Infiltrating T Cells through Inhibition of CXCL12 with NOX-A12 Synergizes with PD-1 Blockade. *Cancer Immunol Res* 5: 950-956.
380. Deng, J., E. S. Wang, R. W. Jenkins, S. Li, R. Dries, K. Yates, S. Chhabra, W. Huang, H. Liu, A. R. Aref, E. Ivanova, C. P. Paweletz, M. Bowden, C. W. Zhou, G. S. Herter-Sprie, J. A. Sorrentino, J. E. Bisi, P. H. Lizotte, A. A. Merlino, M. M. Quinn, L. E. Bufe, A. Yang, Y. Zhang, H. Zhang, P. Gao, T. Chen, M. E. Cavanaugh, A. J. Rode, E. Haines, P. J. Roberts, J. C. Strum, W. G. Richards, J. H. Lorch, S. Parangi, V. Gunda, G. M. Boland, R. Bueno, S. Palakurthi, G. J. Freeman, J. Ritz, W. N. Haining, N. E. Sharpless, H. Arthanari, G. I. Shapiro, D. A. Barbie, N. S. Gray, and K. K. Wong. 2018. CDK4/6 Inhibition Augments Antitumor Immunity by Enhancing T-cell Activation. *Cancer Discov* 8: 216-233.
381. Rachel, A. 2017. The impaired polarisation of CD8+ tumour infiltrating lymphocytes during cytolysis is regulated by PD-1. In *Cellular and Molecular Medicine*. University of Bristol.
382. Edmunds, G. L. 2019. Targeting Adenosine and TIM3 to Improve Anti-Tumour Immunity. In *Cellular and Molecular Medicine*. University of Bristol.
383. Liesche, C., P. Sauer, I. Prager, D. Urlaub, M. Claus, R. Eils, J. Beaudouin, and C. Watzl. 2018. Single-Fluorescent Protein Reporters Allow Parallel Quantification of Natural Killer Cell-Mediated Granzyme and Caspase Activities in Single Target Cells. *Front Immunol* 9: 1840.
384. Kim, J. H., S. R. Lee, L. H. Li, H. J. Park, J. H. Park, K. Y. Lee, M. K. Kim, B. A. Shin, and S. Y. Choi. 2011. High cleavage efficiency of a 2A peptide derived from porcine teschovirus-1 in human cell lines, zebrafish and mice. *PLoS One* 6: e18556.
385. Schindelin, J., I. Arganda-Carreras, E. Frise, V. Kaynig, M. Longair, T. Pietzsch, S. Preibisch, C. Rueden, S. Saalfeld, B. Schmid, J. Y. Tinevez, D. J. White, V. Hartenstein, K. Eliceiri, P. Tomancak, and A. Cardona. 2012. Fiji: an open-source platform for biological-image analysis. *Nat Methods* 9: 676-682.
386. Legland, D., I. Arganda-Carreras, and P. Andrey. 2016. MorphoLibJ: integrated library and plugins for mathematical morphology with ImageJ. *Bioinformatics* 32: 3532-3534.
387. Wu, X., Z. Gu, Y. Chen, B. Chen, W. Chen, L. Weng, and X. Liu. 2019. Application of PD-1 Blockade in Cancer Immunotherapy. *Comput Struct Biotechnol J* 17: 661-674.
388. Restifo, N. P., M. E. Dudley, and S. A. Rosenberg. 2012. Adoptive immunotherapy for cancer: harnessing the T cell response. *Nat Rev Immunol* 12: 269-281.
389. Sutherland, R. M., W. R. Inch, J. A. McCredie, and J. Kruuv. 1970. A multi-component radiation survival curve using an in vitro tumour model. *Int J Radiat Biol Relat Stud Phys Chem Med* 18: 491-495.
390. Nath, S., and G. R. Devi. 2016. Three-dimensional culture systems in cancer research: Focus on tumor spheroid model. *Pharmacol Ther* 163: 94-108.
391. Zhou, S., M. Zhu, F. Meng, J. Shao, Q. Xu, J. Wei, and B. Liu. 2019. Evaluation of PD-1 blockade using a multicellular tumor spheroid model. *Am J Transl Res* 11: 7471-7478.
392. Costa, E. C., A. F. Moreira, D. de Melo-Diogo, V. M. Gaspar, M. P. Carvalho, and I. J. Correia. 2016. 3D tumor spheroids: an overview on the tools and techniques used for their analysis. *Biotechnol Adv* 34: 1427-1441.
393. Sutherland, R. M., B. Sordat, J. Bamat, H. Gabbert, B. Bourrat, and W. Mueller-Klieser. 1986. Oxygenation and differentiation in multicellular spheroids of human colon carcinoma. *Cancer Res* 46: 5320-5329.
394. Herter, S., L. Morra, R. Schlenker, J. Sulcova, L. Fahrni, I. Waldhauer, S. Lehmann, T. Reisländer, I. Agarkova, J. M. Kelm, C. Klein, P. Umana, and M. Bacac. 2017. A novel three-dimensional heterotypic spheroid model for the assessment of the activity of cancer immunotherapy agents. *Cancer Immunol Immunother* 66: 129-140.

395. Sadovska, L., E. Zandberga, K. Sagini, K. Jekabsons, U. Riekstina, Z. Kalnina, A. Llorente, and A. Line. 2018. A novel 3D heterotypic spheroid model for studying extracellular vesicle-mediated tumour and immune cell communication. *Biochem Biophys Res Commun* 495: 1930-1935.
396. Ward, J. P., and J. R. King. 1997. Mathematical modelling of avascular-tumour growth. *IMA J Math Appl Med Biol* 14: 39-69.
397. Curcio, E., S. Salerno, G. Barbieri, L. De Bartolo, E. Drioli, and A. Bader. 2007. Mass transfer and metabolic reactions in hepatocyte spheroids cultured in rotating wall gas-permeable membrane system. *Biomaterials* 28: 5487-5497.
398. Glicklis, R., J. C. Merchuk, and S. Cohen. 2004. Modeling mass transfer in hepatocyte spheroids via cell viability, spheroid size, and hepatocellular functions. *Biotechnol Bioeng* 86: 672-680.
399. Basingab, F. S., M. Ahmadi, and D. J. Morgan. 2016. IFN γ -Dependent Interactions between ICAM-1 and LFA-1 Counteract Prostaglandin E2-Mediated Inhibition of Antitumor CTL Responses. *Cancer Immunol Res* 4: 400-411.
400. Lee, J. K., T. J. Sayers, A. D. Brooks, T. C. Back, H. A. Young, K. L. Komschlies, J. M. Wigginton, and R. H. Wiltrot. 2000. IFN-gamma-dependent delay of in vivo tumor progression by Fas overexpression on murine renal cancer cells. *J Immunol* 164: 231-239.
401. Kedia-Mehta, N., and D. K. Finlay. 2019. Competition for nutrients and its role in controlling immune responses. *Nat Commun* 10: 2123.
402. Corish, P., and C. Tyler-Smith. 1999. Attenuation of green fluorescent protein half-life in mammalian cells. *Protein Eng* 12: 1035-1040.
403. Gomme, E. A., C. Wirblich, S. Addya, G. F. Rall, and M. J. Schnell. 2012. Immune clearance of attenuated rabies virus results in neuronal survival with altered gene expression. *PLoS Pathog* 8: e1002971.
404. Langan, L. M., N. J. Dodd, S. F. Owen, W. M. Purcell, S. K. Jackson, and A. N. Jha. 2016. Direct Measurements of Oxygen Gradients in Spheroid Culture System Using Electron Parametric Resonance Oximetry. *PLoS One* 11: e0149492.
405. Bagheri, V., M. R. Abbaszadegan, B. Memar, M. R. Motie, M. Asadi, R. A. Mahmoudian, and M. Gholamin. 2019. Induction of T cell-mediated immune response by dendritic cells pulsed with mRNA of sphere-forming cells isolated from patients with gastric cancer. *Life Sci* 219: 136-143.
406. Baye, J., C. Galvin, and A. Q. Shen. 2017. Microfluidic device flow field characterization around tumor spheroids with tunable necrosis produced in an optimized off-chip process. *Biomed Microdevices* 19: 59.
407. Ochsenbein, A. F., P. Klenerman, U. Karrer, B. Ludewig, M. Pericin, H. Hengartner, and R. M. Zinkernagel. 1999. Immune surveillance against a solid tumor fails because of immunological ignorance. *Proc Natl Acad Sci U S A* 96: 2233-2238.
408. Giannattasio, A., S. Weil, S. Kloess, N. Ansari, E. H. Stelzer, A. Cerwenka, A. Steinle, U. Koehl, and J. Koch. 2015. Cytotoxicity and infiltration of human NK cells in in vivo-like tumor spheroids. *BMC Cancer* 15: 351.
409. Phan-Lai, V., F. M. Kievit, S. J. Florczyk, K. Wang, M. L. Disis, and M. Zhang. 2014. CCL21 and IFN γ recruit and activate tumor specific T cells in 3D scaffold model of breast cancer. *Anticancer Agents Med Chem* 14: 204-210.
410. Conger, A. D., and M. C. Ziskin. 1983. Growth of mammalian multicellular tumor spheroids. *Cancer Res* 43: 556-560.
411. Akagi, J., M. Kordon, H. Zhao, A. Matuszek, J. Dobrucki, R. Errington, P. J. Smith, K. Takeda, Z. Darzynkiewicz, and D. Wlodkowic. 2013. Real-time cell viability assays using a new anthracycline derivative DRAQ7(R). *Cytometry A* 83: 227-234.
412. Raza, A., H. E. Colley, E. Baggaley, I. V. Sazanovich, N. H. Green, J. A. Weinstein, S. W. Botchway, S. MacNeil, and J. W. Haycock. 2017. Oxygen Mapping of Melanoma Spheroids using Small Molecule Platinum Probe and Phosphorescence Lifetime Imaging Microscopy. *Sci Rep* 7: 10743.

413. Nordmark, M., J. Loncaster, S.-C. Chou, H. Havsteen, J. C. Lindegaard, S. E. Davidson, M. Varia, C. West, R. Hunter, J. Overgaard, and J. A. Raleigh. 2001. Invasive oxygen measurements and pimonidazole labeling in human cervix carcinoma. *International Journal of Radiation Oncology*Biophysics* 49: 581-586.
414. Arteel, G. E., R. G. Thurman, and J. A. Raleigh. 1998. Reductive metabolism of the hypoxia marker pimonidazole is regulated by oxygen tension independent of the pyridine nucleotide redox state. *Eur J Biochem* 253: 743-750.
415. Gillies, R. J., I. Robey, and R. A. Gatenby. 2008. Causes and consequences of increased glucose metabolism of cancers. *J Nucl Med* 49 Suppl 2: 24s-42s.
416. Isaaz, S., K. Baetz, K. Olsen, E. Podack, and G. M. Griffiths. 1995. Serial killing by cytotoxic T lymphocytes: T cell receptor triggers degranulation, re-filling of the lytic granules and secretion of lytic proteins via a non-granule pathway. *Eur J Immunol* 25: 1071-1079.
417. Henrickson, S. E., T. R. Mempel, I. B. Mazo, B. Liu, M. N. Artyomov, H. Zheng, A. Peixoto, M. P. Flynn, B. Senman, T. Junt, H. C. Wong, A. K. Chakraborty, and U. H. von Andrian. 2008. T cell sensing of antigen dose governs interactive behavior with dendritic cells and sets a threshold for T cell activation. *Nat Immunol* 9: 282-291.
418. Zarnitsyna, V. I., J. Huang, F. Zhang, Y. H. Chien, D. Leckband, and C. Zhu. 2007. Memory in receptor-ligand-mediated cell adhesion. *Proc Natl Acad Sci U S A* 104: 18037-18042.
419. Mihm, M. C., Jr., C. G. Clemente, and N. Cascinelli. 1996. Tumor infiltrating lymphocytes in lymph node melanoma metastases: a histopathologic prognostic indicator and an expression of local immune response. *Lab Invest* 74: 43-47.
420. Boissonnas, A., L. Fetler, I. S. Zeelenberg, S. Hugues, and S. Amigorena. 2007. In vivo imaging of cytotoxic T cell infiltration and elimination of a solid tumor. *J Exp Med* 204: 345-356.
421. Breart, B., F. Lemaitre, S. Celli, and P. Bousso. 2008. Two-photon imaging of intratumoral CD8+ T cell cytotoxic activity during adoptive T cell therapy in mice. *J Clin Invest* 118: 1390-1397.
422. Mrass, P., H. Takano, L. G. Ng, S. Daxini, M. O. Lasaro, A. Iparraguirre, L. L. Cavanagh, U. H. von Andrian, H. C. Ertl, P. G. Haydon, and W. Weninger. 2006. Random migration precedes stable target cell interactions of tumor-infiltrating T cells. *J Exp Med* 203: 2749-2761.
423. Michalek, R. D., and J. C. Rathmell. 2010. The metabolic life and times of a T-cell. *Immunol Rev* 236: 190-202.
424. Lee, M. J., M. Y. Woo, Y. J. Chwae, M. H. Kwon, K. Kim, and S. Park. 2012. Down-regulation of interleukin-2 production by CD4(+) T cells expressing TIM-3 through suppression of NFAT dephosphorylation and AP-1 transcription. *Immunobiology* 217: 986-995.
425. Tomkowicz, B., E. Walsh, A. Cotty, R. Verona, N. Sabins, F. Kaplan, S. Santulli-Marotto, C. N. Chin, J. Mooney, R. B. Lingham, M. Naso, and T. McCabe. 2015. TIM-3 Suppresses Anti-CD3/CD28-Induced TCR Activation and IL-2 Expression through the NFAT Signaling Pathway. *PLoS One* 10: e0140694.
426. Clayton, K. L., M. S. Haaland, M. B. Douglas-Vail, S. Mujib, G. M. Chew, L. C. Ndhlovu, and M. A. Ostrowski. 2014. T cell Ig and mucin domain-containing protein 3 is recruited to the immune synapse, disrupts stable synapse formation, and associates with receptor phosphatases. *J Immunol* 192: 782-791.
427. Lee, M. J., S. J. Yun, B. Lee, E. Jeong, G. Yoon, K. Kim, and S. Park. 2020. Association of TIM-3 expression with glucose metabolism in Jurkat T cells. *BMC Immunology* 21: 48.
428. Stelekati, E., H. Shin, T. A. Doering, D. V. Dolfi, C. G. Ziegler, D. P. Beiting, L. Dawson, J. Liboon, D. Wolski, M. A. Ali, P. D. Katsikis, H. Shen, D. S. Roos, W. N. Haining, G. M. Lauer, and E. J. Wherry. 2014. Bystander chronic infection negatively impacts development of CD8(+) T cell memory. *Immunity* 40: 801-813.
429. Hermiston, M. L., Z. Xu, and A. Weiss. 2003. CD45: a critical regulator of signaling thresholds in immune cells. *Annu Rev Immunol* 21: 107-137.
430. Fourcade, J., Z. Sun, M. Benallaoua, P. Guillaume, I. F. Luescher, C. Sander, J. M. Kirkwood, V. Kuchroo, and H. M. Zarour. 2010. Upregulation of Tim-3 and PD-1 expression is

- associated with tumor antigen-specific CD8⁺ T cell dysfunction in melanoma patients. *J Exp Med* 207: 2175-2186.
431. Sakuishi, K., S. F. Ngiow, J. M. Sullivan, M. W. Teng, V. K. Kuchroo, M. J. Smyth, and A. C. Anderson. 2013. TIM3(+)FOXP3(+) regulatory T cells are tissue-specific promoters of T-cell dysfunction in cancer. *Oncoimmunology* 2: e23849.
 432. Sakhdari, A., S. Mujib, B. Vali, F. Y. Yue, S. MacParland, K. Clayton, R. B. Jones, J. Liu, E. Y. Lee, E. Benko, C. Kovacs, J. Gommerman, R. Kaul, and M. A. Ostrowski. 2012. Tim-3 negatively regulates cytotoxicity in exhausted CD8⁺ T cells in HIV infection. *PLoS One* 7: e40146.
 433. Li, X., H. Lu, Y. Gu, X. Zhang, G. Zhang, T. Shi, and W. Chen. 2020. Tim-3 suppresses the killing effect of V γ 9V δ 2 T cells on colon cancer cells by reducing perforin and granzyme B expression. *Experimental Cell Research* 386: 111719.
 434. Lin, W., Y. Suo, Y. Deng, Z. Fan, Y. Zheng, X. Wei, and Y. Chu. 2015. Morphological change of CD4(+) T cell during contact with DC modulates T-cell activation by accumulation of F-actin in the immunology synapse. *BMC Immunol* 16: 49.
 435. Negulescu, P. A., T. B. Krasieva, A. Khan, H. H. Kerschbaum, and M. D. Cahalan. 1996. Polarity of T cell shape, motility, and sensitivity to antigen. *Immunity* 4: 421-430.
 436. Kupfer, A., and S. J. Singer. 1989. Cell biology of cytotoxic and helper T cell functions: immunofluorescence microscopic studies of single cells and cell couples. *Annu Rev Immunol* 7: 309-337.
 437. Li, Y., H. M. Tunbridge, G. J. Britton, E. V. Hill, P. Sinai, S. Cirillo, C. Thompson, F. Fallah-Arani, S. J. Dovedi, D. C. Wraith, and C. Wülfing. 2021. A LAT-Based Signaling Complex in the Immunological Synapse as Determined with Live Cell Imaging Is Less Stable in T Cells with Regulatory Capability. *Cells* 10.
 438. Sinai, P., I. M. Dozmorov, R. Song, P. L. Schwartzberg, E. K. Wakeland, and C. Wülfing. 2014. T/B-cell interactions are more transient in response to weak stimuli in SLE-prone mice. *Eur J Immunol* 44: 3522-3531.
 439. Li, G., X. Liang, and M. T. Lotze. 2013. HMGB1: The Central Cytokine for All Lymphoid Cells. *Frontiers in immunology* 4: 68-68.
 440. Moar, P., and R. Tandon. 2021. Galectin-9 as a biomarker of disease severity. *Cell Immunol* 361: 104287.
 441. Kurtulus, S., A. Madi, G. Escobar, M. Klapholz, J. Nyman, E. Christian, M. Pawlak, D. Dionne, J. Xia, O. Rozenblatt-Rosen, V. K. Kuchroo, A. Regev, and A. C. Anderson. 2019. Checkpoint Blockade Immunotherapy Induces Dynamic Changes in PD-1(-)CD8(+) Tumor-Infiltrating T Cells. *Immunity* 50: 181-194.e186.
 442. Fourcade, J., Z. Sun, O. Pagliano, J. M. Chauvin, C. Sander, B. Janjic, A. A. Tarhini, H. A. Tawbi, J. M. Kirkwood, S. Moschos, H. Wang, P. Guillaume, I. F. Luescher, A. Krieg, A. C. Anderson, V. K. Kuchroo, and H. M. Zarour. 2014. PD-1 and Tim-3 regulate the expansion of tumor antigen-specific CD8⁺ T cells induced by melanoma vaccines. *Cancer Res* 74: 1045-1055.
 443. Lu, X., L. Yang, D. Yao, X. Wu, J. Li, X. Liu, L. Deng, C. Huang, Y. Wang, D. Li, and J. Liu. 2017. Tumor antigen-specific CD8(+) T cells are negatively regulated by PD-1 and Tim-3 in human gastric cancer. *Cell Immunol* 313: 43-51.
 444. Zhang, Y., P. Cai, T. Liang, L. Wang, and L. Hu. 2017. TIM-3 is a potential prognostic marker for patients with solid tumors: A systematic review and meta-analysis. *Oncotarget* 8: 31705-31713.
 445. Li, H., K. Wu, K. Tao, L. Chen, Q. Zheng, X. Lu, J. Liu, L. Shi, C. Liu, G. Wang, and W. Zou. 2012. Tim-3/galectin-9 signaling pathway mediates T-cell dysfunction and predicts poor prognosis in patients with hepatitis B virus-associated hepatocellular carcinoma. *Hepatology* 56: 1342-1351.
 446. John, S., and R. Mishra. 2016. Galectin-9: From cell biology to complex disease dynamics. *J Biosci* 41: 507-534.

447. Zhang, F., M. Zheng, Y. Qu, J. Li, J. Ji, B. Feng, A. Lu, J. Li, M. Wang, and B. Liu. 2009. Different roles of galectin-9 isoforms in modulating E-selectin expression and adhesion function in LoVo colon carcinoma cells. *Molecular Biology Reports* 36: 823-830.
448. Nakajima, A., H. Iijima, M. F. Neurath, T. Nagaishi, E. E. Nieuwenhuis, R. Raychowdhury, J. Glickman, D. M. Blau, S. Russell, K. V. Holmes, and R. S. Blumberg. 2002. Activation-induced expression of carcinoembryonic antigen-cell adhesion molecule 1 regulates mouse T lymphocyte function. *J Immunol* 168: 1028-1035.
449. Huang, Y.-H., C. Zhu, Y. Kondo, A. C. Anderson, A. Gandhi, A. Russell, S. K. Dougan, B.-S. Petersen, E. Melum, T. Pertel, K. L. Clayton, M. Raab, Q. Chen, N. Beauchemin, P. J. Yazaki, M. Pyzik, M. A. Ostrowski, J. N. Glickman, C. E. Rudd, H. L. Ploegh, A. Franke, G. A. Petsko, V. K. Kuchroo, and R. S. Blumberg. 2016. Corrigendum: CEACAM1 regulates TIM-3-mediated tolerance and exhaustion. *Nature* 536: 359-359.
450. Chen, Z., L. Chen, S.-W. Qiao, T. Nagaishi, and R. S. Blumberg. 2008. Carcinoembryonic antigen-related cell adhesion molecule 1 inhibits proximal TCR signaling by targeting ZAP-70. *Journal of immunology (Baltimore, Md. : 1950)* 180: 6085-6093.
451. Kammerer, R., S. Hahn, B. B. Singer, J. S. Luo, and S. von Kleist. 1998. Biliary glycoprotein (CD66a), a cell adhesion molecule of the immunoglobulin superfamily, on human lymphocytes: structure, expression and involvement in T cell activation. *Eur J Immunol* 28: 3664-3674.
452. Donda, A., L. Mori, A. Shamshiev, I. Carena, C. Mottet, M. H. Heim, C. Beglinger, F. Grunert, C. Rochlitz, L. Terracciano, P. Jantschkeff, and G. De Libero. 2000. Locally inducible CD66a (CEACAM1) as an amplifier of the human intestinal T cell response. *Eur J Immunol* 30: 2593-2603.
453. Khairnar, V., V. Duhan, A. M. Patil, F. Zhou, H. Bhat, C. Thoens, P. Sharma, T. Adomati, S. K. Friendrich, J. Bezgovsek, J. D. Dreesen, G. Wennemuth, A. M. Westendorf, G. Zelinsky, U. Dittmer, C. Hardt, J. Timm, J. R. Gothert, P. A. Lang, B. B. Singer, and K. S. Lang. 2018. CEACAM1 promotes CD8(+) T cell responses and improves control of a chronic viral infection. *Nat Commun* 9: 2561.
454. Moriya, H. 2015. Quantitative nature of overexpression experiments. *Molecular biology of the cell* 26: 3932-3939.
455. Stoebel, D. M., A. M. Dean, and D. E. Dykhuizen. 2008. The cost of expression of Escherichia coli lac operon proteins is in the process, not in the products. *Genetics* 178: 1653-1660.
456. Singleton, K. L., K. T. Roybal, Y. Sun, G. Fu, N. R. Gascoigne, N. S. van Oers, and C. Wulfiging. 2009. Spatiotemporal patterning during T cell activation is highly diverse. *Sci Signal* 2: ra15.
457. Garmanchuk, L. V., E. M. Perepelitsyna, M. V. Sidorenko, and L. I. Ostapchenko. 2009. [Kinetics of growth 2-D and 3-D cell models under influence of microenvironment]. *Tsitol Genet* 43: 14-21.
458. Simmons, A., and J. Alberola-Ila. 2016. Retroviral Transduction of T Cells and T Cell Precursors. *Methods in molecular biology (Clifton, N.J.)* 1323: 99-108.
459. Hagani, A. B., I. Rivière, C. Tan, A. Krause, and M. Sadelain. 1999. Activation conditions determine susceptibility of murine primary T-lymphocytes to retroviral infection. *J Gene Med* 1: 341-351.
460. Miller, D. G., M. A. Adam, and A. D. Miller. 1990. Gene transfer by retrovirus vectors occurs only in cells that are actively replicating at the time of infection. *Mol Cell Biol* 10: 4239-4242.
461. Liu, J., G. Di, C. T. Wu, X. Hu, and H. Duan. 2013. CEACAM1 inhibits cell-matrix adhesion and promotes cell migration through regulating the expression of N-cadherin. *Biochem Biophys Res Commun* 430: 598-603.
462. Klaile, E., M. M. Müller, C. Kannicht, B. B. Singer, and L. Lucka. 2005. CEACAM1 functionally interacts with filamin A and exerts a dual role in the regulation of cell migration. *J Cell Sci* 118: 5513-5524.

463. Obrink, B., H. Sawa, I. Scheffrahn, B. B. Singer, K. Sigmundsson, U. Sundberg, R. Heymann, N. Beauchemin, G. Weng, P. Ram, and R. Iyengar. 2002. Computational analysis of isoform-specific signal regulation by CEACAM1-A cell adhesion molecule expressed in PC12 cells. *Ann N Y Acad Sci* 971: 597-607.
464. Varadarajan, N., B. Julg, Y. J. Yamanaka, H. Chen, A. O. Ogunniyi, E. McAndrew, L. C. Porter, A. Piechocka-Trocha, B. J. Hill, D. C. Douek, F. Pereyra, B. D. Walker, and J. C. Love. 2011. A high-throughput single-cell analysis of human CD8⁺ T cell functions reveals discordance for cytokine secretion and cytolysis. *J Clin Invest* 121: 4322-4331.
465. Gao, X., Y. Zhu, G. Li, H. Huang, G. Zhang, F. Wang, J. Sun, Q. Yang, X. Zhang, and B. Lu. 2012. TIM-3 expression characterizes regulatory T cells in tumor tissues and is associated with lung cancer progression. *PLoS One* 7: e30676.
466. Jin, H. T., A. C. Anderson, W. G. Tan, E. E. West, S. J. Ha, K. Araki, G. J. Freeman, V. K. Kuchroo, and R. Ahmed. 2010. Cooperation of Tim-3 and PD-1 in CD8 T-cell exhaustion during chronic viral infection. *Proc Natl Acad Sci U S A* 107: 14733-14738.
467. Hughes, C. S., L. M. Postovit, and G. A. Lajoie. 2010. Matrigel: a complex protein mixture required for optimal growth of cell culture. *Proteomics* 10: 1886-1890.
468. Hirschhaeuser, F., H. Menne, C. Dittfeld, J. West, W. Mueller-Klieser, and L. A. Kunz-Schughart. 2010. Multicellular tumor spheroids: an underestimated tool is catching up again. *J Biotechnol* 148: 3-15.
469. Zheng, Y., Y. Kong, and E. J. Goetzl. 2001. Lysophosphatidic Acid Receptor-Selective Effects on Jurkat T Cell Migration Through a Matrigel Model Basement Membrane. *The Journal of Immunology* 166: 2317-2322.
470. Leppert, D., E. Waubant, R. Galardy, N. W. Bunnett, and S. L. Hauser. 1995. T cell gelatinases mediate basement membrane transmigration in vitro. *The Journal of Immunology* 154: 4379-4389.
471. Xia, M., D. Leppert, S. L. Hauser, S. P. Sreedharan, P. J. Nelson, A. M. Krensky, and E. J. Goetzl. 1996. Stimulus specificity of matrix metalloproteinase dependence of human T cell migration through a model basement membrane. *J Immunol* 156: 160-167.
472. Owen, J. L., V. Iragavarapu-Charyulu, Z. Gunja-Smith, L. M. Herbert, J. F. Grosso, and D. M. Lopez. 2003. Up-regulation of matrix metalloproteinase-9 in T lymphocytes of mammary tumor bearers: role of vascular endothelial growth factor. *J Immunol* 171: 4340-4351.
473. Shao, H., M. Moller, D. Wang, A. Ting, M. Boulina, and Z.-J. Liu. 2020. A Novel Stromal Fibroblast-Modulated 3D Tumor Spheroid Model for Studying Tumor-Stroma Interaction and Drug Discovery. *JoVE*: e60660.
474. Aisenbrey, E. A., and W. L. Murphy. 2020. Synthetic alternatives to Matrigel. *Nature reviews. Materials* 5: 539-551.
475. Nóbrega, A. F., M. S. Maldonado, and G. A. Dos Reis. 1986. Analysis of isolated and combined effects of calcium ionophore and phorbol ester on T lymphocyte activation. *Clin Exp Immunol* 65: 559-569.
476. Markel, G., R. Seidman, N. Stern, T. Cohen-Sinai, O. Izhaki, G. Katz, M. Besser, A. J. Treves, R. S. Blumberg, R. Loewenthal, O. Mandelboim, A. Orenstein, and J. Schachter. 2006. Inhibition of human tumor-infiltrating lymphocyte effector functions by the homophilic carcinoembryonic cell adhesion molecule 1 interactions. *J Immunol* 177: 6062-6071.
477. Markel, G., R. Seidman, Y. Cohen, M. J. Besser, T. C. Sinai, A. J. Treves, A. Orenstein, R. Berger, and J. Schachter. 2009. Dynamic expression of protective CEACAM1 on melanoma cells during specific immune attack. *Immunology* 126: 186-200.

Chapter 8 Supplementary Figures

8.1 FACS gating for isolating GFP-positive retrovirally transduced CL4 T-cells.

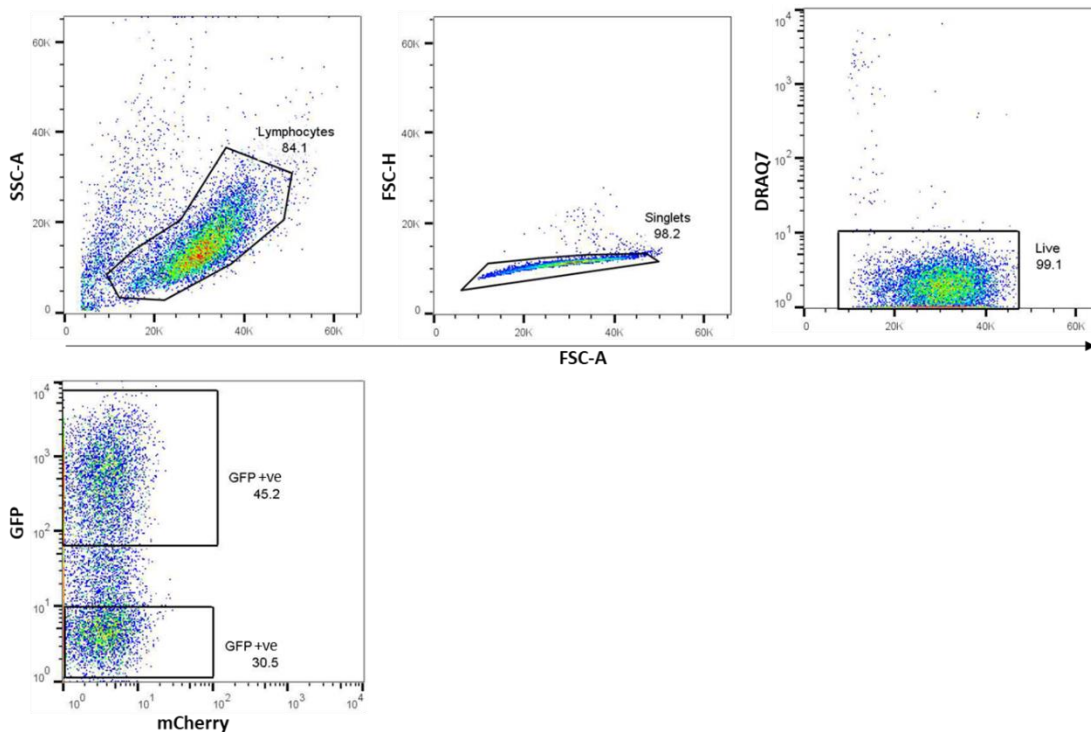


Figure 8.1 Gating strategy for retrovirally transduced CL4 T-cells that were isolated by fluorescence-activated cell sorting (FACS) for GFP-positivity, 72h post-transduction.

Representative gating strategy for sorting of GFP-positive CL4 T-cells. Lymphocytes were gated based on forward scatter-area (FSC-A) and side scatter-area (SSC-A) to remove cell debris, then single cells were isolated based on FSC-A and forward scatter-height (FSC-H). Live cells were isolated based on the fluorescent intensity of DRAQ7 viability dye staining and FSC/A. Successfully transduced CL4 T-cells that overexpressed the GFP-tagged protein of interest were gated based on GFP signal.

8.2 Gating for flow cytometry analysis of RencaHA^{tdT} cells from 2D and 3D culture.

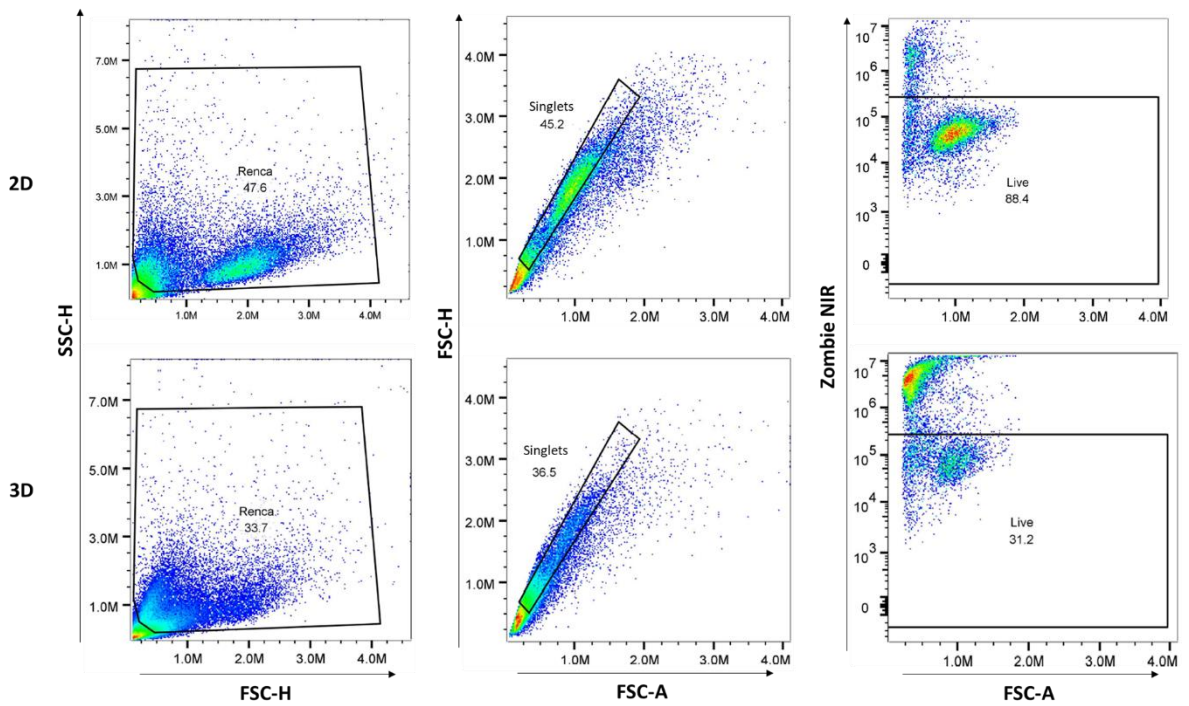


Figure 8.2 Flow cytometric gating strategy for Renca cells from 2D and 3D culture to obtain live single cells for antibody-staining for CEACAM-1, MHC-I and Galectin-9 expression.

Representative gating strategy for comparison of protein expression levels in RencaHA^{tdT} cells cultured in 2D and 3D. Single-suspensions of 2D- (top row) and 3D-cultured (bottom row) RencaHA^{tdT} cells were first gated using FSC-H and SSC-H to remove cell debris. Single RencaHA^{tdT} cells were isolated using FSC-A and FSC-H. Live RencaHA^{tdT} cells were isolated using Zombie Near Infrared (NIR) viability dye.

8.3 Gating strategy to determine TIM3 and CEACAM1 cell surface expression on GFP-positive CL4 T-cells transduced with TIM3-GFP, CEACAM1-TIM3-GFP and CEACAM1-GFP retroviral constructs.

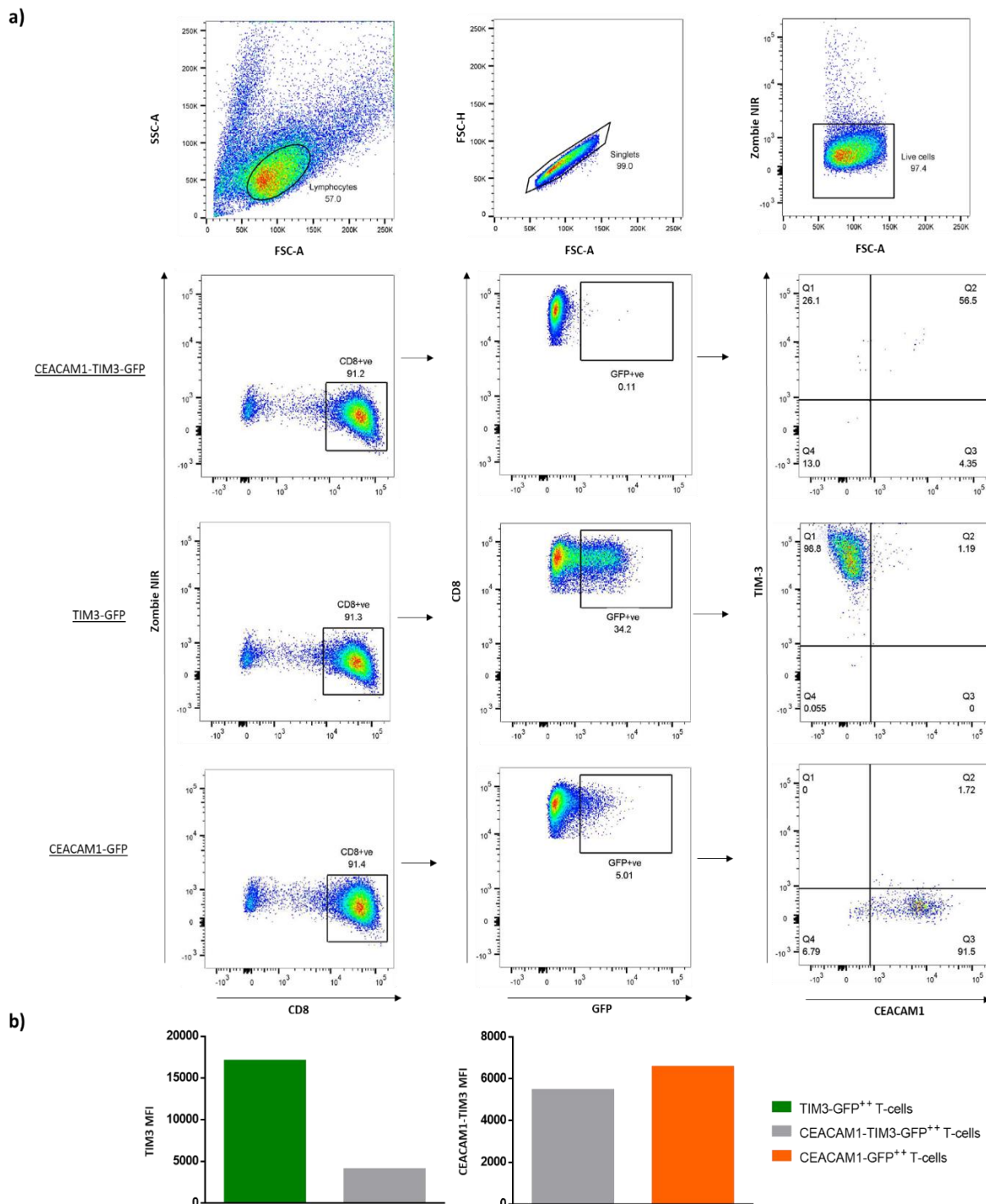


Figure 8.3 TIM3-GFP⁺⁺ cells expressed 1.8-fold more TIM3 than CEACAM1-TIM3-GFP⁺⁺ cells, CEACAM1-GFP cells expressed 1.2-fold more CEACAM1 than CEACAM1-TIM3-GFP⁺⁺ cells. CL4 T-cells that overexpressed CEACAM1-GFP (CEACAM1-GFP⁺⁺), TIM3-GFP (TIM3-GFP⁺⁺) or CEACAM1-TIM3-GFP (CEACAM1-TIM3-GFP⁺⁺) were stained using antibodies for CEACAM1 and TIM3 expression levels; a representative gating strategy is shown. **a)** T-cells were first isolated using SSC-A and FSC-A and then single cells were gated using FSC-H and FSC-A. Zombie NIR was used to isolate live cells. CD8-positive cells were isolated using an anti-CD8 antibody. T-cells were gated for GFP expression. TIM3 and CEACAM1 expression were assessed using anti-TIM3 and anti-

CEACAM1 antibodies. **b)** TIM3-GFP⁺⁺ T-cells expressed ~3-fold higher levels of TIM3 *versus* CEACAM1-TIM3-GFP⁺⁺ T-cells. CEACAM1-TIM3-GFP⁺⁺ and CEACAM1-GFP⁺⁺ T-cells expressed comparable levels of CEACAM1.

8.4 Gating strategy for isolating RencaHA^{tdT} and RencaHA^{CEAC1} cells to confirm CEACAM1 expression levels by antibody-staining and flow cytometry.

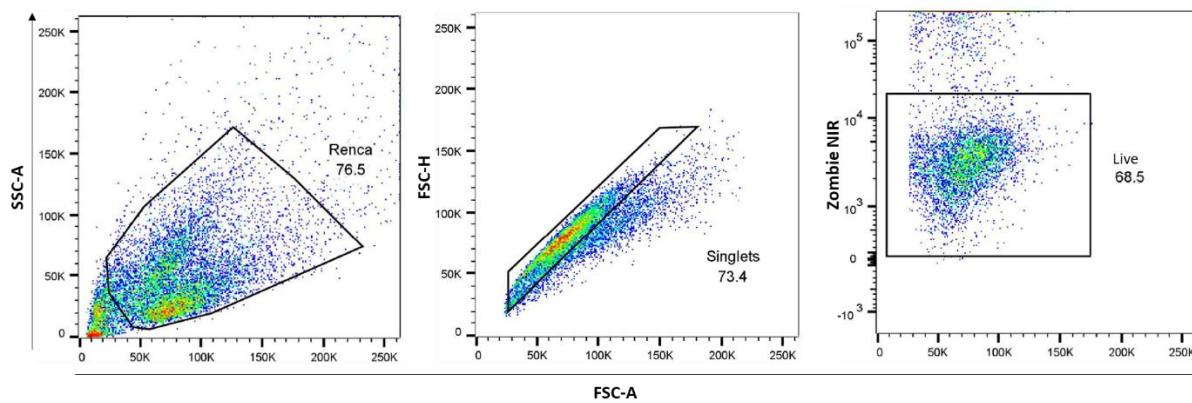


Figure 8.4 RencaHA^{tdT} and RencaHA^{CEAC1} cells were sorted to obtain live single cells.

RencaHA^{tdT} and RencaHA^{CEAC1} cells were isolated using SSC-A and FSC-A to exclude debris. Single cells were isolated using FSC-H and FSC-A. Zombie NIR viability dye was used to isolate live Renca cells.